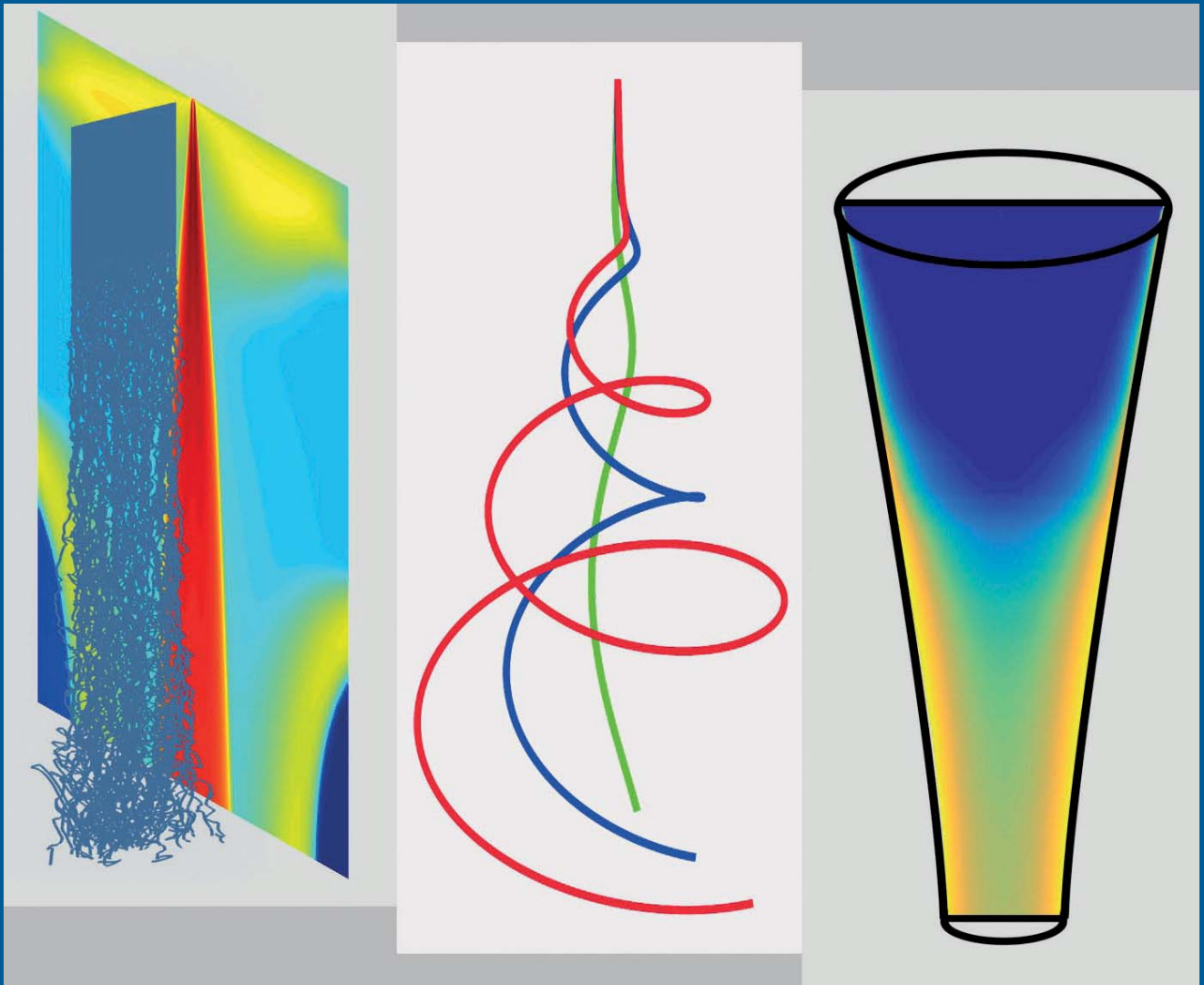


Manuel Wieland

---

# On Modeling and Simulation of Industrial Fiber Spinning Processes: Diffusive Effects, Electrified Jets and Turbulent Airflows



Fraunhofer-Institut für  
Techno- und Wirtschaftsmathematik ITWM

# On Modeling and Simulation of Industrial Fiber Spinning Processes: Diffusive Effects, Electrified Jets and Turbulent Airflows

Manuel Wieland

FRAUNHOFER VERLAG

**Kontakt:**

Fraunhofer-Institut für Techno- und Wirtschaftsmathematik ITWM  
Fraunhofer-Platz 1  
67663 Kaiserslautern  
Telefon +49 631/31600-0  
Fax +49 631/31600-1099  
E-Mail [info@itwm.fraunhofer.de](mailto:info@itwm.fraunhofer.de)  
URL [www.itwm.fraunhofer.de](http://www.itwm.fraunhofer.de)

**Bibliografische Information der Deutschen Nationalbibliothek**

Die Deutsche Nationalbibliothek verzeichnet diese Publikation in der Deutschen Nationalbibliografie; detaillierte bibliografische Daten sind im Internet über <http://dnb.d-nb.de> abrufbar.  
ISBN (Print): 978-3-8396-1573-7

**D 385**

Zugl.: Trier, Univ., Diss., 2019

Titelbild: © Manuel Wieland

Druck: Mediendienstleistungen des  
Fraunhofer-Informationszentrum Raum und Bau IRB, Stuttgart

Für den Druck des Buches wurde chlor- und säurefreies Papier verwendet.

© by **FRAUNHOFER VERLAG**, 2020

Fraunhofer-Informationszentrum Raum und Bau IRB  
Postfach 80 04 69, 70504 Stuttgart  
Nobelstraße 12, 70569 Stuttgart  
Telefon 07 11 9 70-25 00  
Telefax 07 11 9 70-25 08  
E-Mail [verlag@fraunhofer.de](mailto:verlag@fraunhofer.de)  
URL <http://verlag.fraunhofer.de>

Alle Rechte vorbehalten

Dieses Werk ist einschließlich aller seiner Teile urheberrechtlich geschützt. Jede Verwertung, die über die engen Grenzen des Urheberrechtsgesetzes hinausgeht, ist ohne schriftliche Zustimmung des Verlages unzulässig und strafbar. Dies gilt insbesondere für Vervielfältigungen, Übersetzungen, Mikroverfilmungen sowie die Speicherung in elektronischen Systemen.

Die Wiedergabe von Warenbezeichnungen und Handelsnamen in diesem Buch berechtigt nicht zu der Annahme, dass solche Bezeichnungen im Sinne der Warenzeichen- und Markenschutz-Gesetzgebung als frei zu betrachten wären und deshalb von jedermann benutzt werden dürften. Soweit in diesem Werk direkt oder indirekt auf Gesetze, Vorschriften oder Richtlinien (z.B. DIN, VDI) Bezug genommen oder aus ihnen zitiert worden ist, kann der Verlag keine Gewähr für Richtigkeit, Vollständigkeit oder Aktualität übernehmen.

# **On Modeling and Simulation of Industrial Fiber Spinning Processes: Diffusive Effects, Electrified Jets and Turbulent Airflows**

Modellierung und Simulation  
industrieller Fadenspinprozesse:  
Diffusive Effekte, elektrifizierte Jets und  
turbulente Luftströmungen

Vom Fachbereich IV  
der Universität Trier  
zur  
Verleihung des Doktorgrades Dr. rer. nat.  
genehmigte Dissertation

von

Manuel Wieland

Tag der mündlichen Prüfung: 29. November 2019

Gutachter: Prof. Dr. Nicole Marheineke  
Prof. Dr. Axel Klar  
Prof. Dr. Andreas Meister  
Prof. Dr. Volker Schulz

# Zusammenfassung

In der technischen Textilindustrie wächst die Bedeutung von Modellen und Simulationen zugrundeliegender Herstellungsmethoden, um existierende Spinnanlagen zu optimieren und die Entwicklungszeiten für neue Anlagen zu verkürzen. Eine große Bedeutung wird der Studie von Fadendynamiken zugemessen, da die Eigenschaften der gesponnenen Fäden maßgeblich die Beschaffenheit des finalen Produkts bestimmen. Im Zuge der Modellierung industrieller Spinnprozesse muss eine Fülle von Effekten berücksichtigt werden. Dies sind zum Beispiel die wechselseitige Interaktion der Fäden mit einer möglicherweise hoch turbulenten äußeren Luftströmung, diffusive Effekte im Fadeninneren als auch Wärme- und Stoffübergang am Fadenrand auf Grund von Lösungsmittelverdampfung und elektrische Effekte, die auf einen elektrifizierten Jet (englisch für *Fadenstrahl*) in einem äußeren elektrischen Feld einwirken. Auf Grund des zu hohen Rechenaufwandes für die Lösung der zugrundeliegenden dreidimensionalen Multiskalen-Multiphasen-Probleme ist eine direkte numerische Simulation nicht praktikabel. Die spezielle Cosserat Theorie, welche auf einer eindimensionalen Beschreibung eines Fadens mittels dessen Mittellinie und der Orientierung seiner Querschnittsflächen beruht, bildet deshalb unsere Modellbasis. In dieser Arbeit zeigen wir, wie diese Modellbasis auf geeignete Weise erweitert werden kann, dass sämtliche industrierelevanten physikalischen Effekte beschrieben werden können. Für die numerische Lösung der entstehenden Randwertprobleme gewöhnlicher bzw. partieller Differentialgleichungen entwickeln wir auf das jeweilige Problem zugeschnittene Lösungsstrategien. Das Potenzial und die Leistungsfähigkeit unseres Modell-Simulations-Rahmens demonstrieren wir exemplarisch anhand dreier industrieller Spinnprozesse: Trockenspinnen, Elektros핀nen und Meltblown-Prozess (englisch für *Schmelzblasverfahren*). Zum ersten Mal in der Literatur präsentieren wir Simulationsergebnisse von vielen gleichzeitig trocken-gesponnenen Fäden in einer wechselseitigen Interaktion mit der äußeren Luftströmung, eine detaillierte Untersuchung der Whipping-Instabilität (englisch für *Schwingungs-Instabilität*) beim industriellen Elektros핀nenprozess mittels eines rotierenden Bezugssystems und Simulationsergebnisse von Fäden im Meltblown-Prozess, wobei die Einbeziehung von viskoelastischen Materialeffekten und der äußeren turbulenten Luftströmung zu realistisch dünnen Fadendurchmessern führt.



# Abstract

In the technical textile industry models and simulations of underlying manufacturing processes increasingly gain attention in order to optimize existing spinning devices and to shorten development times for new setups. Special attention is paid to studies of fiber dynamics, since the properties of the spun fibers are crucial for the final product. In view of modeling industrial spinning setups plenty of effects have to be taken into account. These are, for example, the two-way interaction of the fibers with a possibly highly turbulent outer airflow, diffusive effects in the fiber interior as well as heat and mass transfer at the fiber boundary due to solvent evaporation, and electric effects when an electrified jet is injected into an outer electric field. Since the underlying three-dimensional multiscale-multiphase problems require unfeasible computation times, direct numerical simulations are not practical. Thus, the special Cosserat theory with one-dimensional descriptions of the fibers in terms of the fiber's centerline and the orientation of its cross-sections build our model basis. In this work we show that this model basis can be suitably extended to describe all physically relevant effects present in industrial setups. For the numerical treatment of resulting boundary value problems of ordinary and partial differential equations we develop problem tailored solution strategies. To show the capability and efficiency of our model-simulation framework we exemplarily investigate three industrial spinning processes: dry spinning, electrospinning, and melt-blowing. For the first time in literature we present simulation results of multiple simultaneously dry spun fibers in a two-way interaction with an outer airflow, a detailed investigation of the fiber's whipping movement present in industrial electrospinning utilizing a rotating reference frame as well as simulation results of melt-blown fibers including viscoelastic and turbulent airflow effects leading to realistically thin fibers.



# Acknowledgments

This work is the result of a cooperation of the Fraunhofer Institute for Industrial Mathematics (ITWM) in Kaiserslautern and Trier University. I want to deeply thank Prof. Dr. Nicole Marheineke for encouraging me and providing the possibility to work on this very interesting research topic. Over the last years we had many fruitful discussions, which were always a helpful input and gave me new insights into the topic. Her constructive feedback and suggestions improved my scientific output in many ways. Furthermore, I express my deeply gratitude to Dr. Raimund Wegener, who always took time for my questions and gave me helpful advice. I benefited greatly from his years of experience in the field of modeling fiber and jet dynamics. Discussions with him were always an inspiration to me. Special thanks also go to Dr. Walter Arne for his support. His knowledge in the simulations of spinning processes, in particular concerning numerical solution strategies, helped me a lot to improve my own numerical procedures. I also want to thank Dr. Robert Feßler for our helpful discussions in the field of analytic solution expressions for the two-dimensional radial heat equation. Furthermore, I thank Dr. Javier Rivero-Rodríguez for sharing his ideas in the field of electrospinning processes with me. The successful cooperation with all these named persons led to several joint scientific publications.

Besides that I want to thank the Flexible Structures group as well as all employees and PhD students at the department of Transport Processes at the Fraunhofer ITWM for the excellent and constructive working atmosphere. In particular, I thank Dr. Dietmar Hietel and Dr. Raimund Wegener for the uncomplicated handling of organizational matters. I also thank the work group Modeling and Numerics at Trier University for their warm welcome and organizational help during my visits there.

I would like to thank my family, in particular my parents, for their unconditional support. Without their help and confirming words I would not have been able to successfully finish this thesis. Last but not least, I deeply thank my girlfriend Marina, who always believed in me and gave me the support I needed.



# Contents

<b>1</b>	<b>Introduction</b>	<b>1</b>
<b>2</b>	<b>Models for fibers and jets</b>	<b>9</b>
2.1	Special Cosserat rod theory . . . . .	10
2.1.1	Reference state . . . . .	10
2.1.2	Kinematic and dynamic equations . . . . .	11
2.1.3	Geometric models . . . . .	14
2.1.4	Material laws . . . . .	16
2.1.5	Nondimensional formulation . . . . .	18
2.1.6	Parameterization in Eulerian description . . . . .	20
2.2	Asymptotic string models . . . . .	23
2.2.1	Viscous strings . . . . .	24
2.2.2	Elastic strings . . . . .	25
2.2.3	Viscoelastic strings . . . . .	25
2.3	External loads . . . . .	27
2.3.1	Gravitational force . . . . .	27
2.3.2	Aerodynamic forces . . . . .	27
<b>3</b>	<b>Numerical framework</b>	<b>31</b>
3.1	Boundary value problems of ordinary differential equations . . . . .	32
3.1.1	Collocation method . . . . .	32
3.1.2	Continuation method . . . . .	34
3.2	Boundary value problems of quasilinear hyperbolic partial differential equations . . . . .	35
3.3	Radial advection-diffusion equations with Robin boundary conditions	37
3.4	Fiber-airflow interaction . . . . .	42
<b>4</b>	<b>Fiber spinning with evaporation effects in airflows</b>	<b>45</b>
4.1	Viscous fiber dry spinning model . . . . .	48
4.1.1	Three-dimensional uni-axial fiber model . . . . .	48
4.1.2	Dimensionally reduced uni-axial fiber model . . . . .	53
4.1.3	Curved fiber model . . . . .	62
4.1.4	Heat and mass transfer models . . . . .	67

4.2	Solution strategy . . . . .	70
4.2.1	Model-specific continuation method . . . . .	72
4.2.2	Product integration method . . . . .	74
4.3	Approximation quality and performance . . . . .	76
4.4	Industrial dry spinning with two-way coupled airflow . . . . .	81
4.4.1	Model closing . . . . .	81
4.4.2	Spinning of uni-axial fibers . . . . .	84
4.4.3	Spinning of curved fibers . . . . .	91
<b>5</b>	<b>Electrified visco-capillary jets in airflows</b>	<b>99</b>
5.1	Viscous fiber electrospinning model . . . . .	102
5.1.1	Stationary model equations . . . . .	102
5.1.2	Capillary and electric forces . . . . .	109
5.2	Solution strategy . . . . .	111
5.3	Performance and parameter study . . . . .	114
5.3.1	Performance of continuation algorithm . . . . .	115
5.3.2	Influence of dimensionless model parameters . . . . .	116
5.4	Strong whipping effects . . . . .	119
<b>6</b>	<b>Fibers in turbulent airflows</b>	<b>125</b>
6.1	Viscoelastic fiber melt-blowing model . . . . .	128
6.1.1	Asymptotic jet model and classification . . . . .	128
6.1.2	Boundary conditions . . . . .	130
6.1.3	Incorporation of turbulent airflow velocity fluctuations . . . . .	134
6.2	Industrial melt-blowing . . . . .	137
6.2.1	Process setup . . . . .	137
6.2.2	Model closing . . . . .	140
6.2.3	Simulation strategy . . . . .	141
6.2.4	Results . . . . .	144
<b>7</b>	<b>Conclusion</b>	<b>151</b>
<b>Appendices</b>		
<b>A</b>	<b>Studies on the UCM string model</b>	<b>157</b>
A.1	Stresses in the elastic limit case . . . . .	157
A.2	Hierarchy of UCM models . . . . .	158
<b>B</b>	<b>Numerical schemes and solution methods</b>	<b>163</b>
B.1	Convergence of the finite volume scheme for quasilinear hyperbolic PDEs on a growing domain . . . . .	163
B.2	Analytic solution for the radial advection-diffusion equation . . . . .	166
B.3	Convergence and stability of the product integration method . . . . .	171

<b>C Studies on electrospinning</b>	<b>173</b>
C.1 Global linear stability analysis . . . . .	173
C.2 Resolution of boundary layers . . . . .	178
<b>Notations</b>	<b>181</b>
<b>Bibliography</b>	<b>187</b>



# 1. Introduction

The spinning of fibers as well as the production of nonwovens are key processes in the industrial manufacturing of technical textiles which are characterized by specific material properties such as flexibility, durability, absorbency, robustness, and insulation capacity. The application of technical textiles ranges from daily life products like diapers or cleaning cloths to high-tech products such as battery separators and medical products. Moreover, they find use in filtration (air or water filters), construction industry (glass wool), plastics industry (lightweight parts), textile industry (protection clothing), and car manufacturing (wall-paneling). At the basis of all such fibers and nonwovens is some sort of molten polymer which is extruded through small nozzles such that polymeric liquid jets evolve. These jets are stretched and solidified before they are either taken up by a roller or laid down onto a conveyor belt. Depending on the required fiber properties and the used polymers there exist different manufacturing processes.

## Fiber and nonwoven manufacturing methods

One of the oldest methods for the production of fibers is wet spinning, which is used for polymers that must be dissolved into a solvent to be able to be spun. The polymeric jets are extruded into a chemical bath that forces the fibers to precipitate and solidify. A similar method is dry spinning. There, a polymer solvent mixture is extruded into a tempered air stream, which leads to evaporation of the solvent and leaves solidified fibers behind. The process of melt spinning is suitable for thermoplastic polymers, i.e., polymers that can be melted and directly be spun. The polymeric fibers solidify by cooling after being extruded from the nozzles. Electrospinning is a method to produce very fine fibers (up to micro- and nano-scale) either from a polymer solvent mixture or also a polymer melt. In this process electric forces bring the electrically charged jet into a whipping motion leading to drastic jet thinning. An alternative method for the production of micro- and nano-fibers is the rotational or centrifugal spinning process. In this process the polymer solvent mixture or polymer melt is first distributed onto a rotating disc. By centrifugal forces the spinning fluid is ejected from the disk, undergoes stretching as well as solidification and the final fibers are deposited on a collector. Concerning the production of nonwovens thousands of fibers are overlaid forming a chaotic

structure. The fibers are bound together either mechanically, thermally or under the use of additional binders. For the production of staple fiber nonwovens the spun fibers are cut into pieces of centimeters length and put into fiber mats. Thereafter, these mats are re-opened, fed into a turbulent air stream and spread on a conveyor belt to form a web (airlay process). In the spunbond process fibers are spun into air, cooled and stretched, and directly deposited on a conveyor belt. Melt-blowing processes are also employed to produce nonwovens. In contrast to spunbond processes the resulting fibers are of much smaller size (diameters of micro- and nano-scale) due to a turbulent high speed air stream leading to a drastic jet thinning. An overview and further details on spinning technologies can be found in [63, 121, 129].

### **Need for simulations and mathematical challenges**

In all fiber and nonwoven manufacturing processes the quality of the final product is crucially determined by the dynamics of the spun jets. The quality depends mainly on the regularity of the fiber characteristics, such as diameter and strength. Regarding industrial spinning devices the challenge is to produce high quality fibers and nonwovens while maintaining a high productivity at the same time. With the help of simulation tools this challenge on quality and productivity can be tackled. Simulations of such complex manufacturing processes provide the opportunity to optimize existing spinning devices and to design new devices in an optimal way. In general, a spinning process forms a multiphase-multiscale problem such that a straightforward simulation of the underlying three-dimensional problem originating from classical continuum mechanics is very challenging. In particular, considering the simultaneous spinning of hundreds and thousands of fibers in mutual interaction with turbulent air and, additionally, the expected high order of fiber elongations lead to unfeasible computation times that make a full three-dimensional simulation of such problems completely unpractical [109]. Thus, the mathematical challenge lies in finding appropriate fiber models that contain all physically relevant effects and remain computationally feasible. In addition, the numerical framework has to be robust and efficient which creates the need for problem tailored solution algorithms.

### **Fiber models and preliminary studies**

In this thesis we focus on the modeling and simulation of fiber dynamics during the actual spinning, since the properties of the spun fibers are crucial for the properties of the final fibrous structure. For modeling and simulation of fiber laydown and web forming we refer to literature, e.g., [43, 54, 109]. Note that

in the following the word 'jet' denotes the viscous polymer stream leaving the nozzle, whereas we call this stream 'fiber' when it has been solidified and behaves mostly elastic.

Without any claim to completeness we give a short survey over previous works in the modeling and simulation of jet and fiber dynamics. First attempts in the modeling of spinning processes started in the 1960s, when Kase and Matsuo [51] as well as Matovich and Pearson [69] developed a one-dimensional, uni-axial, axis-symmetric, steady state jet model considering an isothermal viscous flow on a slender body. First strict asymptotic derivations of uni-axial jet models are given by Dewynn et al. [26] based on Stokes equations and by Howell et al. [49] based on Navier-Stokes equations. Panda, Marheineke and Wegener developed an asymptotic model for the dynamics of curved jets with and without surface tension [67, 77]. Furthermore, Marheineke et al. [65] asymptotically derived a one-dimensional model with viscoelastic material behavior from the three-dimensional upper-convected Maxwell model. The models of all these named works belong to the class of so called string models and the slenderness parameter  $\varepsilon$  as ratio of fiber diameter to length plays a key role in their asymptotic derivation. In particular, string models are asymptotic systems of leading order with respect to  $\varepsilon$ . However, Götz et al. [40] showed that due to the occurrence of singularities the solvability of string models is restricted to certain parameter regimes. To overcome this limitation, Noroozi et al. [73] added higher-order regularization terms to the string equations, yielding stable solutions. Beyond that, a further class of fiber models has been established, the so called rod models. Including angular momentum effects, these rod models can also be seen as a regularization of the associated string models as shown by Arne et al. [3, 6]. Fundamental works in the field of rods were done for example by Entov and Yarin [30, 119] as well as by Ribe [81]. Nevertheless, the use of rod models is not always advantageous over the string models due to their more complex numerical treatment. So in view of simulations of industrial spinning processes the choice of the specific fiber model requires careful considerations in order to achieve numerical computability and efficiency.

## **Aims and results of the thesis**

The Flexible Structures group at Fraunhofer ITWM has been convinced for quite a while that string and rod models offer the basis to model and simulate the fiber dynamics in any industrial spinning process [109]. In particular, a viscous rod model has been used for the simulation of rotational spinning processes [3, 5] and a generalized elastic string model for fiber dynamics in airlay and spunbond processes [43, 54, 109]. In this thesis we provide a model-simulation framework

that extends the applicability of rod and string models to any industrial spinning process. To show the capability of our framework we exemplarily consider three types of spinning processes that are driven by completely different effects: dry spinning, electrospinning, and melt-blowing. We do not claim to be the first ones being able to model and simulate these three spinning processes. But taking a close look at the existing literature, as done below, we find that the available models and simulation results still show the lack of important effects when industrial setups are investigated. We will show that by extending the basic rod/string models with process-specific effects we are able to close this gap between simulations and real world experiments. In the following we give an overview over our main achievements in the modeling and simulation of dry spinning, electrospinning, and melt-blowing with a basic embedding into literature. A detailed discussion of existing literature is given in Chap. 4, Chap. 5, and Chap. 6, respectively.

Considering the spinning of polymer solutions in view of the dry spinning method, the interaction of the spun fibers with the outer air stream is not included in the models of existing literature [16, 35, 74, 75]. Other previous works [41, 42, 88] focus on the simulation of one single fiber in an airflow, which has been measured in experiments or is assumed to be constant. However, in industrial setups several hundred fibers are spun simultaneously, such that mutual fiber-air interaction has to be taken into account. Moreover, industrial dry spinning processes are crucially determined by radial diffusive effects of the fiber quantities due to solvent evaporation leading to a coupled system of one- and two-dimensional model equations [41, 42, 88]. To make the simulation of all fibers in air with these radial diffusive effects feasible an efficiently evaluable model framework is needed, which we develop in this thesis. Our proposed dry spinning fiber model includes heat and mass transfer due to solvent evaporation based on the principle that action equals reaction. The presented numerical framework makes an efficient two-way coupling of fiber and airflow simulations for industrial setups feasible.

In electrospinning processes the whipping motion of the electrified jets is of fundamental importance for the jet thinning. This so called whipping instability has been approached by means of stability analysis in previous papers [58, 59, 80, 120]. In this thesis, we follow the idea of [85] and propose an alternative model framework in which the instability can be computed straightforwardly as the stable stationary solution of an asymptotic Cosserat rod description. For this purpose, the jet dynamics are described with respect to a frame rotating with the a priori unknown whipping frequency, which itself becomes part of the solution. Our numerical procedure makes the efficient and robust simulation of setups with high fiber elongations possible. The numerical results characterize the whipping effect qualitatively well and reveal the helical structure of the fiber curve in more detail than has been achieved in previous works [124, 126].

In previous studies on melt-blowing processes [91, 104, 118, 125] the numerically computed/predicted fiber thickness differs several orders of magnitude from those experimentally measured. Recent works [93, 118] suggest that this discrepancy might arise from the neglect of the turbulent aerodynamic fluctuations in the simulations. In this thesis we confirm this suggestion numerically. Whereas, in [122] a viscoelastic fiber model has been employed for melt-blowing, which is opposed to random pulsations, we develop a simulation framework with direct incorporation of the turbulent nature of the airflow. The turbulent effects are taken into account by a stochastic aerodynamic force model where the underlying velocity fluctuations are reconstructed from a  $k$ - $\epsilon$  turbulence description of the airflow taken from [50]. Our numerical framework for a growing fiber in turbulent air makes the simulation of industrial setups with viscoelastic effects feasible and the simulation results show the significance of the turbulence on the jet thinning. In particular, we achieve fiber diameters of realistic order of magnitude.

## Structure of the work

This thesis is structured as follows. In Chap. 2 we give a survey over existing models for fiber dynamics. Starting with an introduction into the theory of special Cosserat rods we present two possible parameterizations (Lagrangian, Eulerian) of the model equations, which can be equipped with various geometric models (inertia free, standard, incompressible) and material laws (elastic, viscous, viscoelastic). Furthermore, we describe a general transformation concept in order to obtain a non-dimensional form of the model equations. The class of string models is introduced as simplification of the rod models by considering the limit of vanishing slenderness parameter. All together, this chapter serves as 'box of bricks' from which we start to build the specific fiber models for each considered spinning process in the subsequent chapters. Chap. 3 provides the numerical framework for the solution of the fiber models covering boundary value problems of ordinary differential equations and hyperbolic partial differential equations as well as radial advection-diffusion equations with Robin-type boundary conditions. Moreover, the concept of weak iteratively coupling fiber and airflow simulations is introduced. In the subsequent chapters we study the previously named spinning processes: Chap. 4 is dedicated to spinning scenarios with evaporation effects in airflows with particular focus on dry spinning processes. After developing an efficiently evaluable viscous fiber model for uni-axial as well as curved fibers, we demonstrate the accuracy and efficiency of our proposed numerical solution strategy. Moreover, the applicability of our framework to industrial spinning setups with multiple fibers interacting with the airflow is shown. In Chap. 5 we describe the rotating model frame that allows the transition to a stationary consideration of the whipping instability present in electrospinning processes. After demonstrating

the performance of our numerical solution algorithm, the instability is examined with the help of a parameter study. Furthermore, we show the applicability of our framework to electrospinning scenarios with highly evolved whipping. In Chap. 6 we study fibers in turbulent airflows in view of melt-blowing processes. We utilize a viscoelastic fiber model on a growing fiber domain and explain the model closing with appropriate boundary conditions as well as the concept of incorporating turbulent airflow effects. Our proposed numerical simulation strategy makes the simulation of industrial melt-blowing setups feasible and shows final fibers of realistic fineness. In App. A we examine our string model with viscoelastic material behavior. In particular, we give an analytic expression for the stresses in the elastic limit case and embed our model hierarchically into the model base we find in literature. In App. B we validate the convergence of our numerical solution scheme used for the simulation of melt-blowing processes. Furthermore, we give a detailed derivation of an implicit solution expression for the radial advection-diffusion equation which we employ in the modeling of dry spinning processes and show convergence as well as stability properties of the product integration method used to solve the associated integral equation. Finally, in App. C we further examine the electrospinning process. With the help of a global linear stability analysis we show that the whipping instability is also an instability in mathematical sense. Furthermore, we demonstrate that occurring boundary layers are well resolved with our numerical solution algorithm.

### Published works within the scope of this thesis

Within the scope of this thesis the following works have been published:

#### Journal articles:

- M. Wieland, W. Arne, R. Feßler, N. Marheineke, and R. Wegener. Modeling and efficient simulation of dry spinning in airflows. *J. Comput. Phys.*, 384:326–348, 2018. [110]
- M. Wieland, W. Arne, N. Marheineke, and R. Wegener. Modeling and simulation of curved fibers in dry spinning scenarios. *Results Appl. Math.*, 3:100013, 2019. [115]
- W. Arne, N. Marheineke, M. Pérez-Saborid, J. Rivero-Rodríguez, R. Wegener, and M. Wieland. Whipping of electrified visco-capillary jets in airflows. *SIAM J. Appl. Math.*, 78(1):343–371, 2018. [4]
- M. Wieland, W. Arne, N. Marheineke, and R. Wegener. Melt-blowing of viscoelastic jets in turbulent airflows: Stochastic modeling and simulation. *Appl. Math. Model.*, 76:558–577, 2019. [113]

**Peer-reviewed proceedings and contributions to books:**

- M. Wieland, W. Arne, R. Feßler, N. Marheineke, and R. Wegener. Product integration method for simulation of radial effects in dry spinning processes. In *PAMM – Proc. Appl. Math. Mech.*, volume 18, page e201800055. Wiley, 2018. [111]
- M. Wieland, W. Arne, R. Feßler, N. Marheineke, and R. Wegener. On a dry spinning model using two-phase flow. In I. Faragó, F. Izsák, and P. Simon, editors, *Progress in Industrial Mathematics at ECMI 2018*, pages 19–25. Springer, 2019. [112]
- W. Arne, N. Marheineke, R. Wegener, and M. Wieland. Setup and numerical solution of a viscous Cosserat rod model describing electrospinning. In S. Petrik, editor, *NART 2017 – Nanofibers, Applications and Related Technologies*, pages 9–16. Technical University of Liberec, 2017. [8]
- M. Wieland, W. Arne, N. Marheineke, and R. Wegener. Model hierarchy of upper-convected Maxwell models with regard to simulations of melt-blowing processes. In *PAMM – Proc. Appl. Math. Mech.*, volume 19, page e201900018. Wiley, 2019. [114]

All publications are closely related to the three industrial applications that we study in this thesis, namely dryspinning in Chap. 4, electrospinning in Chap. 5, and melt-blowing in Chap. 6. In [110, 115, 111, 112] we investigate the dry spinning process. Regarding these publications the author of this thesis implemented the software in major parts, carried out all simulations and produced the drafts of the papers. The electrospinning process is subject of our studies in [4, 8]. The publications are the result of a collaboration with a group from the University of Sevilla in Spain. The basic idea of describing the jet’s whipping in terms of steady solutions with the help of a rotating reference frame originates from J. Rivero-Rodríguez and has been published by him in [85]. The author of this thesis contributed great parts of the numerical framework, which makes simulations of industrial-relevant parameter setups possible. Furthermore, he implemented major parts of the software, carried out all simulations and drafted the paper [4] in significant parts. The publications [113, 114] deal with the melt-blowing process. Regarding these works the author of this thesis implemented the software, carried out all simulations and drafted the papers. In all named publications the Flexible Structures group at the Fraunhofer ITWM helped to set up the industrial examples (physical parameters, airflow data, device geometries), which are closely related to real setups from their industrial partners. N. Marheineke acted supportively and advised on all stages from the initial idea development to the final versions of all publications.



## 2. Models for fibers and jets

Fibers and jets are slender objects due to their small ratio of cross-sectional diameter to length indicated by the slenderness parameter  $\varepsilon \ll 1$ . Thus, their dynamics can be modeled by one-dimensional equations resulting from averaging the three-dimensional balance laws over their cross-sections. First works developing one-dimensional mass, momentum and energy balances under the assumption of slenderness are [51, 69], an historical overview is given in [129], more recent publications are [26] and in particular [67, 77]. Our model core is built by the special Cosserat rod theory of [1], which specifies the fiber position with the help of a curve and the orientation of its cross-sections by means of an orthonormal triad. The model basis consists of balance laws for mass, linear as well as angular momentum and can be used to describe any material and physical setup. The rod model itself is closed by physically reasonable one-dimensional geometrical relations and material laws as well as models for the acting outer forces. Considering three-dimensional continuum mechanics, the asymptotic limit  $\varepsilon \rightarrow 0$  results in the so called string equations, which omit the angular momentum balance equation and the evaluation of the dynamics of the cross-sectional orientations. For industrial applications string models provide a simpler modeling framework and, therefore, form the basis for more efficient numerical solution algorithms compared to the more sophisticated rod models. However, the solvability of string models is crucially dependent on the physical parameters. Studies on viscous stationary string models, for example, show the loss of solutions for certain parameter regimes due to the occurrence of singularities [3, 6, 40]. The associated viscous rod models do not show these problems and can be seen as  $\varepsilon$ -dependent regularization of the string models.

This chapter is structured as follows. Since the rod model can be formulated with respect to various basis representations (invariant, director or outer basis), parameterizations (Lagrangian or Eulerian), setups (time-dependent or -independent) and dimensions (dimensional or nondimensional), we start with the invariant formulation in Lagrangian description of the kinematic and dynamic rod equations. Thereafter, we introduce possible geometric models (inertia free, cross-section-preserving, and incompressible) as well as material laws (elastic, viscous, and viscoelastic). In addition, we present a dimensionless formulation of the rod equations and explain the concept of parameterizing these equations in the Eulerian

description. Then, we turn to the string models and present three different types for viscous, elastic and viscoelastic material behavior. To close the chapter we consider models for external loads, where we focus on gravitational and aerodynamic forces. To large parts the subsequent presentation is adopted from [2, 89, 109].

## 2.1. Special Cosserat rod theory

As a jet is a slender long object, its dynamics can be reduced to a one-dimensional description by averaging the underlying three-dimensional balance laws over its cross-sections. In the special Cosserat rod theory there are two constitutive elements: a curve  $\vec{r} : \mathcal{D} \rightarrow \mathbb{E}^3$  specifying the jet position (e.g., midline) and an orthonormal director triad  $\{\vec{d}_1, \vec{d}_2, \vec{d}_3\} : \mathcal{D} \rightarrow \mathbb{E}^3$  that is attached to the curve and characterizes the orientation of the cross-sections in the three-dimensional Euclidean space  $\mathbb{E}^3$ , see Fig. 2.1. We assume  $\vec{d}_3 = \vec{d}_1 \times \vec{d}_2$ , such that the director triad forms a right-handed system. The Euclidean space  $\mathbb{E}^3$ , equipped with the Euclidean norm  $\|\cdot\|$ , can be identified with  $\mathbb{R}^3$  by choosing a basis. We particularly use the space-time domain  $\mathcal{D} = \{(\zeta, t) \in \mathbb{R}^2 \mid \zeta \in \mathcal{Q}(t), t \in (0, t_{end}]\}$  with time-dependent space domain  $\mathcal{Q}(t) = (\zeta_L(t), \zeta_R(t))$ , where  $t$  [s] is the time and  $\zeta$  [m] indicates the coordinate of each material point (material determined cross-section) to impose a Lagrangian (material) description. The left and right boundary of the domain are identified with the functions  $\zeta_L, \zeta_R : [0, t_{end}] \rightarrow \mathbb{R}$ , respectively, where  $\zeta_L(t) < \zeta_R(t)$  holds for all  $t \in (0, t_{end}]$ . The end time is represented by  $t_{end}$ . The Lagrangian parameterization is determined up to a constant by choosing an initial orientation and a time-independent reference state with fixed material configuration.

**Notation 2.1.** *In the following we write  $\vec{z}$  for any vector  $\vec{z} \in \mathbb{E}^3$  and use double over-lined capital letters for rank-two tensors  $\vec{\bar{Z}} \in \mathbb{E}^3 \otimes \mathbb{E}^3$ . A vector  $\vec{z} \in \mathbb{E}^3$  can be represented in various ways: We write  $\mathbf{z} \in \mathbb{R}^3$  (italic and bold) for the component tuple with respect to an outer orthonormal basis  $\{\vec{a}_1, \vec{a}_2, \vec{a}_3\} \subset \mathbb{E}^3$ , whereas  $\mathbf{z} \in \mathbb{R}^3$  (bold) addresses the representation of  $\vec{z}$  with respect to the space- and time-dependent director basis  $\{\vec{d}_1, \vec{d}_2, \vec{d}_3\}$ . Moreover, we write  $\cdot$  for scalar products and tensor-vector-operations, and use  $\otimes$  for tensor products. To clarify their meaning, new quantities are introduced with their SI unit in brackets  $[\cdot]$ .*

### 2.1.1. Reference state

The reference state of a Cosserat rod is given by its referential curve  $\vec{r}^\circ : \mathcal{Q}(t^\circ) \rightarrow \mathbb{E}^3$  and the orthonormal referential director triad  $\{\vec{d}_1^\circ, \vec{d}_2^\circ, \vec{d}_3^\circ\} : \mathcal{Q}(t^\circ) \rightarrow \mathbb{E}^3$  with

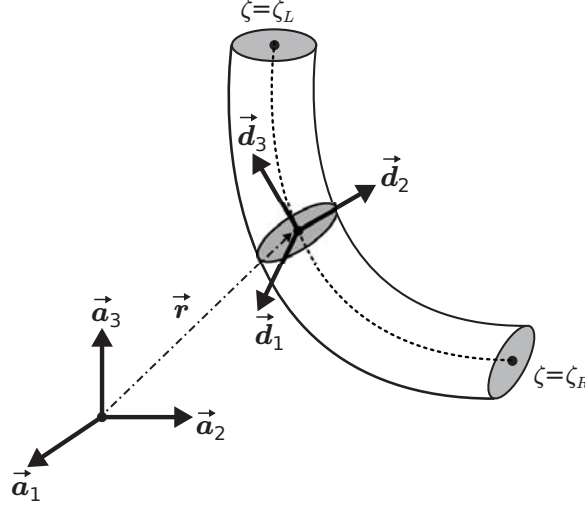


**Figure 2.1.:** Constitutive description of a special Cosserat rod with the help of the curve  $\vec{r}$  and the director triad  $\{\vec{d}_1, \vec{d}_2, \vec{d}_3\}$ .

$\vec{d}_3^\circ = \vec{d}_1^\circ \times \vec{d}_2^\circ$ . The reference time  $t^\circ \in \mathbb{R}$  is fixed and not necessarily contained in the considered time interval  $[0, t_{end}]$ . In particular, the complete reference state must not necessarily be formed by the considered rod but serves as an idealized state. In the reference state we additionally assume

$$e^\circ \vec{d}_3^\circ = \partial_\zeta \vec{r}^\circ, \quad (2.1)$$

with  $e^\circ : Q(t^\circ) \rightarrow \mathbb{R}$ . This means we consider a class of reference states with  $e^\circ$  characterizing the parameterization. A popular choice is  $e^\circ = 1$ , i.e., an arc length parameterized reference state. In the description of the geometry and material models we will utilize the assumption (2.1).

### 2.1.2. Kinematic and dynamic equations

The kinematic equations of the rod are given through the relations

$$\partial_t \vec{r} = \vec{v}, \quad \partial_\zeta \vec{r} = \vec{\tau}, \quad (2.2a)$$

i.e., the velocity  $\vec{v}$  [m/s] of the rod is the temporal and the rod tangent  $\vec{\tau}$  is the spatial derivative of the rod curve  $\vec{r}$  [m]. The director triad  $\{\vec{d}_1, \vec{d}_2, \vec{d}_3\}$  forms an orthonormal system, so there exist vector fields  $\vec{\omega}$  [1/s] and  $\vec{\kappa}$  [1/m] with

$$\partial_t \vec{d}_i = \vec{\omega} \times \vec{d}_i, \quad \partial_\zeta \vec{d}_i = \vec{\kappa} \times \vec{d}_i, \quad (2.2b)$$

$i \in \{1, 2, 3\}$ , indicating the angular velocity and the curvature of the rod, respectively. Assuming sufficient regularity (2.2a) and (2.2b) yield the compatibility conditions

$$\partial_t \vec{\tau} = \partial_\zeta \vec{v}, \quad \partial_t \vec{\kappa} = \partial_\zeta \vec{\omega} + \vec{\omega} \times \vec{\kappa}. \quad (2.2c)$$

The dynamic equations of the rod are given by the conservation laws for mass as well as linear and angular momentum

$$\begin{aligned}\partial_t \varrho_M &= 0, \\ \partial_t(\varrho_M \vec{v}) &= \partial_\zeta \vec{n} + \vec{f}, \\ \partial_t(\vec{J} \cdot \vec{\omega}) &= \partial_\zeta \vec{m} + \vec{\tau} \times \vec{n} + \vec{l}.\end{aligned}\tag{2.3}$$

Due to mass conservation the mass line density  $\varrho_M$  [kg/m] is constant over time in the material description and, hence, only depends on its referential value. External loads are included with the help of the body force line density  $\vec{f}$  [N/m] and the body couple line density  $\vec{l}$  [N]. The contact force  $\vec{n}$  [N] and contact couple  $\vec{m}$  [N m] are modeled with the help of material laws. For the inertia tensor  $\vec{J} \in \mathbb{E}^3 \otimes \mathbb{E}^3$  [m<sup>4</sup>] a geometric model is required.

The invariant formulation for a rod is given by the kinematic equations (2.2a), (2.2b) together with the dynamic equations (2.3).

**System 2.2** (Invariant rod in Lagrangian description).

*Kinematic and dynamic equations in  $\mathcal{D}$ :*

$$\begin{aligned}\partial_t \vec{r} &= \vec{v}, \\ \partial_\zeta \vec{r} &= \vec{\tau}, \\ \partial_t \vec{d}_i &= \vec{\omega} \times \vec{d}_i, \\ \partial_\zeta \vec{d}_i &= \vec{\kappa} \times \vec{d}_i, & i \in \{1, 2, 3\}, \\ \partial_t \varrho_M &= 0, \\ \partial_t(\varrho_M \vec{v}) &= \partial_\zeta \vec{n} + \vec{f}, \\ \partial_t(\vec{J} \cdot \vec{\omega}) &= \partial_\zeta \vec{m} + \vec{\tau} \times \vec{n} + \vec{l}.\end{aligned}$$

Here, any of the kinematic equations in (2.2a) and (2.2b) can be replaced by the corresponding compatibility condition in (2.2c). The preferable formulation of the kinematics is determined by the considered real problem, the boundary conditions as well as the intended numerical solution strategy.

It is common to represent the invariant rod model (System 2.2) with respect to the director basis and an outer basis. This simplifies the subsequent discussion of the geometric models and material laws. Besides the director basis  $\{\vec{d}_1, \vec{d}_2, \vec{d}_3\} \subset \mathbb{E}^3$  we introduce the fixed (space- and time-independent) orthonormal outer basis  $\{\vec{a}_1, \vec{a}_2, \vec{a}_3\} \subset \mathbb{E}^3$ . The director and outer bases are related by the tensor-valued rotation  $\vec{R}$ , i.e.,  $\vec{R} = \sum_{i=1}^3 \vec{a}_i \otimes \vec{d}_i$ . For any quantity  $\vec{z} \in \mathbb{E}^3$  we use the following

coordinate terminology:

$$\vec{\mathbf{z}} = \sum_{i=1}^3 z_i \vec{\mathbf{d}}_i = \sum_{i=1}^3 z_i \vec{\mathbf{a}}_i$$

with  $\mathbf{z} = (z_1, z_2, z_3) \in \mathbb{R}^3$  and  $\mathbf{z} = (z_1, z_2, z_3) \in \mathbb{R}^3$ . Hence, the coordinate triples fulfill  $\mathbf{z} = \mathbf{R} \cdot \mathbf{z}$  with associated orthogonal matrix  $\mathbf{R} = (R_{ij})_{i,j=1,2,3} = (\vec{\mathbf{d}}_i \cdot \vec{\mathbf{a}}_j)_{i,j=1,2,3} \in SO(3)$ . For the temporal and spatial derivatives follows

$$(\vec{\mathbf{d}}_i \cdot \partial_t \vec{\mathbf{z}})_{i=1,2,3} = \partial_t \mathbf{z} + \boldsymbol{\omega} \times \mathbf{z}, \quad (\vec{\mathbf{d}}_i \cdot \partial_\zeta \vec{\mathbf{z}})_{i=1,2,3} = \partial_\zeta \mathbf{z} + \boldsymbol{\kappa} \times \mathbf{z}.$$

Moreover, the kinematic equations for the director triad (2.2b) can be rewritten in terms of the rotational matrix  $\mathbf{R}$

$$\partial_t \mathbf{R} = -\boldsymbol{\omega} \times \mathbf{R}, \quad \partial_\zeta \mathbf{R} = -\boldsymbol{\kappa} \times \mathbf{R}.$$

Here, the cross product between a vector  $\mathbf{b} \in \mathbb{R}^3$  and a matrix  $\mathbf{B} \in \mathbb{R}^{3 \times 3}$  is defined as  $(\mathbf{b} \times \mathbf{B}) \cdot \mathbf{z} = \mathbf{b} \times (\mathbf{B} \cdot \mathbf{z})$  for all  $\mathbf{z} \in \mathbb{R}^3$ . The invariant rod model (System 2.2) is now formulated with respect to the director basis, except the equations for the curve  $\vec{\mathbf{r}}$  which are written in the outer basis.

**System 2.3** (Rod in director/outer basis and Lagrangian description).  
Kinematic and dynamic equations in  $\mathcal{D}$ :

$$\begin{aligned} \partial_t \mathbf{r} &= \mathbf{R}^T \cdot \mathbf{v}, \\ \partial_\zeta \mathbf{r} &= \mathbf{R}^T \cdot \boldsymbol{\tau}, \\ \partial_t \mathbf{R} &= -\boldsymbol{\omega} \times \mathbf{R}, \\ \partial_\zeta \mathbf{R} &= -\boldsymbol{\kappa} \times \mathbf{R}, \\ \partial_t \varrho_M &= 0, \\ \partial_t (\varrho_M \mathbf{v}) &= \varrho_M \mathbf{v} \times \boldsymbol{\omega} + \partial_\zeta \mathbf{n} + \boldsymbol{\kappa} \times \mathbf{n} + \mathbf{f}, \\ \partial_t (\mathbf{J} \cdot \boldsymbol{\omega}) &= (\mathbf{J} \cdot \boldsymbol{\omega}) \times \boldsymbol{\omega} + \partial_\zeta \mathbf{m} + \boldsymbol{\kappa} \times \mathbf{m} + \boldsymbol{\tau} \times \mathbf{n} + \mathbf{l}. \end{aligned}$$

Here,  $\mathbf{J} \in \mathbb{R}^{3 \times 3}$  denotes the matrix representing the inertia tensor  $\bar{\bar{\mathbf{J}}}$  with respect to the director basis, i.e.,  $\bar{\bar{\mathbf{J}}} = \sum_{i,j=1}^3 J_{ij} \vec{\mathbf{d}}_i \otimes \vec{\mathbf{d}}_j$  and  $\mathbf{J} = (J_{ij})_{i,j=1,2,3}$ . The tangent  $\boldsymbol{\tau}$  and curvature  $\boldsymbol{\kappa}$  represent the distortion of the rod and are crucial for the formulation of material laws. In particular,  $\tau_1, \tau_2$  represent the shear strains,  $\tau_3$  the stretching strain,  $\kappa_1, \kappa_2$  the bending and  $\kappa_3$  the torsion of the rod. Analogously,  $n_1, n_2$  are measures for the shear stress,  $n_3$  for the tension,  $m_1, m_2$  for the bending torque and  $m_3$  for the twisting torque. Moreover, we introduce

$$e = \|\boldsymbol{\tau}\|$$

representing a measure for the elongation of the rod.

**Remark 2.4** (Quaternions for rotation). *To parameterize the rotation  $\mathbf{R} \in SO(3)$  we use unit quaternions, i.e.,  $\mathbf{q} = (q_0, q_1, q_2, q_3) \in \mathbb{R}^4$  with  $\|\mathbf{q}\| = 1$ . Consider*

$$\mathbf{R}(\mathbf{q}) = \begin{pmatrix} q_1^2 - q_2^2 - q_3^2 + q_0^2 & 2(q_1q_2 - q_0q_3) & 2(q_1q_3 + q_0q_2) \\ 2(q_1q_2 + q_0q_3) & -q_1^2 + q_2^2 - q_3^2 + q_0^2 & 2(q_2q_3 - q_0q_1) \\ 2(q_1q_3 - q_0q_2) & 2(q_2q_3 + q_0q_1) & -q_1^2 - q_2^2 + q_3^2 + q_0^2 \end{pmatrix},$$

then, the equations  $\partial_t \mathbf{R} = -\boldsymbol{\omega} \times \mathbf{R}$  and  $\partial_\zeta \mathbf{R} = -\boldsymbol{\kappa} \times \mathbf{R}$  in System 2.3 are replaced by

$$\partial_t \mathbf{q} = \mathbf{S}(\boldsymbol{\omega}) \cdot \mathbf{q}, \quad \partial_\zeta \mathbf{q} = \mathbf{S}(\boldsymbol{\kappa}) \cdot \mathbf{q}. \quad (2.4)$$

with the skew-symmetric matrix  $\mathbf{S}$  defined as

$$\mathbf{S}(\mathbf{z}) = \frac{1}{2} \begin{pmatrix} 0 & z_1 & z_2 & z_3 \\ -z_1 & 0 & z_3 & -z_2 \\ -z_2 & -z_3 & 0 & z_1 \\ -z_3 & z_2 & -z_1 & 0 \end{pmatrix}$$

for all  $\mathbf{z} \in \mathbb{R}^3$ . This equivalence is only true if  $\|\mathbf{q}\| = 1$  holds initially for the time evolution and at the boundaries for the space evolution. The unit norm of the quaternions is then guaranteed through the evolution equations (2.4) due to the skew-symmetry of  $\mathbf{S}$  (note that the exponential of a skew-symmetric matrix is an orthogonal matrix). Numerically this can be realized with the help of isometric methods.

### 2.1.3. Geometric models

The geometrical modeling denotes the specification of the inertia tensor  $\bar{\bar{\mathbf{J}}}$ . Here, we consider three geometrical models which all originate from the embedding of the Cosserat rod theory into three-dimensional continuum mechanics. We assume that the rod cross-sections are circular and homogeneous, i.e., the mass density is constant within cross-sections. The geometrical models then give formulations for the inertia tensor associated matrix  $\mathbf{J}$ .

#### Inertia free model

The inertia free model neglects all inertial effects, i.e.,

$$\mathbf{J} = \mathbf{0}.$$

Using this model the angular momentum equation in System 2.3 becomes quasi-stationary and can be used to find explicit expressions for the normal components of the stresses  $\mathbf{n}$ .

### Cross-section-preserving model

The basic assumption for the cross-section-preserving model is that the rod cross-sections do not change over time. Three-dimensional considerations yield

$$\partial_t \mathbf{J} = \mathbf{0},$$

with the following form of the inertia matrix  $\mathbf{J}$

$$\mathbf{J} = \frac{\varrho_M \varrho_V}{e} \mathbf{P}_2,$$

where  $\varrho_V$  [m<sup>2</sup>] is the volume line density and  $\mathbf{P}_x = \text{diag}(1, 1, x)/(4\pi)$  for any  $x \in \mathbb{R}$ . Introducing the area of cross-sections  $A$  [m<sup>2</sup>] as  $A = \varrho_V/e$  and utilizing the conservation of mass yields

$$\partial_t A = 0.$$

This means, the rod cross-sections do not change over time and, therefore, equal the Lagrangian reference state,  $A = A^\circ$  with  $A^\circ$  the referential area of cross-sections. The mass density  $\rho$  [kg/m<sup>3</sup>] is introduced as ratio of mass and volume line densities  $\rho = \varrho_M/\varrho_V$ . Consequently,  $\partial_t(e\rho) = 0$  holds for the cross-section-preserving model, which means  $\rho = e^\circ \rho^\circ/e$  with  $\rho^\circ$  the mass density in the reference state.

### Incompressible model

In contrast to the cross-section-preserving model the incompressible geometry model preserves the volume. It assumes shape-preserving deformations of the cross-sections, such that the cross-sectional areas decrease under stretching and increase under compression maintaining incompressibility (conservation of volume). Three-dimensional considerations yield

$$\partial_t(e\mathbf{J}) = \mathbf{0},$$

with the same form of the inertia matrix  $\mathbf{J}$  as in the cross-section-preserving model

$$\mathbf{J} = \frac{\varrho_M \varrho_V}{e} \mathbf{P}_2.$$

This means the conservation of volume  $\partial_t \varrho_V = 0$  and equivalently

$$\partial_t(eA) = 0,$$

for the area of cross-sections, i.e.,  $A = e^\circ A^\circ/e$ . Furthermore, we obtain  $\partial_t \rho = 0$ , i.e., the mass density is a conservative quantity and  $\rho = \rho^\circ$  holds. If not stated otherwise, we use the incompressible material model in the following.

### 2.1.4. Material laws

Models for the material behavior of rods are used to close the rod theory. Material laws in general relate the contact forces  $\mathbf{n}$  and couples  $\mathbf{m}$  to the distortion measures of the rod  $\boldsymbol{\tau}/e^\circ$ ,  $\boldsymbol{\kappa}/e^\circ$ . In order to ensure objectivity (meaning frame indifference, i.e., rigid body motions and time translations do not affect the material response), these relations are formulated with respect to the director basis and without direct dependence on time. In the following we present material models describing elastic, viscous, and viscoelastic material behavior. Introducing geometrical constraints on the dynamics the number of required material laws can be reduced. By doing so certain components of the contact forces and couples become Lagrangian multipliers to the constraints and, hence, dynamic or algebraic variables of the system.

#### Elastic material behavior

There are numerous models for the elastic material behavior of rods. For the modeling of hardened fibers in industrial spinning applications the Euler-Bernoulli model with inertia free geometric model is mainly used. It gives a linear relation for the contact couples with the curvature. We combine the Euler-Bernoulli model with the classical Kirchhoff constraint that reads under the assumption (2.1) for the parameterization of the reference state

$$\boldsymbol{\tau} = e^\circ \mathbf{e}_3. \quad (2.5a)$$

This Kirchhoff constraint realizes an inextensible ( $\partial_t e^\circ = 0$ ) and unshearable ( $\boldsymbol{\tau} \sim \mathbf{e}_3$ ) rod, where  $\mathbf{e}_i$  ( $i = 1, 2, 3$ ) denotes the  $i$ -th canonical basis vector in  $\mathbb{R}^3$ . Considering the angular momentum equation with respect to the director basis (System 2.3) the contact forces  $\mathbf{n}$  become Lagrangian multipliers to the constraint (2.5a) and only a material model for the contact couples  $\mathbf{m}$  is required. The Euler-Bernoulli model suggests

$$\mathbf{m} = E \frac{\varrho_V^2}{(e^\circ)^3} \mathbf{P}_{1/(1+\nu_p)} \cdot (\boldsymbol{\kappa} - \boldsymbol{\kappa}^\circ).$$

Here,  $E$  [Pa] denotes the elastic modulus (Young's modulus) and the Poisson's ratio  $\nu_p$  indicates the relation of  $E$  to the shear modulus  $G$  [Pa], namely  $E/G = 2(1+\nu_p)$ . Assuming incompressibility  $\nu_p = 1/2$  and, therefore,  $E/G = 3$  holds for three-dimensional material modeling. The time-independent field  $\boldsymbol{\kappa}^\circ$  [1/m] is the curvature for which the rod is momentum-free and can be identified with the curvature in the reference state. The material model is closed by an appropriate model for the elastic modulus  $E$ , which for example can be chosen to be constant or dependent on the rod temperature  $T$  [K].

### Viscous material behavior

We utilize a viscous material model for rods that was first formulated for a stationary setup in [81] and later generalized for unsteady situations in [83]. There, the incompressible geometry model is employed and the generalized Kirchhoff constraint

$$\boldsymbol{\tau} = \tau_3 \mathbf{e}_3 \quad (2.5b)$$

is used. As for the classical Kirchhoff constraint this generalization realizes shear-free rods but allows rod elongations. The overall dilatation  $e = \|\boldsymbol{\tau}\| = \tau_3$  coincides with the elongation such that  $\boldsymbol{\tau} = e \mathbf{e}_3$  holds. Considering the angular momentum equation of System 2.3 the shear stresses  $n_1, n_2$  become Lagrangian multipliers and a material model for the tension  $n_3$  and torques  $\mathbf{m}$  is required

$$n_3 = 3\mu \frac{\rho_V}{e^2} \partial_t e, \quad \mathbf{m} = 3\mu \frac{\rho_V^2}{e^3} \mathbf{P}_{2/3} \cdot \partial_t \boldsymbol{\kappa}.$$

Here,  $\mu$  [Pa s] denotes the dynamic viscosity, which has to be specified by a further model.

### Viscoelastic material behavior

Besides pure elastic and pure viscous material behavior, fibers can show a viscoelastic behavior in industrial spinning processes combining viscous and elastic material properties. In [7] an incompressible viscoelastic material model for Cosserat rods is introduced. There, the incompressible material model as well as the generalized Kirchhoff constraint (2.5b) is employed. The model for the tension  $n_3$  equals the viscous material model, whereas for the torques  $\mathbf{m}$  a Maxwell-like relaxation of the viscous material model is proposed

$$n_3 = 3\mu \frac{\rho_V}{e^2} \partial_t e, \quad \mathbf{m} = 3\mu \frac{\rho_V^2}{e^3} \mathbf{P}_{2/3} \cdot \partial_t \boldsymbol{\kappa} - \theta \partial_t \mathbf{m},$$

with relaxation time  $\theta$  [s] as time scale for stresses to relax under tension. Utilizing the incompressibility assumption (Poisson's ratio  $\nu_p = 1/2$ ) the relation  $\mu/\theta = G = E/3$  holds. In the limit  $\theta \rightarrow 0$  the viscoelastic material model coincides with the viscous material model, whereas in the limit  $\mu \rightarrow \infty, \theta \rightarrow \infty$  with  $\mu/\theta = E/3$  the viscoelastic material model equals the elastic material behavior, if the elastic modulus is assumed to be constant over time, i.e.,  $\partial_t E = 0$ . For further details we refer to [7]. The viscoelastic material model is closed with models for  $\mu$  and  $\theta$ , which are either prescribed by material-dependent functions or determined through further evolution equations.

**Remark 2.5** (Temperature effects). *In industrial spinning applications spun fibers are often affected by cooling and solidification effects. In these cases the material quantities  $E$ ,  $\mu$ , and  $\theta$  are modeled by functions being dependent on the fiber temperature  $T$ . Then, the Cosserat rod model (System 2.3) is extended by an additional equation describing the energy balance. This balance equation yields an equation for the temperature  $T$ , e.g.,*

$$q \partial_t (\varrho_M T) = j$$

with specific heat capacity  $q$  [ $J/(kgK)$ ] and heat source  $j$  [ $W/m$ ]. Further details are given in Chap. 4.

### 2.1.5. Nondimensional formulation

Composite reference values		
Description	Formula	Unit
Length scale	$\zeta_0 = r_0$	m
Time scale	$t_0 = r_0/v_0$	s
Volume line density	$\varrho_{V,0} = d_0^2$	$m^2$
Cross-sectional area	$A_0 = d_0^2$	$m^2$
Mass density	$\rho_0 = \varrho_{M,0}/d_0^2$	$kg/m^3$
Curvature	$\kappa_0 = 1/r_0$	$1/m$
Stress	$n_0 = \varrho_{M,0}v_0^2$	N
Torque	$m_0 = \varrho_{M,0}r_0v_0^2$	N m
Angular velocity	$\omega_0 = v_0/r_0$	$1/s$
Outer force	$f_0 = \varrho_{M,0}v_0^2/r_0$	$N/m$
Outer couple	$l_0 = n_0$	N
Elastic modulus	$E_0 = \mu_0/\theta_0$	Pa
UCM stress	$\sigma_0 = \varrho_{M,0}v_0^2/d_0^2$	Pa
UCM pressure	$p_0 = \sigma_0$	Pa

Dimensionless numbers	
Description	Formula
Slenderness	$\varepsilon = d_0/r_0$
Reynolds	$Re = \varrho_{M,0}v_0r_0/(d_0^2\mu_0)$
Deborah	$De = \theta_0/t_0$
Mach	$Ma = \sqrt{ReDe}$

**Table 2.1.:** Overview over composite reference values used for nondimensionalization and the resulting dimensionless numbers. The following scales are assumed to be given from the specific setup  $\varrho_{M,0}$ ,  $v_0$ ,  $r_0$ ,  $d_0$ ,  $\mu_0$ ,  $\theta_0$ .

For the numerical treatment it is convenient to deal with nondimensional model equations. The nondimensionalization allows a proper scaling of the model equations and inserts characteristic parameters into the rod model. We introduce the dimensionless quantities as  $\tilde{y}(\tilde{\zeta}, \tilde{t}) = y(\zeta_0 \tilde{\zeta}, t_0 \tilde{t})/y_0$  for any scalar or vector field  $y$  and use the reference values  $y_0$ . In general, we choose a reference mass line density  $\varrho_{M,0}$  [kg/m], a scalar reference velocity  $v_0$  [m/s], a typical length scale  $r_0$  [m] as well as a reference diameter  $d_0$  [m]. For the material laws we introduce a referential viscosity  $\mu_0$  [Pa s] and a typical relaxation time  $\theta_0$  [s]. All these scales are chosen depending on the considered setup. Additionally, we introduce reference values that are composites of these setup-specific scales. We call them composite reference values and list them in Tab. 2.1. The introduction of two reference values for the length ( $r_0, d_0$ ) and time scale ( $t_0 = r_0/v_0, \theta_0$ ) respectively as well as the additional reference value for the viscosity ( $\mu_0$ ) leads to the dimensionless numbers given in Tab. 2.1. These are the slenderness ratio  $\varepsilon$ , the Reynolds number  $\text{Re}$  as ratio between inertial and viscous forces, the Deborah number  $\text{De}$  as ratio of the relaxation time to the characteristic time scale and the Mach number  $\text{Ma}$  as ratio of inertial to compressive forces. To keep the notation simple we suppress the label  $\tilde{\phantom{x}}$  in the following. Then, the rod model with respect to the director/outer basis (System 2.3) supplemented with the incompressible geometry model is given in nondimensional form by

**System 2.6** (Nondimensional incompressible rod in director/outer basis and Lagrangian description).

*Kinematic and dynamic equations in  $\mathcal{D}$ :*

$$\begin{aligned}
 \partial_t \mathbf{r} &= \mathbf{R}(\mathbf{q})^T \cdot \mathbf{v}, \\
 \partial_\zeta \mathbf{r} &= \mathbf{R}(\mathbf{q})^T \cdot \boldsymbol{\tau}, \\
 \partial_t \mathbf{q} &= \mathbf{S}(\boldsymbol{\omega}) \cdot \mathbf{q}, \\
 \partial_\zeta \mathbf{q} &= \mathbf{S}(\boldsymbol{\kappa}) \cdot \mathbf{q}, \\
 \partial_t \varrho_M &= 0, \\
 \partial_t \varrho_V &= 0, \\
 \partial_t (\varrho_M \mathbf{v}) &= \varrho_M \mathbf{v} \times \boldsymbol{\omega} + \partial_\zeta \mathbf{n} + \boldsymbol{\kappa} \times \mathbf{n} + \mathbf{f}, \\
 \partial_t \left( \frac{\varrho_M \varrho_V}{e} \mathbf{P}_2 \cdot \boldsymbol{\omega} \right) &= \left( \frac{\varrho_M \varrho_V}{e} \mathbf{P}_2 \cdot \boldsymbol{\omega} \right) \times \boldsymbol{\omega} + \frac{1}{\varepsilon^2} (\partial_\zeta \mathbf{m} + \boldsymbol{\kappa} \times \mathbf{m} + \boldsymbol{\tau} \times \mathbf{n} + \mathbf{l}).
 \end{aligned}$$

Constraints and material laws:

$$\begin{array}{ll}
 \text{Elastic:} & \boldsymbol{\tau} = e^\circ \mathbf{e}_3, & \mathbf{m} = \frac{\varepsilon^2}{\text{Ma}^2} E \frac{\varrho_V^2}{(e^\circ)^3} \mathbf{P}_{2/3} \cdot (\boldsymbol{\kappa} - \boldsymbol{\kappa}^\circ), \\
 \text{Viscous:} & \boldsymbol{\tau} = e \mathbf{e}_3, \quad n_3 = \frac{3}{\text{Re}} \mu \frac{\varrho_V}{e^2} \partial_t e, & \mathbf{m} = \frac{3\varepsilon^2}{\text{Re}} \mu \frac{\varrho_V^2}{e^3} \mathbf{P}_{2/3} \cdot \partial_t \boldsymbol{\kappa}, \\
 \text{Viscoelastic:} & \boldsymbol{\tau} = e \mathbf{e}_3, \quad n_3 = \frac{3}{\text{Re}} \mu \frac{\varrho_V}{e^2} \partial_t e, & \mathbf{m} = \frac{3\varepsilon^2}{\text{Re}} \mu \frac{\varrho_V^2}{e^3} \mathbf{P}_{2/3} \cdot \partial_t \boldsymbol{\kappa} \\
 & & - \text{De} \theta \partial_t \mathbf{m}.
 \end{array}$$

The compatibility conditions (2.2c) read with respect to the director basis

$$\partial_t \boldsymbol{\tau} = \boldsymbol{\tau} \times \boldsymbol{\omega} + \partial_\zeta \mathbf{v} + \boldsymbol{\kappa} \times \mathbf{v}, \quad \partial_t \boldsymbol{\kappa} = \partial_\zeta \boldsymbol{\omega} + \boldsymbol{\kappa} \times \boldsymbol{\omega}. \quad (2.6)$$

**Remark 2.7** (Viscous and elastic limits). *As explained before the viscous and elastic material models can be obtained as limits of the viscoelastic material model. The limit  $\text{De} \rightarrow 0$  obviously results in the viscous material law. The transition  $\text{De} \rightarrow \infty$ ,  $\text{Re} \rightarrow 0$  with  $\text{ReDe} = \text{Ma}^2$  gives under the assumption of a time-independent elastic modulus  $E = 3\mu/\theta$*

$$\boldsymbol{\tau} = e \mathbf{e}_3, \quad \partial_t e = 0, \quad \partial_t \mathbf{m} = \partial_t \left( \frac{\varepsilon^2}{\text{Ma}^2} E \frac{\varrho_V^2}{e^3} \mathbf{P}_{2/3} \cdot \boldsymbol{\kappa} \right).$$

It follows  $e = e^\circ$  and using the integration constant  $\boldsymbol{\kappa}^\circ$  we obtain the elastic material model as given in System 2.6.

### 2.1.6. Parameterization in Eulerian description

For inflow-outflow problems with time-independent flow domain the formulation of the model equations in a spatial (Eulerian) parameterization is beneficial since it avoids the consideration of a free boundary value problem in the material description. In particular, the spatial parameterization allows the transition to steady state for stationary considerations of the flow problem. Introducing a so-called type concept for all unknowns of our rod model simplifies the formulation of the model equations in any time-dependent parameterization. In the Lagrangian setting the parameter  $\zeta \in \mathcal{Q}(t) = (\zeta_L(t), \zeta_R(t))$ ,  $t \in [0, t_{\text{end}}]$  addresses a material point of the rod. A re-parameterization of this material setting is achieved via an oriented time-dependent bijective mapping

$$S(\cdot, t) : [\zeta_L(t), \zeta_R(t)] \rightarrow [s_L(t), s_R(t)], \quad \zeta \mapsto S(\zeta, t).$$

type-0-fields	$\mathbf{r}, \mathbf{q}, \mathbf{v}, \boldsymbol{\omega}, \mathbf{m}, \mathbf{n}, A, \rho, \mu, \theta$
type-1-fields	$\boldsymbol{\tau}, \boldsymbol{\kappa}, \varrho_M, \varrho_V, \mathbf{f}, \mathbf{l}, \mathbf{J}, e$

**Table 2.2.:** Types of the quantities of the rod model (System 2.6) with arbitrary material law (elastic, viscous, viscoelastic).

with  $s_L(t) = S(\zeta_L(t), t)$  and  $s_R(t) = S(\zeta_R(t), t)$ ,  $t \in [0, t_{end}]$ . Then, the Eulerian space-time domain is given by

$$\hat{D} = \{(s, t) \in \mathbb{R}^2 \mid s \in \hat{Q}(t), t \in (0, t_{end}]\},$$

with time-dependent space domain  $\hat{Q}(t) = (s_L(t), s_R(t))$ . Assuming sufficient regularity a scalar convective speed  $u$  and a spatial Jacobian  $j$  corresponding to  $S$  are defined

$$\partial_t S(\zeta, t) = u(S(\zeta, t), t), \quad \partial_\zeta S(\zeta, t) = j(\zeta, t) > 0.$$

Thus, the compatibility condition

$$\partial_s u(S(\zeta, t), t) = \frac{\partial_t j}{j}(\zeta, t) \quad (2.7)$$

holds. The positivity of  $j$  is a result of the definition of the domain and co-domain of the mapping  $S$  fixing its orientation. Following [109] we introduce the concept of type- $n$ -fields,  $n \in \mathbb{Z}$ . The intention of this concept is to preserve the physical character (e.g., densities, derivatives) of each quantity under re-parameterization. A type- $n$ -field  $f$  (scalar-, vector- or tensor-valued) in the Lagrangian description is transformed into the respective unknown in the Eulerian description  $\hat{f}$  by

$$f(\zeta, t) = j^n(\zeta, t) \hat{f}(S(\zeta, t), t).$$

The types of unknowns of our rod model (System 2.6) are given in Tab. 2.2. Using the chain rule yields transformation rules for the derivatives with respect to  $\zeta$  and  $t$

$$\begin{aligned} \partial_t f(\zeta, t) &= j^n(\zeta, t) (\partial_t \hat{f} + n \hat{f} \partial_s u + u \partial_s \hat{f})(S(\zeta, t), t), \\ \partial_\zeta f(\zeta, t) &= j^{n+1}(\zeta, t) \left( \partial_s \hat{f}(S(\zeta, t), t) + n \frac{\partial_\zeta j(\zeta, t)}{j^2(\zeta, t)} \hat{f}(S(\zeta, t), t) \right). \end{aligned}$$

In the Eulerian description the scalar speed  $u$  becomes the Lagrangian multiplier to the assumption of global arc length parameterization  $\|\hat{\boldsymbol{\tau}}\| = \|\partial_s \hat{\mathbf{r}}\| = 1$  and is hence an additional unknown of the system. Due to the generalized Kirchhoff constraint,  $e$  and  $j$  coincide ( $e = j$ ) when the viscous or viscoelastic material law

is used. In view of the elastic material law the classical Kirchhoff constraint yields  $e^\circ = j$  and, thus,  $\partial_s u = 0$  holds due the compatibility condition (2.7) and  $\partial_t e^\circ = 0$ . This means, the Eulerian parameterization is only a (time-dependent) shift of the corresponding Lagrangian one without any benefit for our further considerations. Thus, we omit the Eulerian description for the elastic material law and restrict our presentation to viscous and viscoelastic material behavior.

To simplify the notation we suppress the label  $\hat{\cdot}$  in the following. The type of parameterization (Eulerian or Lagrangian description) will be clear in each application. In total, the incompressible rod model with respect to the director/outer basis in spatial description is given by

**System 2.8** (Nondimensional incompressible rod in director/outer basis and Eulerian description).

*Kinematic and dynamic equations in  $\mathcal{D}$ :*

$$\begin{aligned}\partial_t \mathbf{r} &= \mathbf{R}(\mathbf{q})^T \cdot (\mathbf{v} - u\boldsymbol{\tau}), \\ \partial_s \mathbf{r} &= \mathbf{R}(\mathbf{q})^T \cdot \boldsymbol{\tau}, \\ \partial_t \mathbf{q} &= \mathbf{S}(\boldsymbol{\omega} - u\boldsymbol{\kappa}) \cdot \mathbf{q}, \\ \partial_s \mathbf{q} &= \mathbf{S}(\boldsymbol{\kappa}) \cdot \mathbf{q}, \\ \partial_t \varrho_M + \partial_s(u\varrho_M) &= 0, \\ \partial_t \varrho_V + \partial_s(u\varrho_V) &= 0, \\ \partial_t(\varrho_M \mathbf{v}) + \partial_s(u\varrho_M \mathbf{v}) &= \varrho_M \mathbf{v} \times \boldsymbol{\omega} + \partial_s \mathbf{n} + \boldsymbol{\kappa} \times \mathbf{n} + \mathbf{f}, \\ \partial_t(\varrho_M \varrho_V \mathbf{P}_2 \cdot \boldsymbol{\omega}) + \partial_s(u\varrho_M \varrho_V \mathbf{P}_2 \cdot \boldsymbol{\omega}) &= (\varrho_M \varrho_V \mathbf{P}_2 \cdot \boldsymbol{\omega}) \times \boldsymbol{\omega} \\ &\quad + \frac{1}{\varepsilon^2} (\partial_s \mathbf{m} + \boldsymbol{\kappa} \times \mathbf{m} + \boldsymbol{\tau} \times \mathbf{n} + \mathbf{l}).\end{aligned}$$

*Constraints and material laws:*

$$\text{Viscous:} \quad \boldsymbol{\tau} = \mathbf{e}_3, \quad n_3 = \frac{3}{\text{Re}} \mu \varrho_V \partial_s u,$$

$$\mathbf{m} = \frac{3\varepsilon^2}{\text{Re}} \mu \varrho_V^2 \mathbf{P}_{2/3} \cdot (\partial_t \boldsymbol{\kappa} + \partial_s(u\boldsymbol{\kappa})),$$

$$\text{Viscoelastic:} \quad \boldsymbol{\tau} = \mathbf{e}_3, \quad n_3 = \frac{3}{\text{Re}} \mu \varrho_V \partial_s u,$$

$$\mathbf{m} = \frac{3\varepsilon^2}{\text{Re}} \mu \varrho_V^2 \mathbf{P}_{2/3} \cdot (\partial_t \boldsymbol{\kappa} + \partial_s(u\boldsymbol{\kappa})) - \text{De}\theta(\partial_t \mathbf{m} + u\partial_s \mathbf{m}).$$

Here, the compatibility conditions (2.6) read

$$\begin{aligned}\partial_t \boldsymbol{\tau} + \partial_s(u\boldsymbol{\tau} - \mathbf{v}) &= \boldsymbol{\tau} \times \boldsymbol{\omega} + \boldsymbol{\kappa} \times \mathbf{v}, \\ \partial_t \boldsymbol{\kappa} + \partial_s(u\boldsymbol{\kappa} - \boldsymbol{\omega}) &= \boldsymbol{\kappa} \times \boldsymbol{\omega},\end{aligned}\tag{2.8}$$

and the time derivative in the first expression vanishes inserting any of the two material laws ( $\boldsymbol{\tau} = \mathbf{e}_3$ ). Moreover, from the type concept we follow  $\varrho_V = A$  and  $\varrho_M = \rho A$  in Eulerian description for the incompressible geometry model .

**Remark 2.9** (Euler-stationary system). *As mentioned before the Euler parameterization is suitable for stationary considerations of the flow problem. Transition to steady state in System 2.8 yields the direct relations*

$$\mathbf{v} = u\boldsymbol{\tau}, \quad \boldsymbol{\omega} = u\boldsymbol{\kappa},$$

*i.e., the quantities  $\mathbf{v}$  and  $\boldsymbol{\omega}$  can be eliminated from the equations. Moreover, the mass balance equation degenerates to  $\partial_s(u\varrho_M) = 0$  and the volume balance equation reads  $\partial_s(u\varrho_V)$ . Therefore, we can introduce the constant mass flux  $Q_M = u\varrho_M = \rho uA = \text{const}$  [kg/s] and the constant volume flux  $Q_V = u\varrho_V = uA = \text{const}$  [m<sup>3</sup>/s].*

## 2.2. Asymptotic string models

The previously considered Cosserat rod models do not result from three-dimensional continuum mechanics by considering the asymptotic limit  $\varepsilon \rightarrow 0$  for the slenderness parameter  $\varepsilon$ . This can be seen at the angular momentum equation and the material laws in System 2.6/System 2.8 that include terms of order  $\varepsilon^2$ . In fact, an asymptotic limit from three-dimensional considerations yields the so called string models, which omit the angular momentum equation and the evaluation of the director triad dynamics. Starting from a free boundary value problem based on the three-dimensional Navier-Stokes equations a strict asymptotic derivation of a viscous string model (with and without surface tension) is given in [67, 77]. A string model with viscoelastic material behavior is asymptotically derived from the three-dimensional upper-convected Maxwell model in [65]. In general, having the theory of special Cosserat rods in mind, string models can be achieved as simplification of rods by considering the limit  $\varepsilon \rightarrow 0$ . In the following we examine this limit for the viscous rod model as done in [6]. For the elastic rod model a suitable string model is deduced by the so called low-Mach-number–slenderness limit, i.e.,  $\varepsilon \rightarrow 0$ ,  $\text{Ma} \rightarrow 0$  under constant ratio  $\varepsilon/\text{Ma} = \text{const}$ , see [13]. In view of viscoelastic material behavior we present the UCM string model, which has been asymptotically derived in [65]. Note that it is not the limit  $\varepsilon \rightarrow 0$  of the presented viscoelastic rod model. In the following we formulate all string models in Lagrangian parameterization. Adopting the type concept and employing the transformation rules from Sec. 2.1.6 the associated Eulerian descriptions follow analogously to the rod models.

### 2.2.1. Viscous strings

We consider the angular momentum equation of the rod model in Lagrangian description with respect to the director basis (System 2.6) and the viscous material laws. Assuming vanishing outer couples  $\mathbf{l} = \mathbf{0}$  the asymptotic limit  $\varepsilon \rightarrow 0$  gives

$$\mathbf{m} = \mathbf{0}, \quad \boldsymbol{\tau} \times \mathbf{n} = \mathbf{0}.$$

Utilizing the generalized Kirchhoff constraint yields the form

$$\mathbf{n} = N \frac{\boldsymbol{\tau}}{e} = N e_3$$

for the stress vector, i.e., the shear stresses vanish ( $n_1 = n_2 = 0$ ). The tension  $N = n_3$  is specified by the viscous material law

$$N = \frac{3}{\text{Re}} \mu \frac{\varrho_V}{e^2} \partial_t e.$$

The evaluation of the kinematic equations for the director triad can be neglected and with respect to the outer basis the rod equations reduce to

**System 2.10** (Viscous string in Lagrangian description).

*Kinematic and dynamic equations in  $\mathcal{D}$ :*

$$\begin{aligned} \partial_t \mathbf{r} &= \mathbf{v}, \\ \partial_\zeta \mathbf{r} &= \boldsymbol{\tau}, \\ \partial_t \varrho_M &= 0, \\ \partial_t \varrho_V &= 0, \\ \partial_t (\varrho_M \mathbf{v}) &= \partial_\zeta \left( N \frac{\boldsymbol{\tau}}{e} \right) + \mathbf{f}. \end{aligned}$$

*Material law:*

$$N = \frac{3}{\text{Re}} \mu \frac{\varrho_V}{e^2} \partial_t e.$$

This viscous string model equals the one given in [77], where slender body asymptotic is employed to derive the model from three-dimensional Navier-Stokes equations. In [67] this concept is extended to the inclusion of surface tensions. Due to the occurrence of singularities, the solvability of viscous string models, in particular for steady considerations, is restricted to certain parameter regimes [6, 40]. The corresponding viscous rod model (System 2.6) omits these problems and, therefore, can be seen as a regularization of the associated string model [6].

### 2.2.2. Elastic strings

Employing the same argumentation as for the viscous string the rod model (System 2.6) supplemented with elastic material behavior and the classical Kirchhoff constraint also results in a stress tensor  $\mathbf{n}$  of the form  $\mathbf{n} = N\mathbf{e}_3$ , but does not provide a material law for  $N$ . Alternatively, the low-Mach-number–slenderness limit  $\varepsilon \rightarrow 0$ ,  $\text{Ma} \rightarrow 0$  with  $\varepsilon/\text{Ma} = \text{const}$  can be employed [7, 13]. With the help of an even power series expansion and an asymptotic framework that is exact up to fourth order this limit gives the classical Kirchhoff beam, which is also known as Kirchhoff-Love equations when all angular inertia terms are neglected additionally, for details see [13]. For simplicity we assume an arc length parameterized reference state  $e^\circ = 1$ . The resulting generalized elastic string model with respect to the outer basis is given by

**System 2.11** (Generalized elastic string in Lagrangian description).  
 Kinematic and dynamic equations in  $\mathcal{D}$ :

$$\begin{aligned} \partial_t \mathbf{r} &= \mathbf{v}, \\ \partial_\zeta \mathbf{r} &= \boldsymbol{\tau}, \\ \partial_t \varrho_M &= 0, \\ \partial_t A &= 0, \\ \partial_t (\varrho_M \mathbf{v}) &= \partial_\zeta (S \boldsymbol{\tau}) - \frac{\varepsilon^2}{\text{Ma}^2} \partial_{\zeta\zeta} \left( \frac{EA^2}{4\pi} \partial_\zeta \boldsymbol{\tau} \right) + M (\boldsymbol{\tau} \times \partial_{\zeta\zeta} \boldsymbol{\tau}) + \mathbf{f}. \end{aligned}$$

Constraint and material laws:

$$e = \|\boldsymbol{\tau}\| = 1, \quad \partial_\zeta M = 0.$$

Here,  $S = N - \varepsilon^2/\text{Ma}^2(EA^2)/(4\pi)\|\partial_\zeta \boldsymbol{\tau}\|^2$  is used as Lagrangian multiplier to the constraint. The quantities  $N = n_3$ ,  $M = m_3$  denote tension and twisting torque, respectively. Due to the occurrence of the slenderness parameter  $\varepsilon$  and angular inertia terms in the linear momentum equation System 2.11 is called generalized string model.

### 2.2.3. Viscoelastic strings

Since the rod model with viscoelastic material behavior presented in Sec. 2.1.4 is an ad hoc extension of the viscous material law to provide a consistent transition to elastic rod behavior in the elastic limit and behaves purely viscous in the linear momentum equation, the limit  $\varepsilon \rightarrow 0$  does not result in a consistent string model.

Therefore, we consider the upper-convected Maxwell (UCM) string model that is derived with the help of slender body asymptotics in [65].

**System 2.12** (Viscoelastic string (UCM) in Lagrangian description).

*Kinematic and dynamic equations in  $\mathcal{D}$ :*

$$\begin{aligned}\partial_t \mathbf{r} &= \mathbf{v}, \\ \partial_\zeta \mathbf{r} &= \boldsymbol{\tau}, \\ \partial_t \varrho_M &= 0, \\ \partial_t \varrho_V &= 0, \\ \partial_t(\varrho_M \mathbf{v}) &= \partial_\zeta \left( \varrho_V \sigma \frac{\boldsymbol{\tau}}{e^2} \right) + \mathbf{f}.\end{aligned}$$

*Material laws:*

$$\begin{aligned}\text{De} \left( \partial_t \sigma - (2\sigma + 3p) \frac{\partial_t e}{e} \right) + \frac{\sigma}{\theta} &= \frac{3}{\text{Re}} \frac{\mu}{\theta} \frac{\partial_t e}{e}, \\ \text{De} \left( \partial_t p + p \frac{\partial_t e}{e} \right) + \frac{p}{\theta} &= -\frac{1}{\text{Re}} \frac{\mu}{\theta} \frac{\partial_t e}{e}.\end{aligned}$$

The UCM model formulates material laws for the stress  $\sigma$  [Pa] and the pressure  $p$  [Pa]. The corresponding reference values  $\sigma_0, p_0$  used for the nondimensional formulation are given in Tab. 2.1. In the viscous limit  $\text{De} \rightarrow 0$  the UCM model (System 2.12) coincides with the viscous string model (System 2.10) introducing the tension  $N = \varrho_V \sigma / e$ . The elastic limit  $\text{De} \rightarrow \infty, \text{Re} \rightarrow 0, \text{ReDe} = \text{Ma}^2$  results in explicit solution expressions for the pressure  $p$  and the stress  $\sigma$ , see Appendix A.1.

**Remark 2.13** (Reformulation). *Instead of  $\sigma$  the stress variable  $m = \sigma + p$  can be introduced. Then, the stress occurring in the linear momentum balance is expressed as  $m - p$  and the associated constitutive equation reads*

$$\text{De} \left( \partial_t m - 2m \frac{\partial_t e}{e} \right) + \frac{m}{\theta} = \frac{2}{\text{Re}} \frac{\mu}{\theta} \frac{\partial_t e}{e}.$$

**Remark 2.14** (Small pressure). *As pointed out in [65] the pressure  $p$  is at least one order of magnitude smaller than the stress  $\sigma$  for fibers with high strain rates  $v = \partial_t e / e$  and large Deborah numbers  $\text{De}$ , in particular  $|p| \leq 0.1\sigma$  if  $v \geq 0.35 / (\theta \text{De})$ . This means, the pressure equation can be neglected in such cases. In [122], where the UCM model is used for studies of melt-blowing processes, this simplification is employed instantaneously to the model equations. In our study of melt-blowing processes we will compare the full UCM model (System 2.12) with the simplified (pressure-free) model (cf. Sec. 6.1 and App. A.2).*

## 2.3. External loads

The external loads  $\vec{f}$  for rod and string models and additionally  $\vec{l}$  for rod models are a key-player for the fiber behavior. In the following we assume that external body couples are only caused by outer line force densities  $\vec{f}$ , i.e.,  $\vec{l} = \vec{0}$ . In view of industrial spinning processes various external loads have to be taken into account depending on the specific manufacturing method. Nevertheless, the gravitational force  $\vec{f}_g$  and aerodynamic forces  $\vec{f}_{air}$  act in all these spinning setups. Therefore, we introduce the formulation of the gravitational force with respect to the outer basis in the following. For the aerodynamic line force density we utilize the air drag model given in [68]. Then, the total outer forces are given through  $f = f_g + f_{air}$  and – if necessary – are extended by further outer forces for each specific spinning setup in the subsequent chapters. The body forces in director basis are obtained via transformation  $\mathbf{f} = \mathbf{R} \cdot f$ .

### 2.3.1. Gravitational force

Let  $g$  [ $\text{m}/\text{s}^2$ ] denote the gravitational acceleration and  $\mathbf{e}_g$ ,  $\|\mathbf{e}_g\| = 1$ , be the direction of gravity with respect to the outer basis. The gravitational force reads

$$f_g = \varrho_M g \mathbf{e}_g.$$

Employing the typical force line density  $f_0$  as given in Tab. 2.3 results in the dimensionless formulation

$$f_g = \frac{1}{\text{Fr}^2} \varrho_M \mathbf{e}_g$$

with the dimensionless Froude number  $\text{Fr}$  as ratio of inertial to gravitational forces, see Tab. 2.3.

### 2.3.2. Aerodynamic forces

Note that to distinguish the fiber quantities from the airflow quantities all airflow associated fields are labeled with the index  $\star$ . In particular,  $\mathbf{v}_\star$  denotes the velocity (with respect to the outer basis),  $\rho_\star$  the density, and  $\nu_\star$  the kinematic viscosity of the air. All these quantities are space- and time-dependent fields assumed to be dimensionless and known – for example provided by an external computation. The corresponding reference values used for nondimensionalization are denoted with the index  $_0$  and given in Tab. 2.3.

Adopting the air drag model from [68] the dimensionless aerodynamic drag forces  $f_{air}$  are described by means of a dimensionless air drag function  $\mathbf{F} : \mathbb{S}^2 \times \mathbb{R}^3 \rightarrow \mathbb{R}^3$

Composite reference values		
Description	Formula	Unit
Cross-sectional radius	$R_0 = d_0$	m
Outer force	$f_0 = \varrho_{M,0} v_0^2 / r_0$	N/m
Air velocity	$v_{*,0} = v_0$	m/s

Dimensionless numbers	
Description	Formula
Froude	$Fr = v_0 / \sqrt{g r_0}$
Air drag associated	$A_* = \rho_{*,0} d_0 v_0^2 / f_0$
Air-fiber Reynolds	$Re_* = d_0 v_0 / \nu_{*,0}$

**Table 2.3.:** Overview over composite reference values used for nondimensionalization of the body forces and the resulting dimensionless numbers. The following scales are assumed to be given from the specific considered setup  $\varrho_{M,0}$ ,  $v_0$ ,  $r_0$ ,  $d_0$ ,  $\rho_{*,0}$  [kg/m<sup>3</sup>],  $\nu_{*,0}$  [m<sup>2</sup>/s].

that depends on the normalized direction of the fiber tangent  $\mathbf{t} = \boldsymbol{\tau}/e$  and the relative velocity between airflow and fiber ( $\mathbf{v}_* - \mathbf{v}$ ). It reads in Lagrangian parameterization

$$\mathbf{f}_{air} = e \frac{A_*}{Re_*^2} \frac{\rho_* \nu_*^2}{2R} \mathbf{F} \left( \mathbf{t}, Re_* \frac{2R}{\nu_*} (\mathbf{v}_* - \mathbf{v}) \right), \quad (2.9)$$

$$\mathbf{F}(\mathbf{t}, \mathbf{w}) = r_n(w_n) \mathbf{w}_n + r_t(w_n) \mathbf{w}_t.$$

In particular,  $\mathbf{F}$  is expressed in terms of the tangential  $\mathbf{w}_t = (\mathbf{w} \cdot \mathbf{t}) \mathbf{t}$  and normal velocity components  $\mathbf{w}_n = \mathbf{w} - \mathbf{w}_t$ ,  $w_n = \|\mathbf{w}_n\|$ . The occurring dimensionless numbers are the mixed air-fiber Reynolds number  $Re_*$  and the further air-drag associated number  $A_*$  (cf. Tab. 2.3). The fiber radius is denoted by  $R$  and fulfills  $A = \pi R^2$ . The models for the regularized normal and tangential air resistance coefficients  $r_n$ ,  $r_t$  are taken from [68]

$$r_n(w_n) = \begin{cases} \sum_{j=0}^3 q_{n,j} w_n^j, & w_n < w_0, \\ \frac{4\pi}{S(w_n)} \left( 1 - \frac{S^2(w_n) - S(w_n)/2 + 5/16}{32S(w_n)} w_n^2 \right), & w_0 \leq w_n < w_1, \\ w_n \exp \left( \sum_{j=0}^3 p_{n,j} \log^j(w_n) \right), & w_1 \leq w_n \leq w_2, \\ 2\sqrt{w_n} + 0.5w_n, & w_2 < w_n, \end{cases}$$

$$r_t(w_n) = \begin{cases} \sum_{j=0}^3 q_{t,j} w_n^j, & w_n < w_0, \\ \frac{4\pi}{(2S(w_n)-1)} \left( 1 - \frac{2S^2(w_n) - 2S(w_n) + 1}{16(2S(w_n)-1)} w_n^2 \right), & w_0 \leq w_n < w_1, \\ w_n \exp \left( \sum_{j=0}^3 p_{t,j} \log^j(w_n) \right), & w_1 \leq w_n \leq w_2, \\ 2\sqrt{w_n}, & w_2 < w_n, \end{cases}$$

with  $S(w_n) = 2.0022 - \log(w_n)$ . It is composed of asymptotic Oseen theory, Taylor heuristic and simulations where the transition points  $w_1 = 0.1$  and  $w_2 = 100$  are estimated from a least-square approximation of experimental and numerical data. For tangential incident flow situations ( $w_n \rightarrow 0$ ) a regularization employs the Stokes theory yielding the Stokes limits

$$r_n^S = \frac{4\pi}{\log(4\epsilon^{-1})} - \frac{\pi}{\log^2(4\epsilon^{-1})}, \quad r_t^S = \frac{2\pi}{\log(4\epsilon^{-1})} + \frac{\pi}{2\log^2(4\epsilon^{-1})},$$

as well as the transition point  $w_0 = 2 \exp(2.0022 - 4\pi/r_n^S)$  with the regularization parameter  $\epsilon = 3.5 \cdot 10^{-2}$ . The parameters  $p_{k,j}$  and  $q_{k,j}$  ( $k \in \{n, t\}$ ,  $j \in \{0, 1, 2, 3\}$ ) ensure smoothness,

$$\begin{aligned} p_{n,0} &= 1.6911, & p_{n,1} &= -6.7222 \cdot 10^{-1}, & p_{n,2} &= 3.3287 \cdot 10^{-2}, \\ p_{n,3} &= 3.5015 \cdot 10^{-3}, \\ p_{t,0} &= 1.1552, & p_{t,1} &= -6.8479 \cdot 10^{-1}, & p_{t,2} &= 1.4884 \cdot 10^{-2}, \\ p_{t,3} &= 7.4966 \cdot 10^{-4}, \end{aligned}$$

$$\begin{aligned} q_{k,0} &= r_k^S, & q_{k,1} &= 0, & q_{k,2} &= \frac{3r_k(w_0) - w_0 r'_k(w_0) - 3r_k^S}{w_0^2}, \\ q_{k,3} &= \frac{-2r_k(w_0) + w_0 r'_k(w_0) + 2r_k^S}{w_0^3}, \end{aligned}$$

with  $r'_k = d/(dw)r_k$ .



### 3. Numerical framework

In this chapter we introduce the numerical framework for the solution of our spinning models. Whereas in Chap. 2 we provided the 'model database' for the modeling of industrial spinning processes, this chapter serves as 'toolbox' for the corresponding numerical solution strategies. In general, the choice of the respective numerical scheme crucially depends on the mathematical structure of the problem. We assume that the model equations are equipped with appropriate boundary conditions such that (Euler-)stationary formulations of the viscous rod and string models (System 2.8 and System 2.10), which we utilize as basis for the modeling of dry spinning and electrospinning setups (see Chap. 4 and Chap. 5, respectively), form boundary value problems (BVPs) of ordinary differential equations (ODEs). Furthermore, the viscoelastic string model (System 2.12), which we use for the modeling of melt-blowing processes (see Chap. 6), can be classified as a BVP of quasilinear hyperbolic partial differential equations (PDEs). Our general numerical solution concept for such types of BVPs is as follows: Stationary ODE systems are solved by a continuation-collocation method, where the underlying collocation is based on a Lobatto IIIa formula [45]. For the solution of unsteady PDE problems we adapt a finite volume scheme in space with numerical flux approximation of Lax-Friedrichs type as well as the implicit Euler method in time [55]. Besides these classical numerical methods for basic rod and string models we develop a new strategy to deal with further equations: For the modeling of radial diffusive effects in dry spinning processes we utilize advection-diffusion equations with Robin-type boundary conditions. To solve these equations numerically, we present an efficient algorithmic procedure that is based on the analytical solution of the radial advection-diffusion equations with a Green's function [10, 23, 76]. This implicitly given solution expressions result in Volterra integral equations of second kind for the surface values with singular integration kernel, which can be solved efficiently by the product integration method. In addition, considering industrial spinning devices up to several hundred fibers are spun simultaneously such that the mutual interaction of the fibers with the surrounding medium has to be taken into account in the modeling and simulation of such processes. Whereas for a single spun fiber the consideration of a one-way coupling is sufficient, we employ a two-way fiber-airflow coupling for multiple fibers following the concepts of [21, 22].

This chapter is structured as follows. First, we present the continuation-collocation method for ODE systems in Sec. 3.1. In Sec. 3.2 we introduce the finite volume scheme for hyperbolic PDE systems, where we focus on inflow problems in Lagrangian description. The product integration method for the efficient solution of two-dimensional advection-diffusion equations with Robin boundary conditions is presented in Sec. 3.3. To close the chapter we explain the numerical concept of realizing fiber-airflow interactions in Sec. 3.4. In particular, we present the computation strategy for the outer airflow fields and explain the intended one- and two-way coupling of the fibers with the airflow.

## 3.1. Boundary value problems of ordinary differential equations

We consider a BVP of ODEs

$$\frac{d}{ds}\mathbf{y} = \mathbf{f}(\mathbf{y}), \quad \mathbf{g}(\mathbf{y}(0), \mathbf{y}(1)) = \mathbf{0}, \quad (3.1)$$

depending on multiple parameters on the time-independent space domain  $\mathcal{Q} = (0, 1)$ . Here,  $\mathbf{f} : \mathbb{R}^{N_v} \rightarrow \mathbb{R}^{N_v}$  is the right hand side function,  $\mathbf{g} : \mathbb{R}^{N_v} \times \mathbb{R}^{N_v} \rightarrow \mathbb{R}^{N_v}$  the boundary value function and  $\mathbf{y} : \mathcal{Q} \rightarrow \mathbb{R}^{N_v}$  the vector of unknowns, where  $N_v$  addresses the total number of unknowns. The numerical challenge lies in solving the problem for arbitrary parameter settings, which requires suitable initial guesses of the respective solutions. This problem is tackled by a continuation-collocation method that makes the efficient and robust simulation and navigation through a high-dimensional parameter space possible.

### 3.1.1. Collocation method

To solve a BVP of the form (3.1) we use a three-stage Lobatto IIIa formula as collocation scheme [45]. It is an implicit Runge-Kutta method. The collocation polynomial provides a once continuously differentiable solution that is fourth-order accurate uniformly in  $s \in [0, 1]$ . Mesh selection and error control are based on the residual of the continuous solution [52]. Thus, we have

$$\begin{aligned} \mathbf{y}_{i+1} - \mathbf{y}_i - \frac{h_{i+1}}{6} (\mathbf{f}(\mathbf{y}_i) + 4\mathbf{f}(\mathbf{y}_{i+1/2}) + \mathbf{f}(\mathbf{y}_{i+1})) &= \mathbf{0}, & \mathbf{g}(\mathbf{y}_0, \mathbf{y}_N) &= \mathbf{0}, \\ \text{with } \mathbf{y}_{i+1/2} &= \frac{1}{2}(\mathbf{y}_{i+1} + \mathbf{y}_i) - \frac{h_{i+1}}{8} (\mathbf{f}(\mathbf{y}_{i+1}) - \mathbf{f}(\mathbf{y}_i)), \end{aligned} \quad (3.2)$$

with collocation points  $0 = s_0 < s_1 < \dots < s_N = 1$ , mesh size  $h_i = s_i - s_{i-1}$  and the abbreviation  $\mathbf{y}_i = \mathbf{y}(s_i)$ ,  $i = 0, \dots, N$ . The resulting nonlinear system of  $N + 1$

equations for  $(\mathbf{y}_i)_{i=0,\dots,N}$  is solved using a Newton method with either analytically prescribed or numerically approximated Jacobian. This is a classical approach that is provided in the software MATLAB<sup>1</sup> by the routine `bvp4c.m`. Its applicability depends on the convergence of the Newton method that is crucially determined by the initial guess. We aim for adapting the initial guess iteratively by means of a continuation method, solving a sequence of slightly varying BVPs. Before we explain our continuation method, we summarize some important properties of the collocation scheme (3.2) in Lemma 3.1. These properties are well-known from literature, but we proof them here for the sake of completeness.

**Lemma 3.1.** *The collocation scheme (3.2) based on Lobatto IIIa quadrature is A-but not L-stable. Furthermore, the scheme is isometry preserving.*

*Proof.* The scheme (3.2) can be written in Butcher tableau form

$$\mathbf{y}_{i+1} - \mathbf{y}_i - h_{i+1} \sum_{j=1}^3 b_j \mathbf{k}_j = \mathbf{0}, \quad \mathbf{g}(\mathbf{y}_0, \mathbf{y}_N) = \mathbf{0} \quad \text{with} \quad \mathbf{k}_j = \mathbf{f} \left( \mathbf{y}_i + h_{i+1} \sum_{k=1}^3 A_{jk} \mathbf{k}_k \right),$$

$i \in \{0, \dots, N-1\}$ , and the coefficients

$$\mathbf{A} = (A_{jk})_{j,k=1,2,3} = \frac{1}{24} \begin{pmatrix} 0 & 0 & 0 \\ 5 & 8 & -1 \\ 4 & 16 & 4 \end{pmatrix}, \quad \mathbf{b} = (b_j)_{j=1,2,3} = \frac{1}{6} \begin{pmatrix} 1 \\ 4 \\ 1 \end{pmatrix}.$$

The stability function  $r : \mathbb{C} \rightarrow \mathbb{C}$  is given as

$$r(z) = \mathbf{1} + z \mathbf{b}^T (\mathbf{1} - z \mathbf{A})^{-1} \mathbf{1} = \frac{z^2 + 6z + 12}{z^2 - 6z + 12}.$$

Here,  $\mathbf{1} \in \mathbb{R}^{3 \times 3}$  denotes the identity matrix and  $\mathbf{1} \in \mathbb{R}^3$  the three-dimensional tuple of ones. Let  $\Re(z)$  denote the real part of  $z \in \mathbb{C}$ . Then,  $|r(z)| < 1$  for all  $z \in \mathbb{C}$  with  $\Re(z) < 0$ , yielding A-stability. Furthermore,  $\lim_{|z| \rightarrow \infty} |r(z)| = 1 \neq 0$ , which means that the method is not L-stable. Since  $|r(z)| = 1$  for all  $z \in \mathbb{C}$  with  $\Re(z) = 0$  the scheme is isometry preserving. □

**Remark 3.2** (Isometric scheme for unit quaternions). *Parameterizing the rotational group  $\mathbf{R} \in SO(3)$  of a Cosserat rod with unit quaternions  $\mathbf{q} \in \mathbb{R}^4$ , the property  $\|\mathbf{q}\| = 1$  has to be guaranteed in the numerical treatment of the evolution equations (cf. Rem. 2.4). By the isometry of the collocation scheme (3.2) this property is fulfilled.*

<sup>1</sup>For details see <http://www.mathworks.com>.

### 3.1.2. Continuation method

In the continuation method we embed the BVP of interest (3.1) into a family of problems by introducing a continuation parameter tuple  $\mathbf{p} \in [0, 1]^n$ ,  $n \in \mathbb{N}$ ,

$$\begin{aligned} \frac{d}{ds} \mathbf{y} &= \hat{\mathbf{f}}(\mathbf{y}; \mathbf{p}), & \hat{\mathbf{g}}(\mathbf{y}(0), \mathbf{y}(1); \mathbf{p}) &= \mathbf{0}, & \mathbf{p} &\in [0, 1]^n, \\ \hat{\mathbf{f}}(\cdot; \underline{\mathbf{1}}) &= \mathbf{f}, & \hat{\mathbf{g}}(\cdot, \cdot; \underline{\mathbf{1}}) &= \mathbf{g}, & \hat{\mathbf{f}}(\cdot; \mathbf{0}) &= \mathbf{f}_0, & \hat{\mathbf{g}}(\cdot, \cdot; \mathbf{0}) &= \mathbf{g}_0. \end{aligned}$$

Here,  $\underline{\mathbf{1}} \in \mathbb{R}^n$  denotes the  $n$ -dimensional tuple of ones. The functions  $\mathbf{f}_0, \mathbf{g}_0$  are chosen in such a way that for  $\mathbf{p} = \mathbf{0}$  an analytical solution is known. Given this starting solution, we seek for a sequence of parameter tuples  $\mathbf{0} = \mathbf{p}_0, \mathbf{p}_1, \dots, \mathbf{p}_m = \underline{\mathbf{1}}$  such that the solution to the respective predecessor BVP provides a good initial guess for the successor. The solution associated to  $\mathbf{p} = \underline{\mathbf{1}}$  finally belongs to the original system. With the help of the continuation parameters certain terms in the ODEs can be first excluded, then included. Also the boundary conditions can be varied. The core of a robust continuation procedure are the choice of a continuation path and the step size control to navigate through a high-dimensional parameter space. They decide about failure or success because there are not always existing solutions and several ways might be possible. Whereas the choice of the continuation path is problem-specific, the step size control follows a general strategy. We follow an approach that was successfully employed in studies on glass wool manufacturing [5]. To explain the used procedure, we consider a one-dimensional parameter space  $p \in [0, 1]$ . Proceeding from an initial continuation step size  $\Delta p_0$ , a BVP is always solved twice by using one full step and two half steps. If the full step requires more Newton iterations than both half steps together or  $k_1$ -times more collocation points than the second half step, the continuation step is reduced by a factor  $k_2$ , otherwise it is increased by  $k_2$  for the further computation. If the Newton method fails, the step size is reduced by a factor  $k_3$  and the computation is repeated. Certainly, it can happen that no solutions exist for  $p > p_{crit} \geq 0$ , thus the algorithm for the adaptive step size control has a stopping criterion that is based on a minimal step size  $\Delta p_{min}$ . In particular, we use  $k_1 = 0.1$ ,  $k_2 = 1.5$ ,  $k_3 = 10$ ,  $\Delta p_0 = 10^{-1}$ ,  $\Delta p_{min} = 10^{-14}$ . In a high-dimensional parameter space  $\mathbf{p} \in [0, 1]^n$ ,  $n \gg 1$ , there might be numerous possible but also impossible continuation paths for a specific model problem. We describe the model-dependent continuation strategy for each spinning setup in the corresponding chapters.

## 3.2. Boundary value problems of quasilinear hyperbolic partial differential equations

On the space-time domain  $\mathcal{D} = \{(\zeta, t) \in \mathbb{R}^2 \mid \zeta \in \mathcal{Q}(t), t \in (0, t_{end}]\}$ ,  $\mathcal{Q}(t) = (\zeta_L(t), \zeta_R(t))$ , we consider the general initial-boundary value problem of quasilinear hyperbolic PDEs

$$\begin{aligned} \mathbf{K}(\mathbf{y}) \cdot \partial_t \mathbf{y} + \mathbf{L}(\mathbf{y}) \cdot \partial_\zeta \mathbf{y} + \mathbf{l}(\mathbf{y}) &= \mathbf{0}, & \text{on } \mathcal{D}, \\ \mathbf{g}(\mathbf{y}(\zeta_L(t), t), \mathbf{y}(\zeta_R(t), t)) &= \mathbf{0}, & \text{for } t > 0, \\ \mathbf{h}(\mathbf{y}(\zeta, 0)) &= \mathbf{0}, & \text{for } \zeta \in \bar{\mathcal{Q}}(0), \end{aligned} \quad (3.3)$$

with matrix valued fields  $\mathbf{K}, \mathbf{L} : \mathbb{R}^{N_v} \rightarrow \mathbb{R}^{N_v \times N_v}$ , the vector field  $\mathbf{l} : \mathbb{R}^{N_v} \rightarrow \mathbb{R}^{N_v}$  as well as the boundary condition function  $\mathbf{g} : \mathbb{R}^{N_v} \times \mathbb{R}^{N_v} \rightarrow \mathbb{R}^{N_{bc}}$  and the initial condition function  $\mathbf{h} : \mathbb{R}^{N_v} \rightarrow \mathbb{R}^{N_v}$ . Here,  $\mathbf{y} : \mathcal{D} \rightarrow \mathbb{R}^{N_v}$  denotes the vector of unknowns with  $N_v$  the total number of unknowns and  $N_{bc}$  is the number of boundary conditions being posed. Moreover,  $\bar{\mathcal{Q}}(0)$  indicates the closure of  $\mathcal{Q}(0)$ , i.e.,  $\bar{\mathcal{Q}}(0) = [\zeta_L(0), \zeta_R(0)]$ . We assume that the time-dependent space domain has the form  $\mathcal{Q}(t) = (-t, 0)$ ,  $t \geq 0$ , i.e., the right boundary is fixed ( $\zeta_R(t) = 0$ ) whereas the left boundary is an inflow boundary. This configuration can be interpreted as material description for a growing fiber that enters the initially empty flow domain on the left side (nozzle) with scalar velocity  $v_{in}$  [m/s]. Then, the space domain fulfills  $\mathcal{Q}(t) = (\zeta_L(t), 0)$  with  $d/dt \zeta_L(t) = -v_{in}$ ,  $\zeta_L(0) = 0$ . The choice  $v_0 = v_{in}$  as typical velocity for nondimensionalization leads to  $\zeta_L(t) = -t$  and  $\mathcal{Q}(t) = (-t, 0)$ .

The growing fiber domain is realized by dynamic and static spatial cells according to the discretization concept in [2]. For the spatial discretization we introduce a constant cell size  $\Delta\zeta > 0$  and define the number of dynamic cells  $N(t)$  depending on the fiber length  $|\zeta_L(t)| = t$  at time  $t$

$$N(t) = \left\lfloor \frac{|\zeta_L(t)|}{\Delta\zeta} \right\rfloor.$$

Here  $\lfloor \cdot \rfloor$  denotes the floor function. Furthermore, we introduce discretization points

$$\zeta_{(j+1)/2} = -\left(N(t) - \frac{j}{2}\right) \Delta\zeta, \quad j = 0, \dots, 2N(t).$$

The points  $\zeta_i$ ,  $i = 1, \dots, N(t)$ , denote the cell centers. The dynamic cell closest to the nozzle ( $\zeta = -t$ ) is represented by  $[\zeta_{1/2}, \zeta_{3/2}]$ , whereas  $\zeta_{N+1/2} = 0$  is the fiber end, cf. Fig. 3.1. The jet growth is realized by adding static cells at the nozzle. This means we add new cells at the left side of the computational domain which

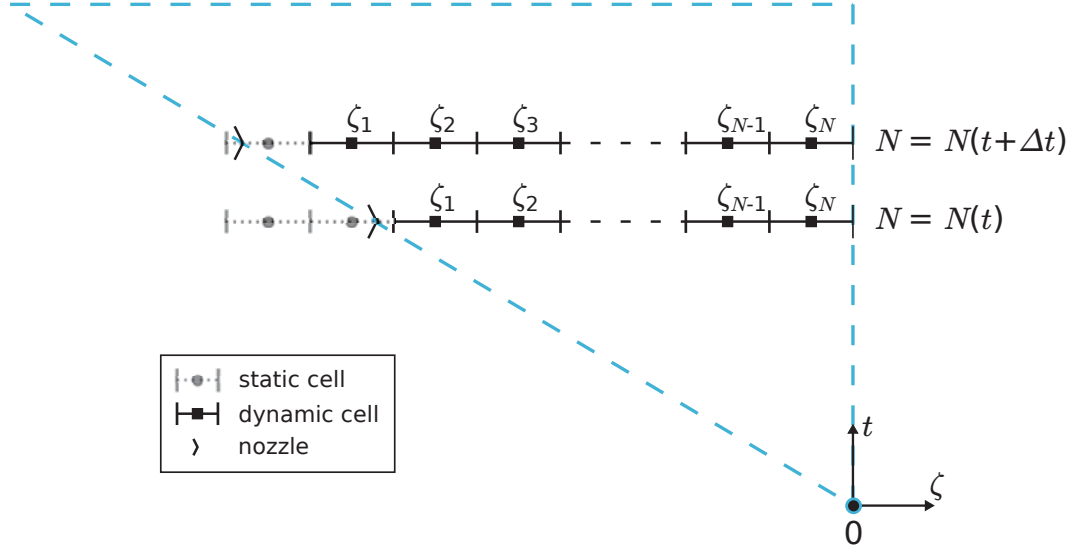


**Figure 3.1.:** Illustration of the spatial discretization of the growing jet domain  $Q(t)$  (marked by the blue dashed line) with  $N(t)$  dynamic cells. Cells are treated as static cells until they completely entered the flow domain.

are initialized by the boundary conditions at the nozzle. The static cells remain static until they have completely left the nozzle. When they have completely entered the flow domain, they are called dynamic cells and only then taken into consideration for the computation. The introduction of static cells at the nozzle allows the suitable initialization of a jet with length  $|\zeta_L(t)| < \Delta\zeta$  and a stable numerical treatment of the temporal evolution.

We define the cell averages  $\mathbf{y}_i$ ,  $i = 1, \dots, N(t)$ , of the unknown quantities

$$\mathbf{y}_i(t) = \frac{1}{\Delta\zeta} \int_{\zeta_{i-1/2}}^{\zeta_{i+1/2}} \mathbf{y}(\zeta, t) d\zeta,$$

integrate the quasilinear system (3.3) over the control cells  $[\zeta_{i-1/2}, \zeta_{i+1/2}]$ ,  $i = 1, \dots, N(t)$ , in which we assume  $\mathbf{X}(\mathbf{y})|_{[\zeta_{i-1/2}, \zeta_{i+1/2}]} = \mathbf{X}(\mathbf{y}_i)$  for  $\mathbf{X} = \mathbf{K}, \mathbf{L}, \mathbf{l}$  and adopt the idea of the Lax-Friedrichs scheme for the approximation of the numerical fluxes as done in [34]. The resulting system of ODEs for the cell averages  $\mathbf{y}_i$  with respect to time has the form

$$\begin{aligned} \mathbf{K}(\mathbf{y}_i) \cdot \frac{d}{dt} \mathbf{y}_i - \mathbf{K}(\mathbf{y}_i) \cdot \frac{1}{2\Delta t} (\mathbf{y}_{i+1} - 2\mathbf{y}_i + \mathbf{y}_{i-1}) \\ + \mathbf{L}(\mathbf{y}_i) \cdot \frac{1}{2\Delta\zeta} (\mathbf{y}_{i+1} - \mathbf{y}_{i-1}) + \mathbf{l}(\mathbf{y}_i) = 0, \end{aligned} \quad (3.4)$$

where  $\Delta t > 0$  denotes the constant time-step size that we will use in the temporal discretization. The incorporation of initial and boundary conditions in our

numerical scheme is realized by extra (ghost) layers. Following [55] quantities not being prescribed at a boundary are extrapolated on the corresponding ghost layer, in particular we choose first order extrapolation.

For the solution of the system of ODEs (3.4) we employ the stiffly accurate implicit Euler scheme with constant time-step size  $\Delta t > 0$

$$\begin{aligned} \mathbf{K}(\mathbf{y}_i^{n+1}) \cdot \left( 2\mathbf{y}_i^{n+1} - \frac{1}{2}\mathbf{y}_{i+1}^{n+1} - \frac{1}{2}\mathbf{y}_{i-1}^{n+1} - \mathbf{y}_i^n \right) + \mathbf{L}(\mathbf{y}_i^{n+1}) \cdot \frac{\Delta t}{2\Delta\zeta} (\mathbf{y}_{i+1}^{n+1} - \mathbf{y}_{i-1}^{n+1}) \\ + \Delta t \mathbf{l}(\mathbf{y}_i^{n+1}) = 0, \end{aligned} \quad (3.5)$$

with  $\mathbf{y}_i^n = \mathbf{y}_i(t^n)$  and  $t^n = n\Delta t$  for  $n = 0, \dots, M$ ,  $t^M = t_{end}$ . The resulting nonlinear system of equations is solved by a Newton-method with Armijo step size control and the Jacobian of the system matrix is prescribed analytically. The break-up criterion of the Newton algorithm is set to an absolute error tolerance  $tol = 10^{-8}$  with respect to the maximum norm.

**Remark 3.3** (Artificial diffusion). *The semi-discrete system (3.4) can be seen as a spatial discretization of*

$$\mathbf{K}(\mathbf{y}) \cdot \partial_t \mathbf{y} + \mathbf{L}(\mathbf{y}) \cdot \partial_\zeta \mathbf{y} + \mathbf{l}(\mathbf{y}) = \mathbf{K}(\mathbf{y}) \cdot \eta \partial_{\zeta\zeta} \mathbf{y}$$

with  $\eta = (\Delta\zeta)^2 / (2\Delta t)$  by means of a central approximation of the flux terms. This means we add artificial diffusion of magnitude  $\eta$  to our system as it is common for classical Lax-Friedrichs schemes.

**Remark 3.4** (Convergence of numerical scheme). *As it is well-known from classical literature (e.g., [55]), the numerical scheme (3.5) provides accuracy of order one with respect to the time and accuracy of order two with respect to the space discretization yielding a combined convergence of order one. In [25, 34, 71] a similar scheme has been investigated with respect to a stability concept for non-conservative hyperbolic PDEs. For a numerical convergence study we refer to Appendix B.1.*

### 3.3. Radial advection-diffusion equations with Robin boundary conditions

We consider a BVP with Robin-type boundary condition of the form

$$\begin{aligned} \partial_x \psi - \frac{1}{r} \partial_r (r \partial_r \psi) = 0, \\ \psi|_{x=0} = \psi_{in}, \quad \partial_r \psi|_{r=0} = 0, \quad \partial_r \psi|_{r=1} = a\psi|_{r=1} + b, \end{aligned}$$

with  $\psi : [0, 1]^2 \rightarrow \mathbb{R}$ ,  $(r, x) \mapsto \psi(r, x)$ , as well as functions  $a, b : [0, 1] \rightarrow \mathbb{R}$  and constant  $\psi_{in} \in \mathbb{R}$ . If the function  $a$  is constant, the solution can be given analytically in terms of an explicit expression. For non-constant  $a$  we treat the Robin boundary condition as Neumann boundary condition depending on  $\psi|_{r=1}$  and find an implicit solution expression for  $\psi$  with Green's function  $g$  in [10, 23, 76], for details see Appendix B.2. The solution expression reads

$$\psi(r, x) = \psi_{in} + 2\pi \int_0^x g(r, x - x') k(x', \psi(1, x')) dx', \quad (3.6)$$

$$\text{with } g(r, z) = \frac{1}{\pi} \left( 1 + \sum_{m=1}^{\infty} \frac{J_0(\beta_m r)}{J_0(\beta_m)} \exp(-\beta_m^2 z) \right), \quad k(x, y) = a(x)y + b(x),$$

where  $J_i$  denote the  $i$ -th Bessel functions of first kind and  $\beta_m > 0$ ,  $m \in \mathbb{N}$ , are the (non-trivial) ascending zeros of the first Bessel function of first kind, i.e.,  $J_1(\beta_m) = 0$ . These values are tabulated in literature, see e.g. [23]. For  $\psi|_{r=1}$  the solution expression yields a Volterra integral equation of second kind

$$\psi(1, x) = \psi_{in} + 2\pi \int_0^x g(1, x - x') k(x', \psi(1, x')) dx', \quad (3.7)$$

$$\text{with } g(1, z) = \frac{1}{\pi} \left( 1 + \sum_{m=1}^{\infty} \exp(-\beta_m^2 z) \right).$$

The integral kernel  $g$  is singular for  $z = 0$ . Therefore, numerical integration in the sense of quadrature formulas cannot be applied directly to the integral in (3.7), because they involve the evaluation of the integrand function at or close to the singularity. Hence, we use the product integration method, which means substituting the function  $k(\cdot, \psi(1, \cdot))$  piecewise by Lagrange interpolation polynomials and employing iterated integration by parts to isolate the singularity of the kernel function  $g$ . We choose two different kinds of interpolation polynomials,

- (i) constant polynomials corresponding to the implicit Euler method,
- (ii) quadratic polynomials with nodes corresponding to the Lobatto IIIa collocation scheme (3.2).

#### Product integration associated to the implicit Euler scheme

Let  $0 = x_0 < x_1 < \dots < x_{N_x} = 1$  be the mesh points in  $x$ -direction. Substituting the integrand function  $k(\cdot, \psi(1, \cdot))$  piecewise by constants in the sense of the implicit

Euler scheme and subsequent integration yields method (i)

$$\begin{aligned}\psi_i &= \psi_0 + 2\pi \sum_{j=1}^i \int_{x_{j-1}}^{x_j} g(1, x_i - x') k(x_j, \psi_j) dx' \\ &= \psi_0 + 2\pi \sum_{j=1}^i \left( -g_{ij}^{(-1)} + g_{ij-1}^{(-1)} \right) k(x_j, \psi_j), \quad i = 1, \dots, N_x,\end{aligned}$$

with  $\psi_i = \psi(1, x_i)$ ,  $\psi_0 = \psi_{in}$ , and the primitive

$$g_{ij}^{(-1)} = g^{(-1)}(1, x_i - x_j), \quad g^{(-1)}(r, x) = \int_0^x g(r, x') dx',$$

which can be evaluated analytically. This results in the linear system of equations

$$(\mathbf{1} - 2\pi\mathbf{H}) \cdot \boldsymbol{\psi} = \boldsymbol{\psi}_0 + 2\pi\mathbf{h}$$

for the unknown vector  $\boldsymbol{\psi} = (\psi_1, \dots, \psi_{N_x}) \in \mathbb{R}^{N_x}$ . Here,  $\boldsymbol{\psi}_0 = \psi_0 \mathbf{1} \in \mathbb{R}^{N_x}$  and the matrix  $\mathbf{H} \in \mathbb{R}^{N_x \times N_x}$  as well as right hand side vector  $\mathbf{h} \in \mathbb{R}^{N_x}$  are given as

$$\mathbf{H} = \mathbf{G} \cdot \text{diag}(\mathbf{a}), \quad \mathbf{h} = \mathbf{G} \cdot \mathbf{b},$$

where  $\mathbf{G} = (G_{ij})_{i,j=1,\dots,N_x} \in \mathbb{R}^{N_x \times N_x}$ ,

$$G_{ij} = \begin{cases} -g_{ij}^{(-1)} + g_{ij-1}^{(-1)} & , \text{if } 1 \leq j \leq i, \\ 0 & , \text{else,} \end{cases}$$

and  $\mathbf{a} = (a_1, \dots, a_{N_x}) \in \mathbb{R}^{N_x}$ ,  $\mathbf{b} = (b_1, \dots, b_{N_x}) \in \mathbb{R}^{N_x}$  using the abbreviations  $a_i = a(x_i)$ ,  $b_i = b(x_i)$ . The system matrix  $(\mathbf{1} - 2\pi\mathbf{H})$  is lower triangular such that the linear system of equations can be solved by forward substitution.

### Product integration associated to the Lobatto IIIa method

We consider method (ii), i.e., we substitute the integrand function  $k(\cdot, \psi(1, \cdot))$  piecewise by quadratic interpolation polynomials with nodes corresponding to the Lobatto IIIa collocation scheme (3.2), which we use for the solution of BVPs of ODEs (cf. Sec. 3.1). For the mesh points  $x_i$ ,  $i = 0, \dots, N_x$ , with mesh size

### 3. Numerical framework

---

$l_i = x_i - x_{i-1}$  we write

$$\begin{aligned} \psi_i = \psi_0 + 2\pi \sum_{j=1}^i \int_{x_{j-1}}^{x_j} g(1, x_i - x') & \left( k(x_{j-1}, \psi_{j-1}) \frac{(x' - x_{j-1/2})(x' - x_j)}{(x_{j-1} - x_{j-1/2})(x_{j-1} - x_j)} \right. \\ & + k(x_{j-1/2}, \psi_{j-1/2}) \frac{(x' - x_{j-1})(x' - x_j)}{(x_{j-1/2} - x_{j-1})(x_{j-1/2} - x_j)} \\ & \left. + k(x_j, \psi_j) \frac{(x' - x_{j-1})(x' - x_{j-1/2})}{(x_j - x_{j-1})(x_j - x_{j-1/2})} \right) dx', \end{aligned}$$

where

$$\begin{aligned} x_{j-1/2} &= \frac{1}{2}(x_{j-1} + x_j), \quad \psi_j = \psi(1, x_j), \\ \psi_{j-1/2} &= \frac{1}{2}(\psi_{j-1} + \psi_j) + \frac{l_j}{8} (k(x_{j-1}, \psi_{j-1}) - k(x_j, \psi_j)). \end{aligned}$$

Applying integration by parts consecutively three times yields again a linear system of equations

$$(\mathbf{1} - 2\pi\mathbf{H}) \cdot \boldsymbol{\psi} = \boldsymbol{\psi}_0 + 2\pi\mathbf{h}$$

for the unknown vector  $\boldsymbol{\psi} = (\psi_1, \dots, \psi_{N_x}) \in \mathbb{R}^{N_x}$  with matrix  $\mathbf{H} = (H_{ij})_{i,j=1,\dots,N_x} \in \mathbb{R}^{N_x \times N_x}$

$$H_{ij} = \begin{cases} a_j(A_{ij+1} + C_{ij}) + D_{j+1}B_{ij+1} + E_jB_{ij} & , \text{if } 1 \leq j < i \wedge i > 1, \\ E_iB_{ii} + a_iC_{ii} & , \text{if } j = i, \\ 0 & , \text{else,} \end{cases}$$

as well as right hand side vectors  $\boldsymbol{\psi}_0 = \psi_0 \mathbf{1} \in \mathbb{R}^{N_x}$  and  $\mathbf{h} = (h_i)_{i=1,\dots,N_x} \in \mathbb{R}^{N_x}$

$$h_i = \psi_0(a_0A_{i1} + D_1B_{i1}/(2\pi)) + \sum_{j=1}^i (b_{j-1}A_{ij} + b_jC_{ij} + F_jB_{ij}).$$

Here, we use the abbreviations

$$\begin{aligned}
 A_{ij} &= g_{ij-1}^{(-1)} - \frac{1}{l_j} \left( g_{ij}^{(-2)} + 3g_{ij-1}^{(-2)} \right) + \frac{4}{l_j^2} \left( -g_{ij}^{(-3)} + g_{ij-1}^{(-3)} \right), \\
 B_{ij} &= \frac{4}{l_j} \left( g_{ij}^{(-2)} + g_{ij-1}^{(-2)} \right) - \frac{8}{l_j^2} \left( -g_{ij}^{(-3)} + g_{ij-1}^{(-3)} \right), \\
 C_{ij} &= -g_{ij}^{(-1)} - \frac{1}{l_j} \left( 3g_{ij}^{(-2)} + g_{ij-1}^{(-2)} \right) + \frac{4}{l_j^2} \left( -g_{ij}^{(-3)} + g_{ij-1}^{(-3)} \right), \\
 D_j &= \frac{1}{2} a_{j-1/2} + \frac{l_j}{8} a_{j-1/2} a_{j-1}, & E_j &= \frac{1}{2} a_{j-1/2} - \frac{l_j}{8} a_{j-1/2} a_j, \\
 F_j &= a_{j-1/2} \frac{l_j}{8} (b_{j-1} - b_j) + b_{j-1/2},
 \end{aligned}$$

as well as  $a_j = a(x_j)$ ,  $b_j = b(x_j)$  and the primitives

$$g_{ij}^{(-\nu)} = g^{(-\nu)}(1, x_i - x_j), \quad g^{(-\nu)}(r, x) = \int_0^x g^{(-(\nu-1))}(r, x') dx', \quad \nu \in \mathbb{N},$$

$$g^{(0)}(r, x) = g(r, x),$$

which can be evaluated analytically. Again the system matrix  $(1 - 2\pi\mathbf{H})$  is lower triangular, such that the linear system of equations can be solved by forward substitution.

**Remark 3.5** (Computation of profiles). *For the computation of the radial profiles we introduce an equidistant grid in  $r$ -direction with points  $0 = r_0 < r_1 < \dots < r_{N_r} = 1$ ,  $N_r \in \mathbb{N}$ . Then, for given solution  $\psi(1, x_i)$  we fix a point  $r_j$ ,  $0 \leq j < N_r$ . Considering the solution expression (3.6) the solution  $\psi(r_j, x_i)$  is calculated straightforwardly for all  $i = 1, \dots, N_x$  by integration utilizing the respective product integration method (i) or (ii).*

**Remark 3.6** (Stability for stiff problems). *Considering the scalar-valued test-problem  $y(s) = 1 + \lambda \int_0^s y(t) dt$  with  $\lambda \in \mathbb{C}$  is usual practice to analyze the stability of numerical methods for the solution of integral equations. Due to the fact that for this test-problem product integration methods are equivalent to the corresponding methods for ODEs, the product integration methods inherit the stability of these underlying methods. This means our method (ii) based on Lobatto IIIa collocation is A-stable but not L-stable (cf. Lemma 3.1). Thus, it can lead to oscillations for very stiff problems. Method (i) possesses A- and L-stability due to the underlying implicit Euler scheme. We will discuss this stability issue as well as the respective order of convergence in App. B.3. For our applications we suggest the following procedure: We choose the higher order method (ii) as standard product integration method. If oscillations occur, we switch this product integration method to method (i) lowering the order of convergence but increasing the stability.*

## 3.4. Fiber-airflow interaction

Considering industrial spinning setups one or multiple fibers are spun by injecting one or several polymeric jets from a nozzle into an air stream. The nature of this airflow has a deep impact onto the behavior of the fibers. If multiple (possibly several hundred) fibers are spun simultaneously, these fibers itself affect the properties of the airflow. Thus, for multiple fibers a two-way coupling between the fibers and the airflow has to be taken into account, whereas for one fiber it is usually sufficient to consider a one-way fiber-airflow coupling neglecting the fiber's impact on the flow.

In three-dimensional modeling the coupling between fibers and airflow can be realized with the help of interface/boundary conditions at the lateral fiber boundary. In our one-dimensional description of the fibers in terms of the special Cosserat theory such lateral boundary conditions cannot be posed. Thus, the coupling has to be realized by exchange models. Regarding the fibers the momentum exchange is realized by the air drag model (2.9) for the force  $\vec{f}_{air}$ . Additionally arising heat and mass exchange are modeled with the help of heat and mass flux terms (see Chap. 4 for heat and mass transfer through solvent evaporation). In the following we representatively consider the heat exchange and denote the associated flux term with  $q_{air}$ . The exchange models for  $\vec{f}_{air}$  and  $q_{air}$  depend on the airflow data. For one-way coupling the required airflow fields are computed once before starting the fiber computation and plugged into the air drag function as well as in the heat and mass transfer models. For two-way coupling additional exchange terms are included in the airflow model. The loads induced by the fibers are denoted by  $\vec{f}_{fib}$  and the heat sources by  $q_{fib}$ . The exchange models are constructed in such a way, that the principle of action equaling reaction is fulfilled, cf. [21, 22]. The two-way fiber-air-interaction is realized by a weak coupling algorithm which iterates between fiber computations and airflow simulations. This procedure allows the combination of self-implemented code for the fiber dynamics as well as a commercial software for the air dynamics and was successfully used in studies on glass wool manufacturing [5].

We employ ANSYS Fluent<sup>2</sup>, a finite-volume-based software, that contains the broad physical modeling capabilities to describe airflow, heat and mass transfer for spinning processes. The airflow is assumed to be stationary and modeled using (Euler-)stationary compressible Navier-Stokes equations on the domain  $Q_* \subset \mathbb{E}^3$  representing the considered spinning device. The equations give relations for the density  $\rho_*$  [kg/m<sup>3</sup>], the velocity  $\vec{v}_*$  [m/s] as well as the temperature  $T_*$  [K] of

---

<sup>2</sup>For details on the commercial software ANSYS Fluent, its models and solvers we refer to <http://www.ansys.com>.

the air (cf. [5])

$$\begin{aligned}
 \nabla \cdot (\rho_* \vec{v}_*) &= 0, \\
 \nabla \cdot (\rho_* \vec{v}_* \otimes \vec{v}_*) &= \nabla \cdot \bar{\bar{\Sigma}}_*^T + \rho_* g \vec{e}_g + \vec{f}_{fib}, \\
 \nabla \cdot (\rho_* e_* \vec{v}_*) &= \bar{\bar{\Sigma}}_* : \nabla \vec{v}_* - \nabla \cdot \vec{q}_* + q_{fib}.
 \end{aligned} \tag{3.8}$$

These equations are supplemented with the Newtonian stress tensor  $\bar{\bar{\Sigma}}_*$  [Pa], the Fourier law for the heat conduction  $\vec{q}_*$  [W/m<sup>2</sup>] as well as thermal and caloric equations of state for an ideal gas

$$\begin{aligned}
 \bar{\bar{\Sigma}}_* &= -p_* \bar{\bar{I}} + \rho_* \nu_* (\nabla \vec{v}_* + (\nabla \vec{v}_*)^T) + \xi_* \nabla \cdot \vec{v}_* \bar{\bar{I}}, \\
 \vec{q}_* &= -\lambda_* \nabla T_*, \\
 p_* &= \rho_* R_* T_*, \quad e_* = \int_0^{T_*} q_*(T) dT - \frac{p_*}{\rho_*}.
 \end{aligned}$$

Here,  $p_*$  [Pa] denotes the pressure,  $e_*$  [J/kg] the inner energy,  $R_*$  [J/(kg K)] the specific gas constant,  $\nu_*$  [m<sup>2</sup>/s] the kinematic viscosity,  $\xi_*$  [Pa s] the second viscosity,  $q_*$  [J/(kg K)] the specific heat capacity and  $\lambda_*$  [W/(m K)] the heat conductivity of air. Moreover,  $\bar{\bar{I}} \in \mathbb{E}^3 \otimes \mathbb{E}^3$  is the identity tensor and  $:$  denotes the scalar product for rank-two tensors. External forces originate from gravity with direction  $\vec{e}_g$  and the induced load from the immersed fibers  $\vec{f}_{fib}$  [N/m<sup>3</sup>]. The fibers also imply a heat source  $q_{fib}$  [W/m<sup>3</sup>] in the energy equation. If solvent evaporates out of the fibers an additional mass balance for the solvent gas in the air is incorporated including a mass source term.

For one-way coupling the fiber induced loads as well as heat and mass sources are neglected, i.e.,  $\vec{f}_{fib} = \vec{0}$ ,  $q_{fib} = 0$ . For two-way coupling the exchange models are constructed in such a way, that the principle of action equaling reaction is fulfilled and hence the momentum, heat and mass is conserved, i.e.,

$$\int_{\mathcal{Q}_V(t)} k_{air}(s, t) ds = - \int_V k_{fib}(\vec{x}, t) d\vec{x}, \quad k \in \{\vec{f}, q\},$$

for an arbitrary domain  $V \subset \mathbb{E}^3$  and  $\mathcal{Q}_V(t) = \{s \in \mathcal{Q}(t) \mid \vec{r}(s, t) \in V\}$ , cf. [5]. To close the equations boundary conditions depending on the specific inflow situation and device geometry have to be chosen. The fiber associated exchange models ( $\vec{f}_{fib}$ ,  $q_{fib}$ , etc.) are incorporated by user defined functions (UDFs).

Considering  $M$  representative fibers,  $M \in \mathbb{N}$ , and neglecting fiber-fiber-interactions, the solutions for all fibers are computed in parallel by either of the numerical solution schemes from Sec. 3.1 or Sec. 3.2, which are implemented in MATLAB.

Because of the different discretizations of airflow and fibers, the exchange of airflow and fiber data between the solvers requires interpolation and averaging. For the air associated exchange models ( $\vec{f}_{air}$ ,  $q_{air}$ , etc.) the airflow data are linearly interpolated on the fiber grid used in the collocation method. For the fiber associated exchange models ( $\vec{f}_{fib}$ ,  $q_{fib}$ , etc.) entering the finite volume scheme, the information of all fibers is spatially averaged over each cell volume. Since the interpolation and averaging strategies are qualitatively different, the conservation principles are only ensured for very fine resolutions. Moreover, note that due to the underlying finite volume approach the computed airflow data are cell-averaged quantities. In this context the numerical cell-averaging can be interpreted as homogenization strategy for the exchange models that is necessary to avoid the occurrence of singularities and the failure of the two-way-coupling. For details we refer to [22] for the two-way-coupling within an asymptotic modeling framework, to [21] for the homogenization and to [5] for the algorithmic procedure.

Let  $\mathcal{S}$  and  $\mathcal{S}_*$  be the algorithmic simulation procedures to obtain the quantities  $\Psi = (\Psi_k)$ ,  $k \in \{1, \dots, M\}$ , of the  $M$  fibers and the quantities  $\Psi_*$  of the airflow, respectively. Then, the basic coupling algorithms have the following form:

**Algorithm 3.7** (One-way fiber-airflow coupling).

- (1) Perform an airflow simulation  $\mathcal{S}_*$  without fibers to obtain  $\Psi_*$ .
- (2) Calculate  $\Psi_k = \mathcal{S}(\Psi_*)$  for all fibers  $k = 1, \dots, M$  (mostly  $M = 1$ ).

**Algorithm 3.8** (Two-way fiber-airflow coupling).

- (1) Perform an airflow simulation  $\mathcal{S}_*$  without fibers to obtain  $\Psi_*^{(1)}$ .
- (2) For  $i \geq 1$ , calculate  $\Psi_k^{(i)} = \mathcal{S}(\Psi_*^{(i)})$  for all fibers  $k = 1, \dots, M$  and afterwards compute the new airflow data  $\Psi_*^{(i+1)} = \mathcal{S}_*(\Psi^{(i)})$ , as long as  $\|\Psi_*^{(i)} - \Psi_*^{(i+1)}\| > tol$  for given tolerance  $tol$ .

**Remark 3.9** (Hardware and software configuration). *If not stated otherwise, all forthcoming computations have been done on a system with an Intel Core i7-6700 CPU (4 cores, 8 threads) and 16 GBytes of RAM. Furthermore, the MATLAB version R2016b and the ANSYS Fluent version 18.1 have been used.*

## 4. Fiber spinning with evaporation effects in airflows

In this chapter we examine fiber production processes which are crucially driven by solvent evaporation effects. In the following we focus exclusively on dry spinning that can be seen as prototype of such processes. Nevertheless, the following strategies and concepts can easily be adopted to other spinning scenarios where solvent evaporation takes place. Dry spinning itself is a widely used production method for fibers which consist of polymers that must be dissolved in solvent, as for example cellulose acetate, polyacrylonitrile, polyurethane, benzene and many more. As schematized in Fig. 4.1 dry spinning devices essentially consist of jet nozzles (spinneret) through which a polymer diluent solution is fed at constant and controllable rate through up to several hundred holes into a spinning duct. From these holes of the spinneret the fibers form out, are pulled down by gravity and either laid down on a conveyor belt or drawn down by a take up roller. In the spinning duct the fibers are dried by a heated airflow, which is often blown in at the bottom of the duct and exhausts at the top such that the air forms a counter-current to the fiber flow direction. During this drying process solvent evaporates out of the jets and leads to thinning and solidification of the spun fibers.

In the last 50 years, several work has been spent to examine the dry spinning process. One of the first mathematical models was developed by [35], who employed a species transport equation to predict the solvent concentration in a combined theoretical experimental study. A comprehensive one-dimensional dry spinning model was introduced in [74, 75]. There, averaged mass balance equations for the two species (polymer and diluent) as well as averaged momentum and energy balance equations were considered. The balances for solvent concentration and temperature were found to depend crucially on the values at the fiber boundary, which involves the need for radial resolution of the process. This was taken into account through two-dimensional balance equations. A coupling was realized by adjusting corresponding boundary conditions for surface values of the fiber. In [16] theoretical results based on a two-dimensional model with concentration-dependent thermal conductivity as well as concentration- and temperature-dependent diffusivity and viscosity were compared with an experi-

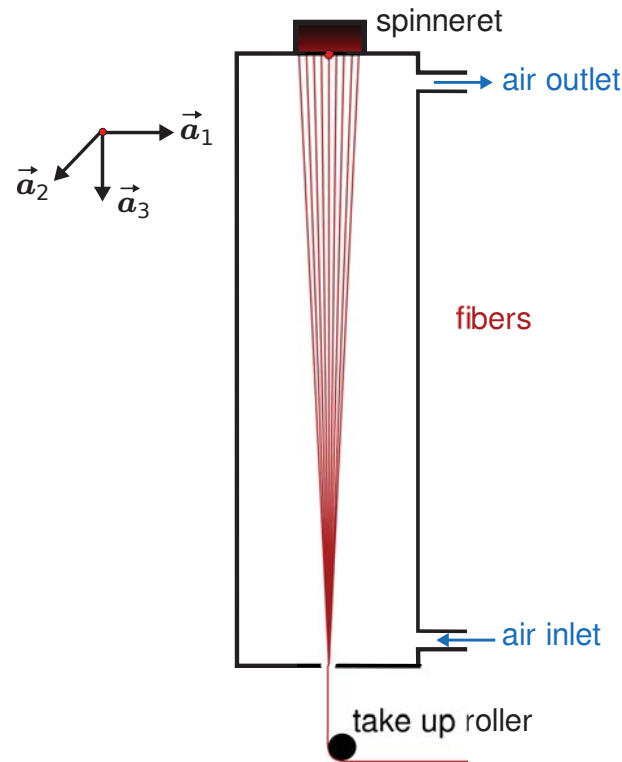


**Figure 4.1.:** Sketch of a typical dry spinning device with take up of the produced fibers at the bottom side of the spinning duct.

mental setup of a cellulose acetate/acetone system. The forming of radial profiles for polymer concentration (mass fraction) and temperature in the fiber was observed. A complete combined theoretical and experimental study of dry spinning of a cellulose acetate/acetone system was presented in [88], where detailed laws for the concentration- and temperature-dependence of physical properties including diffusivity, elongational viscosity, heat and mass transfer coefficients are specified and incorporated in a coupled one- and two-dimensional model setup. All the addressed studies used exclusively viscous constitutive equations. The works of [41, 42] extended the models by incorporating viscoelastic material laws. Apart from that, the effect of solvent evaporation was taken into account in mathematical models for several other spinning processes like wet spinning [127] and electrospinning [117, 120].

Until now the existing literature solely considers interactions of the simulated fibers with an airflow that is assumed to be constant or measured in experiments. However, in industrial applications we are faced with devices having spinnerets with densely packed holes producing many fibers (possibly several hundred) simultaneously, so that also the fibers visibly affect the surrounding air. This creates the need of a fully two-way coupled simulation of the dry spun fibers immersed in the airflow, at which we aim in this chapter. The direct numerical

---

simulation of the three-dimensional multiphase-multiscale problem is computationally extremely demanding and thus in general not possible. Therefore, we employ a dimensionally reduced fiber model in the sense of rods or strings. For such types of models we design efficient solution algorithms such that simulations of dry spinning processes with two-way coupled fiber-airflow interactions become feasible.

Since the rod and string models for fibers as given in Chap. 2 do not contain mass and heat transfer effects induced by solvent evaporation, we extend these models in this chapter to incorporate such effects. We proceed from a three-dimensional free BVP for a viscous uni-axial radially symmetric two-phase flow, from which we deduce a dimensionally reduced fiber model following the asymptotic concepts of string models. Employing cross-sectional averaging we obtain one-dimensional equations for fiber velocity and stress that we combine consistently with two-dimensional advection-diffusion equations covering the cross-sectional variations of polymer mass fraction and temperature. These one-dimensional equations basically equal a viscous string model for an uni-axial fiber in (Euler-)stationary description, cf. System 2.10. In order to describe curved fibers we extend the uni-axial model framework to a viscous Cosserat rod model, which in its basic equations corresponds to System 2.8 in (Euler-)stationary description, cf. Rem. 2.9. For the numerical treatment of the one-dimensional ODEs and the coupling with the two-dimensional PDEs we employ the continuation-collocation algorithm presented in Sec. 3.1. All previously named works concerning dry spinning use some types of finite differences for the solution of the involved two-dimensional problems. We cannot utilize such methods since they are time-consuming and the intended further coupling with airflow simulations easily leads to non-practical computation times. Therefore, we employ our algorithmic procedure based on the analytical solution of the radial advection-diffusion equations with a Green's function and the product integration method for the resulting Volterra integral equations with singular kernel as presented in Sec. 3.3. This approach turns out to be very efficient and allows the realization of two-way coupled fiber-airflow simulations with the help of the coupling procedure presented in Sec. 3.4.

This chapter is structured as follows. Starting from a three-dimensional free BVP for viscous uni-axial dry spinning, we derive our dimensionally reduced (one-two-dimensional) fiber model, which we extend to the description of curved fibers based on the theory of Cosserat rods, in Sec. 4.1. Moreover, we introduce closing models for the heat and mass transfer. In Sec. 4.2 we explain the specific continuation strategy for the numerical solution of the involved one-dimensional parametric BVPs and the utilization of the product integration method for the two-dimensional profiles of mass fraction and temperature. In addition, the coupling of the one- and two-dimensional model equations in combination with the two-way coupling concept for fiber-air interactions is explained. The computational

efficiency of our reduced model as well as its good approximation quality with respect to the original three-dimensional problem are demonstrated in Sec. 4.3. In Sec. 4.4 we consider industrial dry spinning. First we investigate the uni-axial dry spinning setup of [88] with device geometry and air inflow as given in Fig. 4.1 and present simulation results with two-way coupled fiber-air interactions. Subsequently, this setup is modified to an air inflow situation leading to curved fibers. There, we employ our curved fiber dry spinning model and also present simulation results with mutual fiber-air interaction effects. Note that the derivation of the three-dimensional free BVP for viscous uni-axial dryspinning has been pre-published in [112]. The derivation of the dimensionally reduced uni-axial fiber model, the study of its computational efficiency and approximation quality as well as the investigation of the uni-axial industrial setup have been pre-published in [110]. The extension to curved fibers and associated simulation results have been pre-published in [115].

### 4.1. Viscous fiber dry spinning model

In this section we develop our dry spinning models (uni-axial and curved) for a single viscous fiber in a surrounding airflow. Since in dry spinning processes no relevant transient effects occur, we restrict our study to steady considerations. We start with balances for mass, momentum as well as energy for the single phases of a two-phase flow and formulate a three-dimensional free BVP for an uni-axial fiber with the help of the mixture model ansatz. Under the assumptions of radial symmetry and slenderness we derive a dimensionally reduced model that contains the radial diffusion effects of polymer mass fraction and fiber temperature in combination with the tangential information of fiber velocity and stress. To describe curved fibers in dry spinning processes, this dimensionally reduced uni-axial fiber model is extended to a viscous Cosserat rod model. In such curvilinear setups the choice of a Cosserat rod model is appropriate to avoid singularities which might arise for string models in certain parameter regimes, cf. Chap. 2. Finally, appropriate heat and mass transfer models are employed to close the so derived dry spinning models.

#### 4.1.1. Three-dimensional uni-axial fiber model

First, we introduce an (Euler-)stationary three-dimensional dry spinning model for a viscous uni-axial fiber. Let  $\mathcal{Q} \subset \mathbb{E}^3$  be the a priori unknown fiber domain whose boundary  $\partial \mathcal{Q} = \Gamma_{\text{in}} \cup \Gamma_{\text{fr}} \cup \Gamma_{\text{out}}$  consists of the fixed inlet at the nozzle  $\Gamma_{\text{in}}$ , the free lateral fiber surface  $\Gamma_{\text{fr}}$  and the outlet  $\Gamma_{\text{out}}$ . In  $\mathcal{Q}$  we consider balance

laws for mass, momentum and energy for the two phases  $i$ ,  $i \in \{p, d\}$  – polymer and diluent. Thereafter, we employ the mixture model ansatz according to [64] to reduce the balance laws for momentum and energy for the single phases to balance laws for the mixture. The quantities for the single phases are indicated by the respective index  $i$ ,  $i \in \{p, d\}$ . Note that throughout this chapter we use the terms 'diluent' and 'solvent' synonymously.

### Phase balances

We start with an invariant description of the model equations in the Euclidean vector space  $\mathbb{E}^3$ . Let  $\rho_i$  [kg/m<sup>3</sup>] and  $\vec{v}_i$  [m/s],  $i \in \{p, d\}$ , be the partial densities and velocities for the polymer and diluent phases in the mixture. Assuming an Eulerian (spatial) description, the stationary mass balances for the two phases read

$$\nabla \cdot (\rho_i \vec{v}_i) = 0, \quad i \in \{p, d\}. \quad (4.1a)$$

The stationary momentum balances for the polymer and diluent phases are

$$\nabla \cdot (\rho_i \vec{v}_i \otimes \vec{v}_i) = \nabla \cdot \bar{\bar{\Sigma}}_i^T + \vec{f}_i, \quad i \in \{p, d\}, \quad (4.1b)$$

with the respective stress tensors  $\bar{\bar{\Sigma}}_i$  [Pa]. The fields  $\vec{f}_i$  [N/m<sup>3</sup>] denote the body force densities acting on phase  $i$ . Neglecting effects of inner friction, convective terms due to pressure fluctuations as well as energy transfer caused by body forces, the stationary energy balances for the polymer and diluent phases are modeled as

$$\nabla \cdot (\rho h_i \vec{v}_i) = \nabla \cdot (C_i \nabla T), \quad i \in \{p, d\}, \quad (4.1c)$$

where  $h_i$  [J/kg] are the partial specific enthalpies of polymer and diluent in the mixture,  $\rho$  [kg/m<sup>3</sup>] denotes the density of the mixture and the right hand sides represent the energy transport by heat conduction at mixture temperature  $T$  [K] and thermal conductivities  $C_i$  [W/(m K)].

### Mixture model ansatz

The mixture model ansatz according to [64] treats the two phases (polymer and solvent) as interpenetrable continua. Its idea is to consider only one linear momentum equation as sum of the phase balances (4.1b) and only one energy balance equation as sum of (4.1c). The mixture density  $\rho$ , mixture stress tensor  $\bar{\bar{\Sigma}}$ , total body force  $\vec{f}$ , mixture specific enthalpy  $h$  as well as the mixture thermal conductivity  $C$  are the sums of the quantities of the single phases, i.e.,

$$k = k_p + k_d, \quad k \in \{\rho, \bar{\bar{\Sigma}}, \vec{f}, h, C\}.$$

For the mixture we assume ideality, i.e., the volume does not change under mixing and the enthalpy of mixing is zero. This leads to the relations

$$1 = \frac{\rho_p}{\rho_p^0} + \frac{\rho_d}{\rho_d^0}, \quad \rho h_i = \rho_i h_i^0, \quad i \in \{p, d\},$$

where  $\rho_i^0, h_i^0$  denote the material densities and specific enthalpies of pure polymer and solvent. These material parameters might be specified depending on the temperature. Together with the definition of the mixture specific enthalpy  $h$  the relation for the enthalpies results in the more common expression

$$h = \frac{\rho_p}{\rho} h_p^0 + \frac{\rho_d}{\rho} h_d^0.$$

The temperature derivatives of  $h_p^0, h_d^0$  and  $h$  are in particular the specific heat capacities  $q_p^0, q_d^0$  and  $q$  [J/(kg K)] for constant pressure, yielding

$$q = \frac{\rho_p}{\rho} q_p^0 + \frac{\rho_d}{\rho} q_d^0.$$

Here, we used the fact that the mass fractions of the single phases do not explicitly depend on the temperature, i.e.,  $\partial_T(\rho_i/\rho) = 0, i \in \{p, d\}$ . For the stress tensor  $\bar{\bar{\Sigma}}$  we assume incompressibility and a Newtonian fluid with dynamic mixture viscosity  $\mu$  [Pa s], i.e.,  $\bar{\bar{\Sigma}} = -p\bar{\bar{I}} + \mu(\nabla\bar{\mathbf{v}} + (\nabla\bar{\mathbf{v}})^T)$  with mixture pressure  $p$  [Pa], mixture velocity  $\bar{\mathbf{v}}$  [m/s] and  $\bar{\bar{I}} \in \mathbb{E}^3 \otimes \mathbb{E}^3$  denoting the identity tensor. The definition of the mixture velocity  $\bar{\mathbf{v}}$  requires a special treatment: Since the intended consideration of only one linear momentum balance does not close our model, we have to employ constitutive relations for the differences between the phase velocities and the mixture velocity. In our dry spinning scenario we consider the polymer phase as dominating phase and the diluent phase as secondary phase. Therefore, we fix the polymer velocity as mixture velocity, i.e.,  $\bar{\mathbf{v}} = \bar{\mathbf{v}}_p$ . Then, only one constitutive relation for the difference between the mixture velocity and the diluent velocity  $\bar{\mathbf{v}}_{pd} = \bar{\mathbf{v}} - \bar{\mathbf{v}}_d$  is needed. We use Fick's law in a version, which is linear with respect to the diluent mass fraction  $\rho_d/\rho$ , namely  $\rho_d \bar{\mathbf{v}}_{pd} = \rho D \nabla(\rho_d/\rho)$ , with  $D$  [m<sup>2</sup>/s] denoting the diffusion coefficient of the diluent in the polymer. This formulation of Fick's law is appropriate to obtain an efficiently evaluable quasilinear advection-diffusion equation for the polymer mass fraction in the dimensionally reduced fiber model (cf. Sec. 4.1.2). Employing  $\bar{\mathbf{v}} = \bar{\mathbf{v}}_p$  and Fick's law the mass balances for polymer and diluent (4.1a) become

$$\nabla \cdot (\rho_p \bar{\mathbf{v}}) = 0, \quad \nabla \cdot (\rho_d \bar{\mathbf{v}}) - \nabla \cdot \left( \rho D \nabla \left( \frac{\rho_d}{\rho} \right) \right) = 0.$$

Moreover, summing up the momentum phase balances (4.1b) and neglecting diffusive parts in the stresses yields the mixture momentum balance

$$\nabla \cdot (\rho \vec{v} \otimes \vec{v}) - \nabla \cdot \left( \rho D \left( \vec{v} \otimes \nabla \left( \frac{\rho_d}{\rho} \right) + \nabla \left( \frac{\rho_d}{\rho} \right) \otimes \vec{v} \right) \right) = \nabla \cdot \bar{\bar{\Sigma}}^T + \vec{f}.$$

Analogously, using Fick's law and the phase balances (4.1c) we obtain the total energy balance for the mixture

$$\nabla \cdot (\rho h \vec{v}) - \nabla \cdot \left( h_d^0 \rho D \nabla \left( \frac{\rho_d}{\rho} \right) \right) = \nabla \cdot (C \nabla T).$$

### Three-dimensional dry spinning model

Introducing appropriate boundary conditions, the stationary free BVP for the fiber unknowns  $\rho_p$ ,  $p$ ,  $\vec{v}$ ,  $T$  and  $Q$  is given by

**System 4.1** (Three-dimensional free BVP).

Balance laws in  $Q$ :

$$\begin{aligned} \nabla \cdot (\rho_p \vec{v}) &= 0, \\ \nabla \cdot (\rho_d \vec{v}) &= \nabla \cdot \left( \rho D \nabla \left( \frac{\rho_d}{\rho} \right) \right), \\ \nabla \cdot (\rho \vec{v} \otimes \vec{v}) - \nabla \cdot \left( \rho D \left( \vec{v} \otimes \nabla \left( \frac{\rho_d}{\rho} \right) + \nabla \left( \frac{\rho_d}{\rho} \right) \otimes \vec{v} \right) \right) &= \nabla \cdot \bar{\bar{\Sigma}}^T + \vec{g}, \\ \nabla \cdot (\rho h \vec{v}) - \nabla \cdot \left( h_d^0 \rho D \nabla \left( \frac{\rho_d}{\rho} \right) \right) &= \nabla \cdot (C \nabla T). \end{aligned}$$

Kinematic, dynamic, mass and heat flux respective boundary conditions on  $\Gamma_{fr}$ :

$$\begin{aligned} \vec{v} \cdot \vec{n} &= 0, \\ \bar{\bar{\Sigma}} \cdot \vec{n} &= \vec{f}_*, \\ -\rho D \nabla \left( \frac{\rho_d}{\rho} \right) \cdot \vec{n} &= j_c, & j_c &= \gamma \left( \frac{\rho_d}{\rho} - \frac{\rho_{d,*}}{\rho_*} \right), \\ -C \nabla T \cdot \vec{n} &= j_T + j_c (\delta - h_d^0), & j_T &= \alpha (T - T_*). \end{aligned}$$

Inlet boundary conditions on  $\Gamma_{in}$ :

$$\vec{v} = \vec{v}_{in}, \quad \rho_d = \rho_{d,in}, \quad T = T_{in}.$$

Outlet boundary condition on  $\Gamma_{out}$ :

$$\vec{v} = \vec{v}_{out}.$$

Constitutive laws:

$$1 = \frac{\rho_p}{\rho_p^0} + \frac{\rho_d}{\rho_d^0}, \quad h = \frac{\rho_p}{\rho} h_p^0 + \frac{\rho_d}{\rho} h_d^0, \quad \bar{\bar{\Sigma}} = -p \bar{\bar{I}} + \mu (\nabla \vec{v} + (\nabla \vec{v})^T).$$

Here, we consider body forces due to gravity, i.e.,  $\vec{f} = \vec{g}$ , as well as surface forces  $\vec{f}_*$  [Pa] due to the surrounding airflow. The geometry is specified via the kinematic boundary condition on  $\Gamma_{fr}$  with unit outer normal vector  $\vec{n}$ . At the lateral fiber surface the diluent density has a jump due to the solvent evaporation, moreover, it changes rapidly in the boundary layer that the surrounding air forms around the fiber. The diluent mass flux  $j_c$  [kg/(m<sup>2</sup>s)] in the aerodynamic boundary layer can be modeled by the difference of the diluent density in the air at the fiber surface  $\zeta_*$  [kg/m<sup>3</sup>] and away from the fiber  $\rho_{d,*}$  [kg/m<sup>3</sup>] with convective mass transfer coefficient  $\beta$  [m/s], i.e.,  $j_c = \beta(\zeta_* - \rho_{d,*})$ . Let  $c = \rho_p/\rho = 1 - \rho_d/\rho$  be the polymer mass fraction, then we particularly use a formulation for  $j_c$  in terms of the mass fraction associated transfer coefficient  $\gamma = \beta \varrho_*$  [kg/(m<sup>2</sup>s)] with  $\varrho_* = \zeta_* \rho / \rho_d$  [kg/m<sup>3</sup>] in System 4.1. The temperature is continuous at the fiber surface, whereas the heat flux has a jump because of the heat exchange in the air due to the solvent evaporation with evaporation enthalpy  $\delta$  [J/kg] of the diluent. In the aerodynamic boundary layer the heat flux  $j_T$  [W/m<sup>2</sup>] is described – analogously to the mass flux – by the difference of the temperature at the fiber surface and away from the fiber  $T_*$  [K] with heat transfer coefficient  $\alpha$  [W/(m<sup>2</sup>K)]. The parameters  $\delta$  and  $\zeta_*$  might be functions of  $c$  and  $T$ , whereas the transfer coefficients  $\alpha$  and  $\beta$  depend on the state of the surrounding airflow and especially on the relative velocity between fiber and airflow. In System 4.1 the surrounding airflow is assumed to be known in the sense that the quantities  $\vec{f}_*$ ,  $\rho_{d,*}$  and  $T_*$  as well as the airflow dependencies of  $\alpha$  and  $\beta$  are given for each point of the fiber surface. Moreover, the parameters  $D$ ,  $C$  and  $\mu$  might depend on the mass fraction  $c$  and temperature  $T$  with suitable models assumed to be available.

**Remark 4.2** (Mass transfer). *The used formulation of the diluent mass transfer  $j_c$  is motivated from the fact that at the fiber surface the diluent density in the air is mainly linearly proportional to the diluent density in the fiber, i.e.,  $\zeta_* \sim \rho_d$ . Setting  $\zeta_* = (\rho_d/\rho)\varrho_*$  separates the linear part from the remainder  $\varrho_*$ . The mass transfer is principally driven from the linear part in terms of a Robin-type boundary condition, whereas the remainder  $\varrho_*$  is incorporated in the transfer coefficient  $\gamma = \beta \varrho_*$ . This splitting might allow a different treatment of the terms, which becomes essential for our numerical treatment of the problem.*

**Remark 4.3** (Incompressibility). *Considering the mass balance equations for polymer and diluent, assuming constant material densities  $\rho_p^0$ ,  $\rho_d^0$  and using the density relation for an ideal mixture yields*

$$\nabla \cdot \left( \vec{v} - \frac{\rho}{\rho_d^0} D \nabla \left( \frac{\rho_d}{\rho} \right) \right) = 0,$$

*i.e., the flow field is not exactly incompressible with respect to the mixture velocity field  $\vec{v}$ . Nevertheless, we assume an incompressible form of the Newtonian stress*

tensor  $\bar{\bar{\Sigma}}$ , which is justified by very small diffusive velocities being present in industrial applications.

Alternatively, the mixture model theory might also allow the definition of the mixture velocity  $\vec{v}$  as linear combination of each singular phase velocity in such a way that  $\nabla \cdot \vec{v} = 0$  holds. But this ansatz yields diffusive terms in the polymer mass balance equation. Since we aim for a constant polymer flux over the fiber cross-sections, we do not employ it.

### 4.1.2. Dimensionally reduced uni-axial fiber model

In slender body theory viscous fibers are usually described by one-dimensional rod or string models (cf. Chap. 2). However, for dry spinning the radial resolution of mass fraction and temperature is essential due to the evaporation of solvent [74, 75]. Combining the relevant two-dimensional aspects with one-dimensional averaged balances, we propose a dimensionally reduced model that is of good approximation quality and very efficiently evaluable.

Considering a single fiber we introduce the fixed orthonormal basis  $\{\vec{a}_1, \vec{a}_2, \vec{a}_3\} \subset \mathbb{E}^3$  as depicted in Fig. 4.1. The body force satisfies  $\vec{g} = \rho g \vec{a}_3$  with gravitational acceleration  $g$  and the fiber midline is characterized by a constant unit tangent  $\vec{\tau}$ . Without loss of generality we assume  $\vec{\tau} = \vec{a}_3$ . In addition, we impose the following assumptions on setting and relevant effects.

**Assumption 4.4** (Setting and fiber geometry). *The setting is assumed to be uni-axial, radially symmetric for all fiber quantities and model parameters. In particular, the fiber domain  $\mathcal{Q}$  is given by the fiber length  $L$  and the smooth radius function  $R : [0, L] \rightarrow \mathbb{R}^+$  such that*

$$\mathcal{Q} = \{(x_1, x_2, s) \in \mathbb{R}^3 \mid (x_1, x_2) \in \mathcal{A}(s), s \in [0, L]\},$$

with cross-sections

$$\mathcal{A}(s) = \{(x_1, x_2) \in \mathbb{R}^2 \mid x_1 = r \cos \varphi, x_2 = r \sin \varphi, r \in [0, R(s)], \varphi \in [0, 2\pi)\}.$$

Then, the lateral free fiber surface  $\Gamma_{\text{fr}}$  can be parameterized in terms of the bijective function  $\xi : [0, 2\pi) \times [0, L] \rightarrow \Gamma_{\text{fr}}$  with  $\xi(\varphi, s) = (R(s) \cos \varphi, R(s) \sin \varphi, s)$  and its outer normal vector  $\mathbf{n}$  with respect to the fixed basis  $\{\vec{a}_1, \vec{a}_2, \vec{a}_3\}$  (for the coordinate terminology see Notation 2.1) is given by

$$\mathbf{n}(\varphi, s) = \frac{\partial_\varphi \xi \times \partial_s \xi}{\|\partial_\varphi \xi \times \partial_s \xi\|}(\varphi, s) = \frac{1}{\sqrt{1 + (\partial_s R(s))^2}}(\cos \varphi, \sin \varphi, -\partial_s R(s)). \quad (4.2)$$

Obviously,  $\Gamma_{\text{in}}$  can be identified with  $\mathcal{A}(0)$  and  $\Gamma_{\text{out}}$  with  $\mathcal{A}(L)$ . Moreover, it is often convenient to consider the two-dimensional domain  $\mathcal{Q}_{\text{cut}} = \{(r, s) \in \mathbb{R}^2 \mid r \in$

$(0, R(s)), s \in (0, L)\} \subset \mathcal{Q}$  with cylindrical coordinates and the associated orthonormal basis  $\{\vec{\mathbf{a}}_r, \vec{\mathbf{a}}_3\}$ .

For the subsequent dimensional reduction of the three-dimensional model (System 4.1) we propose a further assumption.

**Assumption 4.5** (Diffusive effects). *The diffusive effects in mass and heat transfer are assumed to be small. Because of the fiber slenderness the diffusive terms that contain radial derivatives are considered of relevance, whereas all others are neglected.*

### Dimensional reduction

We proceed from System 4.1. For the cross-sectional averaging we introduce the following notation for any differentiable and integrable scalar-, vector- or tensor-valued function  $f$  on  $\mathcal{Q}$  with  $\mathbf{n} = (n_1, n_2, n_3)$  being the unit outer normal vector of  $\Gamma_{\text{fr}}$ ,

$$\langle f \rangle_{\mathcal{A}(s)} = \int_{\mathcal{A}(s)} f(x_1, x_2, s) dx_1 dx_2, \quad \langle f \rangle_{\partial \mathcal{A}(s)} = \int_{\partial \mathcal{A}(s)} \frac{f}{\sqrt{n_1^2 + n_2^2}} dl.$$

In particular,  $A(s) = |\mathcal{A}(s)| = \langle 1 \rangle_{\mathcal{A}(s)}$  and  $|\partial \mathcal{A}(s)| = \langle 1 \rangle_{\partial \mathcal{A}(s)}$  denote the measures of cross-sectional area and boundary at any point  $s \in [0, L]$ . According to the divergence theorem the averaging rule

$$\langle \nabla \cdot f \rangle_{\mathcal{A}(s)} = \partial_s \langle f^T \cdot \vec{\mathbf{a}}_3 \rangle_{\mathcal{A}(s)} + \langle f^T \cdot \vec{\mathbf{n}} \rangle_{\partial \mathcal{A}(s)}$$

holds [77]. We apply it on the three-dimensional balances for polymer mass and momentum, incorporate the boundary conditions on  $\Gamma_{\text{fr}}$  and make use of Assumptions 4.4 and 4.5. In particular, due to the uni-axial, radially symmetric setting, the averaged momentum balance becomes a scalar-valued equation for the  $s$ -component and the boundary integral simplifies to  $\langle f \rangle_{\partial \mathcal{A}} = f|_{\partial \mathcal{A}} |\partial \mathcal{A}|$ ,

$$\partial_s \langle c \rho v_3 \rangle_{\mathcal{A}} = 0, \quad \partial_s \langle \rho v_3^2 \rangle_{\mathcal{A}} = \partial_s N + \langle \rho g \rangle_{\mathcal{A}} + f_{\text{air}} - (j_c v_3)|_{\partial \mathcal{A}} |\partial \mathcal{A}|,$$

with  $N = \langle (\vec{\Sigma} \cdot \vec{\mathbf{a}}_3) \cdot \vec{\mathbf{a}}_3 \rangle_{\mathcal{A}} = \langle -p + 2\mu \partial_s v_3 \rangle_{\mathcal{A}}$  and  $f_{\text{air}} = \langle \vec{\mathbf{f}} \cdot \vec{\mathbf{a}}_3 \rangle_{\partial \mathcal{A}}$ . Obviously, by the averaging the radial information of the velocity components  $v_3 = \vec{\mathbf{v}} \cdot \vec{\mathbf{a}}_3$ ,  $v_r = \vec{\mathbf{v}} \cdot \vec{\mathbf{a}}_r$  and the pressure  $p$  gets lost. Therefore, we impose the following assumption that – as well as Assumption 4.5 – might be justified by asymptotic analysis (see, e.g., [77] for profiles for  $v_3$  and  $p$ ).

**Assumption 4.6** (Velocity and pressure profiles). *The velocity components are considered to have the form  $v_3(r, s) = u(s)$  and  $v_r(r, s) = r/R(s) v_r|_{\partial \mathcal{A}(s)}(s)$ , while the pressure is  $p(r, s) = -\mu(c, T) \partial_s u(s)$ .*

All together the one-dimensional averaged polymer mass and momentum balances become

$$\begin{aligned}\partial_s(\langle c\rho(c, T)\rangle_{\mathcal{A}}u) &= 0, \\ \partial_s(\langle \rho(c, T)\rangle_{\mathcal{A}}u^2) &= \partial_s N + g\langle \rho(c, T)\rangle_{\mathcal{A}} + f_{air} - u j_c(c, T)|_{\partial\mathcal{A}}|\partial\mathcal{A}|, \\ N &= 3\langle \mu(c, T)\rangle_{\mathcal{A}}\partial_s u,\end{aligned}\quad (4.3)$$

where  $\rho$ ,  $\mu$  and  $j_c$  are functions of mass fraction  $c$  and temperature  $T$ . We conclude the required information about the profiles of  $c$  and  $T$  from two-dimensional advection-diffusion equations. For this purpose we rewrite the three-dimensional balances for diluent mass and energy of System 4.1 by employing the product rule, the total mass balance as well as the definition of the specific heat capacity  $q = \partial_T h$ . The resulting equations

$$\vec{v} \cdot \nabla c - \frac{c}{\rho} \nabla \cdot (\rho D \nabla c) = 0, \quad \rho q \vec{v} \cdot \nabla T + \rho D \nabla h_d^0 \cdot \nabla c - \nabla \cdot (C \nabla T) = 0,$$

are then formulated in cylindrical coordinates on  $\mathcal{Q}_{cut}$ , regarding Assumptions 4.4, 4.5 and 4.6. For the radial velocity component we particularly apply the expression

$$v_r(r, s) = r \frac{\partial_s R(s)}{R(s)} u(s),$$

which is concluded by means of the homogeneous kinematic boundary condition on the free lateral fiber surface,  $v_r|_{\partial\mathcal{A}} - u\partial_s R = 0$  (cf. (4.2)), and Assumption 4.6. In total,

$$\begin{aligned}u \left( \partial_s c + r \frac{\partial_s R}{R} \partial_r c \right) - \frac{c}{\rho(c, T)} \frac{1}{r} \partial_r (r \rho(c, T) D(c, T) \partial_r c) &= 0, \\ \rho(c, T) q(c, T) u \left( \partial_s T + r \frac{\partial_s R}{R} \partial_r T \right) + \rho(c, T) D(c, T) \partial_r h_d^0(T) \partial_r c \\ - \frac{1}{r} \partial_r (r C(c, T) \partial_r T) &= 0.\end{aligned}\quad (4.4)$$

### Modifications for efficient evaluation

Aiming for the simulation of industrial dry spinning with two-way coupled fiber-air interactions the computation of the fiber model itself must be performed very quickly. In spite of the dimensional reduction, the numerical solving of the nonlinear two-dimensional advection-diffusion equations (4.4) is still too time consuming for such setups. Hence, we propose a modified version of the one- and two-dimensional equations (4.3), (4.4) that makes an efficient evaluation possible.

We linearize the advection-diffusion equations (4.4) around the cross-sectionally averaged mass fraction  $\bar{c}$  and temperature  $\bar{T}$ , i.e.,

$$\bar{c} = \frac{1}{A} \langle c \rangle_{\mathcal{A}}, \quad \bar{T} = \frac{1}{A} \langle T \rangle_{\mathcal{A}}.$$

Apart from the leading terms of zeroth order, we take into account the terms of first order with respect to  $c$  in the equation for the mass fraction and, analogously, the terms of first order with respect to  $T$  in the equation for the temperature,

$$\begin{aligned} u \left( \partial_s c + r \frac{\partial_s R}{R} \partial_r c \right) - \bar{c} D(\bar{c}, \bar{T}) \frac{1}{r} \partial_r (r \partial_r c) &= 0, \\ \rho(\bar{c}, \bar{T}) q(\bar{c}, \bar{T}) u \left( \partial_s T + r \frac{\partial_s R}{R} \partial_r T \right) - C(\bar{c}, \bar{T}) \frac{1}{r} \partial_r (r \partial_r T) &= 0. \end{aligned} \quad (4.5)$$

The boundary conditions at the fiber surface  $r = R$  are respectively

$$\begin{aligned} \frac{\rho(\bar{c}, \bar{T}) D(\bar{c}, \bar{T})}{R} \partial_r c \Big|_{r=R} &= j_c(c, T) \Big|_{r=R}, \\ -\frac{C(\bar{c}, \bar{T})}{R} \partial_r T \Big|_{r=R} &= (j_T(T) + j_c(c, T)(\delta(T) - h_d^0(T))) \Big|_{r=R}. \end{aligned}$$

Through the linearized form of the radial equations (4.5) the evaluation and subsequent averaging of the density profiles in the averaged balance laws (4.3) becomes insignificant. Therefore, we apply the simplification that the cross-sectionally averaged mixture density and partial polymer density can be well approximated by

$$\langle \rho(c, T) \rangle_{\mathcal{A}} = \rho(\bar{c}, \bar{T}) A = \varrho_M(\bar{c}, \bar{T}), \quad \langle c \rho(c, T) \rangle_{\mathcal{A}} = \bar{c} \varrho_M(\bar{c}, \bar{T}).$$

As before,  $\varrho_M$  [kg/m] indicates the mass line density. Then, the averaged balance laws (4.3) become

$$\begin{aligned} \partial_s (\bar{c} \varrho_M(\bar{c}, \bar{T}) u) &= 0, \\ \partial_s (\varrho_M(\bar{c}, \bar{T}) u^2) &= \partial_s N + g \varrho_M(\bar{c}, \bar{T}) + f_{air} - 2\pi R u j_c(c, T) \Big|_{r=R}. \end{aligned}$$

Obviously, we do not face a free BVP any more, as the fiber radius  $R$  can be concluded from the constant polymer mass flux  $Q = \bar{c} \varrho_M(\bar{c}, \bar{T}) u = c_{in} \varrho_{M,in} u_{in}$ , with  $\varrho_{M,in} = \rho(c_{in}, T_{in}) \pi R_{in}^2$ , using the boundary conditions at the inlet, i.e.,

$$R(s) = \sqrt{\frac{Q}{\pi (\bar{c} \rho(\bar{c}, \bar{T}) u) \Big|_s}}.$$

For the later numerical treatment in Sec. 4.2 we need suitable initial guesses for the averaged quantities  $\bar{c}$  and  $\bar{T}$ . A good strategy is to solve the radial equations (4.5) averaged over the cross-sections, yielding

$$\begin{aligned}\partial_s \bar{c} &= 2\pi R \frac{\bar{c}^2}{Q} j_c(c, T) \Big|_{r=R}, \\ \partial_s \bar{T} &= -2\pi R \frac{\bar{c}}{Q q(\bar{c}, \bar{T})} \left( j_T(T) + j_c(c, T)(\delta(T) - h_d^0(T)) \right) \Big|_{r=R},\end{aligned}\tag{4.6}$$

with initial data  $\bar{c}(0) = c_{in}$  and  $\bar{T}(0) = T_{in}$ . Utilizing (4.6) we conclude our simplified fiber model for convective speed  $u$ , stress  $N$ , mass fraction  $c$  and temperature  $T$ .

**System 4.7** (Simplified one-two-dimensional BVP).

*One-dimensional equations,  $s \in (0, L)$ :*

$$\begin{aligned}\partial_s u &= \frac{1}{3\langle \mu(c, T) \rangle_{\mathcal{A}}} N, \\ \partial_s N &= \frac{Q}{\bar{c}} \frac{1}{3\langle \mu(c, T) \rangle_{\mathcal{A}}} N - \frac{Q}{\bar{c}} \frac{g}{u} - f_{air},\end{aligned}$$

*with boundary conditions at inlet  $s = 0$  and outlet  $s = L$ :*

$$u(0) = u_{in}, \quad u(L) = u_{out}.$$

*Two-dimensional equations,  $(r, s) \in (0, R) \times (0, L)$ :*

$$\begin{aligned}u \left( \partial_s c + r \frac{\partial_s R}{R} \partial_r c \right) - \bar{c} D(\bar{c}, \bar{T}) \frac{1}{r} \partial_r (r \partial_r c) &= 0, \\ \rho(\bar{c}, \bar{T}) q(\bar{c}, \bar{T}) u \left( \partial_s T + r \frac{\partial_s R}{R} \partial_r T \right) - C(\bar{c}, \bar{T}) \frac{1}{r} \partial_r (r \partial_r T) &= 0,\end{aligned}$$

*with boundary conditions at inlet  $s = 0$ , fiber surface  $r = R$  and symmetry boundary  $r = 0$ :*

$$\begin{aligned}c|_{s=0} &= c_{in}, & \partial_r c|_{r=0} &= 0, \\ \frac{\rho(\bar{c}, \bar{T}) D(\bar{c}, \bar{T})}{R} \partial_r c|_{r=R} &= j_c(c, T) \Big|_{r=R}, \\ T|_{s=0} &= T_{in}, & \partial_r T|_{r=0} &= 0, \\ -\frac{C(\bar{c}, \bar{T})}{R} \partial_r T|_{r=R} &= \left( j_T(T) + j_c(c, T)(\delta(T) - h_d^0(T)) \right) \Big|_{r=R}, \\ j_c(c, T) &= -\gamma(c, T)(c - c_{ref}(c, T)), & j_T(T) &= \alpha(T - T_*).\end{aligned}$$

Constitutive laws and geometric relation:

$$\begin{aligned} \rho^{-1}(c, T) &= c(\rho_p^0)^{-1}(T) + (1-c)(\rho_d^0)^{-1}(T), & q_d^0(T) &= \partial_T h_d^0(T), \\ q(c, T) &= cq_p^0(T) + (1-c)q_d^0(T), & R(s) &= \sqrt{\frac{Q}{\pi(\bar{c}\rho(\bar{c}, \bar{T})u)|_s}}. \end{aligned}$$

Abbreviations:

$$\bar{c} = \frac{1}{\pi R^2} \langle c \rangle_{\mathcal{A}}, \quad \bar{T} = \frac{1}{\pi R^2} \langle T \rangle_{\mathcal{A}}, \quad Q = c_{in} \varrho_{M,in} u_{in}.$$

Here, introducing the referential polymer mass fraction  $c_{ref} = 1 - \rho_{d,*} / \varrho_*$  the diluent mass flux  $j_c$  is formulated with respect to the polymer mass fraction. For simplicity we consider constant inflow profiles,  $c(r, 0) = c_{in} = const$  and  $T(r, 0) = T_{in} = const$ . The simple character of the modified two-dimensional equations (4.5) becomes obvious when we transform the equations onto the unit square  $(r, s) \in (0, 1)^2$  in the subsequent section.

**Remark 4.8** (Dynamic viscosity). *In System 4.7 we could approximate the averaged dynamic viscosity in the same way as the densities, i.e.,  $\langle \mu(c, T) \rangle_{\mathcal{A}} = \mu(\bar{c}, \bar{T})_{\mathcal{A}}$ . However, for reasons of accuracy we do not employ this simplification, as we will discuss in Sec. 4.4.1.*

### Dimensionless formulation and scaling

For the numerics it is convenient to deal with dimensionless model equations. Therefore, we nondimensionalize the System 4.7 using the scaling concept as well as the reference values from Sec. 2.1.5. In addition, we introduce a referential specific heat capacity  $q_0$  [J/(kg K)], a referential temperature  $T_0$  [K], typical heat and mass transfer coefficients  $\alpha_0$  [W/(m<sup>2</sup>K)],  $\gamma_0$  [kg/(m<sup>2</sup>s)] as well as a typical conductivity and diffusivity  $C_0$  [W/(m K)] and  $D_0$  [m<sup>2</sup>/s], respectively. A summary of all reference values is given in Tab. 4.1. Then, dimensionless one-dimensional quantities are given as before

$$\tilde{y}(\tilde{s}) = y(s_0 \tilde{s}) / y_0. \quad (4.7a)$$

Moreover, we introduce dimensionless two-dimensional quantities as

$$\tilde{y}(\tilde{r}, \tilde{s}) = \frac{y(d_0 \tilde{r}, s_0 \tilde{s})}{y_0} \quad (4.7b)$$

for any scalar- or vector-valued quantity  $y$  and corresponding reference value  $y_0$ . Besides the already defined Reynolds number  $Re$ , slenderness parameter  $\varepsilon$

Composite reference values		
Description	Formula	Unit
Length scale	$s_0 = r_0$	m
Fiber length	$L_0 = r_0$	m
Cross-sectional radius	$R_0 = d_0$	m
Mass density	$\rho_0 = \varrho_{M,0}/d_0^2$	kg/m <sup>3</sup>
Scalar velocity	$u_0 = v_0$	m/s
Stress	$N_0 = \varrho_{M,0}v_0^2$	N
Outer force	$f_0 = \varrho_{M,0}v_0^2/r_0$	N/m
Enthalpy	$h_0 = q_0T_0$	J/kg
Evaporation enthalpy	$\delta_0 = h_0$	J/kg
Polymer mass flux	$Q_0 = \varrho_{M,0}u_0$	kg/s
Air temperature	$T_{*,0} = T_0$	K

Dimensionless numbers	
Description	Formula
Slenderness	$\varepsilon = d_0/r_0$
Reynolds	$Re = \varrho_{M,0}v_0r_0/(d_0^2\mu_0)$
Froude	$Fr = v_0/\sqrt{gr_0}$
Drawing	$Dr = u_{out,0}/u_0$
Mass Peclet	$Pe_c = v_0d_0/D_0$
Temperature Peclet	$Pe_T = \varrho_{M,0}v_0q_0/(C_0d_0)$
Mass Stanton	$St_c = \gamma_0d_0^2/(v_0\varrho_{M,0})$
Temperature Stanton	$St_T = \alpha_0d_0^2/(v_0\varrho_{M,0}q_0)$

**Table 4.1.:** Overview over composite reference values used for nondimensionalization of the uni-axial fiber dry spinning model and the resulting dimensionless numbers. Here, the scales  $\varrho_{M,0}$ ,  $v_0$ ,  $r_0$ ,  $d_0$ ,  $\mu_0$ ,  $q_0$ ,  $T_0$ ,  $\alpha_0$ ,  $\gamma_0$ ,  $C_0$ ,  $D_0$ ,  $u_{out,0}$  are assumed to be given from the considered setup.

and Froude number  $Fr$ , we introduce the further dimensionless numbers as given in Tab. 4.1. These are the mass and temperature associated Peclet numbers  $Pe_c$ ,  $Pe_T$  as ratio of advective to diffusive transport rate of mass/heat, the mass and temperature associated Stanton numbers  $St_c$ ,  $St_T$  indicating the ratio of mass/heat transferred into a fluid to the ability to accumulate mass/heat, as well as the drawing number  $Dr$  as ratio of take up to referential velocity.

After nondimensionalization the equations are considered on the nondimensional space domain  $(0, \tilde{L})$  (one-dimensional equations) and  $(0, \tilde{R}(\tilde{s})) \times (0, \tilde{L})$  (two-dimensional equations), respectively. To further simplify the numerical treatment of the equations, we transform one-dimensional equations onto the space domain

$(0, 1)$  and two-dimensional equations onto the space domain  $(0, 1)^2$  via

$$\check{y}(\check{s}) = \check{y}(\check{L}\check{s}), \quad \check{y}(\check{r}, \check{s}) = \check{y}(\check{R}(\check{L}\check{s})\check{r}, \check{L}\check{s}), \quad (4.8)$$

respectively. Since the fiber radius  $R$  is an a priori unknown of the problem, this domain transformation omits domain changes during the numerical solution of the problem, which would require computationally expensive re-meshing of the computational domain. The transformation inserts the unknown  $\check{R}$  into our model equations, but this can efficiently be handled with our numerical solution algorithm, see Sec. 4.2. When we deal with curved fibers in the subsequent Sec. 4.1.3, this transformation is also beneficial in  $s$ -direction: Since for curved fibers the fiber length  $L$  is a priori unknown, transformation (4.8) of the model equations fixes the computational domain also in  $s$ -direction. The insertion of the unknown parameter  $\check{L}$  into the model equations can also be handled by our numerical solution scheme. For straight fibers the fiber length  $L$  is a priori known and choosing  $s_0 = r_0 = L$  would lead to a fiber length equal to one in nondimensional form (i.e.,  $\check{L} = 1$ ).

To keep the notation simple we suppress the labels  $\check{\cdot}$  and  $\check{\cdot}$  in the following and write  $\langle f \rangle_{R^2(s)} = 2\pi R^2(s) \int_0^1 f(r, s) r dr$  for the integrated dimensionless quantity  $f$  under the assumption of radial symmetry (Assumption 4.4). The meaning of each quantity (dimensional or nondimensional) will be clear from the context. The final dimensionless one-two-dimensional fiber model is described by System 4.9.

**System 4.9** (One-two-dimensional BVP for dry spinning of an uni-axial fiber).  
Averaged balance laws,  $s \in (0, 1)$ :

$$\begin{aligned} L^{-1} \partial_s u &= \text{Re} \frac{1}{3 \langle \mu(c, T) \rangle_{R^2}} N, \\ L^{-1} \partial_s N &= \text{Re} \frac{Q}{\bar{c}} \frac{1}{3 \langle \mu(c, T) \rangle_{R^2}} N - \frac{1}{\text{Fr}^2} \frac{Q}{\bar{c}} \frac{1}{u} - f_{air}, \end{aligned} \quad (4.9a)$$

with boundary conditions at inlet  $s = 0$  and outlet  $s = 1$ :

$$u(0) = u_{in}, \quad u(1) = \text{Dr} u_{out}.$$

Radial equations,  $(r, s) \in (0, 1)^2$ :

$$\begin{aligned} L^{-1} u \partial_s c - \frac{1}{\varepsilon \text{Pe}_c} \frac{\bar{c} D(\bar{c}, \bar{T})}{R^2 r} \partial_r (r \partial_r c) &= 0, \\ L^{-1} \rho(\bar{c}, \bar{T}) q(\bar{c}, \bar{T}) u \partial_s T - \frac{1}{\varepsilon \text{Pe}_T} \frac{C(\bar{c}, \bar{T})}{R^2 r} \partial_r (r \partial_r T) &= 0, \end{aligned} \quad (4.9b)$$

with boundary conditions at inlet  $s = 0$ , fiber surface  $r = 1$  and symmetry boundary  $r = 0$ :

$$\begin{aligned} c|_{s=0} &= c_{in}, & \partial_r c|_{r=0} &= 0, \\ \frac{1}{\text{Pe}_c} \frac{\rho(\bar{c}, \bar{T}) D(\bar{c}, \bar{T})}{R} \partial_r c|_{r=1} &= \text{St}_c j_c(c, T)|_{r=1}, \\ T|_{s=0} &= T_{in} & \partial_r T|_{r=1} &= 0, \\ -\frac{1}{\text{Pe}_T} \frac{C(\bar{c}, \bar{T})}{R} \partial_r T|_{r=1} &= (\text{St}_T j_T(T) + \text{St}_c j_c(c, T)(\delta(T) - h_d^0(T)))|_{r=1}, \\ j_c(c, T) &= -\gamma(c, T)(c - c_{ref}(c, T)), & j_T(T) &= \alpha(T - T_*). \end{aligned}$$

Constitutive laws and geometric relation:

$$\begin{aligned} \rho^{-1}(c, T) &= c(\rho_p^0)^{-1}(T) + (1-c)(\rho_d^0)^{-1}(T), & q_d^0(T) &= \partial_T h_d^0(T), \\ q(c, T) &= c q_p^0(T) + (1-c) q_d^0(T), & R(s) &= \sqrt{\frac{Q}{\pi(\bar{c}\rho(\bar{c}, \bar{T})u)|_s}}. \end{aligned}$$

Abbreviations:

$$\begin{aligned} \bar{c} &= \frac{1}{\pi R^2} \langle c \rangle_{R^2}, & \bar{T} &= \frac{1}{\pi R^2} \langle T \rangle_{R^2}, & \langle y \rangle_{R^2(s)} &= 2\pi R^2(s) \int_0^1 y(r, s) r dr, \\ Q &= c_{in} \varrho_{M,in} u_{in}. \end{aligned}$$

Note that due to the transformation of the radial equations onto the unit square the terms containing the radial velocity cancel out. The averaged radial equations (4.6) read in nondimensional form

$$\begin{aligned} L^{-1} \partial_s \bar{c} &= \frac{\text{St}_c}{\varepsilon} 2\pi R \frac{\bar{c}^2}{Q} j_c(c, T)|_{r=1}, \\ L^{-1} \partial_s \bar{T} &= -\frac{1}{\varepsilon} 2\pi R \frac{\bar{c}}{Q} \frac{1}{q(\bar{c}, \bar{T})} (\text{St}_T j_T(T) + \text{St}_c j_c(c, T)(\delta(T) - h_d^0(T)))|_{r=1}. \end{aligned} \tag{4.9c}$$

Except from the averaging of the dynamic viscosity the one-dimensional equations (4.9a) equal a viscous string model for an uni-axial fiber under (Euler-)stationary description, cf. System 2.10, which has additionally been supplemented with two-dimensional advection-diffusion equations describing radial effects in polymer mass fraction  $c$  and temperature  $T$  due to solvent evaporation. Here, the volume balance equation is replaced by the assumption of an ideal mixing behavior of the two phases (diluent and polymer), which yields an explicit expression for the mixture density depending on  $c$  and  $T$ . Aiming at a fiber model describing

curved fibers, this string model can easily be extended by including corresponding kinematic equations and extending the linear momentum equation to three dimensions. Due to the drawbacks of viscous string models (lack of solvability due to singularities, cf. Sec. 2.2.1) we do not employ such models for curved fibers, but extend the uni-axial string model to a Cosserat rod model in the subsequent section. This means we additionally provide an angular momentum equation with suitable material law and corresponding kinematic equations for the director triad.

**Remark 4.10** (Closure models). *The closing of System 4.9 requires appropriate models for the heat transfer coefficient  $\alpha$ , mass transfer coefficient  $\gamma$ , referential mass fraction  $c_{ref}$ , diffusion coefficient  $D$ , thermal conductivity  $C$ , evaporation enthalpy  $\delta$ , specific heat capacities  $q_p^0$ ,  $q_d^0$ , dynamic viscosity  $\mu$  as well as material densities  $\rho_p^0$ ,  $\rho_d^0$ .*

*For the performance and quality analysis of our dimensionally reduced uni-axial fiber model (System 4.9) in Sec. 4.3 we set all these quantities to be constant, whereas for the setup of an industrial dry spinning apparatus in Sec. 4.4 we give detailed models taking the fiber materials and rheological effects into account. For the air drag  $f_{air} = f_{air} \cdot \tau$  in tangential fiber direction the air drag model (2.9) in Eulerian description is employed*

$$f_{air} = f_{air} \cdot \tau = \frac{A_\star}{\text{Re}_\star^2} \frac{\rho_\star v_\star^2}{2R} F\left(\tau, \text{Re}_\star \frac{2R}{v_\star} (v_\star - v)\right) \cdot \tau.$$

*Note that for an uni-axial fiber  $v = u\tau$  holds and we assume  $\tau = \mathbf{e}_3$  without loss of generality. The dimensionless function  $F$  and dimensionless numbers  $A_\star$ ,  $\text{Re}_\star$  are given in Sec. 2.3.*

### 4.1.3. Curved fiber model

We consider an industrial dry spinning device where the air streams horizontally through the spinning duct instead of vertically, cf. Fig. 4.2. Since in such devices the airflow is mainly perpendicular to the fiber flow direction, the assumption of straight fibers is no longer tenable due to expected lateral deflections. Therefore, we extend our model framework to the description of curved fibers in such processes. In general, the derivation of a curved string model describing dry spinning of a single curved fiber can be done with the same concepts as presented for the uni-axial string model (cf. Sec. 4.1.1 and Sec. 4.1.2). However, the asymptotic considerations become more technical and lengthy. Beyond that, due to the lack of solutions for curved string models due to possibly arising singularities (cf. Chap. 2), string models in general are no suitable choice for such setups.

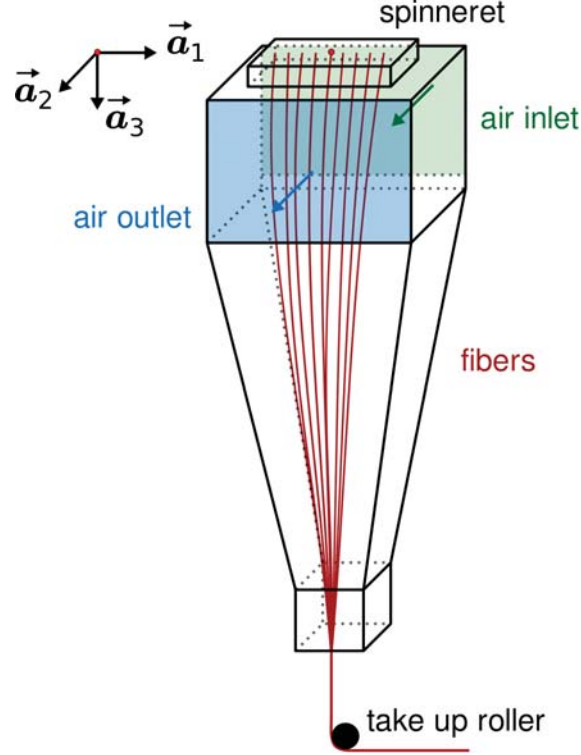


**Figure 4.2.:** Sketch of a dry spinning device with horizontal air inflow in  $\vec{a}_2$ -direction.

Therefore, we omit such a detailed derivation and formulate straightforwardly a Cosserat rod model describing dry spinning of a single curved fiber.

We reformulate the invariant description of the dynamic equations (cf. System 2.2), in particular we consider the mass, volume, linear and angular momentum balances on the Lagrangian space-time domain  $\mathcal{D} = \{(\zeta, t) \in \mathbb{R}^2 \mid \zeta \in \mathcal{Q}(t), t \in (0, t_{end}]\}$  with time-dependent space domain  $\mathcal{Q}(t) = (\zeta_L(t), \zeta_R(t))$

$$\begin{aligned} \partial_t \varrho_M &= -e2\pi R j_c, \\ \partial_t \varrho_V &= -e2\pi R j_V, \\ \partial_t (\varrho_M \vec{v}) &= \partial_\zeta \vec{n} + \vec{f} - e2\pi R j_c \vec{v}, \\ \partial_t (\bar{\mathbf{J}} \cdot \bar{\boldsymbol{\omega}}) &= \partial_\zeta \bar{\mathbf{m}} + \bar{\boldsymbol{\tau}} \times \bar{\mathbf{n}} - e2\pi R \left( \frac{j_c}{\varrho_M} \bar{\mathbf{J}} \cdot \bar{\boldsymbol{\omega}} + \frac{j_V}{\varrho_V} \bar{\mathbf{J}} \cdot \bar{\boldsymbol{\omega}} \right), \end{aligned}$$

and radius function  $R = \sqrt{\varrho_V / (\pi e)}$ . Here,  $j_c$  [kg/(m<sup>2</sup>s)],  $j_V$  [m/s],  $j_T$  [J/(m<sup>2</sup>s)] indicate the diluent mass, volume and heat flux at the lateral fiber surface due to evaporation. We formulate the invariant balance laws with respect to the director triad  $\{\vec{d}_1, \vec{d}_2, \vec{d}_3\}$  (cf. System 2.3) and utilize the incompressible geometry model for the inertia matrix  $\mathbf{J}$ , i.e.,  $\mathbf{J} = \varrho_M \varrho_V / e \mathbf{P}_2$  with  $\mathbf{P}_x = 1/(4\pi) \text{diag}(1, 1, x)$ ,  $x \in \mathbb{R}$ ,

Composite reference values		
Description	Formula	Unit
Length scale	$s_0 = L$	m
Length	$L_0 = r_0$	m
Cross-sectional radius	$R_0 = d_0$	m
Mass density	$\rho_0 = \varrho_{M,0}/d_0^2$	kg/m <sup>3</sup>
Scalar speed	$u_0 = v_0$	m/s
Curvature	$\kappa_0 = 1/r_0$	1/m
Stress	$n_0 = \varrho_{M,0}v_0^2$	N
Torque	$m_0 = \varrho_{M,0}r_0v_0^2$	N m
Outer force	$f_0 = \varrho_{M,0}v_0^2/r_0$	N/m
Enthalpy	$h_0 = q_0T_0$	J/kg
Evaporation enthalpy	$\delta_0 = h_0$	J/kg
Polymer mass flux	$Q_0 = \varrho_{M,0}u_0$	kg/s
Air temperature	$T_{*,0} = T_0$	K

Dimensionless numbers	
Description	Formula
Slenderness	$\varepsilon = d_0/r_0$
Reynolds	$Re = \varrho_{M,0}v_0r_0/(d_0^2\mu_0)$
Froude	$Fr = v_0/\sqrt{gr_0}$
Drawing	$Dr = u_{out,0}/u_0$
Mass Peclet	$Pe_c = v_0d_0/D_0$
Temperature Peclet	$Pe_T = \varrho_{M,0}v_0q_0/(C_0d_0)$
Mass Stanton	$St_c = \gamma_0d_0^2/(v_0\varrho_{M,0})$
Temperature Stanton	$St_T = \alpha_0d_0^2/(v_0\varrho_{M,0}q_0)$

**Table 4.2.:** Composite reference values used for nondimensionalization of the curved fiber dry spinning model and resulting dimensionless numbers. The following scales are assumed to be given from the specific considered setup  $\varrho_{M,0}, r_0, d_0, v_0, \mu_0, q_0, T_0, \alpha_0, \gamma_0, C_0, D_0, u_{out,0}$ .

(cf. Sec. 2.1.3). In total we get

$$\begin{aligned}
 \partial_t \varrho_M &= -e2\pi R j_c, \\
 \partial_t \varrho_V &= -e2\pi R j_V, \\
 \partial_t (\varrho_M \mathbf{v}) &= \varrho_M \mathbf{v} \times \boldsymbol{\omega} + \partial_\zeta \mathbf{n} + \boldsymbol{\kappa} \times \mathbf{n} + \mathbf{f} - e2\pi R j_c \mathbf{v}, \\
 \partial_t \left( \frac{\varrho_M \varrho_V}{e} \mathbf{P}_2 \cdot \boldsymbol{\omega} \right) &= \left( \frac{\varrho_M \varrho_V}{e} \mathbf{P}_2 \cdot \boldsymbol{\omega} \right) \times \boldsymbol{\omega} + \partial_\zeta \mathbf{m} + \boldsymbol{\kappa} \times \mathbf{m} + \boldsymbol{\tau} \times \mathbf{n} \\
 &\quad - e2\pi R \left( j_c \frac{\varrho_V}{e} \mathbf{P}_2 \cdot \boldsymbol{\omega} + j_V \frac{\varrho_M}{e} \mathbf{P}_2 \cdot \boldsymbol{\omega} \right).
 \end{aligned}$$

Applying the product rule on the left hand sides of the equations and utilizing the mass and volume balance equations yields

$$\begin{aligned}
 \partial_t \varrho_M &= -e2\pi R j_c, \\
 \partial_t \varrho_V &= -e2\pi R j_V, \\
 \varrho_M \partial_t \mathbf{v} &= \varrho_M \mathbf{v} \times \boldsymbol{\omega} + \partial_\zeta \mathbf{n} + \boldsymbol{\kappa} \times \mathbf{n} + \mathbf{f}, \\
 \varrho_M \varrho_V \mathbf{P}_2 \cdot \partial_t \left( \frac{1}{e} \boldsymbol{\omega} \right) &= \left( \frac{\varrho_M \varrho_V}{e} \mathbf{P}_2 \cdot \boldsymbol{\omega} \right) \times \boldsymbol{\omega} + \partial_\zeta \mathbf{m} + \boldsymbol{\kappa} \times \mathbf{m} + \boldsymbol{\tau} \times \mathbf{n}.
 \end{aligned} \tag{4.10}$$

As before, we introduce the mass density  $\rho$  through the relation  $\rho = \varrho_M / \varrho_V$  and assume an ideal mixture, i.e.,  $\rho^{-1}(c, T) = c(\rho_p^0)^{-1}(T) + (1 - c)(\rho_d^0)^{-1}(T)$ . As consequence of this explicit expression for  $\rho$  we avoid to set up a detailed model for the volume flux  $j_V$  and, furthermore, are able to omit the consideration of the volume balance in total. Now, we equip the balances (4.10) with the corresponding kinematic rod equations as well as the viscous material laws for  $\mathbf{n}_3$  and  $\mathbf{m}$  (cf. Sec. 2.1.4) and pass over to an Euler stationary consideration in nondimensional form (cf. System 2.8 and Rem. 2.9). The dimensionless quantities  $\tilde{y}$  are introduced as before (see (4.7a) for one- and (4.7b) for two-dimensional equations) and we refer to Tab. 4.2 for the corresponding reference values. The scaling of the model equations is done according to (4.8). Note that for a curved fiber its length  $L$  is a priori unknown and, therefore, becomes an additional unknown of the system. Again we suppress the labels  $\tilde{\cdot}$  and  $\check{\cdot}$  for nondimensional and scaled quantities in the following. This also means we use the symbol  $L$  for the dimensionless unknown fiber length. We expect only moderate fiber bending in industrial applications. So to include radial effects due to diluent evaporation, we employ the same two-dimensional advection-diffusion equations (4.9b) for polymer mass fraction  $c$  and temperature  $T$  as utilized for uni-axial fibers. Moreover, as in the uni-axial case we employ the constant polymer mass flux  $Q = \bar{c} \varrho_M(\bar{c}, \bar{T}) u = c_{in} \varrho_{M,in} u_{in}$  and we consider gravitational and air drag forces as external loads, i.e.,  $\mathbf{f} = \mathbf{R}(\mathbf{q}) \cdot \mathbf{f} = \mathbf{R}(\mathbf{q}) \cdot (\mathbf{f}_g + \mathbf{f}_{air})$  with  $\mathbf{f}_g$  and  $\mathbf{f}_{air}$  according to Sec. 2.3 (for  $\mathbf{f}_{air}$  see also Rem. 4.10). All together the final one-two-dimensional dry spinning Cosserat rod model is given by System 4.11.

**System 4.11** (One-two-dimensional BVP for dry spinning of a curved fiber).  
 One-dimensional equations,  $s \in (0, 1)$ :

$$\begin{aligned}
 L^{-1} \partial_s \mathbf{r} &= \mathbf{R}(\mathbf{q})^T \cdot \mathbf{e}_3, \\
 L^{-1} \partial_s \mathbf{q} &= \mathbf{S}(\boldsymbol{\kappa}) \cdot \mathbf{q}, \\
 L^{-1} \partial_s \mathbf{n} &= \varrho_M u^2 \boldsymbol{\kappa} \times \mathbf{e}_3 + \mathbf{n} \times \boldsymbol{\kappa} + L^{-1} \varrho_M u (\partial_s u) \mathbf{e}_3 - \frac{1}{Fr^2} \varrho_M \mathbf{R}(\mathbf{q}) \cdot \mathbf{e}_3 \\
 &\quad - \mathbf{R}(\mathbf{q}) \cdot \mathbf{f}_{air}, \\
 L^{-1} \partial_s \mathbf{m} &= \varepsilon^2 \frac{\varrho_M^2}{\rho} u^2 \boldsymbol{\kappa} \times \mathbf{P}_2 \cdot \boldsymbol{\kappa} + L^{-1} \varepsilon^2 \frac{\varrho_M^2}{\rho} \mathbf{P}_2 \cdot (u \partial_s (u \boldsymbol{\kappa}) - \boldsymbol{\kappa} u \partial_s u) \\
 &\quad + \mathbf{n} \times \mathbf{e}_3 + \mathbf{m} \times \boldsymbol{\kappa}, \\
 L^{-1} \partial_s u &= \text{Re} \frac{1}{3 \langle \mu(c, T) \rangle_{R^2}} n_3, \\
 L^{-1} \partial_s (u \boldsymbol{\kappa}) &= \frac{\text{Re}}{\varepsilon^2} \frac{\rho}{3 \varrho_M \langle \mu(c, T) \rangle_{R^2}} \mathbf{P}_{2/3}^{-1} \cdot \mathbf{m},
 \end{aligned} \tag{4.11a}$$

with boundary conditions at inlet  $s = 0$  and fiber end  $s = 1$ :

$$\begin{aligned}
 \mathbf{r}(0) &= \mathbf{r}_{in}, & \mathbf{r}(1) &= \mathbf{r}_{out}, & u(0) &= u_{in}, & u(1) &= \text{Dr} u_{out}, \\
 \mathbf{q}(0) &= \mathbf{q}_{in}, & \boldsymbol{\kappa}(0) &= \boldsymbol{\kappa}_{in}, & \boldsymbol{\kappa}(1) &= \boldsymbol{\kappa}_{out}.
 \end{aligned}$$

Radial equations,  $(r, s) \in (0, 1)^2$ :

$$\begin{aligned}
 L^{-1} u \partial_s c - \frac{1}{\varepsilon \text{Pe}_c} \frac{\bar{c} D(\bar{c}, \bar{T})}{R^2 r} \partial_r (r \partial_r c) &= 0, \\
 L^{-1} \rho(\bar{c}, \bar{T}) q(\bar{c}, \bar{T}) u \partial_s T - \frac{1}{\varepsilon \text{Pe}_T} \frac{C(\bar{c}, \bar{T})}{R^2 r} \partial_r (r \partial_r T) &= 0,
 \end{aligned} \tag{4.11b}$$

with boundary conditions at inlet  $s = 0$ , fiber surface  $r = 1$  and symmetry boundary  $r = 0$ :

$$\begin{aligned}
 c|_{s=0} &= c_{in}, & \partial_r c|_{r=0} &= 0, \\
 \frac{1}{\text{Pe}_c} \frac{\rho(\bar{c}, \bar{T}) D(\bar{c}, \bar{T})}{R} \partial_r c|_{r=1} &= \text{St}_c j_c(c, T)|_{r=1}, \\
 T|_{s=0} &= T_{in}, & \partial_r T|_{r=1} &= 0, \\
 -\frac{1}{\text{Pe}_T} \frac{C(\bar{c}, \bar{T})}{R} \partial_r T|_{r=1} &= (\text{St}_T j_T(T) + \text{St}_c j_c(c, T) (\delta(T) - h_d^0(T)))|_{r=1}, \\
 j_c(c, T) &= -\gamma(c, T)(c - c_{ref}(c, T)), & j_T(T) &= \alpha(T - T_\star).
 \end{aligned}$$

*Constitutive laws and geometric relation:*

$$\rho^{-1}(c, T) = c(\rho_p^0)^{-1}(T) + (1-c)(\rho_d^0)^{-1}(T), \quad q_d^0(T) = \partial_T h_d^0(T),$$

$$q(c, T) = cq_p^0(T) + (1-c)q_d^0(T), \quad R(s) = \sqrt{\frac{Q}{\pi(\bar{c}\rho(\bar{c}, \bar{T})u)|_s}}.$$

*Abbreviations:*

$$\bar{c} = \frac{1}{\pi R^2} \langle c \rangle_{R^2}, \quad \bar{T} = \frac{1}{\pi R^2} \langle T \rangle_{R^2}, \quad \langle y \rangle_{R^2(s)} = 2\pi R^2(s) \int_0^1 y(r, s) r dr,$$

$$Q = c_{in} \varrho_{M, in} u_{in}, \quad \mathbf{P}_x = \frac{1}{4\pi} \text{diag}(1, 1, x).$$

For an appropriate closing of the System 4.11 we refer to Remark 4.10. Note that for the determination of the a priori unknown fiber length  $L$  we impose an additional boundary condition: to the 17 equations of (4.11a) with the 18 unknowns  $(\mathbf{r}, \mathbf{q}, u, \boldsymbol{\kappa}, \mathbf{n}, \mathbf{m}, L)$ , we set 18 boundary conditions at  $s = 0$  and  $s = 1$ . The one-dimensional system (4.11a) is the only difference between the curved fiber model (System 4.11) and its uni-axial counterpart (System 4.9). Whereas for curved fibers it contains 18 unknowns, the corresponding one-dimensional uni-axial model is formulated with respect to only two unknowns  $(u, N)$ . The two-dimensional equations (4.9b), (4.11b) are identical.

**Remark 4.12** (Standard form). *For the intended numerical treatment of the one-dimensional model (4.11a) with the continuation-collocation method (cf. Sec. 3.1) the equations have to be written in the form  $d/ds \mathbf{y} = \mathbf{f}(\mathbf{y})$ . In addition to multiplying all equations with  $L$  as it has to be done for (4.9a), we apply the product rule on the  $\partial_s(u\boldsymbol{\kappa})$  term of the second material law and subsequently replace the  $\partial_s u$  term as given by the first material law. Moreover, the mass line density  $\varrho_M$  is replaced by the constant polymer mass flux in all equations, i.e.,  $\varrho_M = Q/(\bar{c}u)$ .*

#### 4.1.4. Heat and mass transfer models

The additional models (heat and mass exchange models) that we use to close our dimensionally reduced dry spinning fiber models (System 4.9 for uni-axial and System 4.11 for curved fibers) are briefly summarized in this subsection (cf. Remark 4.10). Moreover, these models play a crucial role in the intended two-way coupling of fiber and airflow simulations, see Sec. 3.4. To distinguish the fiber quantities from the airflow quantities all airflow-associated fields are labeled with the index  $*$  as before. In particular,  $\mathbf{v}_*$  denotes the velocity,  $T_*$  the temperature,

Composite reference values			Dimensionless numbers	
Description	Formula	Unit	Description	Formula
Mass trans. coeff.	$\beta_0 = \gamma_0/\rho_{*,0}$	m/s	Air-fiber Rey.	$Re_* = d_0 v_0/\nu_{*,0}$
Air velocity	$v_{*,0} = v_0$	m/s	Nusselt	$Nu_* = \alpha_0 d_0/\lambda_{*,0}$
Air temperature	$T_{*,0} = T_0$	K	Prandtl	$Pr_* = q_{*,0}\rho_{*,0}\nu_{*,0}/\lambda_{*,0}$
			Sherwood	$Sh_* = \gamma_0 d_0/(\rho_{*,0}D_{d,*,0})$
			Schmidt	$Sc_* = \nu_{*,0}/D_{d,*,0}$

**Table 4.3.:** Composite reference values used for nondimensionalization of heat and mass transfer models and the resulting dimensionless numbers. Here, the scales  $v_0, d_0, \alpha_0, \gamma_0, \rho_{*,0}, p_{*,0}, q_{*,0}, \nu_{*,0}, \lambda_{*,0}, D_{d,*,0}$  are assumed to be given from the considered setup.

$\rho_*$  the density,  $p_*$  the pressure,  $q_*$  the specific heat capacity,  $\nu_*$  the kinematic viscosity and  $\lambda_*$  the thermal conductivity of the air. Moreover,  $c_{d,*}$  is the diluent mass fraction in air. All these quantities are space-dependent fields assumed to be dimensionless and known – for example provided by an external computation. The corresponding reference values used for nondimensionalization are the fixed scales  $\rho_{*,0}$  [kg/m<sup>3</sup>],  $p_{*,0}$  [Pa],  $q_{*,0}$  [J/(kg K)],  $\nu_{*,0}$  [m<sup>2</sup>/s],  $\lambda_{*,0}$  [W/(m K)], as well as  $v_{*,0}$  [m/s] and  $T_{*,0}$  [K] as given in Tab. 4.3.

### Heat transfer

The model for the dimensionless heat transfer coefficient  $\alpha$  is given by the following relation to the Nusselt number  $Nu_*$  and the associated dimensionless function  $\mathcal{N} : \mathbb{R}^3 \rightarrow \mathbb{R}$

$$\alpha = \frac{1}{Nu_*} \frac{\lambda_*}{2R} \mathcal{N} \left( Re_* \frac{2R}{\nu_*} (\mathbf{v}_* - \mathbf{v}) \cdot \mathbf{t}, Re_* \frac{2R}{\nu_*} \|\mathbf{v}_* - \mathbf{v}\|, Pr_* \frac{q_* \rho_* \nu_*}{\lambda_*} \right). \quad (4.12)$$

Here,  $\mathbf{t} = \boldsymbol{\tau}/e$  is the normalized tangent vector of the fiber. Due to the Euler description (arc length parameterization)  $\mathbf{t} = \boldsymbol{\tau}$  holds. As before  $Re_*$  is the mixed (air-fiber) Reynolds number. The further occurring dimensionless numbers are the Nusselt number  $Nu_*$  indicating the ratio of convective to conductive heat transfer and the Prandtl number  $Pr_*$  describing the ratio of momentum diffusion rate to thermal diffusion rate as defined in Tab. 4.3. The model used for the Nusselt number associated function  $\mathcal{N}$  is heuristic

$$\mathcal{N}(w_t, w, p) = \left( 1 - \frac{1}{2} h_{\mathcal{N}}(w_t, w) \right) \begin{cases} n_{\mathcal{N},1}(w, p), & wp \geq \delta, \\ n_{\mathcal{N},2}(w, p), & wp < \delta, \end{cases}$$

depending on the tangential and absolute relative velocity ( $w_t = \|\mathbf{w}_t\| = \mathbf{w} \cdot \mathbf{t}$ ,  $w = \|\mathbf{w}\|$ ) and the Prandtl number, with  $\delta = 7.3 \cdot 10^{-5}$ . The model goes back to

[95] where originally a stationary perpendicular laminar flow situation ( $w_t = 0$ ) around a cylinder for  $wp \geq \delta$  was studied and has been extended to ensure a smooth transition to the limit value  $\mathcal{N} \rightarrow \mathcal{N}_0 = 0.1$  for vanishing  $wp \rightarrow 0$ ,

$$\begin{aligned} n_{\mathcal{N},1}(w,p) &= a_{\mathcal{N}}(wp)^{0.1} + f_{\mathcal{N}}(p) \frac{(wp)^{0.7}}{1 + b_{\mathcal{N}}(wp)^{0.2}}, \\ n_{\mathcal{N},2}(w,p) &= m_{\mathcal{N},1}(p)(wp)^3 + m_{\mathcal{N},2}(p)(wp)^2 + \mathcal{N}_0, \end{aligned}$$

with the coefficients

$$\begin{aligned} m_{\mathcal{N},1}(p) &= c_{\mathcal{N}} + d_{\mathcal{N}}f_{\mathcal{N}}(p), & m_{\mathcal{N},2}(p) &= e_{\mathcal{N}} + g_{\mathcal{N}}f_{\mathcal{N}}(p), \\ f_{\mathcal{N}}(p) &= \frac{k_{\mathcal{N}}}{(1 + (l_{\mathcal{N}}p^{1/6})^{2.5})^{0.4}} \end{aligned}$$

and the constant parameters

$$\begin{aligned} a_{\mathcal{N}} &= 0.462, & b_{\mathcal{N}} &= 2.79, & c_{\mathcal{N}} &= -3.5636 \cdot 10^{11}, \\ d_{\mathcal{N}} &= -3.1380 \cdot 10^9, & e_{\mathcal{N}} &= 4.0694 \cdot 10^7, & g_{\mathcal{N}} &= 4.0694 \cdot 10^7, \\ k_{\mathcal{N}} &= 2.5, & l_{\mathcal{N}} &= 1.25. \end{aligned}$$

The incorporation of the function  $h_{\mathcal{N}}$  accounts for varying incident flow directions. It is mainly the squared cosine of the angle of attack, which is regularized to ensure smoothness for tangential incident flow situations with regularization parameter  $\epsilon = 10^{-7}$ ,

$$h_{\mathcal{N}}(w_t, w) = \begin{cases} (w_t w^{-1})^2, & w \geq \epsilon, \\ (1 - (w\epsilon^{-1})^2)^2 + (3 - 2(w\epsilon^{-1})^2)(w_t w\epsilon^{-2})^2, & w < \epsilon. \end{cases}$$

### Mass transfer and referential mass fraction

The mass fraction associated transfer coefficient  $\gamma$  and the referential polymer mass fraction  $c_{ref}$

$$\gamma = \beta \varrho_*, \quad c_{ref} = 1 - \frac{\rho_{d,*}}{\varrho_*}$$

are expressed in terms of the mass transfer coefficient  $\beta$ , the mass fraction-scaled diluent density in the air at the fiber surface  $\varrho_*$ , and the diluent density in the air away from the fiber  $\rho_{d,*}$  (cf. Sec. 4.1.1). Making use of the analogy of mass transfer and heat transfer the model for the dimensionless coefficient  $\beta$  is of similar form as that for  $\alpha$  [95]. The Nusselt number  $\text{Nu}_*$  is changed to the Sherwood number  $\text{Sh}_*$  (ratio of convective to diffusive mass transfer) and the Prandtl number  $\text{Pr}_*$

is replaced by the Schmidt number  $Sc_*$  (ratio of the viscous diffusion rate to the mass diffusion rate), see Tab. 4.3,

$$\beta = \frac{1}{Sh_*} \frac{D_{d,*}}{2R} \mathcal{N} \left( Re_* \frac{2R}{v_*} (\mathbf{v}_* - \mathbf{v}) \cdot \mathbf{t}, Re_* \frac{2R}{v_*} \|\mathbf{v}_* - \mathbf{v}\|, Sc_* \frac{v_*}{D_{d,*}} \right)$$

with the diffusion coefficient of diluent in air  $D_{d,*}$  and corresponding reference value  $D_{d,*,0}$  [m<sup>2</sup>/s]. The dimensionless coefficient is modeled as [36]

$$D_{d,*}(T_*, p_*) = \frac{1}{D_{d,*,0}} \mathcal{D}_{d,*}(T_* T_{*,0}, p_* p_{*,0}),$$

$$\mathcal{D}_{d,*}(T_*, p_*) = E \frac{1}{(V_d^{1/3} + V_*^{1/3})^2} \left( \frac{1}{M_d} + \frac{1}{M_*} \right)^{0.5} \frac{T_*^{1.75}}{p_*},$$

with constant  $E = 1.01325 \cdot 10^{-7.5} \text{ m}^4 \text{ kg}^{1/2} \text{ Pa} / (\text{K}^{7/4} \text{ mol}^{7/6} \text{ s})$  as well as  $M_d$ ,  $M_*$  [kg/mol] denoting the molecular weights and  $V_d$ ,  $V_*$  [m<sup>3</sup>/mol] the molar volumes of diluent and air, respectively. Here, we assume  $M_d$ ,  $M_*$ ,  $V_d$ , and  $V_*$  to be constants.

We now consider the diluent density in the air. Away from the fiber it is given by  $\rho_{d,*} = \rho_* c_{d,*}$  with  $\rho_*$  and  $c_{d,*}$  assumed to be known, e.g., from an external computation. At the fiber surface we employ a model for the (dimensionless) mass fraction-scaled diluent density  $\varrho_*$  that is based on [14]

$$\varrho_*(c, T) = \frac{1}{\rho_{*,0}} \mathcal{S}(c, T T_0),$$

$$\mathcal{S}(c, T) = \frac{M_d}{R_u T} p_{vap} \frac{\rho(c, T)}{\rho_d^0(T)} \exp(1 - \phi_d(c, T) + \chi(1 - \phi_d(c, T))^2),$$

$$\phi_d(c, T) = (1 - c) \frac{\rho(c, T)}{\rho_d^0(T)},$$

with the diluent volume fraction  $\phi_d$ , the Flory-Huggins interaction parameter  $\chi = 0.5$  and the universal gas constant  $R_u = 8.3114 \text{ J}/(\text{mol K})$ . For the vapor pressure of the diluent  $p_{vap}$  [Pa] we employ a further model depending on the specific diluent. This model will be given separately for each considered setup.

## 4.2. Solution strategy

The derived fiber models for dry spinning of a single fiber (System 4.9 for an uni-axial fiber and System 4.11 for a curved fiber) are a combined system of one- and two-dimensional model equations. Besides the unknown parameter  $L$

in the curved fiber model, both models have the same structure and, therefore, their numerical treatment can be done similarly. In the following we explain our numerical solution strategy for uni-axial fibers, but give remarks for its adaption to curved fibers.

For given polymer mass fraction  $c$  and mixture temperature  $T$ , the one-dimensional equations (4.9a) form together with the boundary conditions a parametric BVP of ODEs with two variables  $(u, N)$ . The numerical challenge lies in solving the problem for arbitrary parameter settings, which requires suitable initial guesses of the respective solutions. This problem is tackled by the continuation-collocation method presented in Sec. 3.1. The solution of the one-dimensional equations is then iteratively coupled with the solution of the two-dimensional equations (4.9b). Before the first coupling iteration the necessary fields of averaged mass fraction  $\bar{c}$  and temperature  $\bar{T}$  are calculated by the averaged advection-diffusion equations (4.9c) with  $(c, T)|_{r=1} = (\bar{c}, \bar{T})$  as initial guess. The solution of the two-dimensional equations (4.9b) itself is computed using the procedure explained in Sec. 3.3, i.e., the implicitly given solution expressions in terms of Green's functions and Volterra integral equations of second kind with singular kernel for the values at the fiber boundary are solved using a product integration method based on the Lobatto IIIa or implicit Euler quadrature formula. The basic coupling algorithm for the solving of System 4.9 has the following form.

**Algorithm 4.13** (Fiber solution for uni-axial fibers).

- (1) **Initialization step:** Solve the averaged equations (4.9a) and (4.9c) with  $(c, T)|_{r=1} = (\bar{c}, \bar{T})$  and  $\langle \mu(c, T) \rangle_{R^2} = \mu(\bar{c}, \bar{T})\pi R^2$  to obtain  $\mathbf{y}^{(0)} = (u, N, \bar{c}, \bar{T})$ .
- (2) **Coupling step:** For  $i \geq 1$ , solve (4.9b) with given  $\mathbf{y}^{(i-1)}$  to obtain  $(c, T)^{(i)}$  and afterwards compute the new solution of (4.9a) to obtain  $(u, N)^{(i)}$ , which gives in total  $\mathbf{y}^{(i)}$ , as long as  $\|\mathbf{y}^{(i-1)} - \mathbf{y}^{(i)}\| > tol$  for given tolerance  $tol$ .

Finally, the fiber-air interaction is performed by Algorithm 3.8 that weakly couples the fiber calculation and airflow computation via iterative solving. This means, our numerical solution procedure consists of nested iterations: an inner iteration for the fiber solution (coupling of one and two-dimensional fiber equations) and an outer iteration for the coupling of fiber and airflow solutions.

In the following we present the model-dependent continuation strategy for the solution of the one-dimensional equations, which is build on top of the general continuation procedure described in Sec. 3.1.2. Thereafter, we explain the utilization of the product integration method for the efficient solution of the two-dimensional advection-diffusion equations.

**Remark 4.14** (Fiber solution for curved fibers). *The solution of the curved fiber model (System 4.11) is done in an analogous way by replacing the one-dimensional*

equations (4.9a) with (4.11a). Note that the two-dimensional equations (4.9b), (4.11b) are identical.

### 4.2.1. Model-specific continuation method

We consider the solving of the one-dimensional equations (4.9a) for an uniaxial fiber and explain the extension to the curved model equations (4.11a) subsequently. Following Sec. 3.1.2 we consider the family of BVPs

$$\begin{aligned} \frac{d}{ds} \mathbf{y} &= \hat{\mathbf{f}}(\mathbf{y}; \mathbf{p}), & \hat{\mathbf{g}}(\mathbf{y}(0), \mathbf{y}(1); \mathbf{p}) &= \mathbf{0}, & \mathbf{p} &\in [0, 1]^n, \\ \hat{\mathbf{f}}(\cdot; \underline{\mathbf{1}}) &= \mathbf{f}, & \hat{\mathbf{g}}(\cdot, \cdot; \underline{\mathbf{1}}) &= \mathbf{g}, & \hat{\mathbf{f}}(\cdot; \mathbf{0}) &= \mathbf{f}_0, & \hat{\mathbf{g}}(\cdot, \cdot; \mathbf{0}) &= \mathbf{g}_0, \end{aligned}$$

with continuation tuple  $\mathbf{p}$ . For our dry spinning model we apply different continuation strategies for the two steps in Algorithm 4.13. Note that we call Step (1) initialization step, whereas Step (2) is the coupling step.

#### Initialization step

We introduce continuation parameters for the viscous, gravitational and aerodynamic forces as well as for the draw ratio  $p_{\text{Re}}, p_{\text{Fr}}, p_{A_*}, p_{\text{Dr}} \in [0, 1]$ . This means we replace the global Reynolds number  $\text{Re}$  by the term  $p_{\text{Re}}\text{Re} + (1 - p_{\text{Re}})\text{Re}_0$ , analogously for  $\text{Fr}$ ,  $A_*$  and  $\text{Dr}$  with starting values  $\text{Re}_0 = 10$ ,  $\text{Fr}_0 = 100$ ,  $A_{*,0} = 10^{-4}$ ,  $\text{Dr}_0 = u_{\text{in}}/u_{\text{out}}$ . Furthermore, we introduce continuation parameters  $p_c, p_T \in [0, 1]$  on the right hand side of the equations (4.9c) to control the effects of heat and mass transfer over the fiber boundary,

$$\begin{aligned} \partial_s \bar{c} &= \frac{\text{St}_c}{\varepsilon} 2\pi R \frac{\bar{c}^2}{Q} j_c(\bar{c}, \bar{T}) p_c, \\ \partial_s \bar{T} &= -\frac{1}{\varepsilon} 2\pi R \frac{\bar{c}}{Q} \frac{1}{q(\bar{c}, \bar{T})} (\text{St}_T j_T(\bar{T}) + \text{St}_c j_c(\bar{c}, \bar{T}) (\delta(\bar{T}) - h_d^0(\bar{T}))) p_T, \end{aligned}$$

Consequently, we embed the one-dimensional fiber model into a family of BVPs in a six-dimensional parameter space,

$$\mathbf{p} = (p_c, p_T, p_{\text{Re}}, p_{\text{Fr}}, p_{A_*}, p_{\text{Dr}}) \in [0, 1]^6.$$

The choice of the continuation parameters allows the decrease and increase of mass and heat transfer as well as of viscous, gravitational, aerodynamic and drawing effects, that mainly dominate the fiber dynamics.

The starting solution for the continuation that belongs to  $\mathbf{p} = \mathbf{0}$  is a stress-free straight fiber with constant polymer mass fraction, speed and temperature (taken from the inflow), i.e.,

$$u = u_{in}, \quad N = 0, \quad \bar{c} = c_{in}, \quad \bar{T} = T_{in}.$$

Obviously, it satisfies the prescribed boundary conditions at  $s = 0$  and  $s = 1$  (since  $Dr_0 = u_{in}/u_{out}$ ) as well as the equations for  $\bar{c}$ ,  $\bar{T}$ , and  $u$ . The linear momentum equation for  $N$  is approximately fulfilled due to small external forces. The change of each continuation parameter has different effects on the form of the solution and hence on finding appropriate initial guesses in the continuation. To navigate through the six-dimensional parameter space from  $\mathbf{p} = \mathbf{0}$  to  $\mathbf{p} = \underline{\mathbf{1}}$  we follow a strategy that consists of two steps:

(A) From  $\mathbf{p} = \mathbf{0}$  to  $\mathbf{p}^A = (1, 1, 1, 0, 0, 1)$ :

By changing the parameters  $p_c$ ,  $p_T$ ,  $p_{Re}$  and  $p_{Dr}$  from 0 to 1 we include mass and heat transfer due to evaporation as well as viscous and drawing effects.

(B) From  $\mathbf{p}^A$  to  $\mathbf{p} = \underline{\mathbf{1}}$ :

By increasing the parameters  $p_{Fr}$ ,  $p_{A_*}$  from 0 to 1 we incorporate gravitational and aerodynamic effects in our solution.

We use a heuristic that seeks for the diagonal continuation path through the parameter space. In both Steps (A) and (B) it turns out that balancing the physical effects strictly leads to the diagonal path such that the parameter space can be reduced to  $p_c = p_T = p_{Re} = p_{Dr}$  and  $p_{Fr} = p_{A_*}$  respectively. The corresponding one-dimensional search is performed with the adaptive step size control as described in Sec. 3.1.2.

### Coupling step

Let  $\langle \mu(c, T) \rangle_{R^2}^{(i)}$  be the integrated dynamic viscosity of iteration  $i$  in the coupling step (cf. Algorithm 4.13). We introduce a continuation parameter  $p_\mu \in [0, 1]$  for this quantity, i.e., we replace the integrated dynamic viscosity in iteration  $i$  by the linear combination with the viscosity of the previous iteration

$$(1 - p_\mu) \langle \mu(c, T) \rangle_{R^2}^{(i-1)} + p_\mu \langle \mu(c, T) \rangle_{R^2}^{(i)}.$$

For initialization we set  $\langle \mu(c, T) \rangle_{R^2}^{(0)} = \mu(\bar{c}, \bar{T})\pi R^2$ . Again, the corresponding one-dimensional search is performed with the adaptive step size control as described before (cf. Sec. 3.1.2).

**Remark 4.15** (Continuation for curved fibers). *For the one-dimensional rod equations (4.11a) we introduce the additional continuation parameter  $p_{bc}$  in the initial-*

ization step and the modified boundary condition

$$\mathbf{r}(0) - p_{bc} \mathbf{r}_{in} - (1 - p_{bc})(\mathbf{r}_{out} - L \mathbf{R}_{in}^T \cdot \mathbf{e}_3) = 0,$$

with  $\mathbf{R}_{in} = \mathbf{R}(\mathbf{q}_{in})$ . Consequently, we consider the seven-dimensional continuation parameter space

$$\mathbf{p} = (p_c, p_T, p_{bc}, p_{Re}, p_{Fr}, p_{A_*}, p_{Dr}) \in [0, 1]^7,$$

and choose the starting solution (corresponding to  $\mathbf{p} = \mathbf{0}$ )

$$\begin{aligned} \mathbf{r}(s) &= \mathbf{r}_{out} - (1-s)L\mathbf{R}_{in}^T \cdot \mathbf{e}_3, & \mathbf{q} &= \mathbf{q}_{in}, & \mathbf{n} &= \mathbf{0}, & \mathbf{m} &= \mathbf{0}, \\ u &= u_{in}, & \boldsymbol{\kappa} &= \mathbf{0}, & \bar{c} &= c_{in}, & \bar{T} &= T_{in}, \\ L &= (\mathbf{r}_{out} - \mathbf{r}_{in}) \cdot (\mathbf{R}_{in}^T \cdot \mathbf{e}_3) \end{aligned}$$

for  $s \in [0, 1]$ . Basically the initial solution for the rod curve  $\mathbf{r}$  is built by the orthogonal projection of  $(\mathbf{r}_{out} - \mathbf{r}_{in})$  onto the initial fiber direction  $\mathbf{R}_{in}^T \cdot \mathbf{e}_3$ . In total, the initial solution is a stress-free, unbent, straight fiber with constant polymer mass fraction, speed and temperature being extruded from the modified nozzle position  $(\mathbf{r}_{out} - L\mathbf{R}_{in}^T \cdot \mathbf{e}_3)$ . The navigation strategy through the parameter space equals the corresponding procedure for the uni-axial fiber model, at which we additionally include the change of  $p_{bc}$  from 0 to 1 into Step (A). The coupling step remains unchanged.

**Remark 4.16** (Regularization of rod model). Numerical studies show that the angular momentum equation of the rod model (4.11a) is badly scaled with respect to the variable  $\mathbf{m}$ . In order to accelerate the convergence of the continuation-collocation procedure we introduce the scaled couple  $\tilde{\mathbf{m}} = \varepsilon^{-2} \mathbf{m}$ , yielding the angular momentum balance

$$L^{-1} \partial_s \tilde{\mathbf{m}} = \frac{\varrho_M^2}{\rho} u^2 \boldsymbol{\kappa} \times \mathbf{P}_2 \cdot \boldsymbol{\kappa} + L^{-1} \frac{\varrho_M^2}{\rho} \mathbf{P}_2 \cdot (u \partial_s (u \boldsymbol{\kappa}) - \boldsymbol{\kappa} u \partial_s u) + \frac{1}{\varepsilon^2} \mathbf{n} \times \mathbf{e}_3 + \tilde{\mathbf{m}} \times \boldsymbol{\kappa}.$$

Then,  $\varepsilon$  only appears in the term  $\varepsilon^{-2} \mathbf{n} \times \mathbf{e}_3$ . It is considered as regularization parameter (regularization of the associated string model, cf. Sec. 2.2) and, therefore, fixed at the constant value  $\varepsilon_0 = 10^{-1}$ . This approach is reasonable since we expect the angular momentum not to affect the fiber solution significantly but only to act as regularization in view of its numerical treatment. A similar strategy was employed in the study of rotational spinning processes [5]. In the two-dimensional equations (4.11b)  $\varepsilon$  is the actual parameter and directly set as desired.

## 4.2.2. Product integration method

In Sec. 3.3 we presented an algorithmic procedure based on a Green's function and the product integration method for the efficient solution of two-dimensional

advection-diffusion equations with Robin-type boundary condition

$$\begin{aligned} \partial_x \psi - \frac{1}{r} \partial_r (r \partial_r \psi) &= 0, \\ \psi|_{x=0} &= \psi_{in}, \quad \partial_r \psi|_{r=0} = 0, \quad \partial_r \psi|_{r=1} = a\psi|_{r=1} + b, \end{aligned} \quad (4.13)$$

with  $\psi : [0, 1]^2 \rightarrow \mathbb{R}$ ,  $(r, x) \mapsto \psi(r, x)$ , as well as functions  $a, b : [0, 1] \rightarrow \mathbb{R}$  and constant  $\psi_{in} \in \mathbb{R}$ . In the following we explain the applicability of the general form (4.13) to the two-dimensional advection-diffusion equations (4.9b), (4.11b). Assuming non-zero coefficients, the equations (4.9b), (4.11b) for polymer mass fraction  $c$  and mixture temperature  $T$  can be written in the form

$$\partial_s c - \lambda_c \frac{1}{r} \partial_r (r \partial_r c) = 0, \quad \partial_s T - \lambda_T \frac{1}{r} \partial_r (r \partial_r T) = 0,$$

with  $\lambda_c = L\bar{c}D(\bar{c}, \bar{T})/(\varepsilon\text{Pe}_c uR^2)$  and  $\lambda_T = LC(\bar{c}, \bar{T})/(\varepsilon\text{Pe}_T \rho(\bar{c}, \bar{T})q(\bar{c}, \bar{T})uR^2)$ . To obtain the general form (4.13) we transform the unknowns  $c$  and  $T$  by the following rule

$$\psi(r, \Lambda(s)) = \xi(r, s), \quad \text{with} \quad \Lambda(s) = \int_0^s \lambda_\xi(s') ds', \quad \xi \in \{c, T\}.$$

The initial conditions become  $\psi_{in} = c_{in}$  and  $\psi_{in} = T_{in}$ , respectively. The coefficient functions are

$$a(x) = -\text{Pe}_c \text{St}_c \frac{R\gamma(c, T)|_{r=1}}{\rho(\bar{c}, \bar{T})D(\bar{c}, \bar{T})|_{s=\Lambda^{-1}(x)}}, \quad b(x) = -a(x)c_{ref}(c, T)|_{r=1, s=\Lambda^{-1}(x)},$$

for the mass fraction equation and

$$\begin{aligned} a(x) &= -\text{Pe}_T \text{St}_T \frac{R\alpha}{C(\bar{c}, \bar{T})|_{s=\Lambda^{-1}(x)}}, \\ b(x) &= -a(x)T_*|_{s=\Lambda^{-1}(x)} - \text{Pe}_T \text{St}_c \frac{R(j_c(c, T)(\delta(T) - h_d^0(T)))|_{r=1}}{C(\bar{c}, \bar{T})|_{s=\Lambda^{-1}(x)}}, \end{aligned}$$

for the temperature equation, respectively. Considering the iteration procedure in Step (2) of Algorithm 4.13 (coupling step) the coefficient functions  $a$  and  $b$  are evaluated at  $c|_{r=1}$ ,  $\bar{c}$  and  $T|_{r=1}$ ,  $\bar{T}$  of the previous iteration step, i.e., the boundary conditions are treated in a semi-implicit way, such that the linear Robin-type character is preserved. This is certainly the key point for the embedding into the solution framework of Green's functions and product integration method that ensures the desired numerical efficiency.

**Remark 4.17** (Grid resolution). *The mesh points in  $x$ -direction are chosen in such a way that they correspond to the underlying mesh points from the collocation method resulting from a preceding solution of one-dimensional equations (cf. Algorithm 4.13), i.e.,  $x_i = \Lambda(s_i)$ . In view of the computation of profiles an equidistant grid in  $r$ -direction with  $N_r = 101$  grid points is chosen. For given profile  $\psi$  the calculation of the averaged quantity  $\bar{\psi} = \langle \psi \rangle_{R^2} / (\pi R^2)$  is done by numerical quadrature in  $r$ -direction employing the implicit Euler scheme (for product integration method (i)) or the standard Lobatto IIIa collocation method (for product integration method (ii)) (cf. Sec. 3.3 and in particular Rem. 3.5).*

### 4.3. Approximation quality and performance

In this section we analyze the approximation quality of our dimensionally reduced uni-axial fiber model (System 4.9) in comparison to the full three-dimensional model (System 4.1). Besides the approximation quality we also examine the efficiency of our proposed numerical solution framework (Algorithm 4.13). As explained in Sec. 4.2 the intended two-way coupling of fibers with the surrounding airflow leads to nested iterations. To preserve computability the inner iteration, which is the solution of the fiber model, has to be very quick. Considering an academic setup without two-way coupled airflow we show the efficiency of the fiber solution framework which provides the possibility to compute fully two-way coupled simulations in the subsequent section.

To study the approximation quality of the proposed dimensionally reduced fiber model (System 4.9) and the performance of the numerical solution algorithm, we compare our developed procedure for a single uni-axial fiber with the solution of the original three-dimensional problem (System 4.1). As the direct numerical simulation of a three-dimensional thin fiber immersed in an airflow in a spinning duct is computationally extremely demanding due to the required high resolution, we limit ourselves to a three-dimensional axis-symmetric setting of a fiber without any aerodynamic forces and with stress-free end. This implies the boundary conditions  $\bar{\bar{\Sigma}} \cdot \bar{\bar{\mathbf{n}}} = \bar{\bar{\mathbf{0}}}$  on  $\Gamma_{\text{fr}} \cup \Gamma_{\text{out}}$  in System 4.1 and  $f_{\text{air}} = 0$ ,  $N(1) = 0$  in System 4.9. The outlet boundary condition for  $\bar{\mathbf{v}}$  and  $u$  is omitted. Moreover, we consider a dry surrounding, i.e.,  $\rho_{d,*} = 0$  (implying  $c_{\text{ref}} = 1$ ), and take all physical parameters as well as the mass and heat sources as constants yielding  $\mu = q = \alpha = \gamma = C = D = 1$  in nondimensional form.

We denote the three-dimensional problem as reference and solve it with FEniCS<sup>1</sup>, an open-source finite element code with Python interface, which basically needs a

---

<sup>1</sup>For details on the open-source finite element code FEniCS see <http://www.fenicsproject.org>.

<b>Process Parameters</b>			
Description	Symbol	Value	Unit
Fiber length	$L$	0.2	m
Nozzle radius	$R_{in}$	$4.07 \cdot 10^{-4}$	m
Speed at nozzle	$u_{in}$	$5 \cdot 10^{-2}$	m/s
Polym. mass fract. at nozzle	$c_{in}$	0.6	–
Temperature at nozzle	$T_{in}$	363.15	K
Temperature of surrounding	$T_*$	350	K
Diluent density of surrounding	$\rho_{d,*}$	0	kg/m <sup>3</sup>
Drag force	$f_{air}$	0	N/m

<b>Physical Parameters</b>			
Description	Symbol	Value	Unit
Polymer density	$\rho_p^0$	1350	kg/m <sup>3</sup>
Diluent density	$\rho_d^0$	1000	kg/m <sup>3</sup>
Diluent spec. enthalpy	$h_d^0$	$2 \cdot 10^5$	J/kg
Evap. enthalpy diluent	$\delta$	$2.35 \cdot 10^6$	J/kg
Dynamic viscosity	$\mu$	200	Pa s
Specific heat capacity	$q$	2750	m <sup>2</sup> /(s <sup>2</sup> K)
Heat transfer coeff.	$\alpha$	2000	W/(m <sup>2</sup> K)
Mass transfer coeff.	$\gamma$	0.3	kg/(m <sup>2</sup> s)
Thermal conductivity	$C$	0.4	W/(m K)
Diffusion coefficient	$D$	$3.5 \cdot 10^{-10}$	m <sup>2</sup> /s

<b>Setup-specific reference values</b>	
Description	Formula
Mass line density	$\varrho_{M,0} = \rho(c_{in})\pi R_{in}^2$
Curve	$r_0 = L$
Diameter	$d_0 = 2R_{in}$
Velocity	$v_0 = u_{in}$
Temperature	$T_0 = T_{in}$
Further scales	$b_0 = b,$ $b \in \{\mu, q, \alpha, \gamma, C, D\}$

<b>Dimensionless numbers</b>		
Description	Symbol	Value
Slenderness	$\varepsilon$	$4.07 \cdot 10^{-3}$
Reynolds	Re	4.65
Froude	Fr	3.57
Mass Peclet	Pe <sub>c</sub>	$1.16 \cdot 10^7$
Temp. Peclet	Pe <sub>T</sub>	$2.60 \cdot 10^4$
Mass Stanton	St <sub>c</sub>	$6.45 \cdot 10^{-5}$
Temp. Stanton	St <sub>T</sub>	$1.56 \cdot 10^{-4}$

**Table 4.4.:** Process and physical parameters as well as setup-specific reference values and resulting dimensionless numbers used for the performance analysis (cf. Tab. 4.1) .

weak formulation of the PDEs. To overcome the need of re-meshing while solving the reference, we transform the weak form of System 4.1 to the fixed domain  $\tilde{Q}_{cut} = (0, 1)^2$ . The resulting ODE for the fiber radius function  $R$  on the domain boundary  $r = 1$  and the balance equations are solved by iterations. The domain  $\tilde{Q}_{cut}$  is meshed with a triangular grid, which is refined at the nozzle  $\Gamma_{in}$  due to

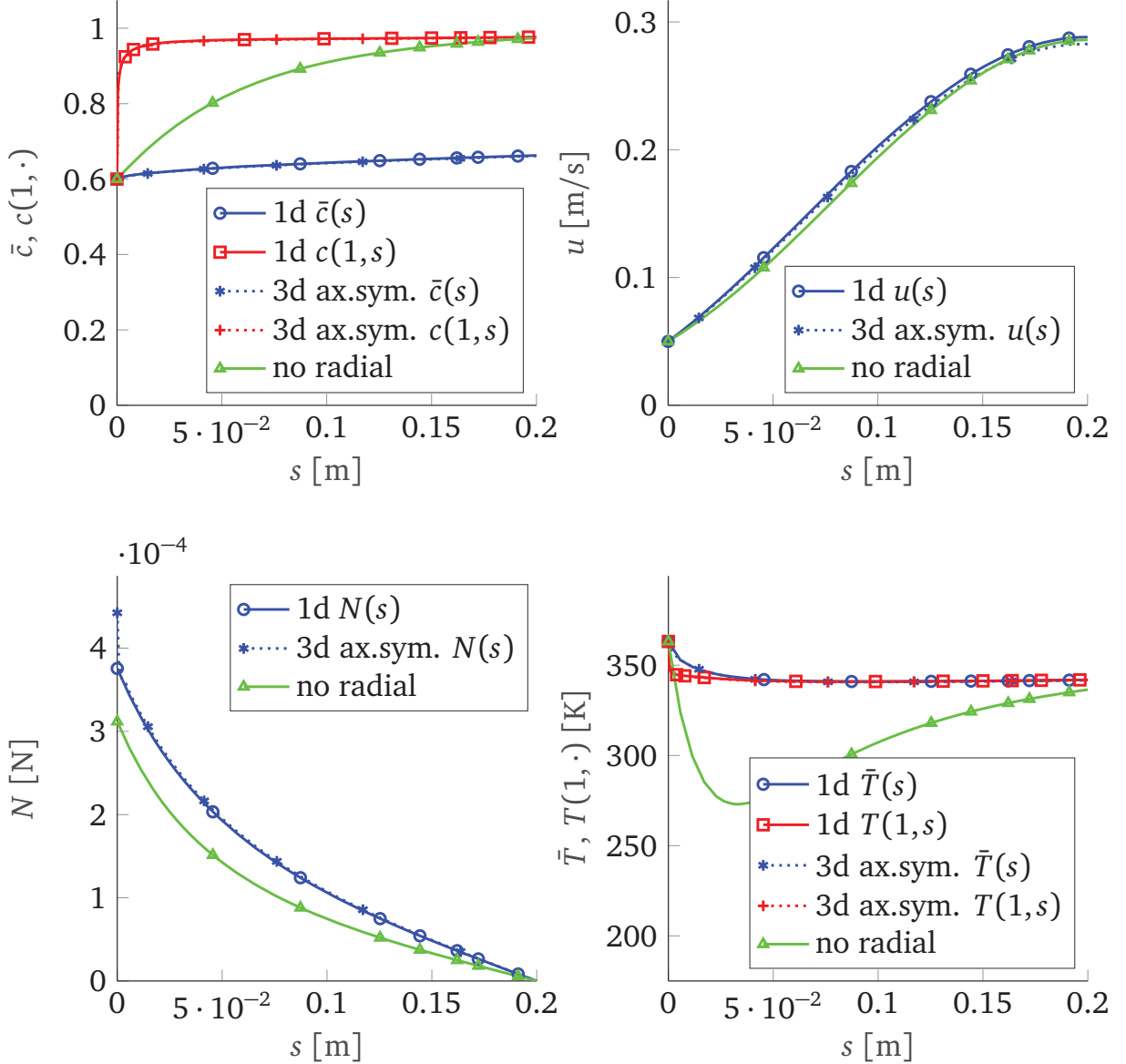


**Figure 4.3.:** One-dimensional fiber solution obtained with and without radial information (*solid lines*) in comparison to the reference solution (*dotted lines*).

expected boundary layers. The nodes of the triangles are  $(r_i, s_j)$  with  $r_i = i/200$ ,  $s_j = (j/40)^{1.5}$  for  $i = 0, \dots, 200$ ,  $j = 0, \dots, 40$ , i.e.,  $16 \cdot 10^3$  triangular elements and 8241 nodes in total. Algorithm 4.13 for the dimensionally reduced fiber model is implemented in MATLAB version R2016b, where the BVP solver `bvp4c.m` is used with the default values. To achieve comparability the reference solution is interpolated on the mesh of the solution of System 4.9, i.e., the mesh with the collocation points used in the boundary value solver (`bvp4c.m`) in  $s$ -direction and 101 equidistant points in  $r$ -direction. As stopping criterion for the iteration in the coupling step of Algorithm 4.13 we use  $tol = 10^{-6}$ .

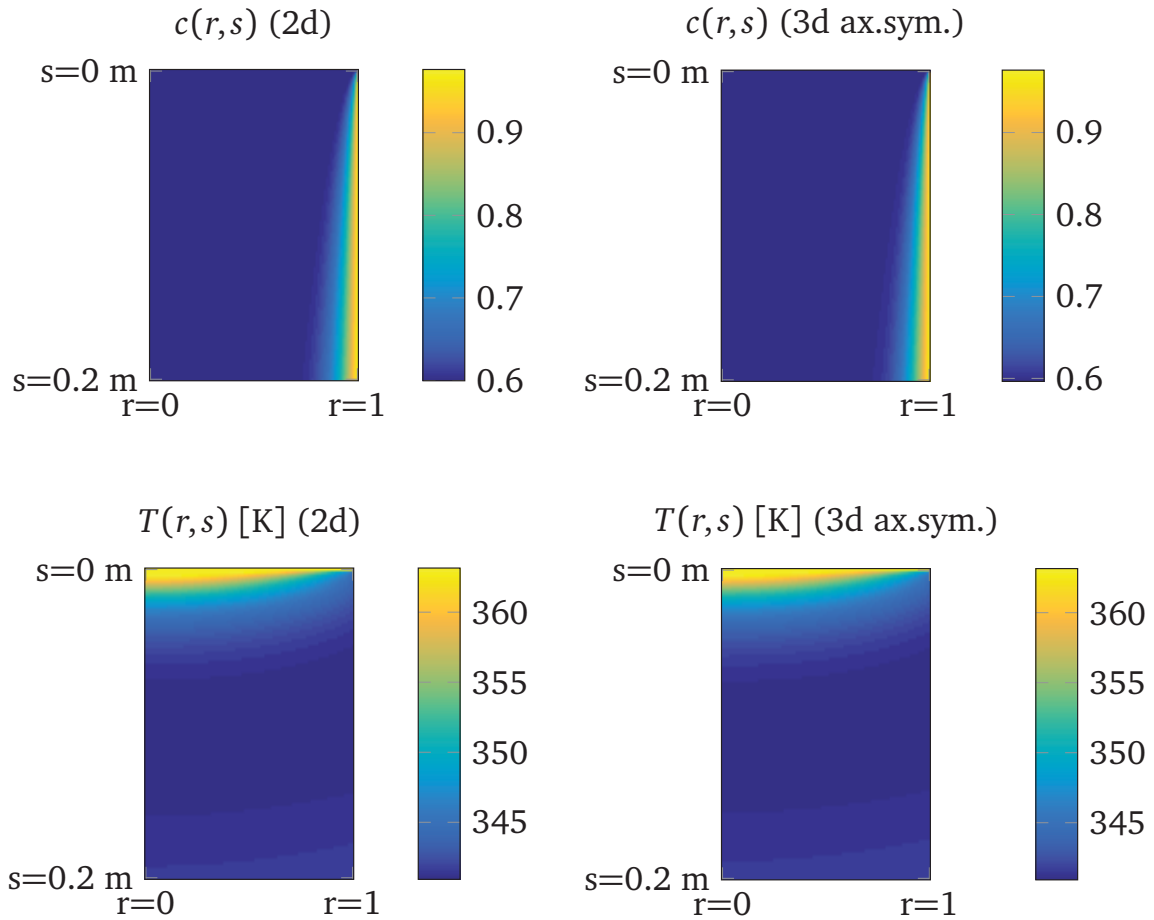


**Figure 4.4.:** Polymer mass fraction and temperature profiles as solution of the one-two-dimensional fiber model (*left*) and the reference model (*right*).

As an example we consider a setup with moderate thinning and evaporation effects. The choice of the physical and process parameters and the resulting dimensionless numbers are given in Tab. 4.4. Fig. 4.3 shows the solution curves obtained from the dimensionally reduced fiber model of System 4.9. This solution we oppose the solution obtained without radial information (which means exiting Algorithm 4.13 after Step (1)) and the three-dimensional axis-symmetric solution of the reference. For the latter the quantities of interest  $\bar{c}$ ,  $\bar{T}$ ,  $u$  and  $N$  are calculated a posteriori according to the definitions in Section 4.1.2. The corresponding two-dimensional profiles for polymer mass fraction  $c$  and temperature  $T$  can be seen in Fig. 4.4. We draw the following conclusions from the solution curves: First, as expected the coupling of the one-dimensional model equations with the two-dimensional equations for  $c$  and  $T$  is absolutely essential, since the solution without that information differs extremely from the reference solution, especially concerning the averaged quantities  $\bar{c}$  and  $\bar{T}$ . This evidence is supported by the non-uniform profiles in Fig. 4.4. Second, the solution of the one-two-dimensional fiber model approximates the reference solution very accurately and takes the important radial

$\bar{c}$	$u$	$N$	$\bar{T}$
$1.8064 \cdot 10^{-3}$	$1.5301 \cdot 10^{-2}$	$4.9611 \cdot 10^{-2}$	$6.4668 \cdot 10^{-4}$
$c(1, \cdot)$	$T(1, \cdot)$	$c$	$T$
$4.3393 \cdot 10^{-3}$	$1.1876 \cdot 10^{-3}$	$4.1332 \cdot 10^{-3}$	$7.2008 \cdot 10^{-4}$

**Table 4.5.:** Relative  $L^2$ -errors between one-two-dimensional solution and reference solution, cf. Figs. 4.3 and 4.4.

effects into account. The relative  $L^2$ -errors between the single components of the solutions, as given in Tab. 4.5, verify the utilization of our model framework with regard to the good approximation quality. In addition, the difference in the computation times is crucial. Whereas the computation of the three-dimensional axis-symmetric reference solution takes around 4228 seconds, which means more than 1.17 hours, the computation of the reduced model takes only around 43 seconds (around 4 seconds for the initialization step (Step (1)) and 39 seconds for the coupling step (Step (2)) of Algorithm 4.13). The good performance is owed to our embedding of the two-dimensional advection-diffusion equations into the solution framework of Green's functions and product integration method. In fact, the achieved efficiency is essential when dealing with more than one fiber and considering fiber-airflow interactions in a spinning duct via two-way coupling. Consequently, our proposed procedure builds a good basis for the simulation of industrial dry spinning processes.

**Remark 4.18** (Temperature behavior). *In this academic example the behavior of the fiber temperature  $T$  might be surprising (cf. Fig. 4.4). Through solvent evaporation associated heat transfer  $T$  drops below  $T_*$  shortly after the nozzle. Due to the relative temperature between fiber and surrounding being negative, i.e.,  $(T - T_*) < 0$ , the fiber is heated up by the surrounding towards the fiber end, when mass transfer effects are not dominating the heat transfer anymore. This behavior is also observed in the subsequent industrial case, when only a one-way coupling of uni-axial fibers with the surrounding airflow is considered (cf. Fig. 4.10). However, regarding full two-way coupled airflow this behavior does not occur.*

## 4.4. Industrial dry spinning with two-way coupled airflow

In industrial dry spinning we are faced with multiple jets being extruded from the spinneret into the spinning duct. The properties of the spun fibers are essentially determined by the fiber-airflow interactions. Hence, we aim at simulations of the dry spinning with two-way coupled airflow. In this section we consider two device setups where the fibers are exposed to different airflow situations. In the first one the airflow forms a counter-current to the fiber flow, cf. Fig. 4.1, such that the fiber curves are expected to remain straight. This means we employ our uni-axial fiber dry spinning model (System 4.9) there. In the second one the airflow is mainly perpendicular to the fiber flow, cf. Fig. 4.2, such that the fiber curves experience lateral deflections. Thus, we employ our curved fiber model (System 4.11) for this setup. In both setups we assume that a cellulose acetate (CA)-acetone mixture is dry spun. This is a typical polymer solvent mixture and has been used in previous studies on dry spinning processes [42, 88]. Before we give a description of each specific process setup and present the corresponding simulation outcomes, we provide all physical parameters and rheological models that close our fiber dry spinning models (uni-axial and curved).

### 4.4.1. Model closing

We consider the dry spinning of a cellulose acetate (CA)-acetone mixture. The physical material parameters for the polymer CA and the diluent acetone are taken from [42, 88], see Tab. 4.6. The additional rheological models that we use to close our dimensionally reduced fiber models (uni-axial and curved) are briefly summarized in this subsection (cf. Remark 4.10). The setup-specific reference values used for the nondimensional form of the model equations are also given in Tab. 4.6.

#### Thermal conductivity and diffusion coefficient

The thermal conductivity  $C$  is chosen as constant  $C = C_{const}/C_0$  with  $C_{const} = 0.2 \text{ W/(m K)}$ , i.e.,  $C = 1$  in nondimensional form. For the diffusion coefficient  $D$  we use a model from [106] that is based on the free volume diffusion model of

#### 4. Fiber spinning with evaporation effects in airflows

Physical Parameters			
Description	Symbol	Value	Unit
CA density	$\rho_p^0$	1300	kg/m <sup>3</sup>
Acetone density	$\rho_d^0$	767	kg/m <sup>3</sup>
CA spec. heat cap.	$q_p^0$	1600	J/(kg K)
Acetone spec. heat cap.	$q_d^0$	2160	J/(kg K)
Molec. weight acetone	$M_d$	$5.81 \cdot 10^{-2}$	kg/mol
Molec. weight air	$M_*$	$2.90 \cdot 10^{-3}$	kg/mol
Molar volume acetone	$V_d$	$6.60 \cdot 10^{-5}$	m <sup>3</sup> /mol
Molar volume air	$V_*$	$2.01 \cdot 10^{-5}$	m <sup>3</sup> /mol

Setup-specific reference values	
Description	Formula
Mass line density	$\varrho_{M,0} = \rho(c_{in})R_{in}^2 \pi$
Curve	$r_0 = H$
Diameter	$d_0 = 2R_{in}$
Velocity	$v_0 = u_{in}$
Viscosity	$\mu_0 = \mu(c_{in}, T_{in})$
Spec. heat cap.	$q_0 = q(c_{in})$
Thermal cond.	$C_0 = C_{const}$
Diffusivity	$D_0 = D(c_{in}, T_{in})$
Take up speed	$u_{out,0} = u_{out}$
Further scales	$b_0 = b_{in}, \quad b \in \{T, \alpha, \gamma, p_*, \lambda_*, \nu_*, q_*, \rho_*, D_{d,*}\}$

**Table 4.6.:** Physical parameters of the industrial dry spinning setups taken from [42, 88] and setup-specific reference values.

[107, 108]

$$D(c, T) = \frac{1}{D_0} \mathcal{D}(c, T T_0),$$

$$\mathcal{D}(c, T) = D_1 (1 - \phi_d(c, T))^2 (1 - 2\chi \phi_d(c, T)) \mathcal{E}(c, T),$$

$$\mathcal{E}(c, T) = \exp\left(-\frac{V_1(1-c) + V_2 c}{K_1(1-c)(T_1 + T) + K_2 c(T_2 + T)}\right),$$

with the parameters

$$V_1 = 4.43 \cdot 10^{-4}, \quad V_2 = 6.38 \cdot 10^{-4}, \quad K_1 = 1.86 \cdot 10^{-6} \text{ 1/K}, \quad K_2 = 5 \cdot 10^{-7} \text{ 1/K},$$

$$T_1 = -53.33 \text{ K}, \quad T_2 = -240 \text{ K}, \quad D_1 = 3.6 \cdot 10^{-8} \text{ m}^2/\text{s}.$$

As before  $\phi_d$  is the diluent volume fraction and  $\chi = 0.5$  is the Flory-Huggins interaction parameter. Due to the considered constant diluent density  $\rho_d^0$  (cf. Tab. 4.6) the diluent volume fraction simplifies to  $\phi_d(c) = (1-c)\rho(c)/\rho_d^0$ .

### Diluent and evaporation enthalpy

Using the constant specific heat capacity for the diluent acetone  $q_d^0$  (cf. Tab. 4.6) we employ the caloric equation of state for the specific enthalpy with respect to the freezing point  $T_f = 178.15$  K, see [70],

$$h_d^0(T) = \frac{1}{h_0} \mathcal{H}(T T_0), \quad \mathcal{H}(T) = q_d^0(T - T_f).$$

The evaporation enthalpy model  $\delta$  is taken from [62], i.e.,

$$\delta(T) = \frac{1}{\delta_0} \vartheta(T T_0), \quad \vartheta(T) = \frac{E_0}{M_d} \exp\left(-\iota \frac{T}{T_\delta}\right) \left(1 - \frac{T}{T_\delta}\right)^\iota,$$

with  $E_0 = 46.95 \cdot 10^3$  J/mol,  $\iota = 0.2826$  and  $T_\delta = 508.2$  K.

### Dynamic viscosity

For the dynamic viscosity  $\mu$  we employ the zero-shear viscosity model from [41, 42], where an approach of [105] is adopted,

$$\begin{aligned} \mu(c, T) &= \frac{1}{\mu_0} \mathcal{M}(c, T T_0), \\ \mathcal{M}(c, T) &= \begin{cases} \mu_a P_n^{3.7} c^7 \exp\left(\frac{\Delta E}{RT}\right), & T \geq 1.2 T_g(c, T), \\ \mu(c, 1.2 T_g(c, T)) \cdot 10^{\mathcal{K}(c, T)}, & T_g \leq T < 1.2 T_g(c, T), \\ \mu(c, T_g(c, T)), & T < T_g(c, T), \end{cases} \\ \mathcal{K}(c, T) &= -B_1(T - 1.2 T_g(c, T))(T_\mu + T - 1.2 T_g(c, T))^{-1}. \end{aligned}$$

Comparing the dimensional temperature  $T$  to the glass transition temperature  $T_g$  [K], the viscosity follows an exponential decay for high temperatures, obeys the Williams-Landel-Ferry (WLF) model for temperatures near to  $T_g$  and stays constant on the viscosity value at  $T_g$  for low temperatures. The parameters are  $\mu_a = 6.6 \cdot 10^{-13}$  Pa s,  $T_\mu = 101.6$  K,  $B_1 = 8.86$ . The degree of polymerization of CA is  $P_n = 200$  and the flow activation energy  $\Delta E = 5.6940 \cdot 10^4$  J/mol. The glass transition temperature is prescribed according to the Kelley-Bueche equation

$$T_g(c, T) = \frac{B_2 \phi_d(c, T) T_{g,d} + \phi_p(c, T) T_{g,p}}{B_2 \phi_d(c, T) + \phi_p(c, T)},$$

using  $B_2 = 2.5$ , the material glass transition temperatures  $T_{g,p} = 468$  K,  $T_{g,d} = 119$  K, as well as the volume fractions  $\phi_p$ ,  $\phi_d$  of CA and acetone, respectively. Due to the considered constant polymer and diluent densities (cf. Tab. 4.6), the volume fractions simplify to  $\phi_p(c) = c\rho(c)/\rho_p^0$  and  $\phi_d(c) = (1 - c)\rho(c)/\rho_d^0$ .

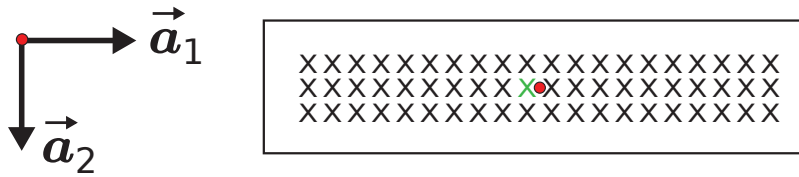


**Figure 4.5.:** Industrial dry spinning setup for uni-axial fibers, sketch of the holes (marked with X) in the spinneret (not in scale). All proceeding simulation results are shown for the fiber extruded from the central position (green X). For the device geometry and the orientation of the outer basis  $\{\vec{a}_1, \vec{a}_2, \vec{a}_3\}$  we refer to Fig. 4.1.

Due to the nonlinear form of the viscosity model including exponential growth, we cannot expect the desired cross-sectionally integrated viscosity  $\langle \mu(c, T) \rangle_{R^2}$  to be well approximated by the viscosity of the averaged fields  $\mu(\bar{c}, \bar{T})\pi R^2$ , cf. Remark 4.8. For reasons of accuracy we thus compute the profiles of the dynamic viscosity  $\mu(c, T)$  in Step (2) of Algorithm 4.13 and integrate them over the fiber cross-sections afterwards to obtain  $\langle \mu(c, T) \rangle_{R^2}$ .

#### 4.4.2. Spinning of uni-axial fibers

We consider the dry spinning setup of [88] where a CA-acetone mixture is pumped from the spinneret through a row of holes into a spinning duct with counter-current airflow (cf. Fig. 4.1). Since the fiber curves are expected to remain straight in this setup, we employ our uni-axial dry spinning model there. Until now the existing literature solely considers fibers immersed in an airflow that is assumed to be unperturbed. This is also the case in [88] where the respective airflow quantities are measured and fixed, i.e., they are not affected by the fiber dynamics, and some characteristics for a single fiber are computed. Consequently, we cannot validate our simulation results, but we check the reasonableness of our model by comparing the intermediate results obtained for a single fiber after the first iteration of our fiber-air coupling algorithm which corresponds to a one-way coupling (as in [88]), cf. Algorithms 3.7, 3.8. In the following we specify the process setup before we present our simulation results.

##### Process setup

A sketch of the device geometry can be found in Fig. 4.1. For a larger emergence of the effects of fiber-air interaction we assume that sixty fibers are spun simultaneously (instead of twenty as in [88]). The corresponding holes in the spinneret are ordered in three parallel rows with twenty holes each, as sketched

Process Parameters			
Description	Symbol	Value	Unit
Device height	$H$	5.1	m
Nozzle radius	$R_{in}$	$3.14 \cdot 10^{-5}$	m
Speed at nozzle	$u_{in}$	5	m/s
Take up speed at bottom	$u_{out}$	10	m/s
Polym. mass fract. at nozzle	$c_{in}$	0.29	–
Temperature at nozzle	$T_{in}$	348.15	K
Total number of fibers	$M$	60	–
Heat transfer at nozzle	$\alpha_{in}$	$5.11 \cdot 10^2$	W/(m <sup>2</sup> K)
Mass transfer at nozzle	$\gamma_{in}$	1.64	kg/(m <sup>2</sup> s)
Air pressure at nozzle	$p_{*,in}$	$1.01 \cdot 10^5$	Pa
Air thermal cond. at nozzle	$\lambda_{*,in}$	$2.42 \cdot 10^{-2}$	W/(m K)
Air kin. viscosity at nozzle	$\nu_{*,in}$	$1.46 \cdot 10^{-5}$	m <sup>2</sup> /s
Air spec. heat cap. at nozzle	$q_{*,in}$	$1.01 \cdot 10^3$	J/(kg K)
Air density at nozzle	$\rho_{*,in}$	1.23	kg/m <sup>3</sup>
Diluent diffusion in air at nozzle	$D_{d,*,in}$	$1.27 \cdot 10^{-5}$	m <sup>2</sup> /s

**Table 4.7.:** Process parameters of the industrial dry spinning setup with vertical airflow (cf. Fig. 4.1) and assuming the airflow without fibers (first step in the fiber-airflow coupling).

in Fig. 4.5. In particular, we consider the fibers of the middle row to be spun in the  $x_1$ - $x_3$ -plane corresponding to  $x_2 = 0$ . At the duct bottom all fibers are drawn down by a take up roller. The length  $L$  of each fiber is given through its inflow position in the spinneret and the position of the take up at the bottom. Concerning the airflow we assume dry air at the inlet, i.e., the inflow contains no diluent. The absolute air inflow velocity (in negative  $\vec{a}_1$ -direction) at the bottom pipe is  $\|\mathbf{v}_*\| = 0.22$  m/s and the air inflow temperature is  $T_* = 330$  K. At each nozzle the CA-acetone mixture forms a drop, from which a jet of initial diameter usually larger than the initial nozzle diameter leaves due to the Barus effect. This effect is also called die swell. Since our model does not take this effect into account, we set  $R_{in}$  according to the initial speed  $u_{in}$  and the initial mixture flux for a single fiber  $A_{in}u_{in} = 1.55 \cdot 10^{-8}$  m<sup>3</sup>/s,  $A_{in} = \pi R_{in}^2$ , as prescribed in [88]. The remaining process parameters are given in Tab. 4.7. Utilizing the setup-specific reference values (cf. Tab. 4.6) the resulting dimensionless numbers are given in Tab. 4.8. In the described spinning setup no considerable lateral forces on the fibers are expected, i.e., the fiber curve is assumed to be straight throughout the whole spinning device. Therefore, we employ our uni-axial dry spinning model given in System 4.9 to simulate this setup.

Dimensionless numbers		
Description	Symbol	Value
Slenderness	$\varepsilon$	$1.23 \cdot 10^{-5}$
Reynolds	Re	$1.79 \cdot 10^3$
Froude	Fr	$7.07 \cdot 10^{-1}$
Drawing	Dr	2.00
Mass Peclet	$Pe_c$	$4.16 \cdot 10^6$
Temperature Peclet	$Pe_T$	$2.73 \cdot 10^3$
Mass Stanton	$St_c$	$3.76 \cdot 10^{-4}$
Temperature Stanton	$St_T$	$5.88 \cdot 10^{-5}$
Air drag associated	$A_*$	$1.14 \cdot 10^2$
Air-fiber Reynolds	$Re_*$	$2.15 \cdot 10^1$
Nusselt	$Nu_*$	1.33
Prandtl	$Pr_*$	$7.44 \cdot 10^{-1}$
Sherwood	$Sh_*$	6.59
Schmidt	$Sc_*$	1.15

**Table 4.8.:** Dimensionless numbers for one representative fiber (cf. Fig. 4.5) in the uni-axial industrial dry spinning setup assuming the airflow without fibers (first step in the fiber-airflow coupling). Note that some dimensionless numbers might vary during the simulation due to the fiber-airflow interaction (cf. Tab. 4.1 and Tab. 4.3).

## Results

For the numerical treatment of the fiber dynamics we use the same mesh parameters and tolerances as in Sec. 4.3. The solver for the airflow meets an accuracy of  $\mathcal{O}(10^{-6})$ . The break-up criterion of the fiber-air coupling algorithm satisfies an error tolerance  $tol = 10^{-5}$ . For the considered industrial setup the fiber-air coupling algorithm converges after 30 iteration steps. The computation time for the presented setup is around six hours.

Since the solutions of the sixty fibers do not show visible differences, we illustrate – as an example – the solution behavior for the fiber that is centrally located in the spinning duct (cf. Fig. 4.5) in Fig. 4.6. The cross-sectionally averaged CA mass fraction increases from  $c_0 = 0.29$  at the inlet to  $\bar{c} = 0.90$  at the outlet, indicating the evaporation of the acetone during the spinning process. The airflow directed contrary to the spinning direction of the fibers induces drag forces that act contrary to the fiber moving direction. Therefore, the spatial point where the fiber speed  $u$  reaches the take up speed ( $u_{out} = 10$  m/s) is shifted from the center of the spinning device towards the nozzle, i.e.,  $u(s) = u_{out}$  for  $s \geq 1$  m approximately. The tensile stress  $N$  increases correspondingly to the changes of  $u$  and the viscosity  $\langle \mu \rangle_A$ . Directly at the nozzle the fiber temperature drops down

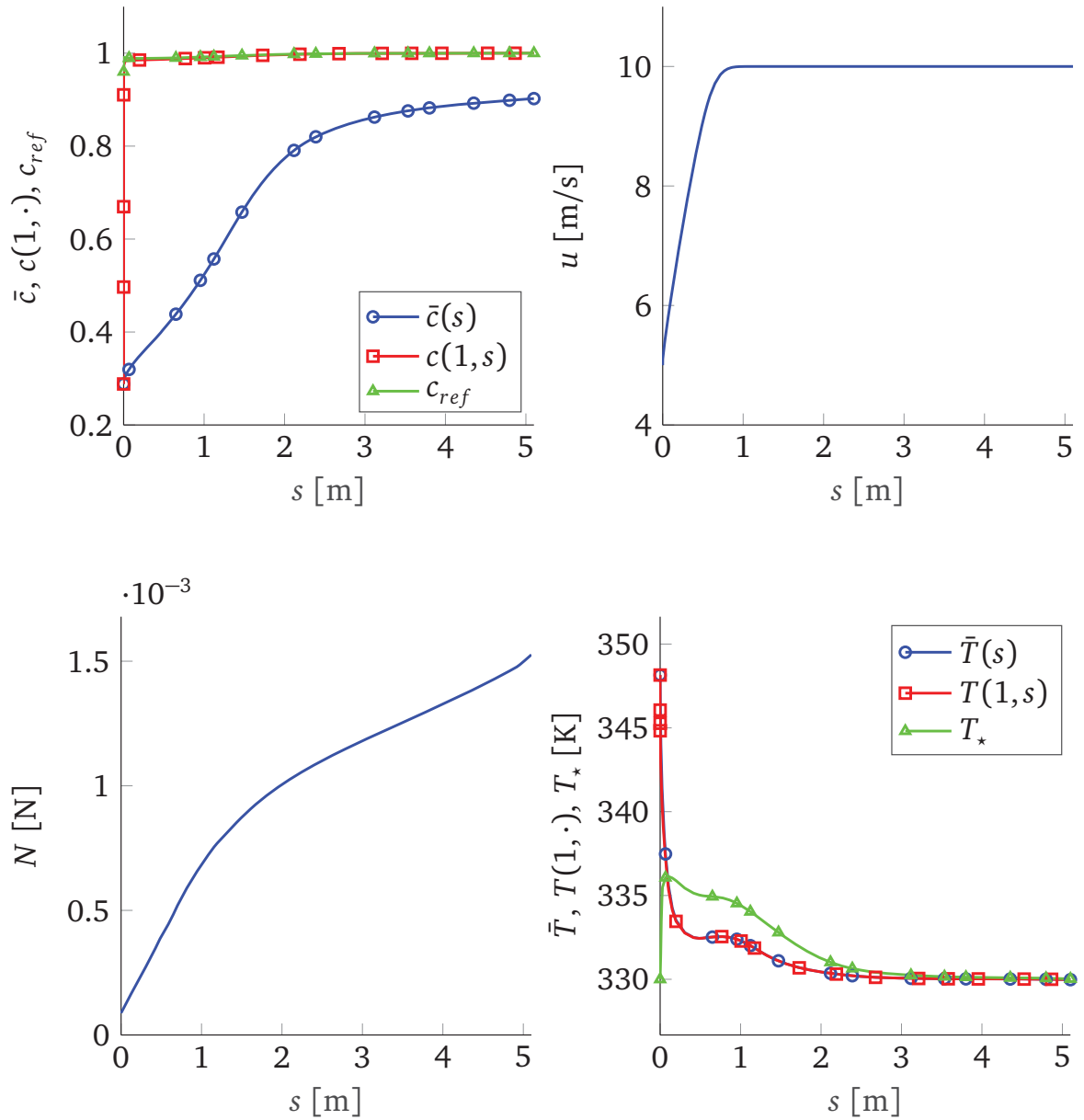


**Figure 4.6.:** Solution quantities of a centrally located fiber (cf. Fig. 4.5). *Top-left:* Polymer (CA) mass fraction (averaged  $\bar{c}$ , at the fiber boundary  $c|_{r=1}$  and referential  $c_{ref}$ ). *Top-right:* Scalar fiber speed  $u$ . *Bottom-left:* Tensile stress  $N$ . *Bottom-right:* Temperature (averaged  $\bar{T}$ , at the fiber boundary  $T|_{r=1}$ , air  $T_*$ ).

due to the immediate set in of the acetone mass transfer caused by evaporation, which is indicated by the rapid rise of the CA mass fraction at the fiber boundary. In a distance sufficiently far away from the nozzle the temperature approaches the temperature of the surrounding air  $T_*$ . The fiber radius decreases from its initial value  $R_0 = 3.14 \cdot 10^{-5}$  m to  $R = 1.06 \cdot 10^{-5}$  m at the fiber end (cf. Fig. 4.7). On the one hand, this fiber thinning is caused by the take up of the fiber at the bottom of the spinning device with a drawing speed that is higher than the initial fiber speed,

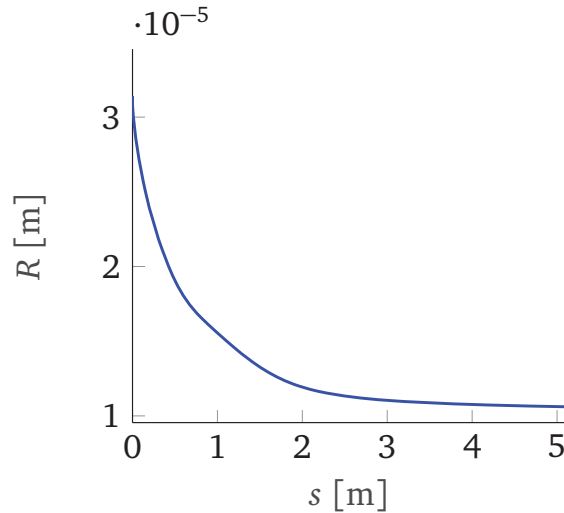


**Figure 4.7.:** Resulting fiber radius  $R$  for the solution quantities in Fig. 4.6.

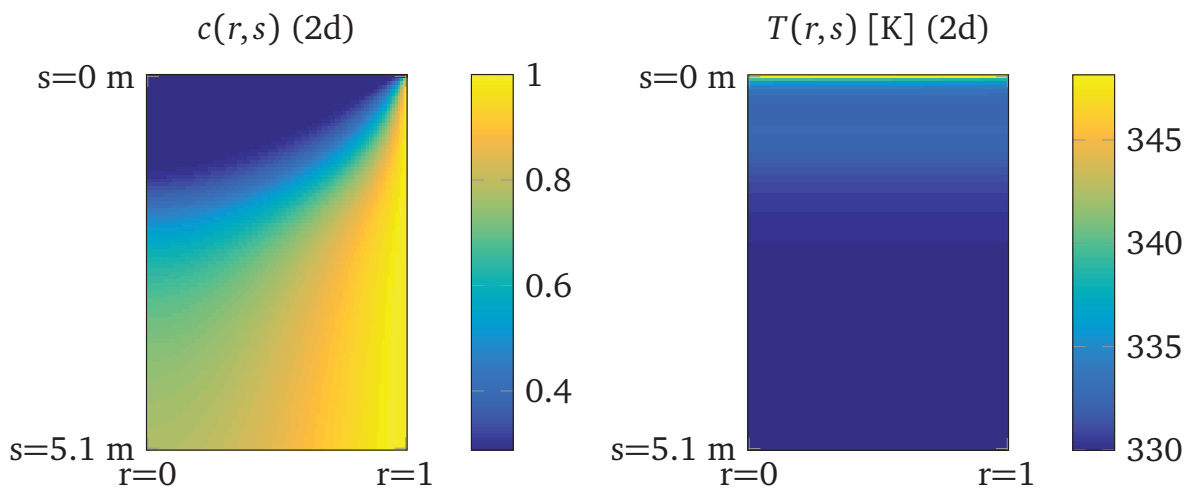


**Figure 4.8.:** Polymer mass fraction and temperature profiles of fiber solution (cf. Figs. 4.5 and 4.6).

i.e.,  $u_{out} > u_{in}$ . On the other hand, the mass transfer due to acetone evaporation gives rise to further fiber thinning, in particular in the region of the spinning duct where the fiber speed has already reached the take up speed ( $s \geq 1$  m). Worth to investigate is the profile for the polymer mass fraction in Fig. 4.8 that indicates an inhomogeneous CA-acetone distribution in radial direction. While the fiber surface is nearly diluent-free and thus completely dried out shortly away from the nozzle, the innermost part of the fiber contains much more diluent over its complete length and is not completely dried at the bottom of the spinning duct. In contrast there are no visible radial effects in the temperature (cf. Fig. 4.8). This is due to the fact that the inverse of the temperature associated Peclet number  $1/Pe_T$  is three magnitudes larger compared to the mass associated one  $1/Pe_c$

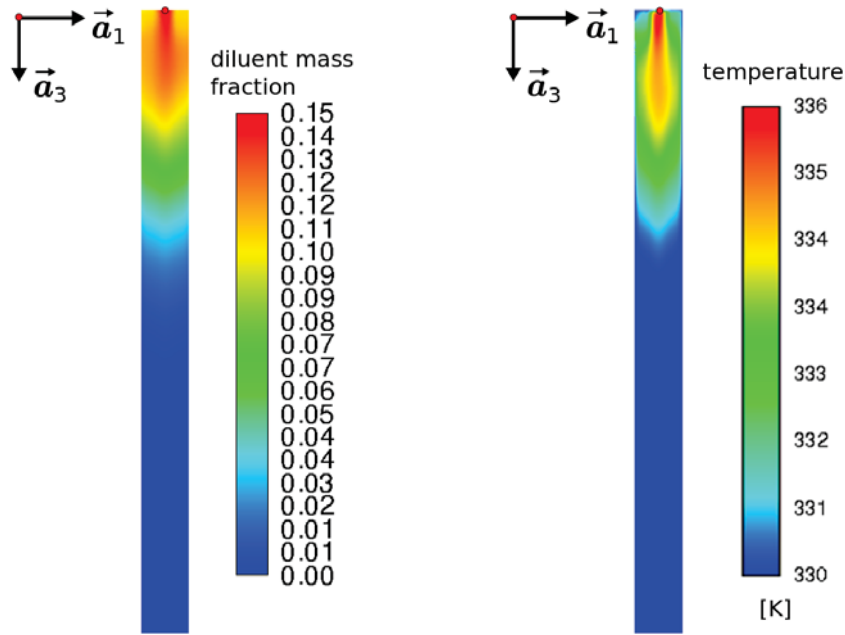


**Figure 4.9.:** Mass fraction of diluent acetone (*left*) and temperature (*right*) in the spinning duct (after convergence of the fiber-air coupling algorithm).

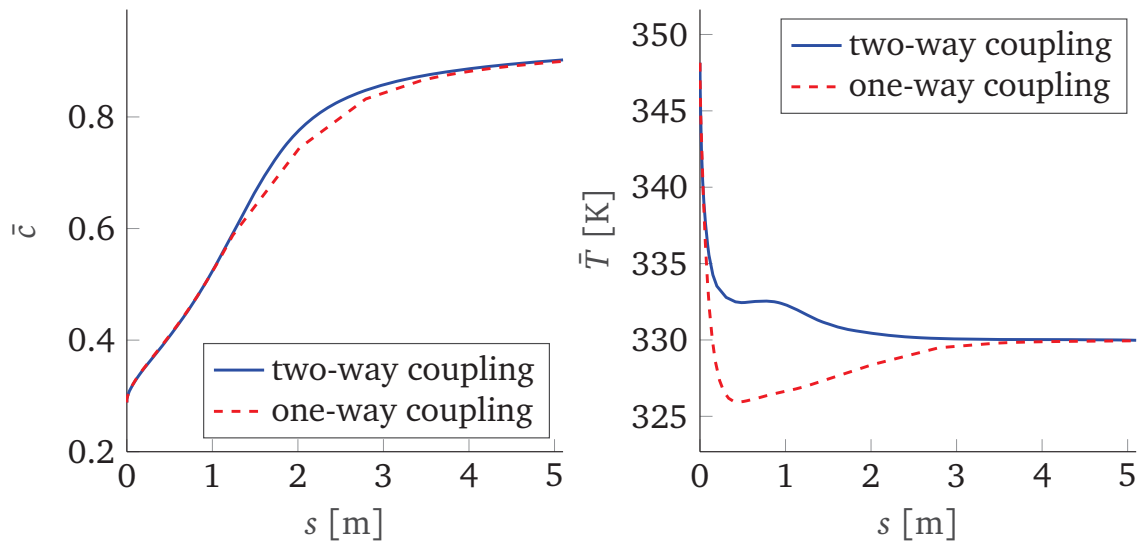


**Figure 4.10.:** Averaged CA mass fraction (*left*) and temperature (*right*) of a centrally located fiber after iteration 1 (one-way coupling) and after iteration 30 (two-way coupling) of the fiber-air coupling algorithm (cf. Fig. 4.5).

(cf. Tab. 4.8) yielding an immediate temperature diffusion in radial direction for sufficiently thin fibers.

The relevance of the effects due to the fiber-air interactions can be clearly seen in Fig. 4.9 and Fig. 4.10. Due to the acetone evaporation the CA mass fraction in the

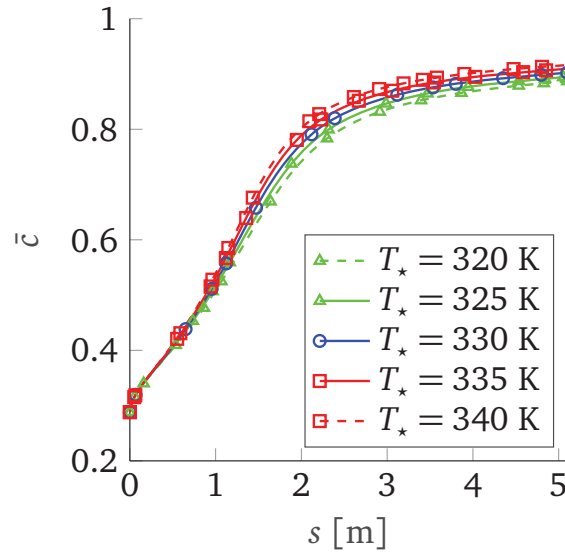


**Figure 4.11.:** Averaged CA mass fraction  $\bar{c}$  for varying air inflow temperature  $T_*$ .

fiber increases to the value  $\bar{c} = 0.90$  at the end  $s = L$  after the first iteration of the fiber-air coupling algorithm (one-way coupling). This means a ratio of acetone mass to CA mass of 0.11 at the fiber end, which coincides with the value computed in [88]. During the two-way coupling with the airflow the evaporated acetone increases its proportion in the surrounding air, such that the referential polymer mass fraction decreases from its initial value  $c_{ref} = 1$  to its minimum  $c_{ref} = 0.96$  directly at the nozzle ( $s = 0$  m), see Fig. 4.6. Considering the temperature the influence of the fiber-air coupling becomes even more evident: in the region around the nozzle the fiber heats the surrounding air due to a positive relative temperature  $(T - T_*) > 0$ . In turn this heated air affects the fiber temperature to decrease more slowly. The minimal fiber temperature after the first iteration is  $\bar{T} = 325.94$  K, while after the 30th iteration it is  $\bar{T} = 329.98$  K. Moreover, the air in the upper part of the duct is heated up to  $T_* = 336.19$  K, which corresponds to a temperature increase of 6.19 K compared to its initial value. This effect of increased air temperature in the nozzle region is also observed in [88], where the air temperature is not calculated but measured from experiments. Away from the nozzle evaporation effects become negligible and the temperature in the spinning duct is not influenced significantly by the fiber temperature anymore. Vice versa the fiber is cooled down and reaches the air temperature in this region of the spinning duct. The temperature curve for our considered fiber after the first iteration (one-way coupling) is qualitatively in good agreement with the temperature curve given in [88], although our simulation shows a less drastic temperature drop at the nozzle. This difference might be due to varying rheological models.

The airflow in the considered dry spinning setup is characterized by the air inflow speed  $\|\mathbf{v}_*\|$  at the bottom of the device and its inflow temperature  $T_*$ . Whereas the inflow speed has a negligible effect on the acetone evaporation since the fiber surface is immediately dried shortly after the nozzle, the air temperature affects the evaporation of the solvent significantly, see Fig. 4.11. The higher the air temperature  $T_*$  is the more acetone evaporates out of the fiber and leads to a higher averaged CA mass fraction  $\bar{c}$  remaining in the fiber, e.g.,  $T_* = 320$  K yields  $\bar{c} = 0.89$ ,  $T_* = 340$  K even  $\bar{c} = 0.92$  at the fiber end.

### 4.4.3. Spinning of curved fibers

Now, we examine an industrial dry spinning setup where our curved fiber model (System 4.11) has to be employed. Again we consider a cellulose acetate (CA)-acetone mixture being dry spun in a spinning duct. In difference to the previous setup (Fig. 4.1 and Sec. 4.4.2) the air streams horizontally through the spinning duct instead of vertically. Thus, the fibers are exposed to a mainly perpendicular airflow. This leads to lateral movements of the fibers such that an uni-axial fiber model is not sufficient to describe this flow situation. Hence, we employ our curved fiber model here. In the following we specify the process setup and present simulation results for the curved fibers with two-way coupled airflow.

#### Process setup

We consider a spinning duct with the airflow situation as depicted in Fig. 4.2. The device geometry is adapted from an actual industrial dry spinning device. To show the capability of our numerical framework we let 500 fibers being spun simultaneously from the holes of a spinneret into the spinning duct instead of 60 in the uni-axial setup (cf. Sec. 4.4.2). These holes are ordered in five parallel rows with 100 holes each, as sketched in Fig. 4.12. We consider the fibers to be injected from the plane  $\{\mathbf{x} \in \mathbb{R}^3 \mid x_3 = 0\}$  and the middle row additionally to lie in  $x_2 = 0$ . At the bottom of the device all fibers are taken up by a roller. As in Sec. 4.4.2, the air contains no diluent at the inlet, the absolute air inflow velocity (in  $\vec{a}_2$ -direction) is  $\|\mathbf{v}_*\| = 0.22$  m/s and the air inflow temperature is  $T_* = 330$  K. The remaining process parameters are given in Tab. 4.9. Utilizing the setup-specific reference values as given in Tab. 4.6, the resulting dimensionless numbers are given in Tab. 4.10.

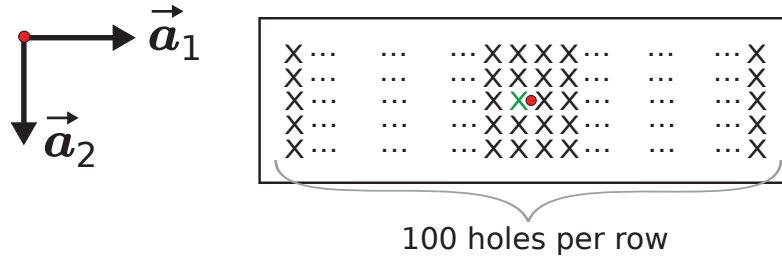


**Figure 4.12.:** Industrial dry spinning setup for curved fibers, sketch of the holes (marked with X) in the spinneret (not in scale). All proceeding simulation results are shown for the fiber extruded from the central position (green X). For the device geometry and the orientation of the outer basis  $\{\vec{a}_1, \vec{a}_2, \vec{a}_3\}$  we refer to Fig. 4.2.

Process Parameters			
Description	Symbol	Value	Unit
Device height	$H$	5.35	m
Nozzle radius	$R_{in}$	$1 \cdot 10^{-4}$	m
Speed at nozzle	$u_{in}$	5	m/s
Take up speed at bottom	$u_{out}$	10	m/s
Polym. mass fract. at nozzle	$c_{in}$	0.29	–
Temperature at nozzle	$T_{in}$	350	K
Curvature at nozzle	$\kappa_{in}$	<b>0</b>	1/m
Curvature at bottom	$\kappa_{out}$	<b>0</b>	1/m
Direction at nozzle	$\mathbf{q}_{in}$	(1,0,0,0)	–
Total number of fibers	$M$	500	–
Heat transfer at nozzle	$\alpha_{in}$	$3.86 \cdot 10^2$	W/(m <sup>2</sup> K)
Mass transfer at nozzle	$\gamma_{in}$	$8.88 \cdot 10^{-1}$	kg/(m <sup>2</sup> s)
Air pressure at nozzle	$p_{*,in}$	$1.01 \cdot 10^5$	Pa
Air thermal cond. at nozzle	$\lambda_{*,in}$	$4.22 \cdot 10^{-2}$	W/(m K)
Air kin. viscosity at nozzle	$\nu_{*,in}$	$3.90 \cdot 10^{-5}$	m <sup>2</sup> /s
Air spec. heat cap. at nozzle	$q_{*,in}$	$1.14 \cdot 10^3$	J/(kg K)
Air density at nozzle	$\rho_{*,in}$	1.39	kg/m <sup>3</sup>
Diluent diffusion in air at nozzle	$D_{d,*,in}$	$1.41 \cdot 10^{-5}$	m <sup>2</sup> /s

**Table 4.9.:** Process parameters of the industrial dry spinning setup with horizontal airflow (cf. Fig. 4.2) in the first fiber-airflow coupling step (airflow without fibers). For the inflow positions  $\mathbf{r}_{in}$  as well as the take up position  $\mathbf{r}_{out}$  of the fibers we refer to Fig. 4.2. The physical parameters remain unchanged to Tab. 4.6.

Dimensionless numbers		
Description	Symbol	Value
Slenderness	$\varepsilon$	$3.74 \cdot 10^{-5}$
Reynolds	Re	$2.08 \cdot 10^3$
Froude	Fr	$6.90 \cdot 10^{-1}$
Drawing	Dr	2.00
Mass Peclet	$Pe_c$	$1.31 \cdot 10^7$
Temperature Peclet	$Pe_T$	$8.69 \cdot 10^3$
Mass Stanton	$St_c$	$2.25 \cdot 10^{-4}$
Temperature Stanton	$St_T$	$3.11 \cdot 10^{-5}$
Air drag associated	$A_*$	$3.77 \cdot 10^1$
Air-fiber Reynolds	$Re_*$	$6.85 \cdot 10^1$
Nusselt	$Nu_*$	2.23
Prandtl	$Pr_*$	$7.44 \cdot 10^{-1}$
Sherwood	$Sh_*$	$1.13 \cdot 10^1$
Schmidt	$Sc_*$	1.04

**Table 4.10.:** Dimensionless numbers for one representative fiber (cf. Fig. 4.12) in the curved industrial dry spinning setup (first step in the fiber-airflow coupling). Note that some dimensionless numbers might vary during the simulation due to the fiber-airflow interaction (cf. Tab. 4.2 and Tab. 4.3).

## Results

For the numerical treatment we use the same tolerances as for the simulation of the uni-axial fiber setup (cf. Sec. 4.4.2), i.e., the solver for the airflow meets an accuracy of  $\mathcal{O}(10^{-6})$  and the break-up criterion of the fiber-air coupling algorithm satisfies an error tolerance  $tol = 10^{-5}$ . In contrast to the uni-axial setup the fiber-air coupling algorithm converges after 10 iteration steps (instead of 30 iteration steps). However, due to the higher number of spun fibers (500 instead of 60) and the finer resolution of the spinning duct for the airflow simulation, which is necessary due to the slightly more complex device geometry, the overall computation time for the presented setup is around 50 hours and, therewith, more computationally demanding than the uni-axial case (6 hours).

Since the solutions of the 500 fibers do not show visible differences, we exemplarily illustrate the solution behavior for the fiber that is centrally located in the spinning duct (cf. Fig. 4.12). In Fig. 4.13 we find the solutions for the CA mass fractions ( $\bar{c}$ ,  $c|_{r=1}$ ,  $c_{ref}$ ), the fiber speed ( $u$ ), the temperatures ( $\bar{T}$ ,  $T|_{r=1}$ ,  $T_*$ ) and the fiber radius ( $R$ ). All these quantities behave similar to the uni-axial case, cf. Sec. 4.4.2. The cross-sectionally averaged CA mass fraction increases from  $c_0 = 0.29$  at the inlet to  $\bar{c} = 0.40$  at the outlet, indicating the evaporation of the acetone during the spinning process. The lower averaged CA mass fraction and, therewith, the

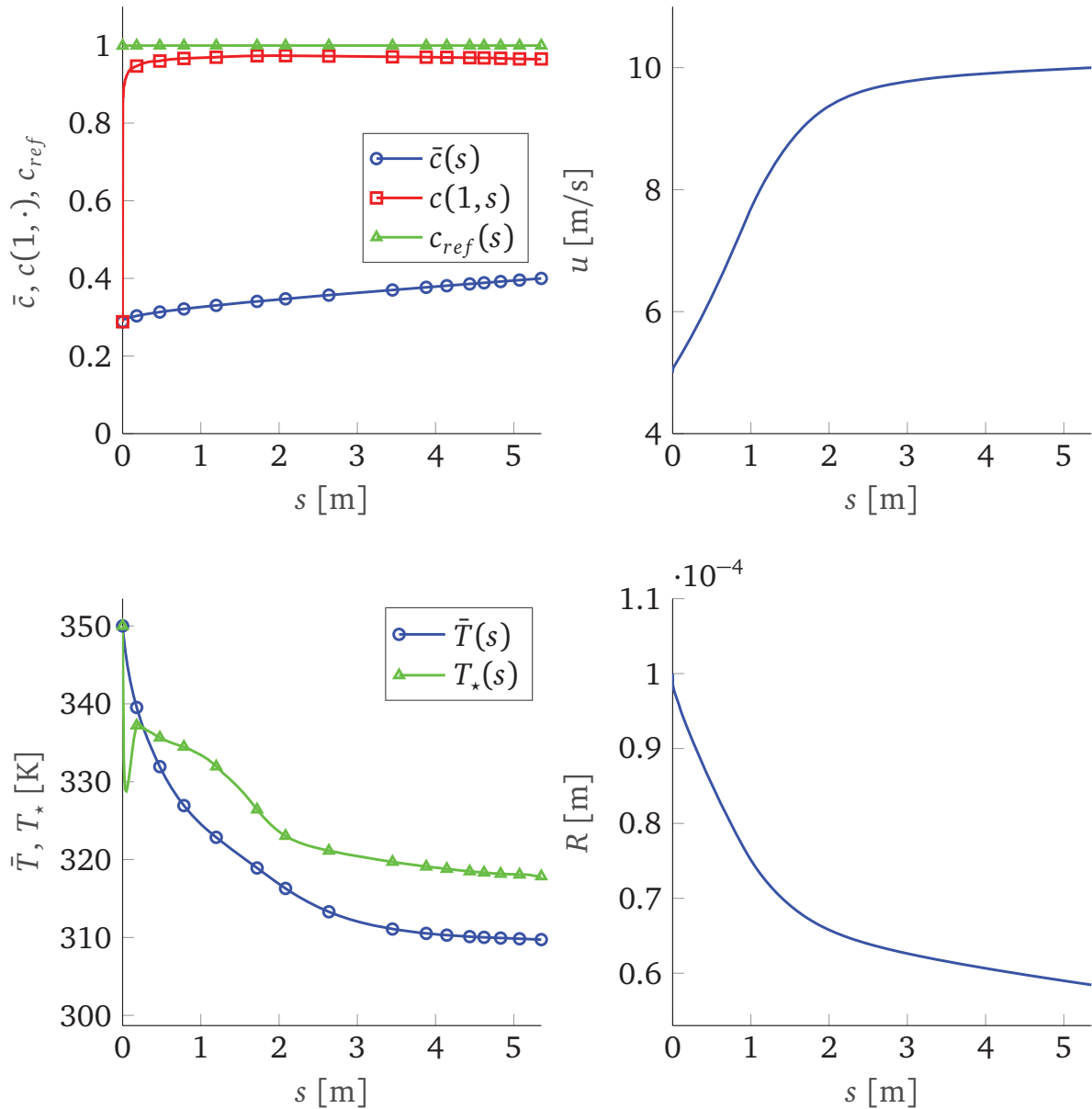


**Figure 4.13.:** Solution quantities of a centrally located fiber (cf. Fig. 4.12). *Top-left:* Polymer (CA) mass fraction (averaged  $\bar{c}$ , at the fiber boundary  $c|_{r=1}$  and referential  $c_{ref}$ ). *Top-right:* Scalar fiber speed  $u$ . *Bottom-left:* Averaged temperature  $\bar{T}$ . *Bottom-right:* Resulting fiber radius  $R$ .

lower evaporation compared to the uni-axial case is owed to the higher thickness of the fiber ( $R_{in} = 10^{-4}$  m instead of  $R_{in} = 3.14 \cdot 10^{-5}$  m in the uni-axial case). As before, the scalar fiber speed  $u$  increases monotonically and reaches the take up speed ( $u_{out} = 10$  m/s) at the device end. As in the uni-axial case the averaged fiber temperature  $\bar{T}$  starts to decrease directly at the nozzle due to the immediate set in of the acetone mass transfer caused by evaporation. Due to the solvent evaporation the fiber reaches the minimal averaged temperature  $\bar{T} = 310$  K which

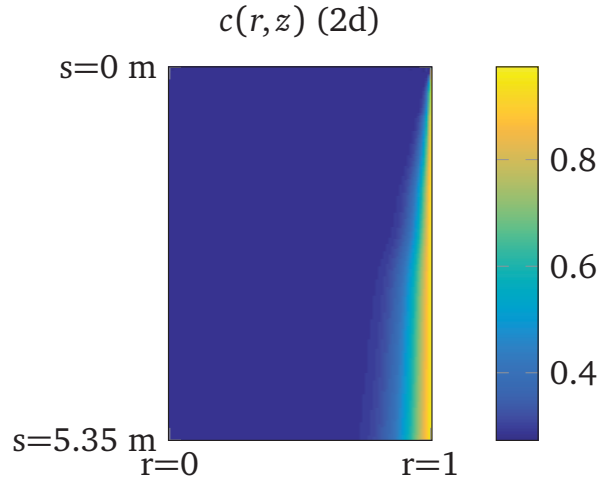


**Figure 4.14.:** Polymer mass fraction of fiber solution (cf. Figs. 4.12 and 4.13).

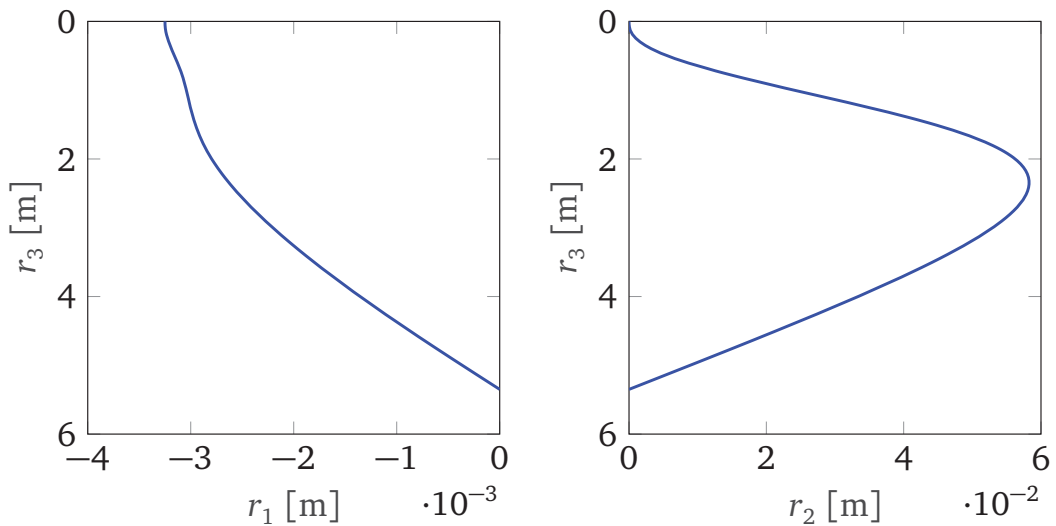


**Figure 4.15.:** Side views of the fiber curve of a centrally located fiber (cf. Fig. 4.12)

is less than the inflow air temperature  $T_* = 330$  K. Also the air temperature  $T_*$  behaves similarly to the uni-axial setup: In the nozzle region the airflow is heated due to the positive relative temperature  $(T - T_*) > 0$  and away from the nozzle the fibers cool the air due to a negative relative temperature  $(T - T_*) < 0$ . Again the fiber thinning is caused by the fiber take up at the bottom of the spinning device as well as by the acetone evaporation. The fiber radius decreases from its initial value  $R_{in} = 10^{-4}$  m to  $R = 5.8 \cdot 10^{-5}$  m at the fiber end. Without acetone evaporation the fixed fiber speed at the take up would lead to the final fiber radius  $R = R_{in}/\sqrt{Dr} = 7.1 \cdot 10^{-5}$  m due to the conservation of mass. Hence, acetone evaporation yields a further reduction of the fiber radius by the factor 1.22. Since the fiber is not completely dried out at its end (but only at its surface), an extension of the spinning device in  $\vec{a}_3$ -direction and, thus, an increased fiber length  $L$  would

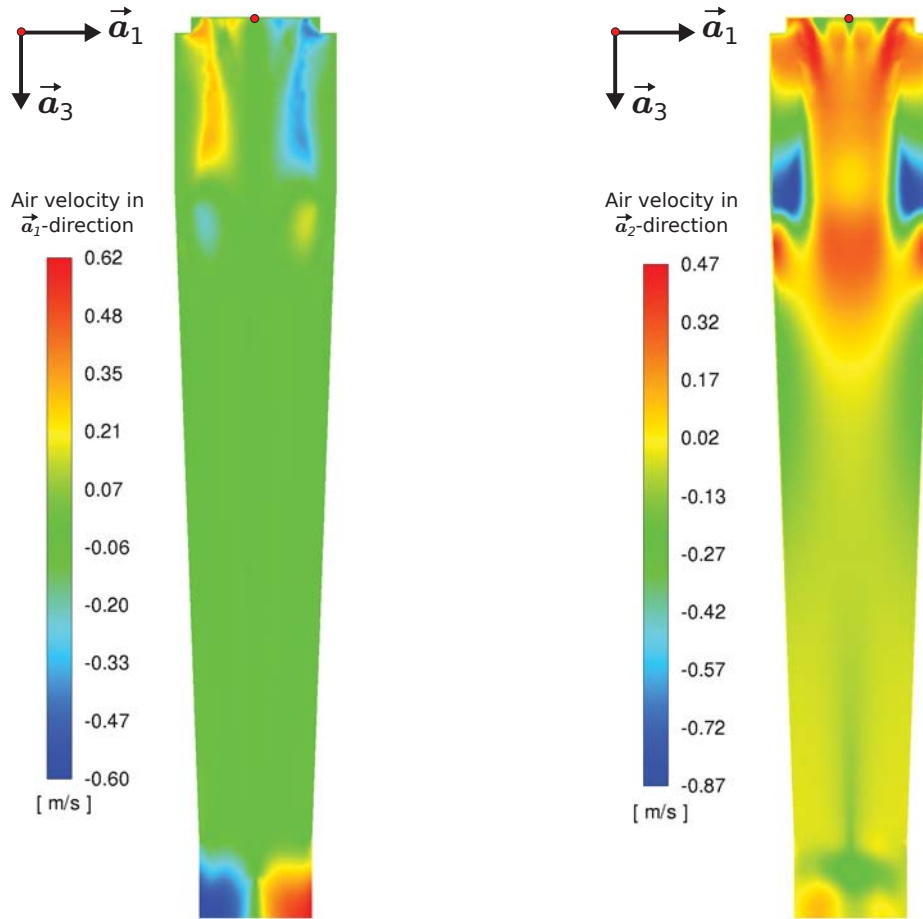


**Figure 4.16.:** Airflow velocity  $\mathbf{v}_*$  in the spinning duct (cf. Fig. 4.2) visualized in the plane  $\{\mathbf{x} \in \mathbb{R}^3 \mid x_2 = 0\}$ . *Left:* Airflow velocity in  $\vec{a}_1$ -direction. *Right:* Airflow velocity in  $\vec{a}_2$ -direction.

lead to more acetone evaporation and, therefore, a further thinning of the fiber. Worth to investigate is the profile for the polymer mass fraction in Fig. 4.14 that indicates an inhomogeneous CA-acetone distribution in radial direction. While the fiber surface is nearly completely dried shortly away from the nozzle, the innermost part of the fiber contains the initial proportion of diluent over its complete length. As in the uni-axial fiber case there are no visible radial effects in the temperature due to the fact that the inverse temperature associated Peclet number  $1/Pe_T$  is four magnitudes larger compared to the mass associated one  $1/Pe_c$  (cf. Tab. 4.10) yielding a homogeneous behavior of the fiber temperature  $T$  in radial direction due to immediate heat diffusion. Hence, we omit the visualization of the fiber temperature at the boundary and the radial temperature profile.

Fig. 4.15 shows the curve for the central fiber and Fig. 4.16 visualizes the airflow velocity in the spinning duct in  $\vec{a}_1$ - and  $\vec{a}_2$ -direction. In  $\vec{a}_1$ -direction the lateral fiber movement is mainly due to the take up of the fiber at the central position at

the bottom ( $x_1 = x_2 = 0$ ). Since the airflow velocity in  $\vec{a}_1$ -direction is approximately zero in the region where the fibers are spun, the airflow does not cause a significant fiber deflection in this direction. However, the fiber shows a strong lateral movement in  $\vec{a}_2$ -direction. This is due to the airflow in  $\vec{a}_2$ -direction that causes tangential forces on the fiber in the upper part of the spinning duct leading to its lateral movement in this direction. The maximal deflection of the fiber in  $\vec{a}_2$ -direction is  $5.8 \cdot 10^{-2}$  m.

Summing up, concerning one-way coupled uni-axial fibers in air we achieve comparable results to [88]. This justifies the transfer of our fiber model from academic axis-symmetric settings to real industrial setups. Moreover, our proposed model-simulation framework makes the simulation of industrial dry spinning processes with multiple simultaneously spun, uni-axial and curved fibers feasible. Radial heat and mass transfer effects as well as mutual fiber-airflow interactions, that are both key players in industrial setups, are efficiently included in the simulations.



## 5. Electrified visco-capillary jets in airflows

In this chapter we examine spinning processes where an electrified jet is injected into an outer electric field. A typical example are electrospinning processes, at which we focus in this chapter. As schematized in Fig. 5.1, electrospinning devices essentially consist of a high-voltage power supply, a metallic nozzle (spinneret) and a grounded collector that acts as counter-electrode. Through the metallic nozzle a conducting material (usually some sort of molten polymer) is fed at a constant rate into the electric field between nozzle and collector. This electric field induces an electric current in the spun jet, which accumulates the electric charge at its surface. This surface charge causes an electric force on the jet that elongates it in the direction of the field. Such interaction of an electric field with the interface between a conducting liquid and a dielectric medium was already reported by Gilbert in 1600 [39] and utilized for the production of micro- and nanostructures in several technological fields [56, 61]. Depending on the electric field one observes different jet behaviors during electrospinning: For low field strength the electrostatic and surface tension forces balance directly at the nozzle and no jet evolves. In this case the drop at the nozzle forms a cone, which is known as Taylor cone [100]. When the electric field strength overcomes a certain threshold the electric forces lead to the ejection of an electrified jet from the cone tip. Depending on the applied voltage and polymer flow rate the jet is dominated either by the so called varicose instability or the bending (whipping) instability. In the first one the jet forms a straight line and breaks into droplets at some distance from the nozzle. This phenomena builds the basis for the electrospray technique [32, 24] with application in, e.g., fine coatings, synthesis of powders, as well as micro- and nanocapsules. In contrast, the jet curve is characterized by fast and violent deflections in the so called bending or whipping instability. Its occurrence can be explained as follows: If a small part of the charged and initially uni-axial jet moves slightly off its axis, the charge distributed along the rest of the jet pushes that part further away from the axis according to Earnshaw's theorem leading to a lateral instability. For sufficiently high values of the applied voltage or the polymer viscosity the jet does not break up and this whipping mode becomes dominating, see Fig. 5.1. This lateral jet movement gives rise to a drastic jet thinning – reduction of jet diameter by several orders

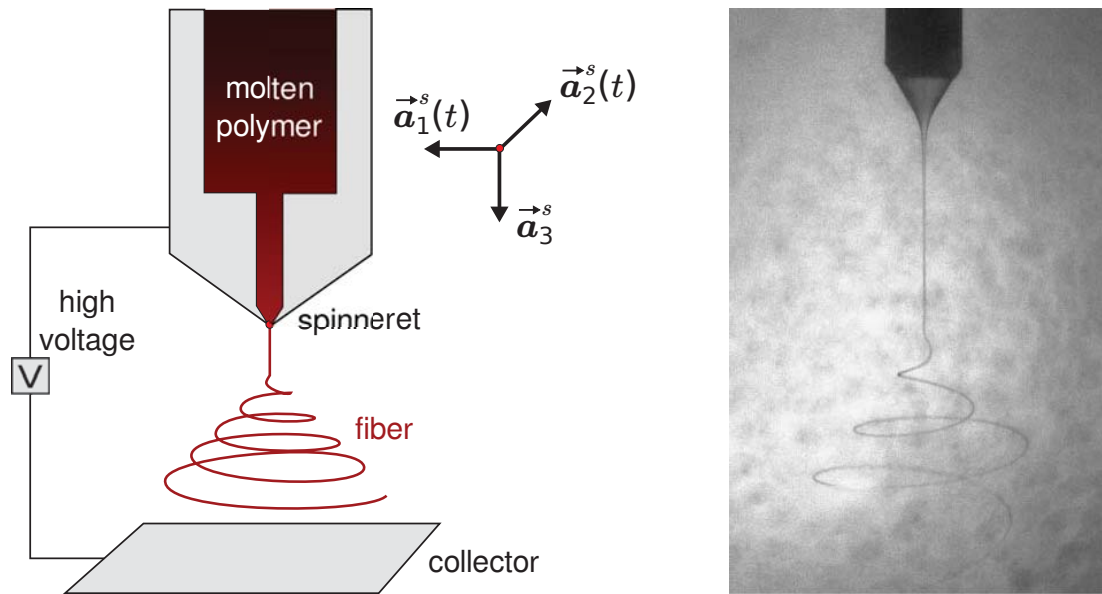


**Figure 5.1.:** *Left:* Sketch of a typical electrospinning device. *Right:* Whipping instability in an electrified jet of glycerine in a bath of hexane (courtesy of A. Gomez-Marin).

of magnitude – and, hence, is of fundamental importance for electrospinning processes [27, 48, 57, 80, 92, 120]. Another mode, the so-called coiling mode [53], is observed when the ground electrode is located sufficiently close to the nozzle so that the jet reaches the collector before being set into whipping motion. The situation is similar to a thin stream of viscous fluid (such as honey) being poured onto a surface from a certain height [81, 82, 83].

In the last decades intensive work has been spent on experimental studies of electrospinning, whose complexity makes empirical determinations of the effects of the parameters very difficult [57, 92]. The trend-setting papers [31, 47, 80] developed theoretical models to predict the behavior of the charged jet. These models use balance equations based on slender-body descriptions for the jet and include the electric field and surface tension. They differ in the constitutive laws, such as models for viscous (Newtonian) and viscoelastic (upper convected Maxwell) jet behavior. Even effects such as evaporation and solidification can be taken into account [120]. Studies [103] show that the final jet radius is mainly determined by the volume charge density, the distance from the nozzle to the collector, the nozzle radius, the relaxation time and the viscosity. The external field and the mutual electric interaction of multiple charged jets influence the jet path and evolution [101]. The whipping instability, which causes jet thinning, has been documented and analyzed in [80, 120] by applying perturbation frequencies. In addition to a linear stability analysis, operating diagrams for different polymer solvents have been developed in [47, 48]. The whipping instability has also been

---

explored via temporal stability analysis in [58, 59]. Numerical simulations can be found in [124, 126]. However, it must be stressed that the nature of the whipping regime makes it very difficult to resolve its detailed structure. Recent experiments show that special setups enlarge the parametric range for which the bending leads to a stable steady-state helicoidal structure with a constant opening angle. This is for example the case, when the conducting jet is spun into a dielectric bath [84] or is surrounded by another coflowing liquid [44]. The liquid bath decreases the frequency of the jet oscillations by several orders of magnitude in comparison to those found in typical electrospinning experiments in air [48, 79], see Fig. 5.1. In the phenomenological study on a glycerine jet in a hexane bath [84], the whipping instability (frequency, amplitude, wavelength) is characterized in terms of flow rate, applied voltage and electrical conductivity.

The observation of the stable steady-state helical structure motivates our subsequent study. We present a model framework in which the whipping instability can be computed straightforwardly as the stable stationary solution of an asymptotic Cosserat rod description. For this purpose, we formulate the jet's whipping as a stationary process by introducing a frame of reference that rotates with an a priori unknown whipping frequency. The whipping frequency becomes part of the solution. A similar transformation has been used in the investigation of viscous rope coiling [81]. This procedure results in a parametric BVP of ODEs that describes the jet behavior in terms of 19 variables in dependence on the viscosity, surface tension, external electric field, self-repulsion of the induced charges and the resistance of the surrounding fluid. The jet model is a variant of the incompressible viscous rod in Eulerian description (System 2.8). To allow stationary considerations the director and outer bases are modified such that they rotate with the a priori unknown whipping frequency. The models used for the electric and capillary forces are taken from [120]. For the air resistance exerting on the jet we employ the drag model (2.9) presented in Sec. 2.3.

The idea of investigating the whipping instability in electrospinning processes with the help of a stationary viscous Cosserat rod model in a rotating reference frame has been established by J. Rivero-Rodríguez, see [9, 85, 86]. We utilize this idea and, in addition, develop a numerical strategy that makes simulations of industrial relevant parameter settings feasible. We suggest a model-specific continuation strategy and solve the resulting BVP of ODEs numerically by the continuation-collocation method presented in Sec. 3.1. To analyze our framework we carry out a parameter study. Although the model is physically comparatively simple in the electric force model, the numerical results are very convincing. They show qualitatively well the characteristic jet behavior in terms of whipping frequency, elongation and throwing range. The presented model framework is able to give a quantitative explanation for the observed strong jet thinning. Indeed, the analysis of the periodic equilibrium states in combination with a temporal global stability

analysis reveals the helical structure in the whipping instability in more details than has been achieved in previous works. In addition, our framework enables us to derive an analytical solution for the 'longtime' behavior of the jet. The combination of the stationary model consideration in terms of a rotating reference frame with our efficient numerical strategy and our analytical description of the jet's 'longtime' behavior led to the collaborative publication [4].

This chapter is structured as follows. Starting from the Cosserat rod model in invariant description (System 2.2), we derive the stationary model framework for the jet's whipping in Sec. 5.1. In Sec. 5.2 we present the model specific continuation-collocation method for the numerical solution of the parametric BVP. We demonstrate the computational efficiency of the proposed algorithm and show numerical results with respect to parameter studies in Sec. 5.3. In Sec. 5.4 the whipping effect is numerically investigated in detail.

## 5.1. Viscous fiber electrospinning model

In the following we consider an electrified visco-capillary jet with circular-shaped cross-sections surrounded by an airflow. To describe its dynamics we proceed from the invariant Cosserat rod model given in System 2.2. In the whipping regime the electrified visco-capillary jet forms a helical structure, see for example the experiments in [48, 84, 120] and Fig. 5.1. To explore the instability numerically, we follow the idea presented in [9, 85, 86] and formulate the jet's whipping as the stationary solution of the Cosserat rod model. For this purpose we introduce a rotating reference frame and explain the transition to a stationary fiber model. Moreover, we present the capillary and electric force models, which insert capillary effects as well as effects due to the external electric field and Coulomb interaction in our model.

### 5.1.1. Stationary model equations

Aiming at a (Euler-)stationary consideration we consider the invariant rod model System 2.2 (cf. Sec. 2.1.6) in Eulerian (spatial) description on the space-time domain  $\mathcal{D} = (0, L) \times (0, t_{end}]$  and introduce a rotating reference frame: Consider a spun jet of certain – a priori unknown – length  $L$  [m] with stress-free end, which is straight at the nozzle. We assume the external electric field  $\vec{E}$  [V/m] to be constant, i.e.,  $\vec{E} = E\vec{a}_3^s$  with  $E = \Phi/H$  [V/m] and  $\|\vec{a}_3^s\| = 1$ , where  $H$  [m] is the distance between nozzle and counter-electrode (device height) and  $\Phi$  [V] is the applied voltage, see Fig. 5.1 (left) for the device-specific direction  $\vec{a}_3^s$ . Because of the electric field, we have a fixed predominant direction in the device, i.e.,

$\vec{\mathbf{a}}_3^s = \vec{\mathbf{d}}_3(0, t)$  is the jet tangent at the nozzle ( $s = 0$ ) for all times  $t$ . We introduce a time-dependent outer basis  $\{\vec{\mathbf{a}}_1^s(t), \vec{\mathbf{a}}_2^s(t), \vec{\mathbf{a}}_3^s\} \subset \mathbb{E}^3$ ,

$$\partial_t \vec{\mathbf{a}}_i^s = \Omega \vec{\mathbf{a}}_3^s \times \vec{\mathbf{a}}_i^s, \quad i = 1, 2, 3, \quad (5.1a)$$

that rotates with the jet's – a priori unknown – whipping frequency  $\Omega$  [1/s]. In addition, the director triad for the jet is modified in order to get stationary boundary conditions [81]. Since the angular velocity of the director triad  $\{\vec{\mathbf{d}}_1, \vec{\mathbf{d}}_2, \vec{\mathbf{d}}_3\}$  is the sum of the angular velocity of the fluid flow and the additional spin affecting  $\vec{\mathbf{d}}_1$  and  $\vec{\mathbf{d}}_2$  directly at the nozzle, a director triad can only be steady in the rotating frame if it follows the whole rotation of the jet. This is achieved by incorporating the additional spin of magnitude  $\Omega$  into the corresponding kinematic equation, giving

$$\partial_t \vec{\mathbf{d}}_i^s = (\vec{\boldsymbol{\omega}} - u\vec{\boldsymbol{\kappa}} + \Omega \vec{\mathbf{d}}_3^s) \times \vec{\mathbf{d}}_i^s, \quad i = 1, 2, 3. \quad (5.1b)$$

A representation of our model equations in these director and outer bases eliminates the time-dependencies and yields a stationary setup, but it obviously introduces fictitious body forces and couples, such as Coriolis, centrifugal and – in this case additionally – spin-associated ones, due to inertia in the model equations. Again we relate the director and outer bases by the tensor-valued rotation  $\vec{\mathbf{R}}$ , i.e.,  $\vec{\mathbf{R}} = \vec{\mathbf{a}}_i^s \otimes \vec{\mathbf{d}}_i^s$ . Adapting the coordinate terminology introduced in Sec. 2.1.2 we use the following analogous notation in this chapter

$$\vec{\mathbf{z}} = \sum_{i=1}^3 z_i \vec{\mathbf{d}}_i^s = \sum_{i=1}^3 z_i \vec{\mathbf{a}}_i^s \in \mathbb{E}^3$$

with  $\mathbf{z} = (z_1, z_2, z_3) \in \mathbb{R}^3$  and  $\mathbf{z} = (z_1, z_2, z_3) \in \mathbb{R}^3$  where  $\mathbf{z} = \mathbf{R} \cdot \mathbf{z}$  and  $\mathbf{R} = (R_{ij})_{i,j=1,2,3} = (\vec{\mathbf{d}}_i^s \cdot \vec{\mathbf{a}}_j^s)_{i,j=1,2,3} \in SO(3)$ . A similar transformation into a stationary setup has been performed in the investigation of viscous rope coiling [81]. We emphasize that with this approach we do not artificially insert whipping into the problem. Because the whipping frequency belongs to the solution of the problem, it can also be  $\Omega = 0$  in certain parameter settings. However, the ansatz for the rotation is only valid if  $\vec{\mathbf{d}}_3(0, t)$  is aligned with  $\vec{\mathbf{a}}_3^s$  as shown with mathematical arguments in [87]. Considering the derivatives we can state the following rules.

**Lemma 5.1.** *Let the outer basis  $\{\vec{\mathbf{a}}_1^s, \vec{\mathbf{a}}_2^s, \vec{\mathbf{a}}_3^s\} \subset \mathbb{E}^3$  be given by (5.1a) and the modified director triad  $\{\vec{\mathbf{d}}_1^s, \vec{\mathbf{d}}_2^s, \vec{\mathbf{d}}_3^s\} \subset \mathbb{E}^3$  of the jet be defined by (5.1b) with  $\vec{\mathbf{a}}_3^s = \vec{\mathbf{d}}_3^s(0, t) = \vec{\mathbf{d}}_3(0, t)$  for all times  $t$ . Then, for any  $\vec{\mathbf{z}} : \mathcal{D} \rightarrow \mathbb{E}^3$  the following rules for its temporal and spatial derivatives hold*

$$\begin{aligned} \left( \vec{\mathbf{d}}_i^s \cdot \partial_t \vec{\mathbf{z}} \right)_{i=1,2,3} &= \partial_t \mathbf{z} + (\boldsymbol{\omega} - u\boldsymbol{\kappa} + \Omega \mathbf{e}_3) \times \mathbf{z}, & \left( \vec{\mathbf{a}}_i^s \cdot \partial_t \vec{\mathbf{z}} \right)_{i=1,2,3} &= \partial_t \mathbf{z} + \Omega \mathbf{e}_3 \times \mathbf{z}, \\ \left( \vec{\mathbf{d}}_i^s \cdot \partial_s \vec{\mathbf{z}} \right)_{i=1,2,3} &= \partial_s \mathbf{z} + \boldsymbol{\kappa} \times \mathbf{z}, & \left( \vec{\mathbf{a}}_i^s \cdot \partial_s \vec{\mathbf{z}} \right)_{i=1,2,3} &= \partial_s \mathbf{z}. \end{aligned}$$

*Proof.* Let  $\vec{z} : \mathcal{D} \rightarrow \mathbb{E}^3$  be given, then we write for its temporal derivative with respect to the modified director triad

$$\begin{aligned}
 (\vec{d}_i^s \cdot \partial_t \vec{z})_{i=1,2,3} &= (\partial_t (\vec{z} \cdot \vec{d}_i^s))_{i=1,2,3} - (\vec{z} \cdot \partial_t \vec{d}_i^s)_{i=1,2,3} \\
 &= \partial_t \mathbf{z} - (\vec{z} \cdot ((\vec{\omega} - u\vec{\kappa} + \Omega \vec{d}_3^s) \times \vec{d}_i^s))_{i=1,2,3} \\
 &= \partial_t \mathbf{z} + (\vec{d}_i^s \cdot ((\vec{\omega} - u\vec{\kappa} + \Omega \vec{d}_3^s) \times \vec{z}))_{i=1,2,3} \\
 &= \partial_t \mathbf{z} + (\boldsymbol{\omega} - u\boldsymbol{\kappa} + \Omega \mathbf{e}_3) \times \mathbf{z},
 \end{aligned}$$

and with respect to the outer basis

$$\begin{aligned}
 (\vec{a}_i^s \cdot \partial_t \vec{z})_{i=1,2,3} &= (\partial_t (\vec{z} \cdot \vec{a}_i^s))_{i=1,2,3} - (\vec{z} \cdot \partial_t \vec{a}_i^s)_{i=1,2,3} \\
 &= \partial_t \mathbf{z} - (\vec{z} \cdot (\Omega \vec{a}_3^s \times \vec{a}_i^s))_{i=1,2,3} \\
 &= \partial_t \mathbf{z} + (\vec{a}_i^s \cdot (\Omega \vec{a}_3^s \times \vec{z}))_{i=1,2,3} \\
 &= \partial_t \mathbf{z} + \Omega \mathbf{e}_3 \times \mathbf{z},
 \end{aligned}$$

where we used (5.1b) and (5.1a), respectively. The formulation of the spatial derivative of  $\vec{z}$  with respect to the modified director triad follows analogously employing the relation  $\partial_s \vec{d}_i^s = \vec{\kappa} \times \vec{d}_i^s$  (cf. (2.2b) in Sec. 2.1.2). Its formulation with respect to the outer basis is obvious. □

Utilizing these rules we can formulate a temporal kinematic equation for the rotational matrix  $\mathbf{R} \in SO(3)$ .

**Lemma 5.2.** *Under the assumptions of Lemma 5.1 the following kinematic equation for the rotational matrix  $\mathbf{R}$  holds*

$$\partial_t \mathbf{R} = -(\boldsymbol{\omega} - u\boldsymbol{\kappa} + \Omega(\mathbf{e}_3 - \mathbf{R} \cdot \mathbf{e}_3)) \times \mathbf{R}.$$

*Proof.* For any  $\vec{z} \in \mathbb{E}^3$  we calculate using Lemma 5.1

$$\begin{aligned}
 (\partial_t \mathbf{R}) \cdot \mathbf{z} &= (\partial_t \mathbf{R}) \cdot \mathbf{z} + \mathbf{R} \cdot \partial_t \mathbf{z} - \mathbf{R} \cdot (\partial_t \mathbf{z} + \Omega \mathbf{e}_3 \times \mathbf{z}) + \Omega(\mathbf{R} \cdot \mathbf{e}_3) \times \mathbf{z} \\
 &= \partial_t (\mathbf{R} \cdot \mathbf{z}) - \mathbf{R} \cdot (\vec{a}_i^s \cdot \partial_t \vec{z})_{i=1,2,3} + \Omega(\mathbf{R} \cdot \mathbf{e}_3) \times \mathbf{z} \\
 &= \partial_t \mathbf{z} - (\vec{d}_i^s \cdot \partial_t \vec{z})_{i=1,2,3} + \Omega(\mathbf{R} \cdot \mathbf{e}_3) \times \mathbf{z} \\
 &= -(\boldsymbol{\omega} - u\boldsymbol{\kappa} + \Omega \mathbf{e}_3) \times \mathbf{z} + \Omega(\mathbf{R} \cdot \mathbf{e}_3) \times \mathbf{z} \\
 &= -(\boldsymbol{\omega} - u\boldsymbol{\kappa} + \Omega(\mathbf{e}_3 - \mathbf{R} \cdot \mathbf{e}_3)) \times \mathbf{z} \\
 &= -(\boldsymbol{\omega} - u\boldsymbol{\kappa} + \Omega(\mathbf{e}_3 - \mathbf{R} \cdot \mathbf{e}_3)) \times (\mathbf{R} \cdot \mathbf{z}).
 \end{aligned}$$

□

We proceed from System 2.2 and employ the incompressible geometry model (cf. Sec. 2.1.3) as well as the viscous material law including the generalized Kirchhoff constraint (cf. Sec. 2.1.4). Utilizing Lemma 5.1 and Lemma 5.2 the derivation of the model equations in Eulerian description with respect to the modified director triad and the rotating outer basis follows the same concepts as the derivation of System 2.8 in Sec. 2.1.6. Special attention has to be paid to the incompressible geometry model and viscous material law since they have been formulated with respect to the material director basis  $\{\vec{\mathbf{d}}_1, \vec{\mathbf{d}}_2, \vec{\mathbf{d}}_3\}$  in Sec. 2.1.3 and Sec. 2.1.4 respectively. Whereas the space and time derivatives can be written according to Lemma 5.1, the scaling matrix  $\mathbf{P}_x$ ,  $x \in \mathbb{R}$ , has to be formulated with respect to the modified director triad. However, it turns out that this matrix does not change when it is represented in the modified director basis.

**Lemma 5.3.** *Let the modified and material director basis be related by the tensor-valued rotation  $\bar{\mathbf{R}}^d = \vec{\mathbf{d}}_i \otimes \vec{\mathbf{d}}_i^s \in SO(3)$  and let the associated matrix be denoted by  $\mathbf{R}^d = (\vec{\mathbf{d}}_i^s \cdot \vec{\mathbf{d}}_j)_{i,j=1,2,3} \in \mathbb{R}^{3 \times 3}$ . Furthermore, assume  $\mathbf{R}^d(s, 0) = \mathbb{1}$  for all  $s \in [0, L]$ . Then, the scaling matrix  $\mathbf{P}_x = 1/(4\pi)\text{diag}(1, 1, x) \in \mathbb{R}^{3 \times 3}$ ,  $x \in \mathbb{R}$ , is invariant with respect to this basis transformation, i.e.,  $\mathbf{R}^d \cdot \mathbf{P}_x \cdot (\mathbf{R}^d)^T = \mathbf{P}_x$ .*

*Proof.* Utilizing the kinematic equation (5.1b) for the triad  $\{\vec{\mathbf{d}}_1^s, \vec{\mathbf{d}}_2^s, \vec{\mathbf{d}}_3^s\}$  and an analogous argumentation as in the proof of Lemma 5.2 the matrix  $\mathbf{R}^d$  fulfills the following kinematic equation

$$\partial_t \mathbf{R}^d = -\Omega \mathbf{e}_3 \times \mathbf{R}^d = -\Omega \begin{pmatrix} 0 & -1 & 0 \\ 1 & 0 & 0 \\ 0 & 0 & 0 \end{pmatrix} \cdot \mathbf{R}^d.$$

Employing  $\mathbf{R}^d(s, 0) = \mathbb{1}$  this ODE has the space-independent solution  $\mathbf{R}^d = \mathbf{R}^d(t)$  which reads

$$\mathbf{R}^d(t) = \exp \left( -\Omega \begin{pmatrix} 0 & -1 & 0 \\ 1 & 0 & 0 \\ 0 & 0 & 0 \end{pmatrix} t \right) = \begin{pmatrix} \cos(\Omega t) & \sin(\Omega t) & 0 \\ -\sin(\Omega t) & \cos(\Omega t) & 0 \\ 0 & 0 & 1 \end{pmatrix}.$$

A simple calculation shows that

$$\mathbf{R}^d \cdot \mathbf{P}_x \cdot (\mathbf{R}^d)^T = \mathbf{P}_x.$$

□

Bringing together the results of Lemma 5.1, Lemma 5.2, and Lemma 5.3, we can formulate the rod equations with respect to the modified director basis. Moreover, as before, we introduce dimensionless quantities as  $\tilde{y}(\tilde{s}, \tilde{t}) = y(s_0 \tilde{s}, t_0 \tilde{t})/y_0$  for

<b>Composite reference values</b>		
Description	Formula	Unit
Length scale	$s_0 = r_0$	m
Time scale	$t_0 = r_0/v_0$	s
Length	$L_0 = r_0$	m
Cross-sectional radius	$R_0 = d_0$	m
Volume line density	$\varrho_{V,0} = d_0^2$	m <sup>2</sup>
Scalar speed	$u_0 = v_0$	m/s
Curvature	$\kappa_0 = 1/r_0$	1/m
Stress	$n_0 = \varrho_{M,0}v_0^2$	N
Torque	$m_0 = \varrho_{M,0}r_0v_0^2$	N m
Angular velocity	$\omega_0 = v_0/r_0$	1/s
Whipping frequency	$\Omega_0 = \omega_0$	1/s
Outer forces	$f_0 = \varrho_{M,0}v_0^2/r_0$	N/m
Air velocity	$v_{*,0} = v_0$	m/s

<b>Dimensionless numbers</b>	
Description	Formula
Slenderness	$\varepsilon = d_0/r_0$
Reynolds	$\text{Re} = \varrho_{M,0}v_0r_0/(d_0^2\mu_0)$
Capillary associated	$\Gamma = d_0\gamma_0/(\varrho_{M,0}v_0^2)$
Potential associated	$\Xi = I_0\Phi_0/(\varrho_{M,0}v_0^3)$
Coulomb repulsion associated	$\Theta = I_0/(\epsilon_{p,*,0}v_0\Phi_0)$
Conduction associated	$\Lambda = d_0\lambda_0\Phi_0/I_0$
Air drag associated	$\Lambda_* = \rho_{*,0}d_0v_0^2/f_0$
Air-fiber Reynolds	$\text{Re}_* = d_0v_0/v_{*,0}$

**Table 5.1.:** Overview over composite reference values used for nondimensionalization and the resulting dimensionless numbers. The following scales are assumed to be given from the specific considered setup  $\mu_0, \gamma_0, \lambda_0, I_0, \Phi_0, \rho_{*,0}, v_{*,0}, \epsilon_{p,*,0}$ . Moreover, we fix  $r_0 = H, \varrho_{M,0} = \rho d_0^2, d_0 = d_{in}\sqrt{\pi}/2, v_0 = v_{in}$ .

any scalar or vector valued quantity  $y$ . The corresponding reference values  $y_0$  are given in Tab. 5.1. Since the fiber length  $L$  is a priori unknown we transform all equations onto the space domain  $(0, 1)$  as done for the dry spinning model (see scaling concept (4.8) in Sec. 4.1). As consequence we do not face a free BVP anymore, but insert the unknown parameter  $L$  into the model equations. For simplicity we suppress the label  $\tilde{\cdot}$  in the following. The meaning of each quantity (dimensional or nondimensional) will be clear from the context. This also means we use the symbols  $L$  and  $\Omega$  for the dimensionless unknowns. The resulting model reads in nondimensional form as follows.

**System 5.4** (Viscous fiber electrospinning model).

Kinematic and dynamic equations as well as material laws,  $s \in (0, 1)$ ,  $t \in (0, t_{end}]$ :

$$\begin{aligned}
 \partial_t \mathbf{r} &= \mathbf{R}^T \cdot (\mathbf{v} - u \mathbf{e}_3 \\
 &\quad - (\boldsymbol{\omega} - u \boldsymbol{\kappa} + \Omega \mathbf{e}_3) \times (\mathbf{R} \cdot \mathbf{r})), \\
 L^{-1} \partial_s \mathbf{r} &= \mathbf{R}^T \cdot \mathbf{e}_3, \\
 \partial_t \mathbf{R} &= -(\boldsymbol{\omega} - u \boldsymbol{\kappa} + \Omega (\mathbf{e}_3 - \mathbf{R} \cdot \mathbf{e}_3)) \times \mathbf{R}, \\
 L^{-1} \partial_s \mathbf{R} &= -\boldsymbol{\kappa} \times \mathbf{R}, \\
 \partial_t \varrho_M + L^{-1} \partial_s (u \varrho_M) &= 0, \\
 \partial_t \varrho_V + L^{-1} \partial_s (u \varrho_V) &= 0, \\
 \partial_t (\varrho_M \mathbf{v}) + L^{-1} \partial_s (u \varrho_M \mathbf{v}) &= \varrho_M \mathbf{v} \times (\boldsymbol{\omega} + \Omega \mathbf{e}_3) + L^{-1} \partial_s \mathbf{n} \\
 &\quad + \boldsymbol{\kappa} \times \mathbf{n} + \mathbf{f}, \\
 \partial_t (\varrho_M \varrho_V \mathbf{P}_2 \cdot \boldsymbol{\omega}) + L^{-1} \partial_s (u \varrho_M \varrho_V \mathbf{P}_2 \cdot \boldsymbol{\omega}) &= (\varrho_M \varrho_V \mathbf{P}_2 \cdot \boldsymbol{\omega}) \times (\boldsymbol{\omega} + \Omega \mathbf{e}_3) \\
 &\quad + \frac{1}{\varepsilon^2} (L^{-1} \partial_s \mathbf{m} + \boldsymbol{\kappa} \times \mathbf{m} + \mathbf{e}_3 \times \mathbf{n}), \\
 L^{-1} \partial_s u &= \frac{\text{Re}}{3} \frac{1}{\mu \varrho_V} n_3, \\
 \partial_t \boldsymbol{\kappa} + L^{-1} \partial_s (u \boldsymbol{\kappa}) &= \frac{\text{Re}}{3 \varepsilon^2} \frac{1}{\mu \varrho_V^2} \mathbf{P}_{2/3}^{-1} \cdot \mathbf{m} + \Omega \boldsymbol{\kappa} \times \mathbf{e}_3.
 \end{aligned}$$

Basically, this model equals the Eulerian rod model given in System 2.8 with additional terms due to the additional spin in the modified director triad  $\{\vec{\mathbf{d}}_1^s, \vec{\mathbf{d}}_2^s, \vec{\mathbf{d}}_3^s\}$ . Transition to stationarity in System 5.4 leads to explicit expressions for the linear velocity  $\mathbf{v}$  and angular velocity  $\boldsymbol{\omega}$

$$\mathbf{v} = u \mathbf{e}_3 + \Omega \mathbf{R} \cdot (\mathbf{e}_3 \times \mathbf{r}), \quad \boldsymbol{\omega} = u \boldsymbol{\kappa} + \Omega (\mathbf{R} \cdot \mathbf{e}_3 - \mathbf{e}_3). \quad (5.2)$$

Moreover, considering the mass and volume balances the corresponding flow rates become constant, i.e.,  $Q_M = u \varrho_M = \text{const}$  and  $Q_V = u \varrho_V = \text{const}$ . The particular choice of the reference values (cf. Tab. 5.1) leads to  $Q_M = Q_V = 1$ , such that  $\varrho_M$  and  $\varrho_V$  can be replaced by  $1/u$ . In addition, due to (5.2) the linear and angular velocities can be expressed in terms of the other variables.

For the spun jet that leaves the nozzle vertically and straight-lined we pose the following geometric and kinematic boundary conditions at the nozzle ( $s = 0$ ) as well as stress-free conditions at the end ( $s = 1$ )

$$\mathbf{r}(0) = \mathbf{0}, \quad \mathbf{R}(0) = \mathbb{1}, \quad \boldsymbol{\kappa}(0) = \mathbf{0}, \quad u(0) = 1, \quad \mathbf{n}(1) = \mathbf{0}, \quad \mathbf{m}(1) = \mathbf{0},$$

with  $\mathbb{1} \in \mathbb{R}^{3 \times 3}$  the identity matrix. To determine the further two unknowns of the problem that are the jet length  $L$  and the whipping frequency  $\Omega$ , we impose two

additional geometric conditions on the end point of the curve. We prescribe its phase and its height in the device geometry

$$r_1(1) = 0, \quad r_3(1) = 1,$$

which means fixing the jet end at the counter-electrode. In spite of the posed condition on the phase, the choice of the outer basis  $\{\vec{\mathbf{a}}_1^s(t), \vec{\mathbf{a}}_2^s(t), \vec{\mathbf{a}}_3^s\} \subset \mathbb{E}^3$  still leaves one further degree of freedom, e.g., the sign of  $r_2(1)$ . Moreover, the sign of  $\Omega$  is free. Thus, four stationary solutions are similarly possible in this model framework:  $\Omega \geq 0$  or  $\Omega \leq 0$  as well as  $r_2(1) \geq 0$  or  $r_2(1) \leq 0$ . The form of the solutions is invariant, the resulting jets only differ in the rotational direction of the whipping and in the position of the end point with respect to the  $\vec{\mathbf{a}}_2^s$ -half-space. We aim for the case:  $\Omega \geq 0$  and  $r_2(1) \geq 0$ . This implies a positive rotation in the outer frame, a positive Rossby number that characterize the relation between the inertial and rotational forces as well as an end point in the positive  $\vec{\mathbf{a}}_2^s$ -half-space.

In total, the nondimensional stationary model for the jet's whipping regime is given by

**System 5.5** (Stationary viscous fiber electrospinning model).

*Kinematic and dynamic equations as well as material laws,  $s \in (0, 1)$ :*

$$\begin{aligned} L^{-1} \partial_s \mathbf{r} &= \mathbf{R}(\mathbf{q})^T \cdot \mathbf{e}_3, \\ L^{-1} \partial_s \mathbf{q} &= \mathbf{S}(\boldsymbol{\kappa}) \cdot \mathbf{q}, \\ L^{-1} \partial_s \mathbf{n} &= \mathbf{n} \times \boldsymbol{\kappa} + L^{-1}(\partial_s u) \mathbf{e}_3 + u \boldsymbol{\kappa} \times \mathbf{e}_3 + 2\Omega(\mathbf{R}(\mathbf{q}) \cdot \mathbf{e}_3) \times \mathbf{e}_3 \\ &\quad + \frac{\Omega^2}{u} \mathbf{R}(\mathbf{q}) \cdot (\mathbf{e}_3 \times (\mathbf{e}_3 \times \mathbf{r})) - \mathbf{f}, \\ L^{-1} \partial_s \mathbf{m} &= \mathbf{m} \times \boldsymbol{\kappa} + \mathbf{n} \times \mathbf{e}_3 + \varepsilon^2 \frac{1}{u} \mathbf{P}_2 \cdot (L^{-1} \partial_s (u \boldsymbol{\kappa}) - L^{-1}(\partial_s u) \boldsymbol{\kappa} - \Omega \boldsymbol{\kappa} \times \mathbf{e}_3) \\ &\quad - \varepsilon^2 \frac{\Omega}{u^2} \mathbf{P}_2 \cdot (L^{-1} \partial_s u (\mathbf{R}(\mathbf{q}) \cdot \mathbf{e}_3 - \mathbf{e}_3) + (u \boldsymbol{\kappa} - \Omega \mathbf{e}_3) \times (\mathbf{R}(\mathbf{q}) \cdot \mathbf{e}_3)) \\ &\quad - \varepsilon^2 \frac{1}{u^2} (\mathbf{P}_2 \cdot (u \boldsymbol{\kappa} + \Omega(\mathbf{R}(\mathbf{q}) \cdot \mathbf{e}_3 - \mathbf{e}_3))) \times (u \boldsymbol{\kappa} + \Omega(\mathbf{R}(\mathbf{q}) \cdot \mathbf{e}_3 - \mathbf{e}_3)), \\ L^{-1} \partial_s u &= \frac{\text{Re } 1}{3} \frac{1}{\mu} u n_3, \\ L^{-1} \partial_s (u \boldsymbol{\kappa}) &= \frac{\text{Re } u^2}{3 \varepsilon^2} \frac{1}{\mu} \mathbf{P}_{2/3}^{-1} \cdot \mathbf{m} + \Omega \boldsymbol{\kappa} \times \mathbf{e}_3, \end{aligned}$$

with boundary conditions at inlet  $s = 0$  and fiber end  $s = 1$ :

$$\begin{array}{llll} \mathbf{r}(0) = \mathbf{0}, & \mathbf{q}(0) = (1, 0, 0, 0), & \boldsymbol{\kappa}(0) = \mathbf{0}, & u(0) = 1, \\ r_1(1) = 0, & r_3(1) = 1, & \mathbf{n}(1) = \mathbf{0}, & \mathbf{m}(1) = \mathbf{0}. \end{array}$$

Here, we parameterize the rotation  $\mathbf{R} \in SO(3)$  with the help of unit quaternions  $\mathbf{q} \in \mathbb{R}^4$ ,  $\|\mathbf{q}\| = 1$ , and the skew-symmetric matrix  $\mathbf{S} \in \mathbb{R}^4$  (cf. Remark 2.4). The outer forces  $\mathbf{f}$  consist of capillary, electric and air resistance forces, i.e.,  $\mathbf{f} = \mathbf{f}_{ca} + \mathbf{f}_{el} + \mathbf{f}_{air}$ . Since we expect high electric forces in  $\vec{\mathbf{a}}_3^s$ -direction due to the presence of a strong electric field, gravitational effects are neglected. For the aerodynamic forces we employ the air drag model presented in Sec. 2.3 in Eulerian description and with respect to the director triad, i.e.,

$$\mathbf{f}_{air} = \frac{A_* \rho_* \nu_*^2}{\text{Re}_*^2} \frac{2R}{2R} \mathbf{F} \left( \mathbf{t}, \text{Re}_* \frac{2R}{\nu_*} (\mathbf{v}_* - \mathbf{v}) \right)$$

with the fiber unit tangent  $\mathbf{t} = \mathbf{e}_3$  and the fiber velocity  $\mathbf{v}$  given by (5.2). The dimensionless air drag function  $\mathbf{F}$  equals (2.9). The nondimensional fiber radius  $R$  is given through  $R = 1/\sqrt{\pi u}$ . The models for the capillary and electric forces are presented in the subsequent section.

**Remark 5.6** (Standard form). *For the intended numerical treatment of System 5.5 with the continuation-collocation method (cf. Sec. 3.1) the equations have to be written in the form  $d/ds \mathbf{y} = \mathbf{f}(\mathbf{y})$ . This is easily achieved by scaling all equations with  $L$  as well as applying the product rule on the  $\partial_s(u\boldsymbol{\kappa})$  terms with subsequent replacement of the  $\partial_s u$  term as given by the material law.*

**Remark 5.7** (Temporal stability analysis). *To explore the whipping of the jet, stability analysis has been performed in previous works using classical perturbation theory [48, 59, 80, 120]. We also find a strong connection between the whipping instability observed in experiments and the unstable solutions of our electrospinning model, for details we refer to the temporal stability analysis in App. C.1.*

### 5.1.2. Capillary and electric forces

The capillary and electric forces are included according to [120]. Employing local approximations the capillary forces are given in invariant form as

$$\vec{\mathbf{f}}_{ca} = \pi\gamma\partial_s(R\vec{\mathbf{d}}_3), \quad (5.3)$$

with  $\gamma$  [N/m] the surface tension coefficient and  $R$  the fiber radius. Introducing a reference surface tension  $\gamma_0$ , employing the reference values as given in Tab. 5.1

and suppressing the label  $\tilde{\cdot}$  for dimensionless quantities, the capillary force reads in nondimensional form with respect to the modified director triad

$$\mathbf{f}_{ca} = \Gamma \pi R \gamma \left( \boldsymbol{\kappa} \times \mathbf{e}_3 - L^{-1} \frac{1}{2u} (\partial_s u) \mathbf{e}_3 \right),$$

with  $R = 1/\sqrt{\pi u}$  the nondimensional fiber radius. The capillary force is characterized by the dimensionless number  $\Gamma$ , which equals a scaled inverse of the capillary number that indicates the ratio of viscous drag forces to surface tension forces, see Tab. 5.1.

The electric forces are assumed to be split into two parts, the effects due to the external unperturbed constant electric field  $\vec{\mathbf{E}} = E \vec{\mathbf{a}}_3^s$ ,  $E = \Phi/H$ , and the ones due to the Coulomb interactions of the induced charges on the jet. As before  $\Phi$  [V] is the applied voltage and  $H$  [m] the device height. The self-repulsion is modeled with the help of a local interaction approximation [120] in terms of the surface charge density of the fiber  $\zeta$  [As/m<sup>2</sup>], the permittivity of the air  $\epsilon_{p,*}$  [As/(Vm)] and the device height  $H$  as typical (cutoff) length. By Coulomb's law the electric force of repulsion between two small jet surface elements results in the proportionality to the square of the surface charge density  $\zeta$ . The stated interaction term follows then from integration using the cutoff length  $H$ . In total the electric force reads in invariant form

$$\vec{\mathbf{f}}_{el} = 2\pi R \zeta \left( \vec{\mathbf{E}} - \frac{R\zeta}{2\epsilon_{p,*}} \log\left(\frac{H}{R}\right) \vec{\boldsymbol{\kappa}} \times \vec{\mathbf{d}}_3 \right).$$

Since the surface charge density  $\zeta$  is in no situation a constant parameter, but an unknown in the problem, our Cosserat rod model (System 5.5) is still not closed. Instead of  $\zeta$ , we consider the electric current  $I$  [A] resulting from convection and conduction, i.e.,  $I = 2\pi R \zeta u + \pi R^2 \lambda \vec{\mathbf{E}} \cdot \vec{\mathbf{d}}_3$  with the jet's electrical conductivity  $\lambda$  [A/(Vm)]. In the transition to stationarity the current  $I$  becomes constant. The current is still unknown but can be measured in experiments. In literature different phenomenological relations of the form  $I \sim Q_V^m \Phi^n$ ,  $m, n \in \mathbb{R}$  are documented, see e.g. [15, 24, 48, 84, 92, 102]. The powers vary with the material properties and device geometry, the proportionality constant crucially depends on the experimental conditions. However, we do not employ such a phenomenological relation, but treat the electric current  $I$  as a parameter, yielding

$$\vec{\mathbf{f}}_{el} = \left( \frac{I}{u} - \frac{\pi R^2 \lambda \Phi}{uH} \vec{\mathbf{a}}_3^s \cdot \vec{\mathbf{d}}_3 \right) \left( \frac{\Phi}{H} \vec{\mathbf{a}}_3^s - \frac{1}{4\epsilon_{p,*} \pi} \left( \frac{I}{u} - \frac{\pi R^2 \lambda \Phi}{uH} \vec{\mathbf{a}}_3^s \cdot \vec{\mathbf{d}}_3 \right) \log\left(\frac{H}{R}\right) \vec{\boldsymbol{\kappa}} \times \vec{\mathbf{d}}_3 \right).$$

We introduce referential quantities for the current  $I_0$ , the potential  $\Phi_0$ , the jet's electrical conductivity  $\lambda_0$  as well as the air permittivity  $\epsilon_{p,*,0}$  and employ the

further reference values as given in Tab. 5.1. Then, the electric force reads in nondimensional form with respect to the modified director triad

$$\mathbf{f}_{el} = \frac{\Xi}{4} I \Phi \left( 1 - \varepsilon \Lambda \frac{\lambda \Phi}{u I} (\mathbf{R}(\mathbf{q}) \cdot \mathbf{e}_3) \cdot \mathbf{e}_3 \right) \left( \frac{4}{u} \mathbf{R}(\mathbf{q}) \cdot \mathbf{e}_3 - \Theta \frac{I}{u^2 \varepsilon_{p,*} \pi \Phi} \left( 1 - \varepsilon \Lambda \frac{\lambda \Phi}{u I} (\mathbf{R}(\mathbf{q}) \cdot \mathbf{e}_3) \cdot \mathbf{e}_3 \right) \log \left( \frac{1}{\varepsilon} \frac{1}{R} \right) \boldsymbol{\kappa} \times \mathbf{e}_3 \right),$$

with radius  $R = 1/\sqrt{\pi u}$ . The electric force is characterized by the potential-current-associated numbers  $\Xi$ ,  $\Theta$  and  $\Lambda$  (cf. Tab. 5.1). The conductive effects are represented by  $\Lambda$ . This characteristic number shows the limitation of our comparatively simple electric force model that assumes a constant external electric field and the current as a parameter. Assuming the reference parameters  $\lambda_0$ ,  $I_0$ , and  $\Phi_0$  chosen as the respective inflow quantities at the nozzle ( $s = 0$ ) the relation  $\varepsilon \Lambda < 1$  must hold. Otherwise the acting electric forces at  $s = 0$  point into the nozzle which is not physical. In the following we neglect the term, i.e.,  $\Lambda = 0$ , and hence overestimate the electric forces by assuming pure convection.

## 5.2. Solution strategy

The derived Cosserat rod model for the jet's whipping (System 5.5) is a parametric BVP of ODEs with 19 variables. Again, the numerical challenge lies in solving the problem for arbitrary parameter settings, which requires suitable initial guesses of the respective solutions. For viscous rope coiling the difficulty of finding a suitable guess was already addressed in [81] and treated there manually. We employ our more sophisticated continuation-collocation method, that navigates automatically through a high-dimensional parameter space, cf. Sec. 3.1. In the following we describe our model specific continuation strategy. The Jacobian for the Newton method is prescribed analytically.

We extend the Cosserat rod equations of System 5.5 by introducing continuation parameters for the viscous, capillary, electric and aerodynamic forces  $p_\varepsilon, p_{Re}, p_\Gamma, p_\Xi, p_\Theta, p_{A_*} \in [0, 1]$ . This means we replace each of the parameters  $k \in \{\varepsilon, Re, \Gamma, \Xi, \Theta, A_*\}$  by the term  $p_k k + (1 - p_k) k_0$  with starting values  $k_0$ . Moreover, we introduce a continuation parameter  $p_{fict} \in [0, 1]$  for the fictitious forces appearing due to the formulation with respect to the director basis and the rotating

reference frame and modify the linear and angular momentum equations

$$\begin{aligned}
 L^{-1}\partial_s \mathbf{n} &= \mathbf{n} \times \boldsymbol{\kappa} + L^{-1}(\partial_s u)\mathbf{e}_3 + p_{fict} \left( u\boldsymbol{\kappa} \times \mathbf{e}_3 + 2\Omega(\mathbf{R}(\mathbf{q}) \cdot \mathbf{e}_3) \times \mathbf{e}_3 \right. \\
 &\quad \left. + \frac{\Omega^2}{u} \mathbf{R}(\mathbf{q}) \cdot (\mathbf{e}_3 \times (\mathbf{e}_3 \times \mathbf{r})) \right) - \mathbf{f}, \\
 L^{-1}\partial_s \mathbf{m} &= \mathbf{m} \times \boldsymbol{\kappa} + \mathbf{n} \times \mathbf{e}_3 + p_{fict} \left( \varepsilon^2 \frac{1}{u} \mathbf{P}_2 \cdot (L^{-1}\partial_s(u\boldsymbol{\kappa}) - L^{-1}(\partial_s u)\boldsymbol{\kappa} - \Omega\boldsymbol{\kappa} \times \mathbf{e}_3) \right. \\
 &\quad - \varepsilon^2 \frac{\Omega}{u^2} \mathbf{P}_2 \cdot (L^{-1}\partial_s u(\mathbf{R}(\mathbf{q}) \cdot \mathbf{e}_3 - \mathbf{e}_3) + (u\boldsymbol{\kappa} - \Omega\mathbf{e}_3) \times (\mathbf{R}(\mathbf{q}) \cdot \mathbf{e}_3)) \\
 &\quad \left. - \varepsilon^2 \frac{1}{u^2} (\mathbf{P}_2 \cdot (u\boldsymbol{\kappa} + \Omega(\mathbf{R}(\mathbf{q}) \cdot \mathbf{e}_3 - \mathbf{e}_3))) \times (u\boldsymbol{\kappa} + \Omega(\mathbf{R}(\mathbf{q}) \cdot \mathbf{e}_3 - \mathbf{e}_3)) \right).
 \end{aligned}$$

This system is supplemented with the originally posed boundary conditions

$$\mathbf{r}(0) = \mathbf{0}, \quad \mathbf{q}(0) = (1, 0, 0, 0), \quad u(0) = u_{in}, \quad r_3(1) = 1,$$

and the following – slightly modified – ones

$$\begin{aligned}
 \boldsymbol{\kappa}(0) - (1 - p_1)\mathbf{e}_2 &= \mathbf{0}, \\
 p_2 r_1(1) - (1 - p_2)r_2(1) &= 0, \\
 (1 - p_7)[(1 - p_3 + p_3\Omega)\mathbf{R}(\mathbf{q}(1)) \cdot (\mathbf{e}_3 \times \mathbf{r}(1)) + u(1)\mathbf{e}_3 \\
 &\quad - (1 - p_4)(\mathbf{e}_2 + \mathbf{e}_3)] + p_7 \mathbf{n}(1) = \mathbf{0}, \\
 (1 - p_7)[(1 - p_5 + p_5\Omega)(\mathbf{R}(\mathbf{q}(1)) \cdot \mathbf{e}_3 - \mathbf{e}_3) + u(1)\boldsymbol{\kappa}(1) \\
 &\quad + (1 - p_6)(\mathbf{e}_1 - \mathbf{e}_2 + \mathbf{e}_3)] + p_7 \mathbf{m}(1) = \mathbf{0}.
 \end{aligned}$$

Consequently, we embed the fiber model into a family of BVPs in a high-dimensional parameter space,

$$\mathbf{p} = (p_1, \dots, p_7, p_{fict}, p_\varepsilon, p_{Re}, p_\Gamma, p_\Xi, p_\Theta, p_{A_*}) \in [0, 1]^{14}.$$

The choice of the continuation parameters allows the variation of the boundary conditions (fiber end with lay-down or without stresses) as well as the exclusion and inclusion of the fictitious, viscous, capillary, electric and air drag effects that mainly dominate the jet dynamics. We summarize the dimensionless model parameters in the tuple

$$\mathcal{P} = (\varepsilon, Re, \Gamma, \Xi, \Theta, A_*).$$

The remaining model parameter  $Re_*$  is always directly set as desired and not considered in the continuation.

The starting solution for the continuation that belongs to  $\mathbf{p} = \mathbf{0}$  is taken from the study on viscous rope coiling [81], i.e.,

$$\begin{aligned} \mathbf{r}(s) &= (1 - \cos(\pi s/2), 0, \sin(\pi s/2)), & \boldsymbol{\kappa} &= (0, 1, 0), & u &= u_{in}, & \mathbf{n} &= \mathbf{m} = \mathbf{0}, \\ \mathbf{q}(s) &= (\cos(\pi s/4), 0, -\sin(\pi s/4), 0), & L &= \pi/2, & \Omega &= 0. \end{aligned} \quad (5.4)$$

It describes a (non-coiling) jet having the form of a quarter circle in the absence of inertia, surface tension and outer forces,  $\text{Re}_0 = \Gamma_0 = \Xi_0 = A_{*,0} = 0$ . The initialization is consistent to our aim  $\Omega \geq 0$  and  $r_2(1) \geq 0$ . The corresponding parameter tuple is denoted by  $\mathcal{P}_0 = (\varepsilon_0, \text{Re}_0, \Gamma_0, \Xi_0, \Theta_0, A_{*,0})$  with

$$\varepsilon \leq \varepsilon_0 = \bar{\varepsilon}, \quad 0 \leq \Theta_0 = \bar{\Theta} \leq \Theta,$$

using intermediate parameters  $\bar{\varepsilon}$ ,  $\bar{\Theta}$ . In addition, we introduce the tuple  $\bar{\mathcal{P}}$  of intermediate parameters that allow for moderate physical effects,

$$\text{Re}_0 \leq \bar{\text{Re}} \leq \text{Re}, \quad \Gamma_0 \leq \bar{\Gamma} \leq \Gamma, \quad \Xi_0 \leq \bar{\Xi} \leq \Xi, \quad A_{*,0} \leq \bar{A}_* \leq A_*.$$

In particular, we choose  $\bar{\mathcal{P}} = (1 \cdot 10^{-1}, 2 \cdot 10^{-1}, 6 \cdot 10^2, 3.5 \cdot 10^3, 12, 0)$ . The starting solution (5.4) satisfies the desired stress-free condition  $\mathbf{n}(1) = \mathbf{m}(1) = \mathbf{0}$  that belongs to  $p_7 = 1$ . However, the change of each continuation parameter has different effects on the form of the solution and hence on finding appropriate initial guesses in the continuation. To navigate through the high-dimensional parameter space from  $\mathbf{p} = \mathbf{0}$  to  $\mathbf{p} = \underline{\mathbf{1}}$  we follow a strategy that consists of four parts:

- (A) from  $\mathbf{p} = \mathbf{0}$  to  $\mathbf{p}^A = (1, 1, 1, 1, 1, 1, 0, 0, 0, 0, 0, 0, 0, 0)$ :  
By changing the boundary conditions we obtain the solution associated to viscous rope coiling with dimensionless model parameters  $\mathcal{P}_0$  and vanishing linear and angular velocities at the jet end,  $p_i = 1$  for  $i = 1, \dots, 6$ .
- (B) from  $\mathbf{p}^A$  to  $\mathbf{p}^B = (1, 1, 1, 1, 1, 1, 0, 1, 0, p_{\bar{\text{Re}}}, p_{\bar{\Gamma}}, p_{\bar{\Xi}}, 0, p_{\bar{A}_*})$ :  
By changing  $p_{\text{fict}}$  we introduce fictitious forces. Moreover, by increasing the parameters  $p_{\text{Re}}, p_{\Gamma}, p_{\Xi}, p_{A_*}$  to intermediate values we incorporate moderate forming of the viscous, capillary, electric and air drag effects and achieve a solution corresponding to the parameter tuple  $\bar{\mathcal{P}}$ . Note that  $\bar{\varepsilon} = \varepsilon_0$  and  $\bar{\Theta} = \Theta_0$ .
- (C) from  $\mathbf{p}^B$  to  $\mathbf{p}^C = (1, 1, 1, 1, 1, 1, 1, 1, 0, p_{\bar{\text{Re}}}, p_{\bar{\Gamma}}, p_{\bar{\Xi}}, 0, p_{\bar{A}_*})$ :  
By changing  $p_7$  we switch from lay-down to stress-free boundary conditions.
- (D) from  $\mathbf{p}^C$  to  $\mathbf{p} = \underline{\mathbf{1}}$ :  
By the final increase of the parameters  $p_\varepsilon, p_{\text{Re}}, p_{\Gamma}, p_{\Xi}, p_\Theta, p_{A_*}$  we incorporate all inertial, capillary, electric and aerodynamic effects as desired.

We use a heuristic that seeks for the diagonal continuation path through the parameter space. In Part A we use a tree search algorithm: Consider an equidistant

grid on the parameter space with size  $\Delta p$  in every dimension and apply a tree search algorithm where the grid points (parameter tuples) are the nodes in the tree. The traversal of the tree is described by a recursion. Because from a given node there is more than one possible next node when changing one parameter, we use a heuristic to order the nodes. We apply a depth-first search to explore a continuation path as far as possible before backtracking when the solution to a BVP cannot be found. The step from one node to the next node is performed by solving the associated BVP directly, i.e., without the adaptive step size control described in Sec. 3.1. To accelerate the algorithm we use a heuristic that prefers the diagonal navigation through the parameter space and register all visited nodes on a forbidden list. As grid size we take  $\Delta p = 10^{-1}$ , implying  $10^6$  nodes in total. In Part B it turns out that balancing the physical effects strictly leads to the diagonal path such that the parameter space can be reduced to  $p_{fict} = p_{Re} = p_{\Gamma} = p_{\Xi} = p_{A_*}$ . The corresponding one-dimensional search is performed with the adaptive step size control (cf. Sec. 3.1), the same holds for Part C. In Part D we also use the one-dimensional search by increasing every parameter to the target value successively. A good heuristic is to start with the parameter  $p_{\Gamma}$  and continue increasing the remaining parameters in the fixed order  $p_{\Theta}, p_{\Xi}, p_{Re}, p_{A_*}, p_{\varepsilon}$ .

**Remark 5.8** (Selective preconditioning). *Due to boundary layers occurring in the solution to the variables  $\mathbf{n}$  and  $\mathbf{m}$  at the nozzle, which we analyze later, the system of ODEs (System 5.5) is badly scaled with respect to these quantities. Therefore, our numerical approach includes scaling of these variables using the component-wise maximum norm. This means we solve the System (5.5) with variables  $n_i$  and  $m_i$  ( $i = 1, 2, 3$ ) that are scaled equal to one. This procedure equals a selective preconditioning. In contrast to our dry spinning fiber model a scaling of the angular momentum equation with the slenderness parameter  $\varepsilon$  is not sufficient to achieve acceptable convergence of the electrospinning model. Moreover, treating the parameter  $\varepsilon$  as a regularization parameter in view of the associated string equation, i.e., fixing it at a moderate constant value  $\varepsilon_0 > \varepsilon$ , is not practical here. This is due to the fact that the shape of the bending instability crucially depends on  $\varepsilon$ , which we will show in a parameter study (Sec. 5.3).*

### 5.3. Performance and parameter study

For the forthcoming numerical simulations the solver `bvp4c.m` is used with the default values. The only modification is that we update the Jacobian every Newton step. In the following we demonstrate the performance of our setup-specific continuation algorithm presented in Sec. 5.2 and examine the influence of the dimensionless model parameter on the jet's whipping, its elongation and its throwing range.

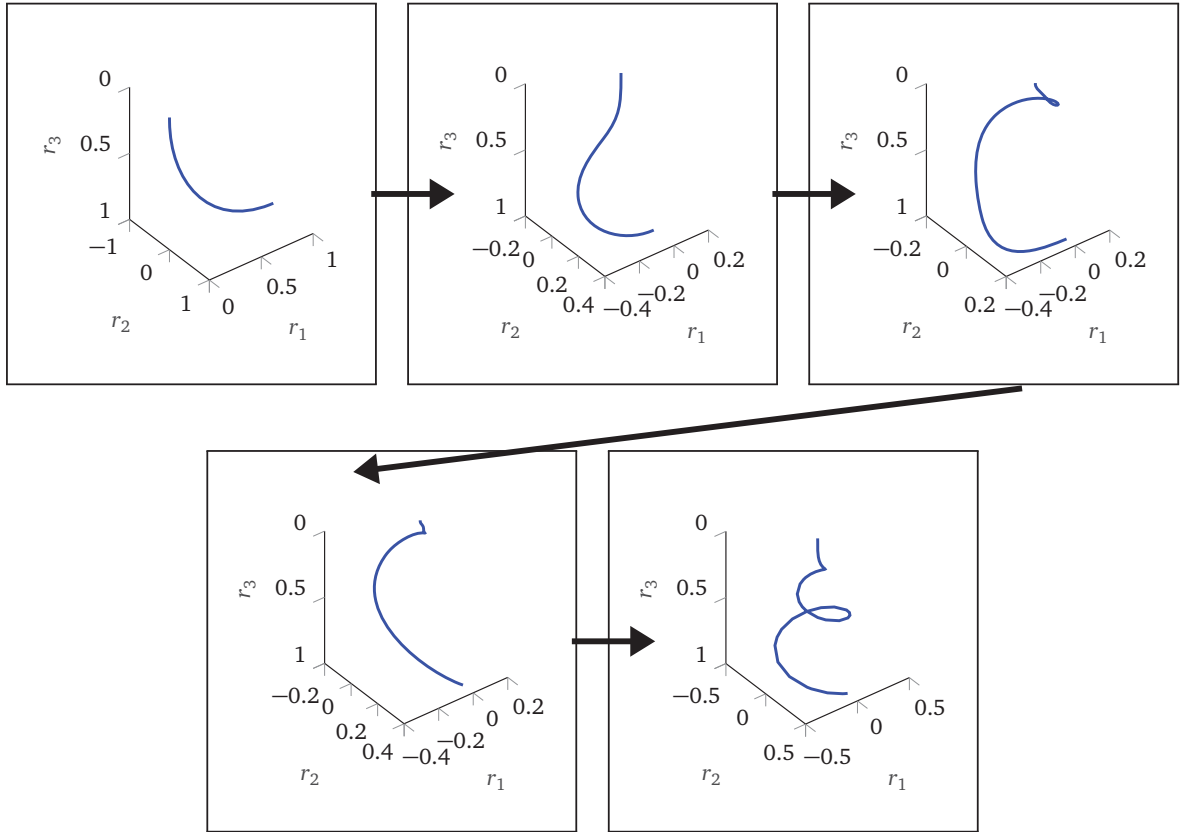


**Figure 5.2.:** Jet curve during continuation procedure. *From top left to bottom right:* Starting solution to  $\mathcal{P}_0$ , after Part A, after Part B (solution with lay-down end to  $\bar{\mathcal{P}}$ ), after Part C and after Part D (desired solution with stress-free end to  $\mathcal{P}^{ref}$ ).  $Re_* = 3$ .

Part	Computing Time [s]	Percentage	Continuation Steps
A	551.28	49.9%	736
B	267.95	24.2%	93
C	89.17	8.1%	22
D	196.92	17.8%	76
total	1105.32	100%	927

**Table 5.2.:** Performance of continuation procedure. Computing time of each Part A-D and the number of respective continuation steps to reach the reference parameter tuple  $\mathcal{P}^{ref}$  (cf. Fig. 5.2).

### 5.3.1. Performance of continuation algorithm

For the performance study of the continuation algorithm we choose a parameter tuple inducing moderate emergence of all involved effects in the numerical

solution. In particular, we set

$$\mathcal{P}^{ref} = (7 \cdot 10^{-2}, 1, 8 \cdot 10^1, 5 \cdot 10^4, 8 \cdot 10^1, 5 \cdot 10^{-3}), \quad \text{Re}_*^{ref} = 3.$$

Moreover, we assume a constant setup, i.e., the electric current  $I$ , the potential  $\Phi$ , the surface tension  $\gamma$ , and the airflow quantities  $\epsilon_{p,*}$ ,  $\rho_*$ ,  $\nu_*$  are constant in space and time. In particular we choose the reference values for nondimensionalization such that  $I = \Phi = \gamma = \epsilon_{p,*} = \rho_* = \nu_* = 1$  in nondimensional form. Furthermore, we assume unmovable air, i.e.,  $\mathbf{v}_* = \mathbf{0}$ .

Fig. 5.2 shows the jet curve during the continuation procedure. We initialize with the prescribed solution (5.4) forming a quarter circle without any inertia, surface tension and outer forces. After changing the boundary conditions in continuation Part A the jet shows a coiling onto the lay-down plane. Incorporating viscous, capillary and outer forces in Part B causes the onset of the whipping mode due to the Coulomb interactions, whereas the external electric field straightens the jet. After Part C, we clearly see a stress-free jet end. Finally, the inclusion of all effects in their full magnitude gives rise to the whipping of the jet after Part D. Considering the computational performance of the algorithm in Tab. 5.2 we see that the preparatory Part A takes a CPU time of 551 s. Each step (including rejection) requires less than 1 s. In view of the huge tree with  $10^6$  nodes and the fact that the continuation path is by no means the diagonal, this is a very good performance. Since the jet's end is nearly stress-free after Part B there are only 22 continuation steps in Part C with a CPU time of approximately 89 s. Part B and D contain the actual continuation and need together 42% of the total computation time. These parts take several minutes, the minimal step size is of order  $\min \Delta p \sim \mathcal{O}(10^{-5})$ . However, with only 169 steps in total (instead of  $10^5$  for the respective fixed step size), it clearly stresses the efficiency of the presented adaptive step size control.

### 5.3.2. Influence of dimensionless model parameters

Proceeding from the reference solution associated with  $\mathcal{P}^{ref}$  we investigate the jet characteristics under variation of the single model parameters. We particularly study the jet curve, the elongation of the jet end and the throwing range, see Figs. 5.3, 5.4 and 5.5 respectively. The elongation at the jet's end  $e(1)$  is given by the Euclidean norm of the jet's tangent in material (Lagrangian) description and corresponds to the convective speed  $u(1)$ , since  $e(1) = A(0)/A(1) = \varrho_V(0)/\varrho_V(1) = u(1)/u(0)$  holds due to the conservation of volume. The throwing range characterizes the width of the envelope enclosing the three-dimensional jet curve and is defined as the distance from the jet's end to the vertical axis, i.e.,  $r_2(1)$ .

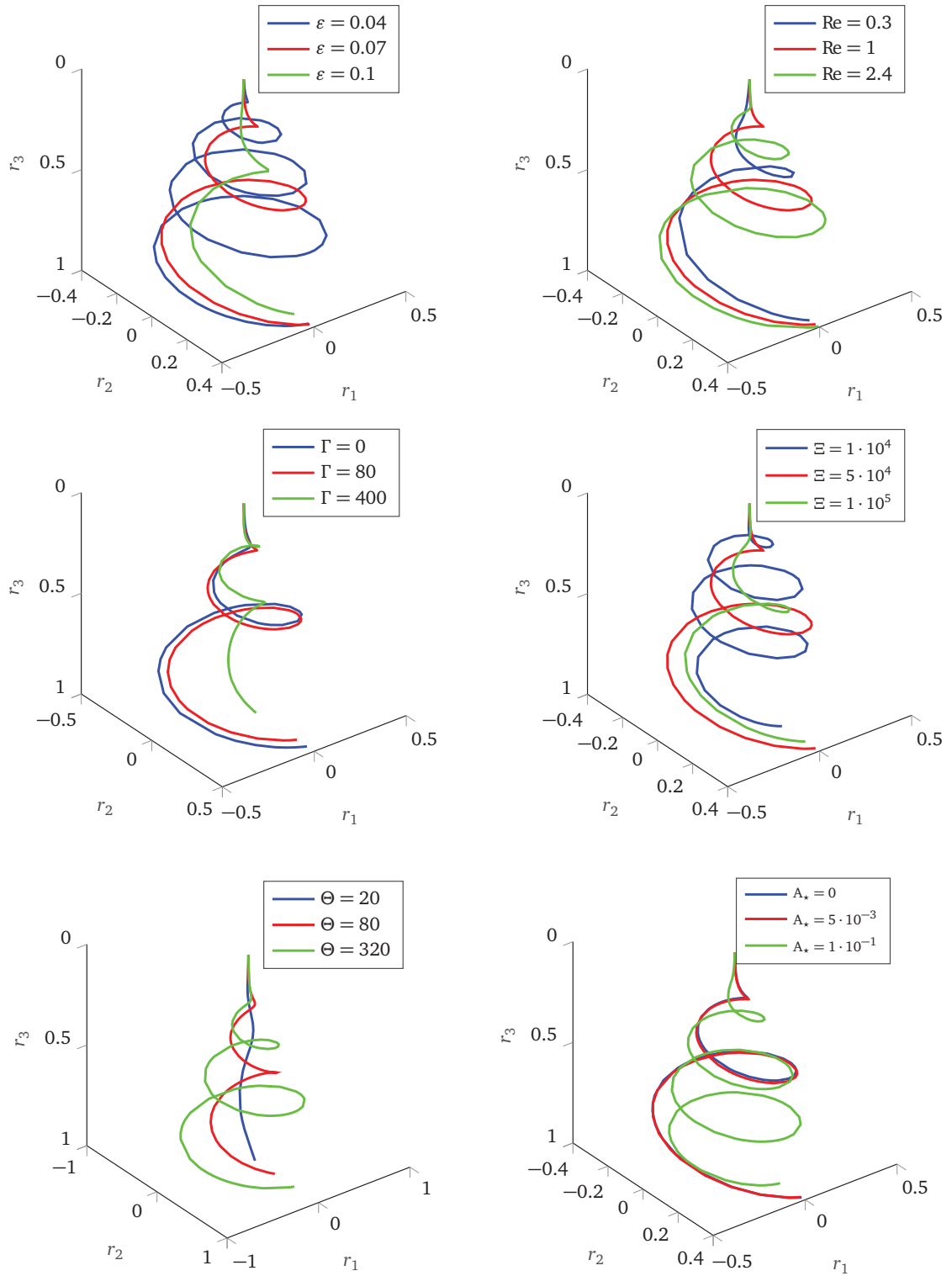


**Figure 5.3.:** Jet curves for variations of single model parameters proceeding from reference  $\mathcal{P}^{ref}$ ,  $Re_*^{ref}$ . The reference jet is visualized in *red* in all plots. The jets associated to increased/decreased parameters are given in *green/blue*.

## 5. Electrified visco-capillary jets in airflows

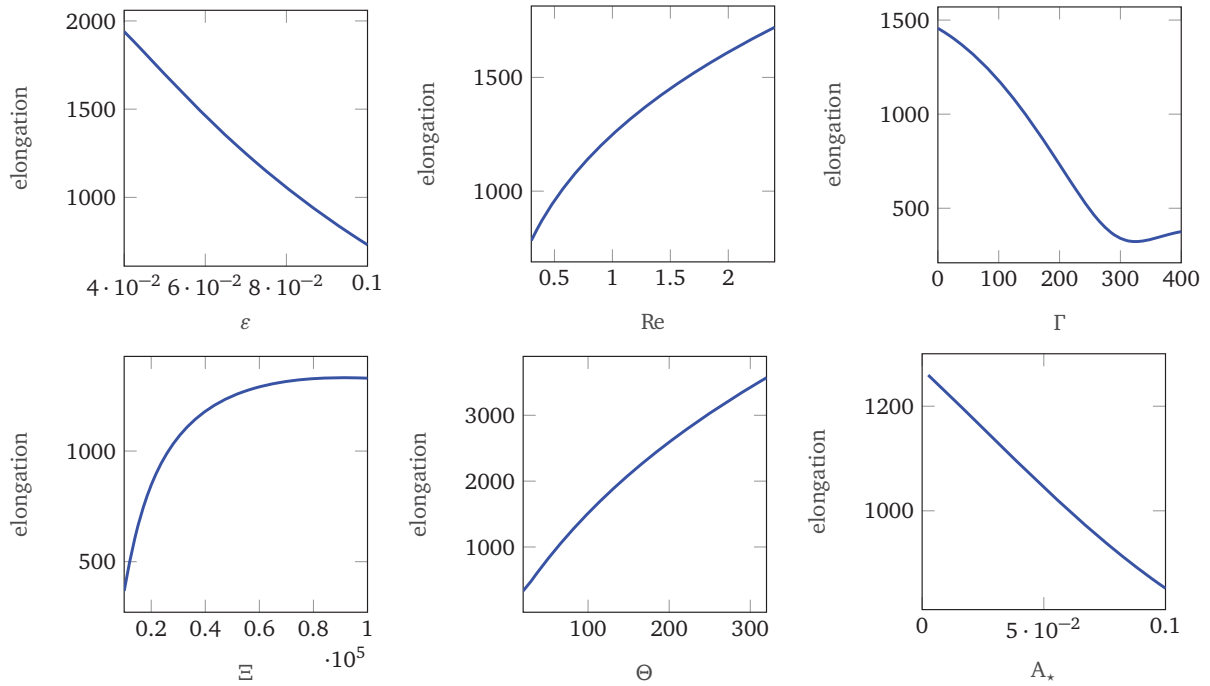


**Figure 5.4.:** Elongation of jet end in the regions  $\varepsilon \in [0.04, 0.1]$ ,  $Re \in [0.3, 2.4]$ ,  $\Gamma \in [0, 400]$ ,  $\Xi \in [10^4, 10^5]$ ,  $\Theta \in [20, 320]$ ,  $A_* \in [0, 0.1]$ , proceeding from  $\mathcal{P}^{ref}$ .

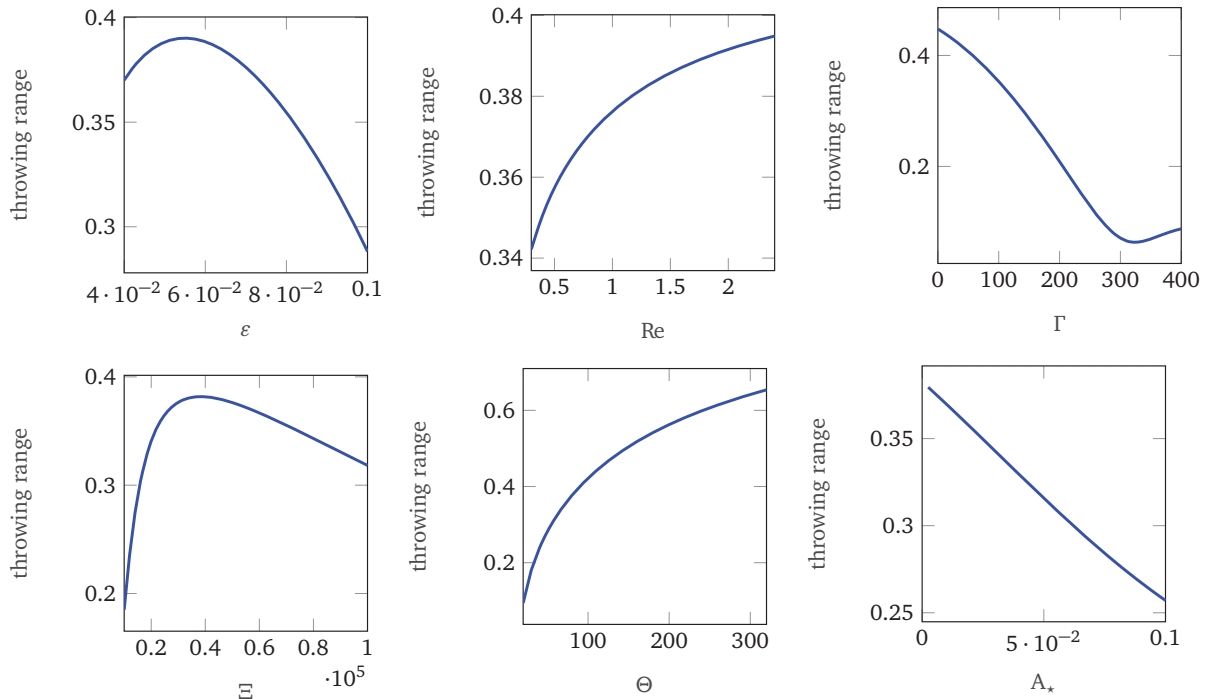


**Figure 5.5.:** Jet's throwing range indicating the width of the curve's envelope in the regions  $\varepsilon \in [0.04, 0.1]$ ,  $Re \in [0.3, 2.4]$ ,  $\Gamma \in [0, 400]$ ,  $\Xi \in [10^4, 10^5]$ ,  $\Theta \in [20, 320]$ ,  $A_* \in [0, 0.1]$ , proceeding from  $\mathcal{P}^{ref}$  (cf. Fig. 5.4).

As we see, decreasing the slenderness parameter  $\varepsilon$  leads to a intense increase of turning points. This is clear because – following the definition – a decrease of this parameter equals an increase of the distance from the nozzle to the ground collector while holding the diameter of the nozzle constant. Therefore, the bending jet has more space in  $\vec{a}_3^s$ -direction to propagate and, thus, forms more turning points in total. This higher number of turning points leads to a higher elongation of the jet's end. The throwing range forms a maximum for values at the left side of the chosen parameter region around  $\varepsilon = 5.5 \cdot 10^{-2}$  approximately. An increase of the Reynolds number  $Re$  induces a higher number of turning points coming along with a higher elongation and an increased throwing range, which can be explained as follows: Increasing  $Re$  equals decreasing the viscous forces under constant inertia. This reduces the thinning of the jet and thus leads to a larger jet surface. As a result we expect a higher surface charge, which comes along with higher Coulomb repulsion inducing a more intense bending profile including higher elongations and wider throwing range. In contrast, an increase of the inverse capillary number  $\Gamma$  reduces the elongation and the throwing range of the jet including a complete narrowing of the jet's envelope. This takes place due to increasing surface tension forces, which form a counteracting force to the Coulomb repulsion. Elongation and throwing range reach a minimum around  $\Gamma = 3 \cdot 10^2$  approximately. Furthermore, we observe that increasing the parameter  $\Xi$  induces a more uniform bending due to the stabilizing effect of the outer electric field. This stabilization procedure is indicated by the formation of a maximal throwing range inside the tested parameter region, around  $\Xi = 4 \cdot 10^4$  approximately. The elongation tends to an asymptotic bound for large  $\Xi$ . Varying the parameter  $\Theta$  simply means increasing or decreasing the effect of Coulomb repulsion. The effect of stronger Coulomb repulsion is indicated by a higher number of turning points, larger elongation and wider throwing range. Because an increase of  $Re_*$  simply means a higher air drag acting on the jet and the analog for decrease, we examine the effect of air drag by varying the parameter  $A_*$  only. Increasing  $A_*$  narrows the envelope of the jet considerably and leads to an extensive increase of number of turning points. A higher air drag acts as higher counteracting force to the Coulomb repulsion and thus narrows the envelope, which forms a helical structure as soon as air drag and Coulomb repulsion balance. This effect is also indicated by the decrease of elongation and throwing range for larger air drag parameters.

## 5.4. Strong whipping effects

In industrial electrospinning we are faced with parameter settings involving high whipping frequencies inducing large numbers of turning points in the jet curve and

Dimensionless numbers		
Description	Symbol	Value(s)
Slenderness	$\varepsilon$	$\{1.5 \cdot 10^{-2}, 5 \cdot 10^{-2}\}$
Reynolds	Re	2.4
Capillary associated	$\Gamma$	60
Potential associated	$\Xi$	$10^5$
Coulomb force associated	$\Theta$	360
Air drag associated	$A_*$	$\{0, 10^{-1}\}$
Air-fiber Reynolds	$Re_*$	3

**Table 5.3.:** Dimensionless numbers for the electrospinning setup generating high jet elongations.

high elongations at the jet end. Our stationary model and the proposed numerical scheme are able to handle such situations. However, the required resolution is often computationally very demanding. Hence, we make use of the numerical results to formulate an analytical solution for the jet's 'longtime' behavior – in the sense of Lagrangian time starting at the nozzle. This means that we analytically explore the asymptotic jet behavior at a sufficiently large distance far away from the nozzle.

Motivated from the parameter study in the previous subsection, we consider a setting with a highly developed whipping. The corresponding dimensionless parameters are given in Tab. 5.3. Again we assume  $I = \Phi = \gamma = \epsilon_{p,*} = \rho_* = \nu_* = 1$  in nondimensional form as well as unmovable air, i.e.,  $\mathbf{v}_* = \mathbf{0}$ . Concerning the two dimensionless model parameters  $\varepsilon$  and  $A_*$  we point out: On the one hand, we neglect two-way coupling between the jet and the surrounding air, that means we overestimate air drag forces in general. On the other hand, as seen previously a high air drag-associated number  $A_*$  and a small slenderness ratio  $\varepsilon$  induce large numbers of turning points of the jet curve, which can easily require a high numerical resolution and thus lead to an unpractical number of discretization points in our collocation method. Thus, we focus our considerations on two examples:

$$\text{Example 1: } (\varepsilon, A_*) = (1.5 \cdot 10^{-2}, 0)$$

$$\text{Example 2: } (\varepsilon, A_*) = (5 \cdot 10^{-2}, 0.1).$$

In Example 1 any air drag-associated effects are neglected, see Fig. 5.6 (top). The jet curve bends strongly and its envelope can nearly be described by a circular right cone. The dimensionless convective speed  $u$  indicating the jet's elongation  $e$  describes a rapid growth directly at the nozzle with lower increase afterwards. At the jet end we reach approximately  $e(1) = 2.6 \cdot 10^4$ . In Example 2 the additional air drag causes a considerable increase in the number of turning points under

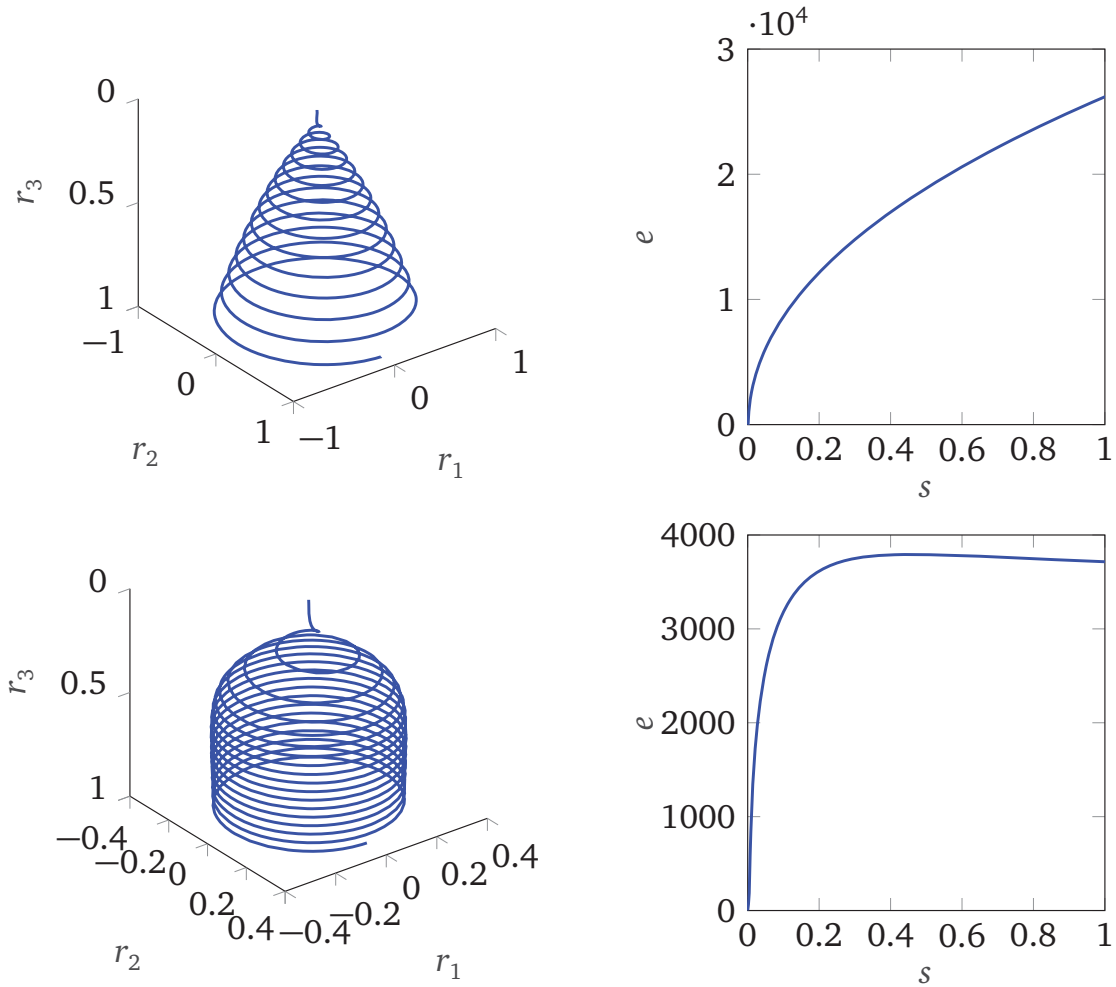


**Figure 5.6.:** *Top:* Results for Example 1,  $(\varepsilon, A_*) = (1.5 \cdot 10^{-2}, 0)$ . *Bottom:* Results for Example 2,  $(\varepsilon, A_*) = (5 \cdot 10^{-2}, 0.1)$ . *Left:* Jet curve characterized by strong whipping. *Right:* Jet's elongation over arc length.

decrease of the throwing range, see Fig. 5.6 (bottom). Due to the additional resistance caused by the surrounding air the convective speed remains in more moderate regions compared to the first example. In the components of curvature  $\kappa$ , contact force  $\mathbf{n}$  and couple  $\mathbf{m}$  a boundary layer arises directly at the nozzle (Fig. 5.7). As we show in App. C.2, this boundary layer is not a numerical artifact but an essential characteristic of our solution.

Considering the contact force  $\mathbf{n}$  and couple  $\mathbf{m}$  in Fig. 5.7 more closely, these quantities seem to vanish beyond the described boundary layer at the nozzle. This observation serves as motivation to examine the rod model in terms of completely vanishing contact forces and couples. Because the resulting solution is expected to describe the jet's 'longtime' behavior, we neglect all initial conditions and also leave the jet length  $L$  and whipping frequency  $\Omega$  arbitrary. Surprisingly, fixing  $\mathbf{n} = \mathbf{m} = \mathbf{0}$  in our rod model (System 5.5) leads to an analytically solvable system.

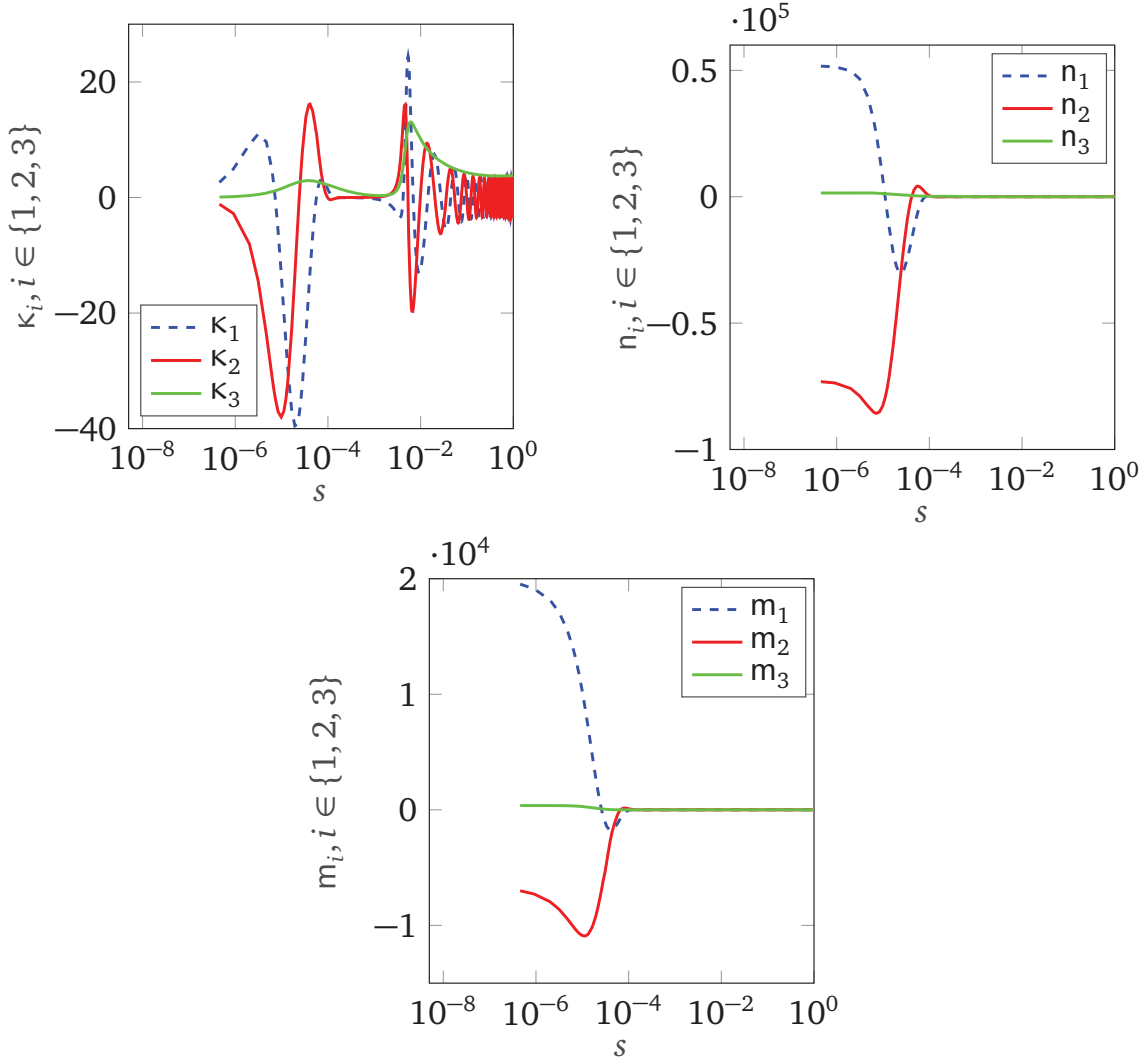


**Figure 5.7.:** Boundary layer at the nozzle in the components of curvature  $\kappa$  (top left), contact force  $\mathbf{n}$  (top right) and couple  $\mathbf{m}$  (bottom) for the parameters of Example 2.

A solution thereof is

$$\begin{aligned}
 r_1(s) &= -\frac{2a_0a_1L}{b_0 + b_1} \sin((b_0 + b_1)s + c_0 + c_1), \\
 r_2(s) &= -\frac{2a_0a_1L}{b_0 + b_1} \cos((b_0 + b_1)s + c_0 + c_1), & r_3(s) &= L(a_0^2 - a_1^2)s + d_3, \\
 q_0(s) &= a_0 \cos(b_0s + c_0), & q_1(s) &= a_1 \sin(b_1s + c_1), \\
 q_2(s) &= a_1 \cos(b_1s + c_1), & q_3(s) &= a_0 \sin(b_0s + c_0), \\
 \kappa_1(s) &= k_1 \cos\left(\frac{\Omega L}{U}s + k_2\right), & \kappa_2(s) &= -k_1 \sin\left(\frac{\Omega L}{U}s + k_2\right), & \kappa_3(s) &= k_3, \\
 u(s) &= U,
 \end{aligned} \tag{5.5}$$

with 13 parameters  $\mathbf{y} = (a_0, a_1, b_0, b_1, c_0, c_1, d_3, k_1, k_2, k_3, U, \Omega, L) \in \mathbb{R}^{13}$  being implicitly given by the highly nonlinear system of equations

$$\begin{aligned}
 \frac{L}{2} \left( k_1 a_1 + k_3 a_0 \right) &= -a_0 b_0, & \frac{L}{2} \left( -k_1 a_0 + k_3 a_1 \right) &= a_1 b_1, \\
 b_1 - b_0 &= \frac{\Omega L}{U}, & c_1 - c_0 &= k_2, & a_0^2 + a_1^2 &= 1, \\
 \frac{1}{4\pi U} \left( 4a_0 a_1 \Omega k_3 - 4a_0 a_1 \frac{\Omega^2}{U} + 2a_0 a_1 \frac{\Omega^2}{U} (a_0^2 - a_1^2) + U k_1 k_3 - k_1 \Omega \right) &= 0, \\
 U + \frac{4\Omega a_0 a_1}{k_1} - \Gamma \sqrt{\frac{\pi}{U}} \gamma + \Xi \Theta \frac{I^2}{U^2 \epsilon_{p,*} \pi} \log \left( \frac{1}{\epsilon} \sqrt{\pi U} \right) - \frac{2a_0 a_1 \Omega^2 L}{k_1 U (b_0 + b_1)} &= 0, \\
 -\Xi \frac{4I\Phi}{U} + A_* \frac{r_n(w_n)}{w_n} \frac{4\rho_*}{\nu_*} \frac{\Omega^2 L^2}{\sqrt{\pi U}} \frac{|a_0 a_1| |a_0^2 - a_1^2| (a_0^2 - a_1^2)}{|b_0 + b_1| (b_0 + b_1)} &= 0, \\
 -\Xi \frac{4I\Phi}{U} (a_0^2 - a_1^2) - A_* \frac{r_t(w_n)}{w_n} \frac{4\rho_*}{\nu_*} \frac{\Omega L}{\sqrt{\pi U}} \frac{|a_0 a_1| |a_0^2 - a_1^2|}{|b_0 + b_1|} \left( \frac{4a_0^2 a_1^2 \Omega L}{b_0 + b_1} - U \right) &= 0,
 \end{aligned} \tag{5.6}$$

with air drag associated normal velocity components

$$w_n = \text{Re}_* \frac{4}{\nu_*} \frac{\Omega L}{\sqrt{\pi U}} \frac{|a_0 a_1| |a_0^2 - a_1^2|}{|b_0 + b_1|}.$$

Note that  $I = \Phi = \gamma = \epsilon_{p,*} = \rho_* = \nu_* = 1$  in the considered setup. With the particular choice

$$\begin{aligned}
 \mathbf{y} = & (7.155 \cdot 10^{-1}, -7 \cdot 10^{-1}, -8.26, 1.072 \cdot 10^2, 0, 1.571, 3.445 \cdot 10^{-1}, 3.3, \\
 & 1.571, 3.8, 3.45 \cdot 10^3, 1.238 \cdot 10^4, 2.988 \cdot 10^1)
 \end{aligned}$$

the system (5.6) is approximately fulfilled. The corresponding solution (5.5) forms a helical jet curve that is approached by the numerically computed jet curve of Example 2, see Fig. 5.8. So in the regime of strong whipping we are able to give an analytical description of the jet's 'longtime' behavior.

Summing up, despite the simplicity of the employed electric force model where the current is considered as a constant parameter and conduction is neglected, the numerical results are convincing and characterize qualitatively well the known whipping effects. However, for quantitative comparisons with experiments we lack respective measurements. Experimental studies in literature investigated intensively the whipping characteristics in dependence of various parameter settings, but the underlying potential-current relations of the used setups are mostly not quantitatively documented. An exception is [47, 92] where experiments with a solvent of polyethylene oxide in water were performed. But due to the high conductivity of the solvent, we can not benefit from these results. Thus, a combined experimental and numerical study is left to future research.

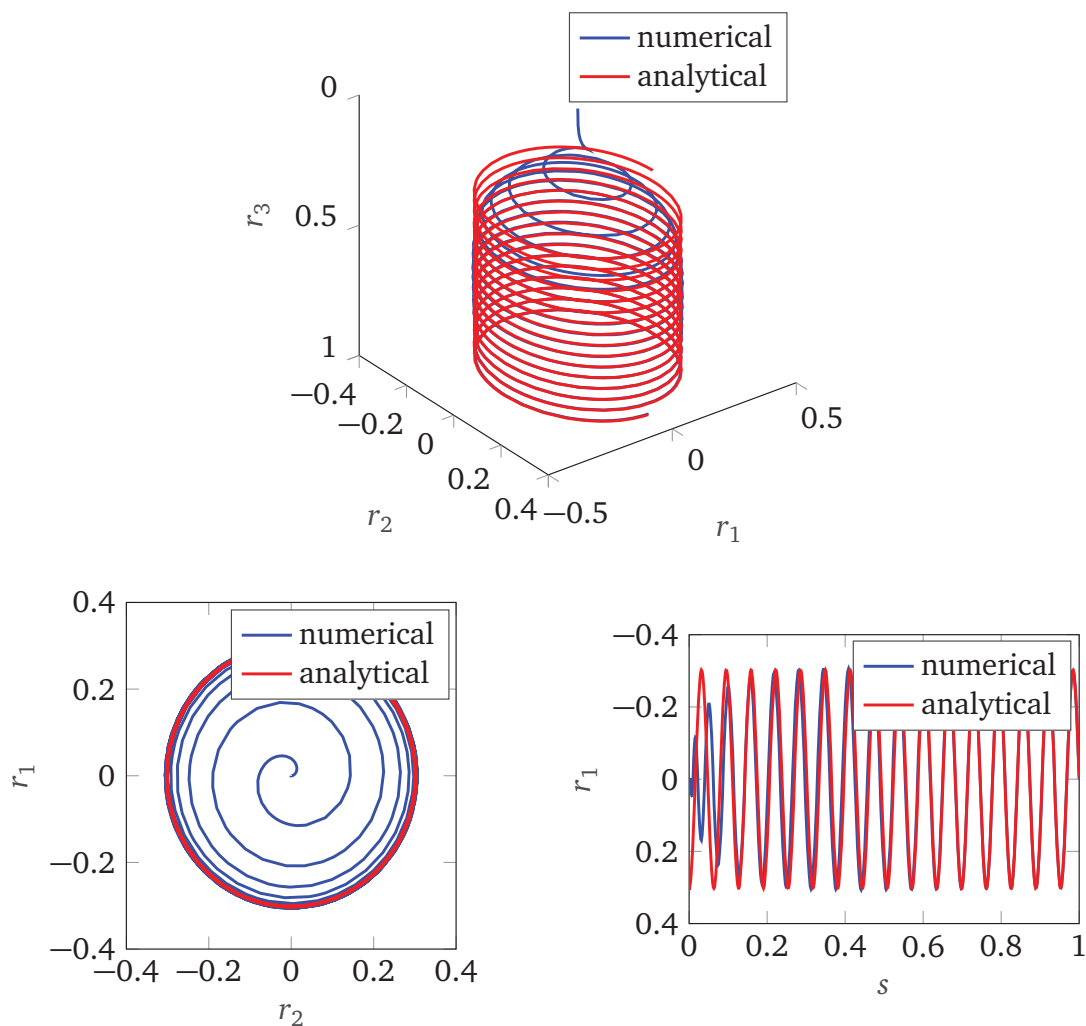


**Figure 5.8.:** Jet's 'longtime' behavior in Example 2. The numerical solution approaches the analytical description (5.5) for sufficiently large arc length parameter  $s$ . *Top:* Three-dimensional jet curve. *Bottom:* Top view of jet curve shows similar throwing range (*left*). Component  $r_1$  shows similar number of turning points in  $s$  (analogously for  $r_2$ ) (*right*).

## 6. Fibers in turbulent airflows

In many fiber spinning processes aerodynamic forces are the key player for fiber thinning. A typical example are melt-blowing processes, which we study in this chapter. Melt-blowing is a widely used production method for polymer micro- and nanofibers that is economically attractive due to low production costs. Fabrics of meltblown fibers are nonwovens which are used, e.g., as filters, hygiene products, battery separators. Details on the technology can be found in [28, 78]. A typical setup of a melt-blowing device is illustrated in Fig. 6.1. In the process molten polymer is fed through nozzles into a forward-flowing high-speed and highly turbulent air stream. By this airflow the polymeric jets are stretched and cooled. The resulting fibers are laid down onto some collector, e.g., conveyor belt. In contrast to melt-spinning processes, where the stretching is caused by a mechanical take-up, and dry spinning processes, where additionally the evaporation of solvent causes fiber thinning, the fiber jet thinning in melt-blowing is due to the driving high-velocity air stream with its turbulent nature. We note that the following strategies and concepts can be easily adopted to other spinning scenarios where the achieved fiber thickness is also crucially determined by the airflow.

To deepen the understanding on the mechanism of jet thinning in melt-blowing extensive diverse studies have been performed in the last years, covering experimental investigations, e.g., [11, 17, 29, 116, 118], combined experimental numerical works, e.g., [46, 93, 99, 104, 122], as well as numerical computations, e.g., [18, 20, 91, 96, 125, 128]. However, so far, there is an obvious gap between the experimental and numerical results for the achieved fiber thickness in literature. The existing numerical simulations underestimate the fiber elongation by several orders of magnitude, cf. [91, 104, 118, 125]. While experimental studies show fiber elongations  $e \sim \mathcal{O}(10^6)$ ,  $e = A_{in}/A = d_{in}^2/d^2$ , meaning a reduction of  $10^3$  in diameter  $d$  and of  $10^6$  in cross-sectional area  $A$  compared to the values at the nozzle (indicated by the index  $in$ ), simulated elongations are of order  $e \sim \mathcal{O}(10^4)$ . This is likely due to assumptions of steady conditions and the neglect of turbulent aerodynamic effects [18, 19, 91]. Assuming an incompressible steady fiber jet the relation  $Au = A_{in}u_{in}$  holds true due to the conservation of mass (cf. System 2.8 and Remark 2.9). Hence, the computed elongation is restricted by the velocity  $\mathbf{v}_*$  of the surrounding air stream, i.e.,  $e = u/u_{in} < \|\mathbf{v}_*\|_\infty/u_{in}$ . This estimate turns out to be valid also in (unsteady) melt-blowing simulations where

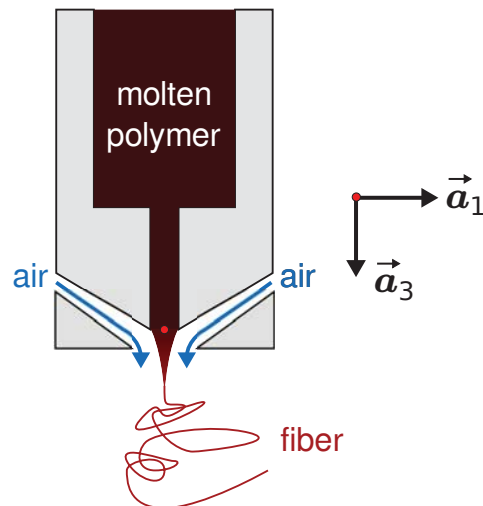


Figure 6.1.: Sketch of a typical melt-blowing setup.

the surrounding airflow is computed (even) on basis of a turbulence model when only mean airflow informations are taken into account in the aerodynamic driving of the fiber jet [46, 96, 125]. Experiments reported in [93, 118] indicate the relevance of the turbulent effects for the jet thinning. In [122] a viscoelastic fiber model based on an upper convected Maxwell description (UCM) has been employed for melt-blowing, which is opposed to random pulsations. This is done by applying perturbation frequencies on a rectilinear fiber jet leading to bending instabilities and causing significant stretching and thinning of the jet. The examination has been extended to multiple fibers, focusing on the prediction of fiber deposition patterns and fiber-size distributions in the resulting nonwovens in [123]. Latest works deal with the numerical investigation of the fiber lay-down on a rotating drum, the effect of uptake velocity as well as the angular fiber distribution [37, 38, 94]. The effect of fiber viscoelasticity, especially the influence of different rheological models on the numerical results, has been studied in [20, 99, 128]. Regarding Newtonian, UCM, Phan-Thien and Tanner (PTT), and Giesekus constitutive equations, fiber diameters and diameter distributions have been computed and analyzed in an uni-axial setting with steady straight fiber curve and compared to experiments, [99, 128]. In [20] the investigation on the rheology was extended to the unsteady fiber model of [122] and a parameter study was carried out to identify the key factor for the whipping of the fiber curve, which occurs to be the turbulent nature of the air stream. In [50] the significance of turbulence for melt-blowing has been approached by studying the effect of turbulent aerodynamic velocity fluctuations on a simplified fiber model consisting of ODEs. There, a  $k-\epsilon$  turbulence description of the high-speed airflow serves as basis for the reconstruction of the velocity fluctuations, yielding a stochastic aerodynamic force acting on the fiber jet. Since the airflow is crucial for the fiber forming, the influence of the air nozzle geometry on the airflow field as well as

---

the effect of associated air outflow conditions have been examined in [98]. In [97] numerical optimization of an air nozzle was performed to achieve optimal airflow properties in view of velocity and temperature decay.

The aim of the subsequent study is to establish a numerical framework for fibers in turbulent air that makes the simulations of industrial melt-blowing processes feasible. For this purpose we bring together the two described approaches: we extend the random field sampling of [50] to the unsteady viscoelastic UCM fiber model of [122]. Since the aerodynamic forces are the key player for the fiber dynamics, we employ a one-way coupling of the outer air stream with the fiber with the help of our aerodynamic force model (2.9) and the coupling Algorithm 3.7. Of importance is the efficient and robust realization that enables us presenting numerical results of an industrial setup with an appropriate viscoelastic description of the fiber, the inclusion of temperature effects and the direct incorporation of the turbulence structure of the outer air stream for the first time in literature.

The viscoelastic UCM fiber model of [122] essentially equals our previously presented viscoelastic string model (System 2.12) on a growing space-time domain (cf. Remark 2.14). To include temperature effects we additionally supply this model with an energy balance equation and introduce rheological laws for the temperature dependence of fiber viscosity and relaxation time. In Lagrange description this UCM model can uniquely be written as quasilinear hyperbolic first order system of PDEs. Its classification with respect to the growing fiber domain gives requirements on boundary conditions with regard to well-posedness of the mathematical problem formulation. The effects of turbulent fluctuations are calculated by the turbulence reconstruction procedure described in [50] and coupled into the fiber model by our aerodynamic force function (2.9). The resulting unsteady problem is solved using the finite volume scheme in space with implicit Euler time discretization as presented in Sec. 3.2. For an industrial melt-blowing setup we show the applicability of our model and numerical solution framework and demonstrate the relevance of the turbulent fluctuations causing fiber elongations of the expected higher order of magnitude compared to stationary simulations. From the repeated random sampling of fibers in the sense of the Monte Carlo method a distribution of the final fiber diameters is obtained that predicts fiber diameters of realistic order of magnitude.

This chapter is structured as follows. In Sec. 6.1 we start with the unsteady viscoelastic UCM fiber model, regarding its classification and correct closing with boundary conditions. Furthermore, we give a short survey on reconstructing the turbulent fluctuations of an underlying air stream. After that we consider an industrial melt-blowing setup, for which we present simulation results covering the turbulent effects due to the high-speed air stream in Sec. 6.2. In great parts this chapter has been pre-published in [113].

## 6.1. Viscoelastic fiber melt-blowing model

For the melt-blowing of a single fiber in a turbulent air stream we employ the unsteady viscoelastic UCM string model (System 2.12) in Lagrangian description. We classify the resulting quasilinear system of PDEs of first order and discuss the appropriate closing by boundary conditions. The choice of the boundary conditions suggests a description with respect to a fiber tangent associated basis. The fiber tangent  $\boldsymbol{\tau}$  with norm  $e = \|\boldsymbol{\tau}\|$  and direction  $\boldsymbol{t} = \boldsymbol{\tau}/\|\boldsymbol{\tau}\|$  is in particular parameterized with the help of spherical coordinates. Moreover, we introduce the stochastic modeling concept by which the effects of the turbulent aerodynamic velocity fluctuations are incorporated in the fiber system.

### 6.1.1. Asymptotic jet model and classification

The extrusion of a fiber jet from a nozzle into an air stream can be seen as an inflow problem with a domain enlarging over time. Let  $\mathcal{D} = \{(\zeta, t) \in \mathbb{R}^2 \mid \zeta \in \mathcal{Q}(t), t \in (0, t_{end}]\}$  be the space-time domain with time-dependent growing space  $\mathcal{Q}(t) = (\zeta_L(t), 0)$ , where  $d/dt \zeta_L(t) = -v_{in}(t)$ ,  $\zeta_L(0) = 0$ , with  $v_{in}$  being the (scalar) inflow velocity at the nozzle. In the following we assume a constant inflow velocity, i.e.,  $v_{in} = const$ , and the reference  $v_0 = v_{in}$  for nondimensionalization. This yields  $v_{in} = 1$  as well as  $\zeta_L(t) = -t$  and  $\mathcal{Q}(t) = (-t, 0)$  in nondimensional form. The fiber end corresponds to the material parameter  $\zeta = 0$ , whereas the material points entering the fiber (flow) domain at the nozzle are  $\zeta = -t$ . We assume incompressibility of the fiber jet and constant mass and volume line densities at the nozzle yielding  $\varrho_M = e_{in} \rho d_{in}^2 \pi/4$  and  $\varrho_V = e_{in} d_{in}^2 \pi/4$  due to the conservation of mass and volume (cf. System 2.12). Here,  $\rho$  is the constant fiber density,  $d_{in}$  the nozzle diameter and  $e_{in}$  the fiber elongation at the nozzle. We introduce the reference value  $\varrho_{V,0} = d_0^2$  (cf. Tab. 6.1) and assume  $\varrho_{M,0} = \rho d_0^2$  and  $d_0 = d_{in} \sqrt{\pi}/2$  as well as  $e_{in} = 1$ . This yields  $\varrho_M = \varrho_V = 1$  in dimensionless form. Furthermore, to include temperature effects we supply the UCM fiber model (System 2.12) with a time-dependent temperature equation in Lagrangian description. This equation is adapted from (4.9c), where it has been derived for dry spun fibers in an Euler-stationary setting (cf. Sec. 4.1.2). Here, we assume no relevant radial temperature effects and write  $T$  for the averaged one-dimensional temperature field (instead of  $\bar{T}$  before). Since no mass transfer takes place the mass flux over the boundary is zero ( $j_c = 0$ ). Then, the nondimensional model

Composite reference values		
Description	Formula	Unit
Length scale	$\zeta_0 = r_0$	m
Time scale	$t_0 = r_0/v_0$	s
Volume line density	$\varrho_{V,0} = d_0^2$	m <sup>2</sup>
Stress	$\sigma_0 = \varrho_{M,0}v_0^2/d_0^2$	Pa
Pressure	$p_0 = \sigma_0$	Pa
Outer forces	$f_0 = \varrho_{M,0}v_0^2/r_0$	N/m
Air velocity	$v_{*,0} = v_0$	m/s
Air temperature	$T_{*,0} = T_0$	K

Dimensionless numbers	
Description	Formula
Slenderness	$\varepsilon = d_0/r_0$
Reynolds	$Re = \varrho_{M,0}v_0r_0/(d_0^2\mu_0)$
Deborah	$De = \theta_0/t_0$
Mach	$Ma = \sqrt{ReDe}$
Froude	$Fr = v_0/\sqrt{gr_0}$
Temperature Stanton	$St_T = d_0^2\alpha_0/(q_0\varrho_{M,0}v_0)$
Air drag associated	$A_* = \rho_{*,0}d_0v_0^2/f_0$
Air-fiber Reynolds	$Re_* = d_0v_0/v_{*,0}$
Nusselt	$Nu_* = \alpha_0d_0/\lambda_{*,0}$
Prandtl	$Pr_* = q_{*,0}\rho_{*,0}v_{*,0}/\lambda_{*,0}$
Turbulence degree	$Tu_* = k_{*,0}^{1/2}/v_0$
Turbulent time	$Tt_* = \varepsilon_{*,0}r_0/(k_{*,0}v_0)$

**Table 6.1.:** Composite reference values used for nondimensionalization of the fiber melt-blowing model and resulting dimensionless numbers. The following scales are assumed to be given from the specific considered setup  $r_0$ ,  $\mu_0$ ,  $\theta_0$ ,  $q_0$ ,  $T_0$ ,  $\alpha_0$ ,  $\rho_{*,0}$ ,  $v_{*,0}$ ,  $q_{*,0}$ ,  $\lambda_{*,0}$ ,  $k_{*,0}$ ,  $\varepsilon_{*,0}$ . Furthermore, we fix  $\varrho_{M,0} = \rho d_0^2$ ,  $d_0 = d_{in}\sqrt{\pi}/2$ ,  $v_0 = v_{in}$ .

equations for a single fiber in melt-blowing processes read on the domain  $\mathcal{D}$

$$\begin{aligned}
 \partial_t \mathbf{r} &= \mathbf{v}, \\
 \partial_\zeta \mathbf{r} &= \boldsymbol{\tau}, \\
 \partial_t \mathbf{v} &= \partial_\zeta \left( \sigma \frac{\boldsymbol{\tau}}{e^2} \right) + \frac{1}{Fr^2} \mathbf{e}_g + \mathbf{f}_{air}, \\
 \partial_t T &= -\frac{St_T}{\varepsilon} \frac{e}{q} \pi d \alpha (T - T_*), \\
 De \left( \partial_t \sigma - (2\sigma + 3p) \frac{\partial_t e}{e} \right) + \frac{\sigma}{\theta} &= \frac{3}{Re} \frac{\mu}{\theta} \frac{\partial_t e}{e}, \\
 De \left( \partial_t p + p \frac{\partial_t e}{e} \right) + \frac{p}{\theta} &= -\frac{1}{Re} \frac{\mu}{\theta} \frac{\partial_t e}{e},
 \end{aligned} \tag{6.1}$$

with  $e = \|\boldsymbol{\tau}\|$ . Utilizing the assumption of incompressibility and in particular the conservation of volume, yields the dimensionless diameter function  $d : \mathcal{D} \rightarrow \mathbb{R}^+$  with

$$d = \frac{2}{\sqrt{\pi e}}.$$

In contrast to before we use the diameter function  $d$  instead of the radius function  $R$ . This is due to industrial setups, where fiber diameter distributions are considered. The acting outer line force densities arise from gravity with direction  $\mathbf{e}_g$ ,  $\|\mathbf{e}_g\| = 1$ , as well as from the surrounding airflow. Under the assumption of incompressibility the relation  $\mu/\theta = E/3$  with elastic modulus  $E$  holds. We model the dynamic viscosity and relaxation time dependent on the temperature  $T$ , i.e.,  $\mu = \mu(T)$ ,  $\theta = \theta(T)$ . The corresponding rheological laws for an industrial example are specified in Sec. 6.2.2. The reference values used for nondimensionalization and the system characterizing dimensionless parameters are given in Tab. 6.1. As pointed out in Remark 2.14 the pressure is negligibly small for high strain rates  $v = \partial_t e/e \geq 0$ . In [122] this simplification is employed instantaneously to the UCM model for melt-blowing. A detailed comparison to our fiber model is done in Appendix A.2.

The dimensionless fiber model (6.1) can uniquely be written as a quasilinear system of PDEs of first order [65]

$$\partial_t \boldsymbol{\varphi} + \mathbf{M}(\boldsymbol{\varphi}) \cdot \partial_\zeta \boldsymbol{\varphi} + \mathbf{m}(\boldsymbol{\varphi}) = \mathbf{0} \quad (6.2)$$

with the vector of unknowns  $\boldsymbol{\varphi} = (\mathbf{r}, \boldsymbol{\tau}, \mathbf{v}, T, \sigma, p) : \mathcal{D} \rightarrow \mathbb{R}^{12}$ . The system is classified mathematically by the spectrum of the system matrix  $\mathbf{M}$  that consists of the eigenvalues

- $\lambda_1 = 0$  (multiplicity 6),
- $\lambda_{2,3} = \pm \sqrt{\sigma}/e$  (multiplicity 2 each),
- $\lambda_{4,5} = \pm \sqrt{w}/e$  (multiplicity 1 each),  $w = (3\mu(T)/(\theta(T)\text{Ma}^2) + \sigma + 3p)$ .

The system is of hyperbolic type if  $\sigma > 0$  and  $w > 0$ . Otherwise, it is mixed elliptic-hyperbolic, or even shows a parabolic deficiency if  $\sigma = 0$  and/or  $w = 0$ . Since the hyperbolic case is relevant for the application, we focus on it and discuss the closing of the system by appropriate boundary and initial conditions.

### 6.1.2. Boundary conditions

At the fiber jet end, which corresponds to a fixed material point in Lagrangian description ( $\zeta = 0$ ), the characteristic related to the eigenvalue  $\lambda_i$  runs from the

nozzle to the jet end if  $\lambda_i > 0$  and from the jet end towards the nozzle if  $\lambda_i < 0$ . At the nozzle ( $\zeta = -t$ ) the orientations of the characteristics depend on the scalar inflow velocity of the fiber jet, which reads  $v_{in} = 1$  in nondimensional form. If  $\lambda_i > -v_{in} = -1$  for  $i \in \{1, \dots, 5\}$ , the corresponding characteristic propagates from the nozzle into the fiber domain (not necessarily towards the jet end), otherwise the other way round. The orientations of the characteristics yield requirements on the boundary conditions with regard to the well-posedness of the problem. Since  $\lambda_3 < 0$  (multiplicity 2) and  $\lambda_5 < 0$  (multiplicity 1), we have to pose three boundary conditions at the fiber jet end. Because of the spinning setup we model the fiber end ( $\zeta = 0$ ) as stress-free, i.e.,

$$\sigma(0, t) = 0, \quad p(0, t) = 0,$$

for  $t \in (0, t_{end}]$ . Employing the viscoelastic material law for  $\sigma$  yields a constant fiber elongation at the fiber end over time, i.e.,  $\partial_t e(0, t) = 0$ . To preserve this compatibility condition we pose ( $t \in (0, t_{end}]$ )

$$e(0, t) = 1,$$

assuming the fiber jet to leave the nozzle unstretched. The eigenvalues  $\lambda_1, \lambda_2, \lambda_4$  are non-negative and thus imply nine boundary conditions at the nozzle ( $\zeta = -t$ ,  $t \in [0, t_{end}]$ ),

$$\mathbf{r}(-t, t) = \mathbf{r}_{in}, \quad (\boldsymbol{\tau}/e)(-t, t) = \mathbf{t}_{in}, \quad \mathbf{v}(-t, t) = v_{in} \mathbf{t}_{in}, \quad T(-t, t) = T_{in}.$$

Here, the nozzle position  $\mathbf{r}_{in}$  and the fiber direction at the nozzle  $\mathbf{t}_{in}$  are assumed to be constant. Due to  $v_{in} = 1$  in nondimensional form, the boundary condition for the velocity reduces to  $\mathbf{v}(-t, t) = \mathbf{t}_{in}$ . Moreover, we set the following initial conditions for  $t = 0$ ,

$$\sigma(0, 0) = \sigma_{in}, \quad p(0, 0) = p_{in}, \quad e(0, 0) = 1.$$

Depending on the propagation speed of the characteristics at the nozzle we pose further boundary conditions: we additionally prescribe for  $t \in (0, t_{end}]$

$$\begin{aligned} \sigma(-t, t) &= \sigma_{in}, & p(-t, t) &= p_{in}, & \text{if } \lambda_{3,in} > -1 \text{ (multiplicity 2),} \\ e(-t, t) &= 1 & & & \text{if } \lambda_{5,in} > -1 \text{ (multiplicity 1)} \end{aligned}$$

with  $\lambda_{3,in} = -\sqrt{\sigma_{in}}$  and  $\lambda_{5,in} = -\sqrt{3\mu(T_{in})/(\text{Ma}^2\theta(T_{in})) + \sigma_{in} + 3p_{in}}$ . The total time-derivative of the fiber curve  $\mathbf{r}$  at the nozzle yields the compatibility condition  $\mathbf{v}(-t, t) = \boldsymbol{\tau}(-t, t)$  for all times  $t$ . Through the above choice of the boundary conditions for  $\mathbf{v}$ ,  $\boldsymbol{\tau}/e$ , and  $e$  at the nozzle this condition is inherently fulfilled.

The choice of the boundary conditions and in particular the decomposition of the fiber tangent  $\boldsymbol{\tau} = e\mathbf{t}$  into elongation  $e = \|\boldsymbol{\tau}\|$  and direction  $\mathbf{t}$ ,  $\|\mathbf{t}\| = 1$ , suggests

a reformulation of the corresponding dynamic equation  $\partial_\zeta \mathbf{r} = \boldsymbol{\tau}$ . Making use of the compatibility condition  $\partial_t \boldsymbol{\tau} = \partial_\zeta \mathbf{v}$  (cf. (2.2c)) yields an equation for the elongation  $e$

$$\partial_t e - \mathbf{t} \cdot \partial_\zeta \mathbf{v} = 0.$$

The normalized tangent  $\mathbf{t}$  can be parameterized by means of spherical coordinates

$$\mathbf{t}(\vartheta, \varphi) = (\sin \vartheta \cos \varphi, \sin \vartheta \sin \varphi, \cos \vartheta), \quad \vartheta \in [0, \pi], \quad \varphi \in [0, 2\pi).$$

Then, its time-derivative reads  $\partial_t \mathbf{t} = \mathbf{n} \partial_t \vartheta + \mathbf{b} \partial_t \varphi$  with normal  $\mathbf{n}$  and binormal  $\mathbf{b}$

$$\begin{aligned} \mathbf{n}(\vartheta, \varphi) &= (\cos \vartheta \cos \varphi, \cos \vartheta \sin \varphi, -\sin \vartheta), \\ \mathbf{b}(\vartheta, \varphi) &= (-\sin \vartheta \sin \varphi, \sin \vartheta \cos \varphi, 0). \end{aligned}$$

The set  $\{\mathbf{t}, \mathbf{n}, \mathbf{b}\} \subset \mathbb{R}^3$  forms an orthogonal basis with  $\|\mathbf{t}\| = \|\mathbf{n}\| = 1$ . Employing

$$\partial_t \mathbf{t} = \partial_t \left( \frac{\boldsymbol{\tau}}{e} \right) = \frac{1}{e} (\mathbb{1} - \mathbf{t} \otimes \mathbf{t}) \cdot \partial_\zeta \mathbf{v}$$

with identity matrix  $\mathbb{1} \in \mathbb{R}^{3 \times 3}$  gives relations for the polar angle  $\vartheta$  and azimuth angle  $\varphi$

$$\partial_t \vartheta = \frac{1}{e} \mathbf{n} \cdot \partial_\zeta \mathbf{v}, \quad \sin^2 \vartheta \partial_t \varphi = \frac{1}{e} \mathbf{b} \cdot \partial_\zeta \mathbf{v}.$$

Summing up, our viscoelastic unsteady fiber model on a growing domain in Lagrangian description is given by System 6.1.

**System 6.1** (Unsteady viscoelastic fiber melt-blowing model).

*Kinematic and dynamic equations as well as material laws in  $\mathcal{D}$ :*

$$\begin{aligned} \partial_t \mathbf{r} - \mathbf{v} &= \mathbf{0}, \\ \partial_t e - \mathbf{t} \cdot \partial_\zeta \mathbf{v} &= 0, \\ \partial_t \vartheta - \frac{1}{e} \mathbf{n} \cdot \partial_\zeta \mathbf{v} &= 0, \\ \sin^2 \vartheta \partial_t \varphi - \frac{1}{e} \mathbf{b} \cdot \partial_\zeta \mathbf{v} &= 0, \\ \partial_t \mathbf{v} - \partial_\zeta \left( \sigma \frac{\mathbf{t}}{e} \right) - \frac{1}{\text{Fr}^2} \mathbf{e}_g - \mathbf{f}_{air} &= \mathbf{0}, \\ \partial_t T + \frac{\text{St}_T}{\varepsilon} \frac{e}{q} \pi d \alpha (T - T_*) &= 0, \\ \text{De} \partial_t \sigma + \left( -\text{De} (2\sigma + 3p) - \frac{\mu}{\theta} \frac{3}{\text{Re}} \right) \frac{\mathbf{t}}{e} \cdot \partial_\zeta \mathbf{v} + \frac{\sigma}{\theta} &= 0, \\ \text{De} \partial_t p + \left( \text{De} p + \frac{\mu}{\theta} \frac{1}{\text{Re}} \right) \frac{\mathbf{t}}{e} \cdot \partial_\zeta \mathbf{v} + \frac{p}{\theta} &= 0, \end{aligned}$$

*Initial-boundary conditions at the nozzle,  $\zeta = -t$ ,  $t \in [0, t_{end}]$ :*

$$\begin{aligned} \mathbf{r}(-t, t) &= \mathbf{r}_{in}, & \vartheta(-t, t) &= \vartheta_{in}, & \varphi(-t, t) &= \varphi_{in}, \\ \mathbf{v}(-t, t) &= \mathbf{t}(\vartheta_{in}, \varphi_{in}), & T(-t, t) &= T_{in}, \end{aligned}$$

*Initial conditions,  $\zeta = 0$ ,  $t = 0$ :*

$$e(0, 0) = 1, \quad \sigma(0, 0) = \sigma_{in}, \quad p(0, 0) = p_{in},$$

*Boundary conditions at the nozzle,  $\zeta = -t$ ,  $t \in (0, t_{end}]$ :*

$$\begin{aligned} \text{if } \lambda_{3,in} > -1: & \quad \sigma(-t, t) = \sigma_{in}, & p(-t, t) &= p_{in}, \\ \text{if } \lambda_{5,in} > -1: & \quad e(-t, t) = 1, \end{aligned}$$

*Boundary conditions at the fiber end,  $\zeta = 0$ ,  $t \in (0, t_{end}]$ :*

$$e(0, t) = 1, \quad \sigma(0, t) = 0, \quad p(0, t) = 0.$$

The System 6.1 is closed by models for the aerodynamic line force density  $f_{air}$ , the heat transfer coefficient  $\alpha$  as well as rheological laws for the dynamic viscosity  $\mu$  and the relaxation time  $\theta$ . We consider one-way coupling of the airflow with the fiber, neglecting feedback effects of the fiber on the airflow. The corresponding air drag model  $f_{air}$  equals (2.9) introduced in Sec. 2.3. For the heat transfer coefficient we employ the Nusselt number model (4.12) previously introduced in Sec. 4.1.4. Again all airflow fields are assumed to be provided by an external computation. The rheological laws for  $\mu$  and  $\theta$  will be introduced in the considered industrial setup (Sec. 6.2.2).

System 6.1 is a BVP of a quasilinear system of PDEs of first order on a growing domain. We reformulate it as

$$\mathbf{K}(\mathbf{y}) \cdot \partial_t \mathbf{y} + \mathbf{L}(\mathbf{y}) \cdot \partial_\zeta \mathbf{y} + \mathbf{l}(\mathbf{y}) = \mathbf{0} \quad (6.3)$$

with the vector of unknowns  $\mathbf{y} = (\mathbf{r}, e, \vartheta, \varphi, \mathbf{v}, T, \sigma, p) : \mathcal{D} \rightarrow \mathbb{R}^{12}$  on the space-time domain  $\mathcal{D} = (-t, 0) \times (0, t_{end}]$ . The introduction of the matrix  $\mathbf{K}$  avoids a singularity for  $\sin \vartheta = 0$ . For  $\sin \vartheta \neq 0$ ,  $\mathbf{K}$  is invertible revealing the unique quasilinear form (6.2). Utilizing formulation (6.3) System 6.1 is discretized with the scheme described in Sec. 3.2, i.e., we use finite volumes in space based on a central flux approximation with Lax-Friedrichs stabilization and the implicit Euler method in time. The one-sided fiber-airflow coupling is realized by Algorithm 3.7.

### 6.1.3. Incorporation of turbulent airflow velocity fluctuations

A direct numerical simulation of the turbulent airflow in the application is not possible due to the required high resolution. Hence, a statistical turbulence description is used where the airflow velocity  $\mathbf{v}_*$  is assumed to consist of a mean (deterministic) part  $\bar{\mathbf{v}}_*$  and a fluctuating (stochastic) part  $\mathbf{v}'_*$ , i.e.,

$$\mathbf{v}_* = \bar{\mathbf{v}}_* + \mathbf{v}'_*$$

This splitting is called Reynolds decomposition. Inserting the Reynolds decomposition for velocity  $\mathbf{v}_*$ , pressure  $p_*$ , density  $\rho_*$  and temperature  $T_*$  into the unsteady version of the compressible Navier-Stokes equations (3.8) presented in Sec. 3.4 and applying ensemble as well as Favre averaging yields the so called compressible Reynolds-averaged Navier-Stokes (RANS) equations [33, 90]. The RANS equations contain an additional term called the Reynolds stress tensor that consists of tuple correlations of the velocity fluctuations, which are additional unknowns of the problem. To close the RANS equations so called turbulence models are employed. In the following we employ the  $k_*$ - $\epsilon_*$  turbulence model. However, any turbulence model only provides information for the tuple correlations of the velocity fluctuations. To obtain  $\mathbf{v}'_*$  explicitly as random field we apply a turbulence reconstruction that has been developed in [50] on basis of a  $k_*$ - $\epsilon_*$  turbulence model. Assuming dimensionless space-time-dependent fields for the turbulent kinetic energy  $k_*$  and the viscous dissipation of the turbulent motions per unit mass  $\epsilon_*$  to be given, the general concept of the turbulence reconstruction is to model the local turbulent fluctuations as homogeneous, isotropic, incompressible Gaussian random fields in space and time,  $\mathbf{v}'_{*,loc} = \mathbf{v}'_{*,loc}(\mathbf{x}, t; \nu_*, \bar{\mathbf{v}}_*)$ , as done in [66, 68]. These local fluctuations depend parametrically on the kinematic viscosity  $\nu_*$  and mean velocity  $\bar{\mathbf{v}}_*$  of the airflow and have the expectation  $\mathbb{E}(\mathbf{v}'_{*,loc}) = \mathbf{0}$ . Their covariance function is prescribed as product of the initial correlations transported with the local mean velocity and their temporal decay

$$\mathbb{E}\left(\mathbf{v}'_{*,loc}(\mathbf{x} + \mathbf{y}, t + s; \xi, \mathbf{w}) \otimes \mathbf{v}'_{*,loc}(\mathbf{x}, t; \xi, \mathbf{w})\right) = \boldsymbol{\gamma}(\mathbf{y} - \mathbf{w}t; \xi) \Phi(s)$$

with  $\boldsymbol{\gamma} : \mathbb{R}^3 \times \mathbb{R} \rightarrow \mathbb{R}^3$  isotropic and  $\Phi : \mathbb{R} \rightarrow \mathbb{R}$  even for any  $\mathbf{x}, \mathbf{y}, \mathbf{w} \in \mathbb{R}^3$  and  $t, s, \xi \in \mathbb{R}_0^+$ . Regarding the local kinetic turbulent energy and dissipation rate the following relations (in dimensionless formulation) hold

$$\begin{aligned} \frac{1}{2} \mathbb{E}\left(\mathbf{v}'_{*,loc}(\mathbf{x}, t; \xi, \mathbf{w}) \cdot \mathbf{v}'_{*,loc}(\mathbf{x}, t; \xi, \mathbf{w})\right) &= 1, \\ \mathbb{E}\left(\nabla_{\mathbf{x}} \mathbf{v}'_{*,loc}(\mathbf{x}, t; \xi, \mathbf{w}) : \nabla_{\mathbf{x}} \mathbf{v}'_{*,loc}(\mathbf{x}, t; \xi, \mathbf{w})\right) &= \frac{1}{\xi}, \end{aligned}$$

where  $:$  denotes the scalar product for matrices and  $\nabla_{\mathbf{x}}$  the nabla operator with respect to the variable  $\mathbf{x}$ . Due to the assumptions of isotropy and incompressibility

the Fourier-transform  $\mathcal{F}_\gamma$  of the initial correlations  $\gamma$  can be expressed in terms of a single scalar-valued function, the so-called energy spectrum  $E : \mathbb{R}_0^+ \times \mathbb{R}_0^+ \rightarrow \mathbb{R}_0^+$ , i.e.,

$$\mathcal{F}_\gamma(\mathbf{y}; \xi) = \frac{1}{(2\pi)^3} \int_{\mathbb{R}^3} \exp(-i\mathbf{y} \cdot \mathbf{x}) \gamma(\mathbf{x}; \xi) d\mathbf{x} = \frac{1}{4\pi} \frac{E(\|\mathbf{y}\|; \xi)}{\|\mathbf{y}\|^2} \left( \mathbb{1} - \frac{1}{\|\mathbf{y}\|^2} \mathbf{y} \otimes \mathbf{y} \right).$$

Then, the above relations for turbulent energy and dissipation rate become (cf. [66])

$$\int_{\mathbb{R}_0^+} E(y; \xi) dy = 1, \quad \int_{\mathbb{R}_0^+} y^2 E(y; \xi) dy = \frac{1}{2\xi}. \quad (6.4)$$

In contrast to [66, 68], we use a simplified energy spectrum

$$E(y; \xi) = \begin{cases} \frac{1}{2} y^{-5/3}, & y_1 \leq y \leq y_2, \\ 0, & \text{else,} \end{cases} \quad y_i = y_i(\xi)$$

which only reflects Kolmogorov's 5/3-Law but ensures the differentiability of the Gaussian field and enables the corresponding distribution function  $F_E : [y_1, y_2] \times \mathbb{R}_0^+ \rightarrow [0, 1]$  and its inverse  $F_E^{-1} : [0, 1] \times \mathbb{R}_0^+ \rightarrow [y_1, y_2]$  to be stated explicitly by analytic expressions

$$F_E(y; \xi) = \frac{3}{4} (y_1(\xi)^{-2/3} - y^{-2/3}), \quad F_E^{-1}(z; \xi) = \left( y_1(\xi)^{-2/3} - \frac{4}{3} z \right)^{-3/2}.$$

The  $\xi$ -dependent wave numbers  $y_i$ , ( $i = 1, 2$ ),  $0 < y_1 < y_2$ , can be concluded from the relations (6.4) and read

$$y_i = \left( \frac{3}{2(\sqrt{z_E + 1} + (-1)^{i+1})} \right)^{3/2}, \quad z_E = \frac{1}{2} \left( b_E + \sqrt{\frac{2a_E}{b_E} - b_E^2} \right),$$

with

$$a_E = (54/8\xi)^2, \quad b_E = (c_E/18^{1/3} - (128/3)^{1/3} a_E/c_E)^{1/2}, \\ c_E = \left( 9a_E^2 + \sqrt{786a_E^3 + 81a_E^4} \right)^{1/3}.$$

The analytic expressions are advantageous in the sampling of the random field as they speed up drastically the numerical computations. Concerning the temporal correlation function we use the model of [50, 68]

$$\Phi(t) = \exp\left(-\frac{t^2}{2t_L^2}\right)$$

with  $t_L = 0.212$  being the dimensionless decay time of the turbulent structures.

To form the large-scale structure of the global turbulence the local fluctuation fields are superposed based on a Global-from-Local assumption. The globalization strategy according to [50] yields

$$\mathbf{v}'_{\star} = \text{Tu}_{\star} k_{\star}^{1/2} \mathbf{v}'_{\star,loc} \left( \frac{\text{Tt}_{\star}}{\text{Tu}_{\star}} \frac{\epsilon_{\star}}{k_{\star}^{3/2}} \mathbf{r}, \text{Tt}_{\star} \frac{\epsilon_{\star}}{k_{\star}} t; \frac{\epsilon}{\text{Re}_{\star}} \frac{\text{Tt}_{\star}}{\text{Tu}_{\star}^2} \frac{\epsilon_{\star}}{k_{\star}^2} \mathbf{v}_{\star}, \frac{1}{\text{Tu}_{\star}} \frac{1}{k_{\star}^{1/2}} \bar{\mathbf{v}}_{\star} \right). \quad (6.5)$$

Besides the slenderness ratio  $\epsilon$  and the air-fiber Reynolds number  $\text{Re}_{\star}$ , the occurring dimensionless numbers are the degree of turbulence  $\text{Tu}_{\star}$  and the turbulent time scale ratio  $\text{Tt}_{\star}$  as given in Tab. 6.1.

In summary, plugging the airflow velocity  $\mathbf{v}_{\star} = \bar{\mathbf{v}}_{\star} + \mathbf{v}'_{\star}$  into the air drag model (2.9) and heat transfer model (4.12) directly includes the effects of the turbulent velocity fluctuations of the underlying airflow into our UCM fiber model System 6.1. For resulting lift forces on the fiber see Remark 6.2. Note that the occurring turbulent length and time scales give requirements on the spatial and temporal resolution in our numerical solution algorithm (cf. Rem. 6.3). For details on the general sampling procedure providing a fast and accurate sampling of the random fields we refer to [50].

**Remark 6.2** (Fluctuating lift forces). *In industrial melt-blowing processes fluctuating lift forces [72] on a fiber are created through airflow vortices approaching the fiber and by vortex shedding at the back of the fiber. While the latter can be neglected since the fiber is mainly following the turbulent air stream, the first mechanism is included with the help of the following ansatz: the local turbulent unsteady velocity fluctuations  $\mathbf{v}'_{\star}$  are plugged into the air drag model (2.9), meaning local observations are mapped into a stationary far field consideration. This leads to aerodynamic forces on the fiber acting also perpendicular to the  $(\bar{\mathbf{v}}_{\star} - \mathbf{v})$ - $\tau$ -plane. In view of particle dynamics the underlying mechanism is known as turbulent dispersion.*

**Remark 6.3** (Spatial and temporal resolution). *The temporal and spatial grid sizes have to be chosen in such a way that the turbulent scales of the underlying airflow are resolved properly. In particular,  $l'_{\star} = \text{Tu}_{\star} / \text{Tt}_{\star} k_{\star}^{3/2} / \epsilon_{\star}$  is the dimensionless turbulent length scale indicating the expected length of the large-scale vortices, and  $t'_{\star} = 1 / \text{Tt}_{\star} k_{\star} / \epsilon_{\star}$  is the dimensionless turbulent time scale describing the expected creation and break-up time of the vortices (cf. turbulence reconstruction (6.5)). Furthermore, the time that a vortex needs to pass a fixed material point of the fiber due to their relative velocity has to be considered for the temporal resolution. In total, the requirements for a successful simulation in terms of the spatial  $\Delta\zeta$  and temporal  $\Delta t$  mesh size read*

$$\Delta\zeta \leq \frac{l'_{\star}}{e}, \quad \Delta t \leq \min \left( t'_{\star}, \frac{l'_{\star}}{\|\mathbf{v}_{\star} - \mathbf{v}\|} \right). \quad (6.6)$$

In our numerical scheme appropriate grid sizes are estimated by computing the bounds for all given airflow data with assumptions on the maximal fiber velocity and elongation.

**Remark 6.4** (Viscous Cosserat rod fiber model). In [89] the described reconstruction approach of turbulent airflow velocity fluctuations has been applied to a viscous Cosserat rod fiber model. However, longtime simulations of melt-blowing processes failed due to arising instabilities in the numerical scheme. This might be due to the introduction of several Lagrangian multipliers leading to an artificially inflated system. There, the introduction of these additional variables was necessary to reduce the index of the underlying differential algebraic equations and to stabilize the corresponding kinematic fiber equations. In the following, we will see that our viscoelastic UCM fiber model in combination with our robust numerical scheme does not have this problem.

## 6.2. Industrial melt-blowing

In this section we investigate an industrial melt-blowing scenario that has been studied in [50] with the help of a simplified ODE model for the fiber jet position, velocity and elongation. We employ our more sophisticated PDE fiber jet model (System 6.1), which additionally contains a viscoelastic material behavior and thermal effects describing the jet cooling and solidification. The PDE model is solved numerically with the finite volume scheme in space and the implicit Euler method in time as described in Sec. 3.2. Before we present our simulation results, we specify the industrial setup and state the closing models for the dynamic viscosity as well as relaxation time and elastic modulus. In the scenario we face step size restrictions (cf. Remark 6.3) that prevent the computability of the whole fiber from nozzle to conveyor belt. To handle this numerical problem we suggest and discuss an appropriate simulation strategy.

### 6.2.1. Process setup

In the considered melt-blowing setup a high-speed air stream is directed vertically downwards in direction of gravity and enters the domain of interest via thin slot dies. The spinning nozzles are located in between and extrude the polymeric fiber jets in the same direction, see Fig. 6.2. We choose an outer orthonormal basis  $\{\vec{a}_1, \vec{a}_2, \vec{a}_3\} \subset \mathbb{E}^3$ , where  $\vec{a}_3$  points in the direction of gravity (i.e.,  $\vec{a}_3 = \vec{e}_g$ ) and  $\vec{a}_2$  is aligned with the slot inlet. The mean quantities of the turbulent airflow are time-independent and homogeneous in  $\vec{a}_2$ -direction such that a stationary

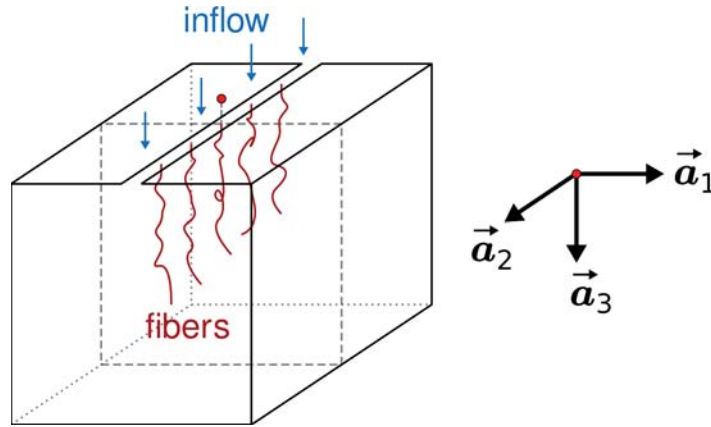


**Figure 6.2.:** Illustration of the considered industrial melt-blowing process. The two-dimensional cut ( $\vec{a}_1$ - $\vec{a}_3$ -plane, marked by dashed line) represents the whole flow domain due to homogeneity in  $\vec{a}_2$ -direction.

Process and physical parameters			
Description	Symbol	Value	Unit
Device height	$H$	$1.214 \cdot 10^{-1}$	m
Nozzle diameter	$d_{in}$	$4 \cdot 10^{-4}$	m
Speed at nozzle	$v_{in}$	$1 \cdot 10^{-2}$	m/s
Polar angle at nozzle	$\vartheta_{in}$	0	–
Azimuth angle at nozzle	$\varphi_{in}$	0	–
Temperature at nozzle	$T_{in}$	$5.532 \cdot 10^2$	K
Heat transfer at nozzle	$\alpha_{in}$	$1.595 \cdot 10^3$	W/(m <sup>2</sup> K)
Air thermal conductivity at nozzle	$\lambda_{*,in}$	$2.42 \cdot 10^{-2}$	W/(m K)
Air kinematic viscosity at nozzle	$\nu_{*,in}$	$1.8 \cdot 10^{-5}$	m <sup>2</sup> /s
Air specific heat capacity at nozzle	$q_{*,in}$	$1.006 \cdot 10^3$	J/(kg K)
Air density at nozzle	$\rho_{*,in}$	1.187	kg/m <sup>3</sup>
Air turbulent kinetic energy at nozzle	$k_{*,in}$	$2.181 \cdot 10^2$	m <sup>2</sup> /s <sup>2</sup>
Air viscous dissipation rate at nozzle	$\epsilon_{*,in}$	$1.808 \cdot 10^7$	m <sup>2</sup> /s <sup>3</sup>
End time	$t_{end}$	$2.00 \cdot 10^{-3}$	s
Fiber density	$\rho$	$7 \cdot 10^2$	kg/m <sup>3</sup>
Fiber specific heat capacity	$q$	$2.1 \cdot 10^3$	J/(kg K)

**Table 6.2.:** Overview over process and physical parameters in the industrial melt-blowing setup according to [50].

$k_*$ - $\epsilon_*$  simulation for a representative two-dimensional cut showing the  $\vec{a}_1$ - $\vec{a}_3$ -plane ( $x_2 = 0$ ) is reasonable. The origin of the outer basis is aligned with the external given airflow data, such that the considered nozzle is at the position  $\mathbf{r}_{in} = (0, 0, 2.85 \cdot 10^{-2})$  m in the airflow field. We use the same  $k_*$ - $\epsilon_*$  simulation results as in [50], supplemented with an additional temperature profile as depicted in Fig. 6.3. The melt-blown fiber polymer is of polypropylene (PP) type with

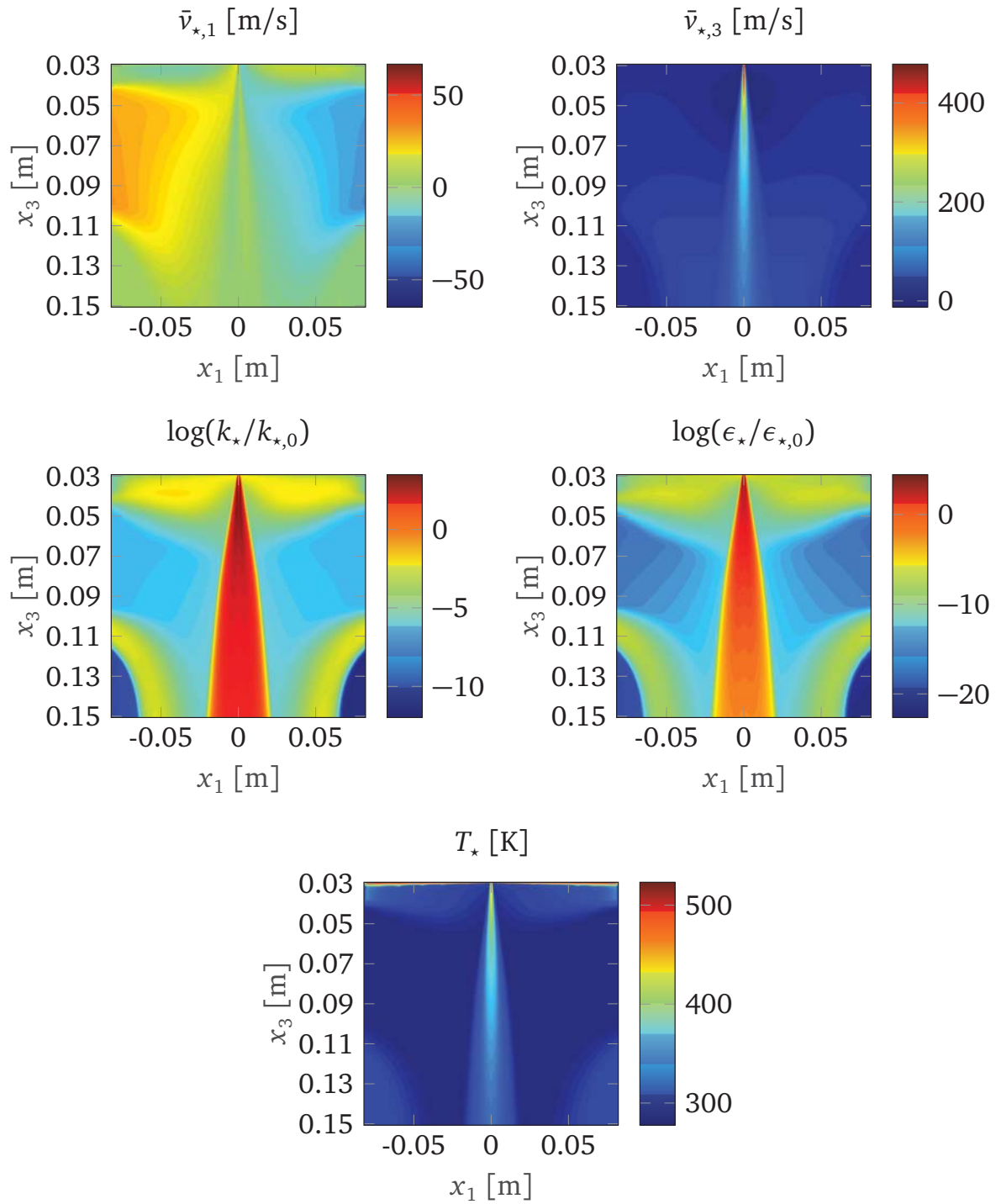


**Figure 6.3.:** Airflow simulation of the representative two-dimensional flow domain (cf. Fig. 6.2). *Top:* Components of mean airflow velocity  $\bar{v}_*$  in  $\vec{a}_1$ - and  $\vec{a}_3$ -direction (denoted by  $\bar{v}_{*,1}$  and  $\bar{v}_{*,3}$  respectively). *Middle:* Dimensionless turbulent kinetic energy  $k_*/k_{*,0}$  and dissipation rate  $\epsilon_*/\epsilon_{*,0}$  in logarithmic scale. *Bottom:* Temperature  $T_*$ .

Setup-specific reference values		
Description	Formula	Unit
Mass line density	$\varrho_{M,0} = \rho d_0^2$	kg/m
Curve	$r_0 = H$	m
Diameter	$d_0 = d_{in} \sqrt{\pi}/2$	m
Dynamic viscosity	$\mu_0 = \mu(T_0)$	Pa s
Relaxation time	$\theta_0 = \theta(T_0)$	s
Specific heat capacity	$q_0 = q$	J/(kg K)
Further scales	$b_0 = b_{in},$ $b \in \{v, T, \alpha, \rho_*, v_*, q_*, \lambda_*, k_*, \epsilon_*\}$	

Dimensionless numbers		
Description	Symbol	Value
Slenderness	$\varepsilon$	$2.92 \cdot 10^{-3}$
Reynolds	Re	$2.99 \cdot 10^{-1}$
Deborah	De	$4.94 \cdot 10^{-2}$
Mach	Ma	$1.22 \cdot 10^{-1}$
Froude	Fr	$9.16 \cdot 10^{-3}$
Temperature Stanton	$St_T$	$1.08 \cdot 10^{-1}$
Air drag associated	$A_*$	$5.81 \cdot 10^{-1}$
Air-fiber Reynolds	$Re_*$	$1.97 \cdot 10^{-1}$
Nusselt	$Nu_*$	$2.34 \cdot 10^1$
Prandtl	$Pr_*$	$8.89 \cdot 10^{-1}$
Turbulence degree	$Tu_*$	$1.48 \cdot 10^3$
Turbulent time	$Tt_*$	$1.01 \cdot 10^6$

**Table 6.3.:** Setup-specific reference values and resulting dimensionless numbers for the industrial melt-blowing setup according to [50] (cf. Tab. 6.2).

material parameters taken from [50]. The process and physical parameters are listed in Tab. 6.2. The setup-specific reference values as well as the resulting dimensionless numbers are given in Tab. 6.3.

### 6.2.2. Model closing

For the temperature-dependent dynamic viscosity of the PP-type fiber material we employ the Arrhenius law. The corresponding relation for the dimensionless viscosity  $\mu$  depending on the temperature  $T$  is given by

$$\mu(T) = \frac{1}{\mu_0} \mathcal{M}(T T_0), \quad \mathcal{M}(T) = a_\mu \exp\left(\frac{b_\mu}{T - c_\mu}\right).$$

The polymer-specific constants coming from measurements are  $a_\mu = 0.1352$  Pa s,  $b_\mu = 852.323$  K,  $c_\mu = 273.15$  K. We choose the following heuristic model for the relaxation time

$$\theta(T) = \frac{1}{\theta_0} \mathcal{T}(TT_0), \quad \mathcal{T}(T) = 3 \frac{\mathcal{M}(T) + b_\theta}{a_\theta}$$

with  $a_\theta = 10^9$  Pa and  $b_\theta = 2 \cdot 10^8$  Pa s showing a meaningful limit behavior: for  $T \rightarrow \infty$  the dimensional relaxation time is of order  $\mathcal{T} \sim \mathcal{O}(10^{-1}$  s), which is typical for melt-blown polymers, see for example [122]. Furthermore, employing the relation  $\mu/\theta = E/3$  the resulting dimensionless elastic modulus  $E$  reads

$$E(T) = \frac{\theta_0}{\mu_0} \mathcal{E}(T_0T), \quad \mathcal{E}(T) = 3 \frac{\mathcal{M}(T)}{\mathcal{T}(T)}.$$

For  $T \rightarrow c_\mu = 273.15$  K the dimensional elastic modulus  $\mathcal{E}$  approaches  $\mathcal{E} = a_\theta = 10^9$  Pa – a typical value for hardened polymer, see for example [12].

### 6.2.3. Simulation strategy

Expecting a maximal fiber elongation  $e = 10^6$  and a maximal dimensionless relative velocity between fiber and airflow  $\|\mathbf{v}_* - \mathbf{v}\| \leq \|\mathbf{v}_*\| = 4.78 \cdot 10^4$  (in dimensionless form) in the industrial melt-blowing, the step size restriction for the spatial and temporal fiber discretization (6.6) gives

$$\Delta\zeta \leq 5.77 \cdot 10^{-10}, \quad \Delta t \leq 1.21 \cdot 10^{-6} \quad (6.7)$$

(cf. Fig. 6.3). Such a resolution implies computationally impractical runtimes. However, to make a simulation for the setup feasible, we suggest the following strategy that is motivated from observations of the process.

In the region close to the nozzle the high-speed air stream pulls the slowly extruded fiber jet rapidly down without any lateral bending. The hot air temperatures prevent fiber cool-down and solidification. Thus, the magnitude of the Deborah number  $De$  at the nozzle (cf. Tab. 6.3) allows the consideration of the viscous limit case  $De \rightarrow 0$  (see Sec. 2.2.3). Moreover, the fiber jet behavior is mainly determined by the mean airflow, turbulent effects play a negligible role. Hence, we assume that in the nozzle region (i.e., deterministic region) the polymer jet can be described by a steady uni-axial viscous fiber model with deterministic aerodynamic force and heat transfer. This model follows from System 6.1 by a re-parameterization into Euler (spatial) description, transition to steady-state, and the limit  $De \rightarrow 0$ . The resulting BVP of ODEs is solved by the continuation-collocation method presented in Sec. 3.1. Further details on the model and its

numerical treatment are given in Remark 6.5. Note that the use of the viscous fiber model is not only physically reasonable, but it also simplifies crucially the numerical treatment. Concerning the viscoelastic fiber model, the rapid changes of the fiber quantities in the nozzle region caused by the immediate pull down of the fiber yields multiple changes in the structure of the quasilinear system matrix in view of its eigenvalues and its resulting classification. This means that the runs of the characteristics change their direction several times. In the steady uni-axial model this leads to singular system matrices and closing problems with appropriate boundary conditions making the numerical treatment extremely complicated. This issue has been addressed by [60] in the context of existence regimes for solutions of an uni-axial UCM fiber model under gravitational forces. We circumvent these problems when using the viscous fiber model where no mathematical regime changes take place.

In the region away from the nozzle the turbulent aerodynamic fluctuations crucially affect the fiber behavior (i.e., stochastic region). By means of the uni-axial steady fiber solution (from the nozzle region) we identify a coupling point, from where on the further fiber behavior downwards to the bottom is described by the unsteady viscoelastic fiber model (System 6.1) accounting for turbulent effects. The simulation with the numerical scheme from Sec. 3.2 becomes here feasible since the expected elongation and relative velocities in this domain are much smaller and hence the spatial and temporal step size restrictions weaken compared to (6.7).

The coupling between the stationary and unsteady fiber simulations is done in the following way: Let the spatial fiber domain in the Eulerian parameterization  $Q(t) = Q_d \cup Q_s(t)$  be divided into the time-independent deterministic part  $Q_d$ , where the fiber is uni-axially stretched, and the time-dependent stochastic part  $Q_s(t)$ , where the fiber is strongly affected by the turbulent fluctuations. Consider  $C = Q_d \cap Q_s(t)$  to be the time-independent coupling point between the deterministic and the stochastic domain. First, we perform the simulation of the steady viscous fiber model (System 6.6 in Remark 6.5) for the whole fiber domain, i.e.,  $Q_d = Q$ , yielding solutions for the scalar fiber speed  $u$ , temperature  $T$ , stress  $\sigma$  and pressure  $p$ . Second, we determine the coupling point  $C$  by the ratio of the relative velocity between fiber and airflow  $v_{rel} = \|\mathbf{v}_* - u\boldsymbol{\tau}\|$  and the turbulent velocity scale  $k_*^{1/2}$ , in particular

$$C = \min \left\{ s \in Q \left| \left( \frac{v_{rel} v_0}{(k_* k_{*,0})^{1/2}} \right) (s) \leq 10 \right. \right\}.$$

Thus, the coupling point is the nearest point to the nozzle where the ratio of the relative velocity and the turbulent velocity scale is below one order of magnitude. At  $C$  the (dimensional) quantities of the stationary solution are denoted by  $u_C$ ,  $T_C$ ,  $\sigma_C$ ,  $p_C$ . Third, for the subsequent solving of the unsteady viscoelastic fiber model

(System 6.1) on  $\mathcal{Q}_s(t)$  (reformulated in Lagrangian coordinates) we adjust the typical values and adapt the initial conditions. We particularly set the reference values used for the nondimensionalization to be

$$r_0 = (1 - C)H, \quad d_0 = \frac{\sqrt{\pi}}{2} \sqrt{\frac{v_{in}}{u_C}} d_{in}, \quad v_0 = u_C, \quad T_0 = T_C,$$

then the dimensionless numbers change accordingly. The altered initial conditions read

$$\sigma_{in} = \sigma_C, \quad p_{in} = p_C.$$

These modifications can be interpreted as putting a fictitious nozzle with adjusted extrusion conditions at the spatial position of the coupling point  $\mathcal{C}$ . The diameter of the fictitious nozzle reflects the pre-elongations of the extruded fiber by the factor  $u_C/v_{in}$  compared to  $d_{in}$  of the original nozzle.

In the setup the crucial stretching of the fiber takes place in the upper part of the device and ends when the fiber is nearly solidified. Since we are interested in the maximal achieved fiber elongations as well as in the corresponding fiber diameter distribution but not in the lay-down process, it is sufficient to cut off the fiber before it reaches the bottom of the device. We choose to cut off the fiber, when it reaches the height corresponding to  $x_3 = 9.45 \cdot 10^{-2}$  m. Below this point the airflow temperature satisfies  $T_* < 353.15$  K (see Fig. 6.3). We expect the fiber dynamic viscosities to be of magnitude  $\mu \sim \mathcal{O}(10^3 \text{ Pa s})$ , implying that no noticeable further fiber elongations take place.

**Remark 6.5** (Stationary viscous uni-axial model). *Starting from System 6.1 the stationary problem in Euler description (cf. Sec. 2.1.6) for an uni-axial fiber with orientation  $\tau = e_g$  and purely viscous material behavior ( $De \rightarrow 0$ ) is given in nondimensional form by System 6.6 on the stationary space domain  $\mathcal{Q} = (0, 1)$  with tangential aerodynamic force  $f_{air}$ , i.e.,  $f_{air} = f_{air} \cdot \tau$ . The pressure of the viscous fiber jet model satisfies the relation  $p = -\sigma/3$ .*

**System 6.6** (Stationary viscous uni-axial melt-blowing fiber model).

*Kinematic equations as well as material law in  $\mathcal{Q}$ :*

$$\begin{aligned} L^{-1} \partial_s \sigma &= \frac{\text{Re}}{3\mu} \sigma \left( u + \frac{\sigma}{u} \right) - \frac{1}{\text{Fr}^2} - f_{air} u, \\ L^{-1} \partial_s T &= -\frac{\text{St}_T}{\varepsilon} \frac{1}{q} \pi d \alpha (T - T_*), \\ L^{-1} \partial_s u &= \frac{\text{Re}}{3\mu} \sigma, \end{aligned}$$

*Boundary conditions:*

$$\sigma(1) = 0, \quad T(0) = T_{in}, \quad u(0) = v_{in}.$$

Again,  $L$  denotes the nondimensional fiber length and becomes one for an appropriate choice of the associated reference value ( $L_0 = r_0$ ). Moreover,  $q = T_{in} = v_{in} = 1$  for the setup-specific reference values given in Tab. 6.3. Basically, System 6.6 equals the uni-axial version of the viscous string model (System 2.10) re-parameterized in Eulerian description under the assumption of stationarity ( $\mathbf{v} = u\boldsymbol{\tau}$ ) and employing the relation  $N = \rho_v \sigma = \sigma/u$ .

System 6.6 is a BVP of ODEs of first order on a fixed domain. For its numerical solution we employ the continuation-collocation method from Sec. 3.1. We introduce a single continuation parameter  $p_{cont} \in [0, 1]$  for the viscous, gravitational and aerodynamic forces as well as for the heat exchange. In particular we set

$$\begin{aligned} L^{-1} \partial_s \sigma &= \frac{\text{Re}}{3(p_{cont}\mu + (1 - p_{cont}))} \sigma \left( u + \frac{\sigma}{u} \right) - p_{cont} \left( \frac{1}{\text{Fr}^2} + f_{air} u \right), \\ L^{-1} \partial_s T &= -p_{cont} \frac{\text{St}_T}{\varepsilon} \frac{1}{q} \pi d \alpha (T - T_*), \\ L^{-1} \partial_s u &= \frac{\text{Re}}{3(p_{cont}\mu + (1 - p_{cont}))} \sigma. \end{aligned}$$

The starting solution for the continuation that belongs to  $p_{cont} = 0$  is a stress-free straight fiber with constant speed and temperature taken from the inflow, i.e.,  $\sigma = 0$ ,  $T = T_{in}$  and  $u = v_{in}$ .

## 6.2.4. Results

In the following we present the numerical results for the industrial spinning setup described in Sec. 6.2.1. While all computations for a single fiber realization have been done on our previously described system (cf. Rem. 3.9), the Monte Carlo simulation has been performed on a MPI cluster (dual Intel Xeon E5-2670, 16 CPU cores per node, 64 GB RAM) with one CPU core for each fiber realization.

Fig. 6.4 shows the results for scalar speed  $u$ , induced elongation  $e$ , stress  $\sigma$ , pressure  $p$ , and temperature  $T$  of the steady viscous uni-axial fiber model in an Eulerian parameterization that spans the whole (spatial) domain  $\mathcal{Q}$ . The maximal fiber speed is  $u = 1.39 \cdot 10^2$  m/s and the corresponding maximal fiber elongation is  $e_{sim} = 1.39 \cdot 10^4$ . This indicates that a stationary fiber simulation is not physically reasonable for the whole domain  $\mathcal{Q}$ , since much higher fiber elongations for the melt-blowing setup are expected. Nevertheless, the steady viscous solution serves as adequate approximation of the fiber behavior in the nozzle region as described in Sec. 6.2.3. For the further unsteady viscoelastic simulation we determine the spatial position of the coupling point  $\mathcal{C}$  and put a fictitious nozzle at  $\mathbf{r}_{in} = (0, 0, 3.84 \cdot 10^{-2})$  m. The corresponding fiber quantities

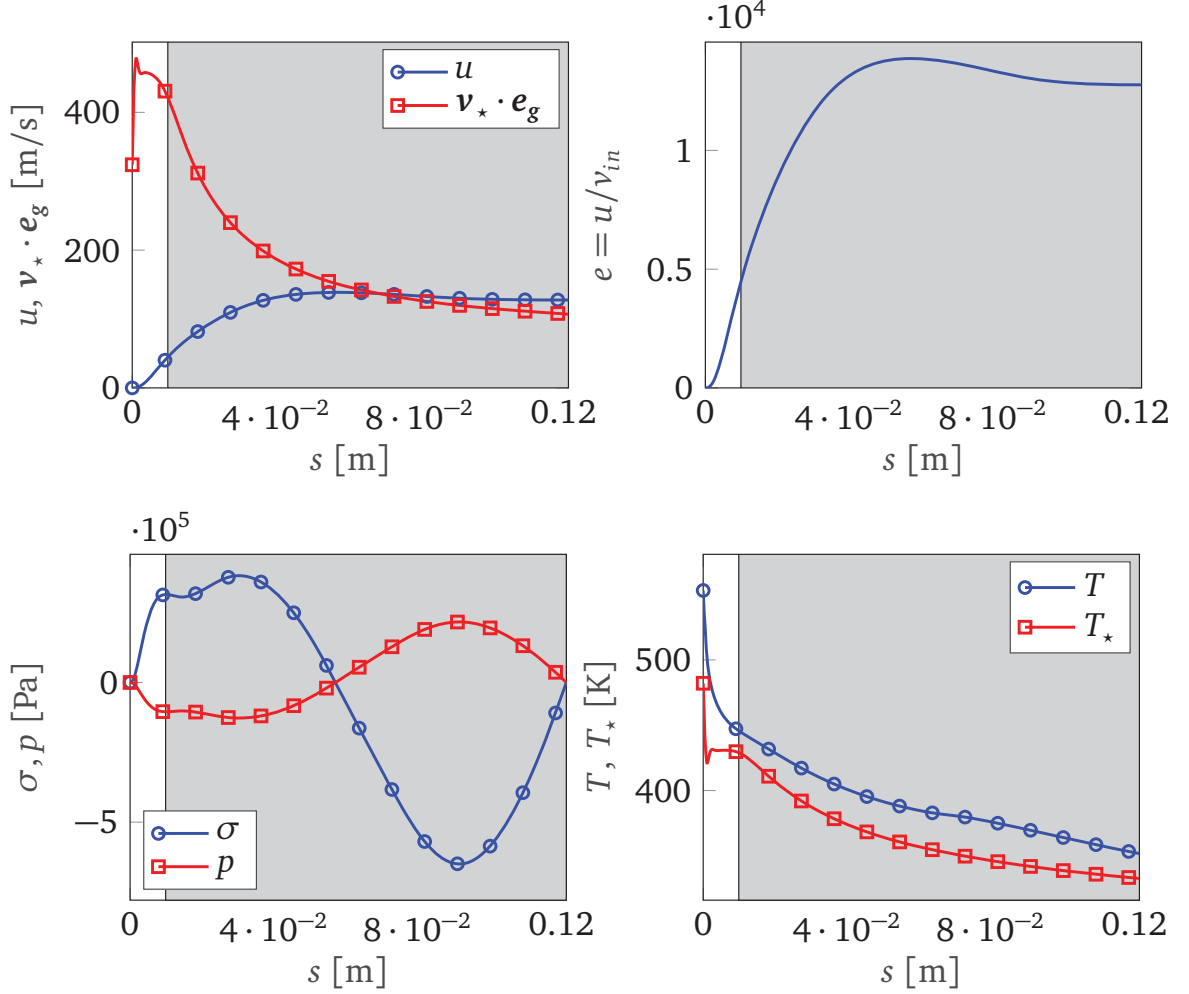


**Figure 6.4.:** Top left to bottom right: Scalar speed  $u$ , elongation  $e$ , stress  $\sigma$ , pressure  $p$  and temperature  $T$  of the steady viscous uni-axial fiber model in Eulerian coordinates. The stochastic region, where the unsteady viscoelastic fiber model (System 6.1) is employed, is shaded in gray.

at this fictitious nozzle are

$$u_c = 44.71 \text{ m/s}, \quad \sigma_c = 70.40 \text{ Pa}, \quad p_c = -23.47 \text{ Pa}, \quad T_c = 445.7 \text{ K},$$

and the dimensionless numbers change accordingly, see Tab. 6.4.

Considering the stochastic region, the numerical step size restriction (6.6) for the fiber discretization weakens compared to (6.7)

$$\Delta\zeta \leq 3.35 \cdot 10^{-5}, \quad \Delta t \leq 8.31 \cdot 10^{-4},$$

we choose  $\Delta\zeta = \Delta t = 10^{-5}$  for our computation. As expected the turbulent fluctuations of the airflow cause a swirling of the fiber jet such that the fiber curve leaves the  $\vec{a}_3$ -axis shortly away from the fictitious nozzle. Fig. 6.5 shows

Dimensionless numbers		
Description	Symbol	Value
Slenderness	$\varepsilon$	$4.76 \cdot 10^{-5}$
Reynolds	Re	$1.85 \cdot 10^2$
Deborah	De	$2.40 \cdot 10^2$
Mach	Ma	$2.11 \cdot 10^2$
Froude	Fr	$4.28 \cdot 10^1$
Temperature Stanton	$St_T$	$1.92 \cdot 10^{-4}$
Air drag associated	$A_*$	$2.50 \cdot 10^1$
Air-fiber Reynolds	$Re_*$	$1.32 \cdot 10^1$
Nusselt	$Nu_*$	2.77
Prandtl	$Pr_*$	$6.23 \cdot 10^{-1}$
Turbulence degree	$Tu_*$	$8.39 \cdot 10^{-1}$
Turbulent time	$Tt_*$	$1.29 \cdot 10^2$

**Table 6.4.:** Dimensionless numbers characterizing the fiber behavior in the stochastic region.

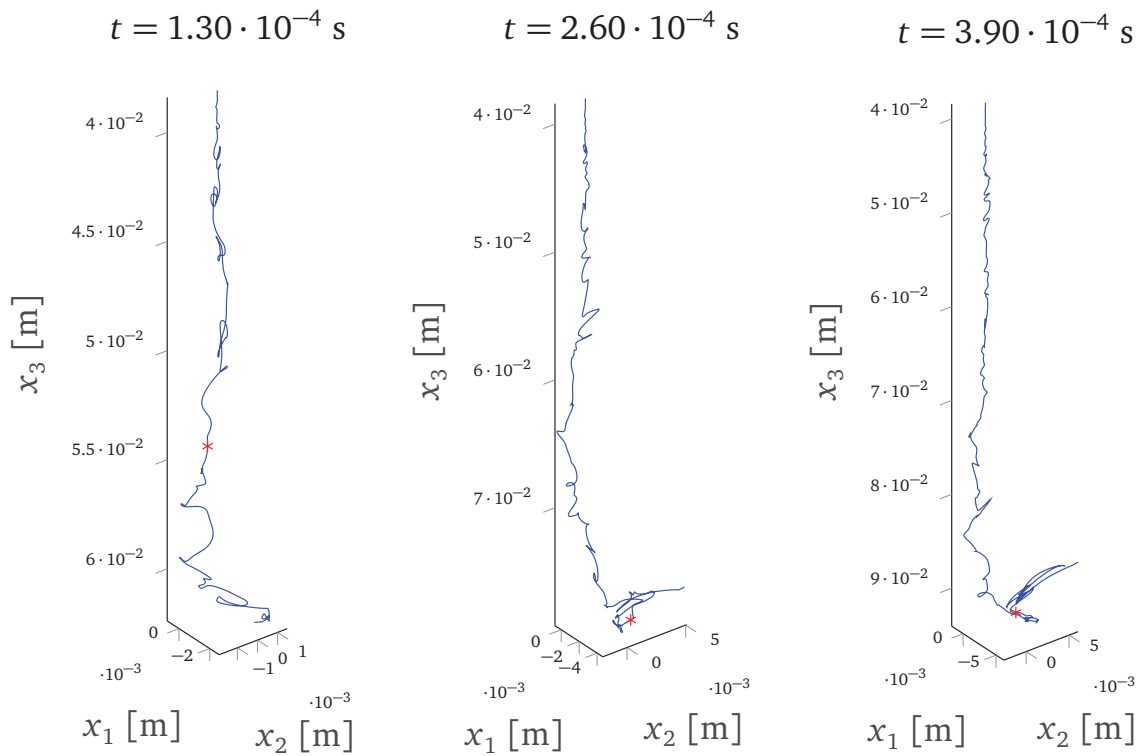


**Figure 6.5.:** Snapshots of one representative fiber curve  $\mathbf{r}$  before reaching the cutoff height ( $x_3 = 9.45 \cdot 10^{-2}$  m) at times  $t \in \{1.30 \cdot 10^{-4}$  s,  $2.60 \cdot 10^{-4}$  s,  $3.90 \cdot 10^{-4}$  s}. We track the material point  $\zeta_{N-2369}$  (marked with a red star) and present the temporal evolution of all fiber quantities at that point in Fig. 6.6.

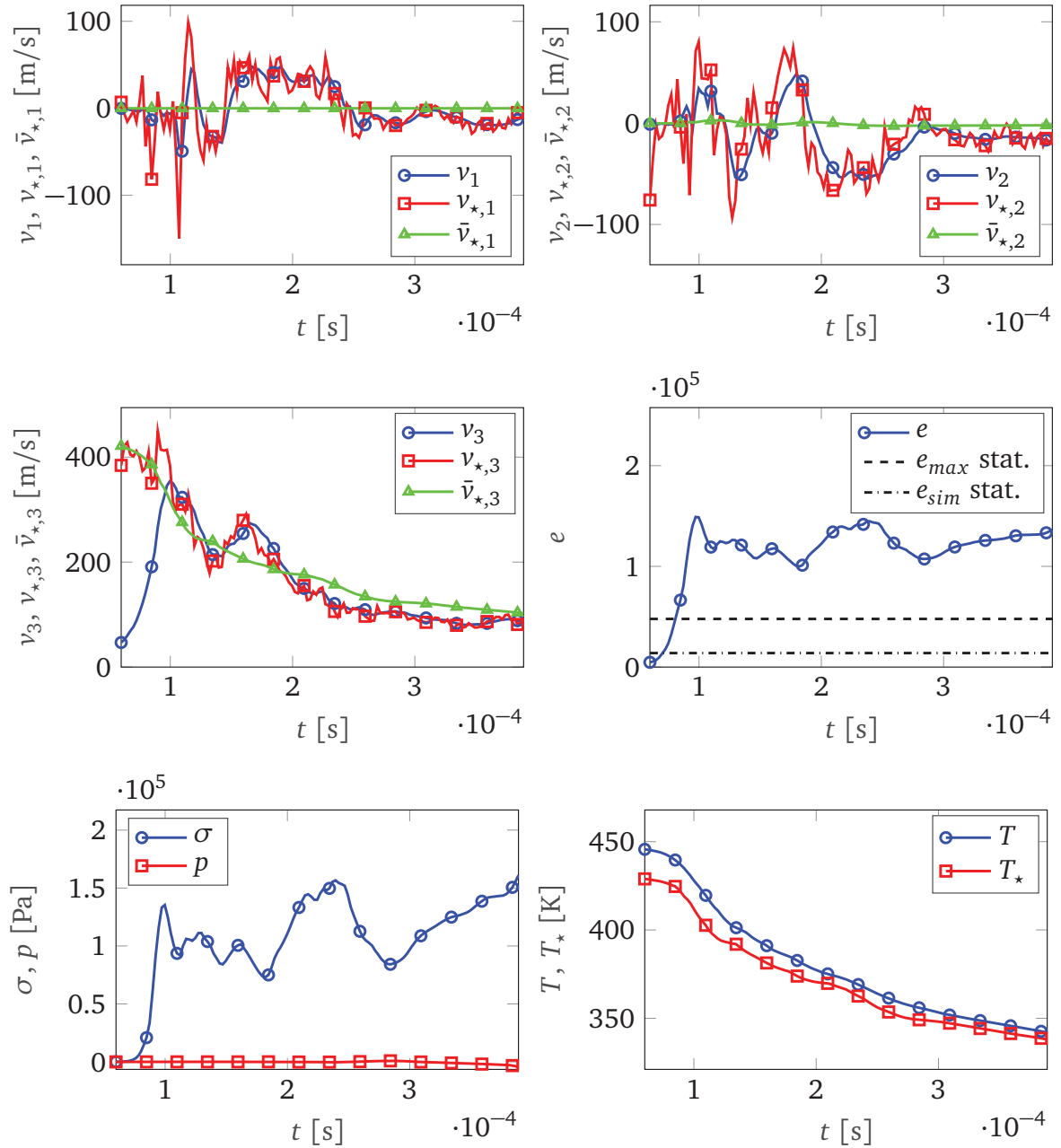


**Figure 6.6.:** Solution plots for the material point  $\zeta_{N-2369}$  (cf. Fig. 6.5) that enters the flow domain at time step 2370 ( $t = 5.91 \cdot 10^{-5}$  s). *Top and middle left:* Fiber velocities  $v_i$  (blue) as well as airflow velocities  $v_{*,i}$ ,  $\bar{v}_{*,i}$  with (red) and without (green) turbulent fluctuations respectively,  $i \in \{1, 2, 3\}$ . *Middle right:* Elongation  $e$  as rate of fiber stretching compared to the original nozzle and  $e_{max}$  indicating the maximal achievable elongation in stationary simulations. Furthermore,  $e_{sim}$  indicates the actual achieved elongation in the stationary simulation (cf. Fig 6.4). *Bottom:* Pressure  $p$ , stress  $\sigma$  as well as fiber temperature  $T$  and air temperature  $T_*$ .

temporal snapshots of the curve for one representative fiber before its cutoff (at  $x_3 = 9.45 \cdot 10^{-2}$  m). The fluctuations move the fiber jet not only downwards but also upwards such that the fiber curve creates loops. In these loops high aerodynamic forces act on the fiber due to high relative velocity gradients causing the fiber to elongate. Fig. 6.6 shows exemplarily the temporal evolution of the fiber quantities for one material point. Obviously the material point experiences high elongations: Directly after entering the flow domain high relative velocities in  $\vec{a}_3$ -direction between the fiber velocity  $v_3$  and the deterministic airflow velocity  $\bar{v}_{*,3}$  cause a fiber stretching. When the fiber velocity  $v_3$  reaches the corresponding deterministic airflow velocity  $\bar{v}_{*,3}$  the fiber experiences a further stretching due to the velocity fluctuations, in which the mean stretching takes place in regions where high lateral air velocities  $v_{*,1}, v_{*,2}$  create swirls. The final elongation at this material point is of magnitude  $e \sim \mathcal{O}(10^5)$  and therewith clearly exceeds the theoretically possible deterministic expectations. In particular, the computed elongation in a stationary simulation is obviously restricted by the velocity of the air stream, i.e.,  $e_{max} = u/v_{in} < \|\mathbf{v}_*\|_\infty/v_{in} = 4.78 \cdot 10^4$ . Furthermore, as shown before (cf. Fig. 6.4) the stationary uni-axial viscous simulation only achieves  $e_{sim} = 1.39 \cdot 10^4$ . In the region of high fiber stretching the material point experiences high stresses  $\sigma$  that partly dissipate due to the elastic material behavior before the fiber completely solidifies. The pressure  $p$  is orders of magnitude smaller compared to the stress  $\sigma$  and, therefore, could be neglected in the simulation as already pointed out in Remark 2.14. The fiber temperature  $T$  approaches the air temperature  $T_*$  leading to a cool-down and induced solidification of the jet.

When a fiber reaches the cutoff height  $x_3 = 9.45 \cdot 10^{-2}$  m, we cut off its end, track the fiber elongations  $e$  as well as the corresponding fiber diameters  $d$  and document the occurring relative frequencies until the end time  $t_{end} = 2.00 \cdot 10^{-3}$  s is reached, see Fig. 6.7. To achieve comparability with experiments, we weight the relative frequencies of the fiber diameters with the associated fiber elongations  $e$  leading to a diameter distribution in the sense of an Eulerian (spatial) parameterization of the fibers. The resulting elongation and fiber diameter distributions are computed with the help of a Monte Carlo simulation with 64 samples. We observe a mean elongation  $e = 7.90 \cdot 10^4$  again exceeding the deterministic expectations. The mean fiber diameter is  $d = 1.39 \cdot 10^{-6}$  m. This is a typical value for fibers produced in industrial melt-blowing setups, see for example [29]. So our unsteady viscoelastic fiber model using an adjusted nozzle as well as employing fluctuation reconstruction of the underlying turbulence effects from an airflow simulation predicts quantitatively well the fiber jet thinning observed in experiments, which is not possible with a pure steady deterministic simulation neglecting the turbulent aerodynamics velocity fluctuations.

Summing up, our proposed procedure makes the simulations of industrial melt-blowing processes with inclusion of turbulent and viscoelastic effects as well as

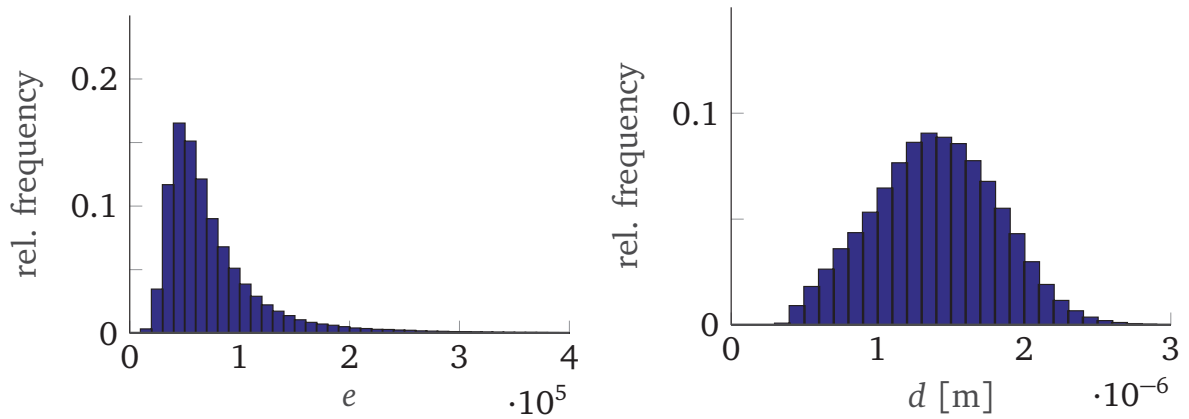


**Figure 6.7.:** *Left:* Fiber elongation distribution at the cutoff point for a Monte Carlo simulation based on 64 realizations. *Right:* Resulting fiber diameter distribution at the cutoff point in the sense of an Eulerian fiber parameterization.

temperature dependencies feasible. Including turbulent effects acting on the fiber with the help of reconstructing the turbulent structure of the outer air stream yields a jet thinning exceeding the deterministic expectations and produces final fiber diameters of realistic order of magnitude. So our presented modeling and solution framework provides the basis for further parameter studies and the optimization of melt-blowing processes. The computation time for the presented setup is around 96.4 hours. A combined experimental and numerical study is left to future research.

**Remark 6.7** (Influence of material models). *To describe viscoelastic material behavior the UCM model is only one possible choice. A drawback of this model is that the stress  $\sigma$  is unbounded for increasing strain rate  $v = \partial_t e/e$ . As consequence, the final fiber diameters reach a plateau beyond a critical value for the shear stress  $f_{air} \cdot t$  [128]. To overcome this issue, alternative viscoelastic material models, such as the Phan-Thien and Tanner (PTT), the Rolie-Poly (RP), as well as the Giesekus model, were studied for melt-blown fibers in [20, 99, 128]. Comparing the results to the ones of the UCM model, it turned out that the PTT model predicts smaller fiber diameters but results in a fiber diameter equal to zero beyond a critical value for the shear stress. The final fiber diameters from the Giesekus model are also smaller than those of the UCM model but larger than those of the PTT model. The Giesekus model shows neither an unbounded stress nor vanishing fiber diameters for large strain rates (or shear stresses) [128]. Although the resulting fiber diameters vary for the different material models, the shape of the fiber curve is predicted to be similar [20]. Since the focus of our numerical study is on the influence of the turbulent airflow on the fibers, we use the UCM description which builds the basis for the more sophisticated nonlinear material models, such as PTT, RP and Giesekus model. However, when altering the constitutive equations we expect a similar behavior for the fiber diameters and curves obtained from our simulations as in [20, 99, 128].*



## 7. Conclusion

In the modeling and simulation of industrial spinning processes we face highly complex three-dimensional multiscale-multiphase problems that are practically impossible to simulate. This creates the need to find suitable mathematical surrogate models in combination with problem tailored numerical solution algorithms. In this work we established a model-based simulation framework based on the special Cosserat theory that makes simulations of such multiscale-multiphase problems with various industrial relevant effects possible.

To show the capability of our model-based simulation framework we exemplarily investigated three different industrial production processes for fibers and non-wovens which are commonly used in the technical textile industry: dry spinning, electrospinning, and melt-blowing. Based on Cosserat rods and strings we deduced a suitable model for each process and developed numerical algorithms for the efficient solution of these models. Our simulation results provide the opportunity for a better understanding of physical mechanisms and further process optimization.

We started with the special Cosserat rod theory and considered a general model formulation in material (Lagrangian) description which allows the utilization of different material (elastic, viscous, viscoelastic) and geometrical models (inertia free, cross-section-preserving, incompressible). In view of stationary considerations we presented a re-parameterization concept that allows the formulation of the model equations in spatial (Eulerian) description. String models were introduced as asymptotic limits of rod models for vanishing slenderness parameter  $\varepsilon$ . These rod and string models serve as a 'box of bricks' in order to set up the specific fiber model for each considered industrial spinning processes.

From a mathematical point of view we deal with boundary value problems formed by either a system of ordinary differential equations or quasilinear hyperbolic partial differential equations, which we solve numerically. For the first type we employ a continuation-collocation scheme, where the collocation is based on a Lobatto IIIa scheme and the continuation method ensures the convergence of the underlying Newton method while navigating through a high-dimensional parameter space. For the latter we use a finite volume scheme in space based on a Lax-Friedrichs flux approximation with the implicit Euler scheme in time. To

take fiber-air interaction into account, a coupling of fiber and airflow simulations is done by iterations based on the principle that action equals reaction.

The simulation of dry spinning processes requires the treatment of multiple fibers interacting with an surrounding airflow. Until now, there were no models and methods with the necessary efficiency to make such a simulation feasible. Hence, we deduced a dimensionally reduced viscous fiber model of one- and two-dimensional equations that covers the radial diffusion effects of mass fraction and temperature in combination with the tangential information of convective speed and tensile stress. Its good approximation qualities were shown in a comprehensive study regarding the solution of an underlying three-dimensional benchmark problem. The embedding of the two-dimensional equations in the solution framework of Green's functions and production integration method led together with a robust model specific continuation strategy for the one-dimensional equations to a very efficiently evaluable algorithm. The good performance of our proposed procedure allowed the simulation of an industrial dry spinning setup with two-way coupled fiber-air interactions in reasonable computation time. An extension of our model to curved fibers was straightforwardly done and allows the simulation of industrial dry spinning setups with two-way coupled fiber-air interactions, where lateral fiber movements take place. Consequently, our work builds a good basis for optimization and optimal design of dry spinning processes.

In view of experiments with electrified visco-capillary jets, as they are present in electrospinning setups, a whipping instability is observed in which the fiber curve forms rapid slashes and the fiber diameter is enormously decreased. We showed that the whipping instability can be directly approached with the stable stationary solutions of a viscous Cosserat rod model. Our proposed continuation-collocation method for the respective boundary value problems assures efficient and accurate simulations including the automatic navigation through high-dimensional parameter spaces. We qualitatively verified the jet characteristics (whipping frequency, elongation, throwing range) to changes of the model parameters and showed the computability of parameter settings involving drastic jet thinning. Even analytical solutions for the 'longtime' behavior of the whipping could be derived. In view of quantitative predictions a combined experimental and numerical study is left to future research.

Concerning industrial melt-blowing processes we presented a model-simulation framework that allows the numerical investigation of the physical mechanism being responsible for the strong fiber thinning. Considering an asymptotic unsteady viscoelastic UCM fiber jet model driven by turbulent aerodynamic forces, the random field sampling strategy provides an efficient numerical procedure for the realization of the turbulent airflow fluctuations. The computed fiber diameters are much lower than those obtained from previous stationary simulations applying a

pure deterministic aerodynamic force on the fiber. Our simulation results clearly stress the significance of the turbulent effects as key player for the production of micro- and nano-scale fibers. We suppose that further parameter studies and an optimization of the industrial process setup might provide the opportunity of simulating fibers with elongations of order  $e \sim \mathcal{O}(10^6)$  compared to the nozzle diameter. In view of more quantitative predictions of the resulting nonwovens a combined experimental and numerical study with experimentally measured temperature-dependencies of polymer properties (e.g., relaxation time) is aimed at in future.



# Appendices



# A. Studies on the UCM string model

We investigate the viscoelastic UCM string model (System 2.12). In particular, we find explicit solution expressions for the pressure  $p$  and the stress  $\sigma$  in the elastic limit case ( $De \rightarrow \infty$ ,  $Re \rightarrow 0$ ,  $ReDe = Ma^2$ ). Furthermore, we show that the pressure  $p$  is at least one order of magnitude smaller than the stress  $\sigma$  for high strain rates and large Deborah numbers such that the associated pressure equation can be neglected in such cases. With the help of an academical melt-blowing setup we compare our UCM model (System 2.12) with this simplified model.

## A.1. Stresses in the elastic limit case

We consider the viscoelastic UCM string model as given in System 2.12. The elastic limit  $De \rightarrow \infty$ ,  $Re \rightarrow 0$ ,  $ReDe = Ma^2$  results in the following equations for the stress  $\sigma$  and the pressure  $p$

$$\begin{aligned}\partial_t \sigma &= \frac{\partial_t e}{e} \left( 2\sigma + 3p + \frac{3}{Ma^2} \frac{\mu}{\theta} \right), \\ \partial_t p &= \frac{\partial_t e}{e} \left( -p - \frac{1}{Ma^2} \frac{\mu}{\theta} \right).\end{aligned}\tag{A.1}$$

We can solve these equations analytically yielding explicit solution expressions for the stress  $\sigma$  and the pressure  $p$  in the elastic limit case.

**Theorem A.1.** *Let the elongation  $e$ , relaxation time  $\theta$  and the Mach number  $Ma$  be strictly positive and assume  $\mu$ ,  $\theta$  to be constant with respect to time, then (A.1) has the explicit solutions*

$$\begin{aligned}\sigma &= \sigma(e) = \frac{e^2}{(e^\circ)^2} \left( \sigma^\circ + p^\circ + \frac{1}{Ma^2} \frac{\mu}{\theta} \right) - \frac{e^\circ}{e} \left( p^\circ + \frac{1}{Ma^2} \frac{\mu}{\theta} \right), \\ p &= p(e) = \frac{e^\circ}{e} \left( p^\circ + \frac{1}{Ma^2} \frac{\mu}{\theta} \right) - \frac{1}{Ma^2} \frac{\mu}{\theta}\end{aligned}\tag{A.2}$$

with time-independent fields  $e^\circ, \sigma^\circ = \sigma(e^\circ), p^\circ = p(e^\circ)$ , where  $e^\circ(\zeta) > 0$  for all  $\zeta \in Q(t^\circ)$ .

*Proof.* The statement can be easily verified by plugging (A.2) into the equations (A.1). □

Under the assumptions of Theorem A.1 the explicit solution for the stress variable  $m = \sigma + p$  reads

$$m(e) = \frac{e^2}{(e^\circ)^2} \left( m^\circ + \frac{1}{\text{Ma}^2} \frac{\mu}{\theta} \right) - \frac{1}{\text{Ma}^2} \frac{\mu}{\theta}.$$

Assuming an arc length parameterized as well as stress- and pressure-free reference state, i.e.,  $e^\circ = 1$ ,  $\sigma^\circ = p^\circ = m^\circ = 0$ , yields

$$\sigma = \frac{1}{\text{Ma}^2} \frac{\mu}{\theta} \left( e^2 - \frac{1}{e} \right), \quad p = \frac{1}{\text{Ma}^2} \frac{\mu}{\theta} \left( \frac{1}{e} - 1 \right), \quad m = \frac{1}{\text{Ma}^2} \frac{\mu}{\theta} (e^2 - 1). \quad (\text{A.3})$$

This means the stress  $m$  depends quadratically on the elongation  $e$ , whereas the pressure  $p$  shows a reciprocal dependency on  $e$ . The stress variable  $\sigma$  contains quadratic as well as reciprocal terms. For jet stretching ( $e > 1$ ) we obtain a positive stress  $m > 0$  and a negative pressure  $p < 0$ . The stress variable  $\sigma$  is positive. For jet squeezing ( $0 < e < 1$ ) the jet's stress is negative  $m < 0$  and the pressure is positive  $p > 0$ . The mixed stress variable  $\sigma$  is negative. For an unstretched jet ( $e = 1$ ) the jet remains stress- and pressure-free  $m = p = \sigma = 0$ . Obviously, the resulting string model in the elastic limit case is not closely related to the generalized elastic string model given in System 2.11. Whereas the material law of the UCM string shows the stress-elongation-relation (A.3) in the elastic limit case, the generalized elastic string (System 2.11) is based on a classical Kirchhoff constraint ( $e = 1$ ) and a linear momentum-curvature-relation yielding a Lagrangian multiplier and a regularizing term in the linear momentum equation. The different structure of the models is owed to their completely different origin. Whereas the UCM string model is derived by strict asymptotic considerations (cf. [65]) and the elastic behavior is obtained by subsequent transition to the elastic limit, the generalized elastic string model (System 2.11) is the low-Mach-number-slenderness limit of the associated elastic rod model and still contains curvature effects.

## A.2. Hierarchy of UCM models

Concerning the modeling of melt-blowing processes an UCM model was employed in [93, 122]. This model is a simplification of our UCM fiber model (System 6.1), which was derived asymptotically in its basic form from a three-dimensional

unsteady BVP [65]. In the following, we want to link and compare these two models. With the help of an academical melt-blowing setup we present simulation results for the model hierarchy and discuss them with respect to accuracy and efficiency in view of more complex industrial setups. Parts of the following study have been pre-published in [114].

We consider our melt-blowing model (System 6.1) with corresponding initial and boundary conditions as presented in Sec. 6.1 and investigate the stresses according to [65]. Assuming a known and non-negative strain rate for each material point  $\zeta$ , i.e.,  $v(\zeta, \cdot) = (\partial_t e/e)(\zeta, \cdot) = (\mathbf{t}/e \cdot \partial_\zeta \mathbf{v})(\zeta, \cdot) \geq 0$ , the equations for the stress  $m = \sigma + p$  and pressure  $p$  can be identified with the two decoupled ODEs of first order

$$\begin{aligned}\partial_t m &= \left(2v - \frac{1}{\text{De}} \frac{1}{\theta}\right) m + \frac{2}{\text{ReDe}} \frac{\mu}{\theta} v, \\ \partial_t p &= -\left(v + \frac{1}{\text{De}} \frac{1}{\theta}\right) p - \frac{1}{\text{ReDe}} \frac{\mu}{\theta} v.\end{aligned}$$

Obviously, the pressure equation has an attracting solution  $p^*$

$$p^* = -\frac{\mu v}{\text{Re}(1 + \text{De}\theta v)} \leq 0,$$

whereas the behavior of the stress  $m$  depends on the sign of  $(2v - 1/(\text{De}\theta))$ . If  $\text{De}\theta v \geq 0.5$ , the stress  $m$  grows exponentially and thus the pressure  $p$  is negligibly small. If  $\text{De}\theta v < 0.5$ , the stress equation has an attracting solution

$$m^* = \frac{2\mu v}{\text{Re}(1 - 2\text{De}\theta v)} \geq 0.$$

We now examine the ratio of pressure to stress in that case

$$\frac{|p^*|}{m^*} = \frac{1 - 2\text{De}\theta v}{2(1 + \text{De}\theta v)},$$

from where a simple calculation shows that  $|p^*| \leq 0.1m^*$  if  $\text{De}\theta v \geq 0.36$ . Analogously we calculate

$$\frac{|p^*|}{\sigma^*} = \frac{|p^*|}{m^* - p^*} = \frac{1}{3}(1 - 2\text{De}\theta v),$$

from where we conclude that  $|p^*| \leq 0.1\sigma^*$  if  $\text{De}\theta v \geq 0.35$ . So under the assumption of a positive strain rate and the relation  $v \geq 0.35/(\text{De}\theta)$  the absolute pressure  $|p|$  is at least one order of magnitude smaller than the stress  $\sigma$  and can be neglected (cf. Rem. 2.14). Re-writing our melt-blowing UCM model (System 6.1) with respect to the stress variable  $m$  instead of  $\sigma$  and setting  $p = 0$  leads to a

<b>Process and physical parameters</b>			
Description	Symbol	Value	Unit
Device height	$H$	$1.214 \cdot 10^{-1}$	m
Nozzle diameter	$d_{in}$	$4 \cdot 10^{-4}$	m
Speed at nozzle	$v_{in}$	10	m/s
Polar angle at nozzle	$\vartheta_{in}$	0	–
Azimuth angle at nozzle	$\varphi_{in}$	0	–
Temperature at nozzle	$T_{in}$	$5.232 \cdot 10^2$	K
Heat transfer at nozzle	$\alpha_{in}$	$8.107 \cdot 10^2$	W/(m <sup>2</sup> K)
Air thermal conductivity at nozzle	$\lambda_{*,in}$	$2.42 \cdot 10^{-2}$	W/(m K)
Air kinematic viscosity at nozzle	$\nu_{*,in}$	$1.8 \cdot 10^{-5}$	m <sup>2</sup> /s
Air specific heat capacity at nozzle	$q_{*,in}$	$1.006 \cdot 10^3$	J/(kg K)
Air density at nozzle	$\rho_{*,in}$	1.047	kg/m <sup>3</sup>
Air turbulent kinetic energy at nozzle	$k_{*,in}$	$2.05 \cdot 10^3$	m <sup>2</sup> /s <sup>2</sup>
Air viscous dissipation rate at nozzle	$\epsilon_{*,in}$	$1.27 \cdot 10^7$	m <sup>2</sup> /s <sup>3</sup>
End time	$t_{end}$	$2.43 \cdot 10^{-3}$	s
Fiber density	$\rho$	$7 \cdot 10^2$	kg/m <sup>3</sup>
Fiber specific heat capacity	$q$	$2.1 \cdot 10^3$	J/(kg K)

<b>Dimensionless numbers</b>		
Description	Symbol	Value
Slenderness	$\varepsilon$	$2.92 \cdot 10^{-3}$
Reynolds	Re	$8.50 \cdot 10^1$
Deborah	De	$2.47 \cdot 10^4$
Mach	Ma	$1.50 \cdot 10^1$
Froude	Fr	9.16
Temperature Stanton	$St_T$	$5.52 \cdot 10^{-5}$
Air drag associated	$A_*$	$5.12 \cdot 10^{-1}$
Air-fiber Reynolds	$Re_*$	$1.97 \cdot 10^2$
Nusselt	$Nu_*$	$1.19 \cdot 10^1$
Prandtl	$Pr_*$	$7.83 \cdot 10^{-1}$
Turbulence degree	$Tu_*$	4.53
Turbulent time	$Tt_*$	$7.54 \cdot 10^1$

**Table A.1.:** Overview over process and physical parameters in the academical melt-blowing setup and the resulting dimensionless numbers.

pressure-free UCM fiber model. This resulting pressure-free model is instantaneously employed in [93, 122] for the modeling of melt-blowing processes. The boundary conditions change accordingly.

We compare the asymptotic and the pressure-free fiber UCM model with the help of an academical setup where we choose all airflow fields being constant

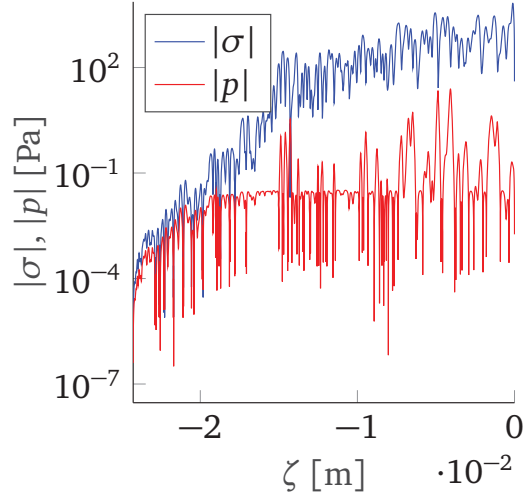


**Figure A.1.:** Absolute values of fiber stress  $\sigma$  and pressure  $p$  over material parameter  $\zeta$  in the academical melt-blowing setup at time  $t_{end} = 2.43 \cdot 10^{-3}$  s. The nozzle is located at  $\zeta = -2.43 \cdot 10^{-2}$  m.

in space and time. This means the fields  $\rho_*$ ,  $\nu_*$ ,  $c_{p,*}$ ,  $\lambda_*$ ,  $k_*$  and  $\epsilon_*$  become one in the nondimensional formulation. Furthermore, the deterministic air speed is  $\bar{\mathbf{v}}_* = (100 \text{ m/s})\mathbf{e}_g$  with  $\mathbf{e}_g$  the direction of gravity and the airflow temperature is  $T_* = 310$  K. The fiber dynamic viscosity and relaxation time are also assumed to be constant in space and time. In particular, we fix  $\mu = 10$  Pa s and  $\theta = 3 \cdot 10^{-2}$  s. All further parameters and the resulting dimensionless numbers are given in Tab. A.1. The setup-specific reference values are chosen as in the industrial melt-blowing setup, see Tab. 6.3 in Sec. 6.2.1. At the inflow boundary we set  $\sigma_{in} = p_{in} = m_{in} = 0$ .

The reconstruction of the airflow velocity fluctuations from the  $k_*$ - $\epsilon_*$  turbulence description of the airflow is done as presented in Sec. 6.2.2. For the solution of the fiber models we employ the numerical scheme described in Sec. 3.2, i.e., the spatial discretization is realized with a finite volume scheme with Lax-Friedrichs flux approximation and the implicit Euler scheme is used for the temporal discretization. For the computation we choose the mesh sizes  $\Delta\zeta = \Delta t = 10^{-5}$ . Although the strain rate  $v$  is not exclusively positive in this academical setup, the pressure in the asymptotic model (System 6.1) is orders of magnitude smaller than the stress  $\sigma$  shortly away from the nozzle ( $\zeta = -2.43 \cdot 10^{-2}$  m), see Fig. A.1. Comparing the solutions at time  $t_{end} = 2.43 \cdot 10^{-3}$  s the relative  $L^2$ -error in all variables (except the pressure  $p$ ) between the asymptotic and pressure-free model is  $5.14 \cdot 10^{-4}$ . The computation times are 6.2 h for the asymptotic and 5.4 h for the pressure-free model. Consequently, the simplified model might be preferred for efficiency reasons, but since the additional effort for the computation of the complete asymptotic model is not excessive, we stick to the full System 6.1 for industrial melt-blowing setups.



## B. Numerical schemes and solution methods

In the following we study our numerical schemes and solution methods. First, we numerically show the convergence of our finite volume scheme for hyperbolic quasilinear PDEs on a growing space-time domain, which we presented in Sec. 3.2. Thereafter, we give a detailed derivation of the implicit solution expressions in terms of a Green's function for the radial advection-diffusion equation that we use to describe heat and mass diffusion in the fiber due to solvent evaporation, cf. Sec. 4.1. This solution expression can be used to set up a product integration method for the values at the fiber boundary, cf. Sec. 3.3. The convergence and stability of this product integration method is examined subsequently.

### B.1. Convergence of the finite volume scheme for quasilinear hyperbolic PDEs on a growing domain

In this section we numerically analyze the convergence behavior of our solution method for hyperbolic quasilinear PDE systems on a growing space-time domain as presented in Sec. 3.2. This means we use finite volumes in space with a Lax-Friedrichs flux approximation and discretize the resulting ODE system with respect to the time variable using the implicit Euler scheme. The growing space-time domain is treated with static and dynamic cells.

Since the numerical framework is used for the solution of our fiber melt-blowing model (System 6.1), we utilize the same UCM string model for our convergence study here. For simplicity we assume only gravitational forces to act on the fiber and omit any airflow associated effects (deterministic and stochastic), i.e.,  $\mathbf{f}_{air} = \mathbf{0}$ . Furthermore, we exclude temperature effects and hence omit the equation for the temperature  $T$ . The fiber dynamic viscosity  $\mu$  and relaxation time  $\theta$  are fixed as constants  $\mu = 10 \text{ Pa s}$ ,  $\theta = 0.1 \text{ s}$  and become unity in nondimensional form. The further parameters and resulting dimensionless numbers are given in Tab. B.1.

<b>Process and physical parameters</b>			
Description	Symbol	Value	Unit
Device height	$H$	$1 \cdot 10^{-1}$	m
Nozzle diameter	$d_{in}$	$1 \cdot 10^{-4}$	m
Speed at nozzle	$v_{in}$	1	m/s
Polar angle at nozzle	$\vartheta_{in}$	$\pi/2$	–
Azimuth angle at nozzle	$\varphi_{in}$	$\pi/4$	–
Nozzle position	$\mathbf{r}_{in}$	$(0, 0, 2.85 \cdot 10^{-2})$	m
Stress at nozzle	$\sigma_{in}$	$10^{-3}$	Pa
Pressure at nozzle	$p_{in}$	$-1/3 \cdot 10^{-4}$	Pa
End time	$t_{end}$	$2 \cdot 10^{-2}$	s
Fiber density	$\rho$	$5 \cdot 10^2$	kg/m <sup>3</sup>

<b>Dimensionless numbers</b>		
Description	Symbol	Value
Reynolds	Re	5.00
Deborah	De	1.00
Mach	Ma	2.24
Froude	Fr	1.01

**Table B.1.:** Overview over process and physical parameters and the resulting dimensionless numbers for the convergence study.

The setup-specific reference values are chosen as in the industrial melt-blowing setup, see Tab. 6.3 in Sec. 6.2.1.

We compute the solution on an equidistant space-time grid with grid sizes  $\Delta\zeta$  and  $\Delta t$  respectively. For the convergence study we choose  $\Delta\zeta, \Delta t \in \{2^i \cdot 10^{-4} \mid i = 1, \dots, 6\}$ , and calculate the reference solution with  $\Delta\zeta = \Delta t = 10^{-4}$ . Fig. B.1 shows the convergence behavior that we expect from literature (cf. Remark 3.4), i.e., convergence of order two with respect to space, order one with respect to time and a combined convergence of order one.

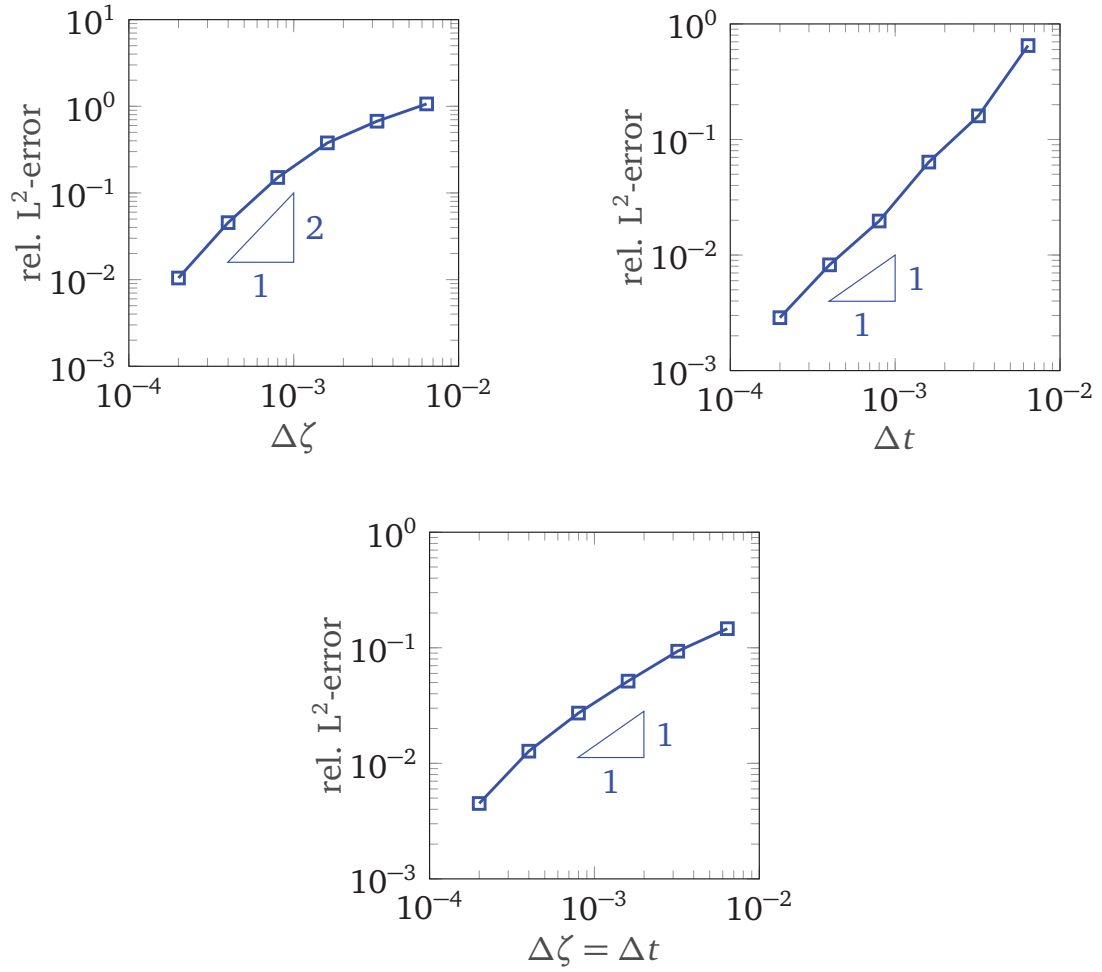


**Figure B.1.:** Top left to bottom: Spatial, temporal and combined convergence behavior of the numerical scheme for quasilinear hyperbolic PDE systems based on the academical setup on a growing domain.

## B.2. Analytic solution for the radial advection-diffusion equation

To include radial diffusive effects into our fiber models – like heat/mass diffusion due to solvent evaporation present in dry spinning processes –, we have to solve a BVP with Robin-type boundary condition of the form (cf. (4.13))

Find  $\psi = \psi(r, x)$  with

$$\begin{aligned} \partial_x \psi - \frac{1}{r} \partial_r (r \partial_r \psi) &= 0, & \text{for } 0 < x \leq 1, \quad 0 < r < 1, \\ \psi|_{x=0} &= \psi_{in}, & \text{for } 0 \leq r \leq 1, \\ \partial_r \psi|_{r=0} &= 0, & \text{for } 0 < x \leq 1, \\ \partial_r \psi|_{r=1} &= a\psi|_{r=1} + b, & \text{for } 0 < x \leq 1, \end{aligned} \tag{B.1}$$

with functions  $a, b : [0, 1] \rightarrow \mathbb{R}$  and  $\psi_{in} \in \mathbb{R}$ . In order to make an efficient numerical solution of this problem feasible, we derive an implicitly given solution expression based on a Green's function. First, we consider the following slightly modified problem

Find  $G = G(r, x; r', x')$  with

$$\begin{aligned} \partial_x G - \frac{1}{r} \partial_r (r \partial_r G) - \delta(x - x') \frac{\delta(r - r')}{2\pi r'} &= 0, & \text{for } x > x', \quad 0 < r < 1, \\ G|_{x \leq x'} &= 0, & \text{for } 0 \leq r \leq 1, \\ \partial_r G|_{r=0} &= 0, & \text{for } x > x', \\ \partial_r G|_{r=1} &= 0, & \text{for } x > x', \end{aligned} \tag{B.2}$$

with parameters  $r', x' \in [0, 1]$  and  $\delta$  denoting the Dirac delta function. We can state the following connection between the radial advection-diffusion problem (B.1) and the modified problem (B.2).

**Lemma B.1.** *Let  $G = G(r, x; r', x')$  be a solution of the modified problem (B.2), then a solution of the original problem (B.1) is implicitly given through*

$$\begin{aligned} \psi(r, x) &= 2\pi\psi_{in} \int_0^1 G(r, x; r', 0) r' dr' \\ &\quad + 2\pi \int_0^x G(r, x; 1, x') (a(x')\psi(1, x') + b(x')) dx'. \end{aligned}$$

*Proof.* We mainly follow the calculations given in [76]. Every solution of (B.1) fulfills

$$\frac{1}{r'} \partial_{r'}(r' \partial_{r'} \psi(r', x')) = \partial_{x'} \psi(r', x'), \quad (\text{B.3})$$

for  $x' < x$ ,  $0 < r' < 1$ , and for every solution of (B.2) the relation

$$\frac{1}{r'} \partial_{r'}(r' \partial_{r'} G) + \delta(x' - x) \frac{\delta(r' - r)}{2\pi r'} = -\partial_{x'} G, \quad (\text{B.4})$$

for  $x' < x$ ,  $0 < r' < 1$  holds. Note that the negative sign on the right hand side of (B.4) is due to the dependency of  $G$  on the term  $(x - x')$ . We multiply (B.3) with the function  $G$  and (B.4) with the function  $\psi$  and consider their difference

$$\left( G \frac{1}{r'} \partial_{r'}(r' \partial_{r'} \psi) - \psi \frac{1}{r'} \partial_{r'}(r' \partial_{r'} G) \right) - \psi \delta(x' - x) \frac{\delta(r' - r)}{2\pi r'} = \partial_{x'}(\psi G).$$

Integration over  $[0, 1] \times [0, x]$  yields

$$\begin{aligned} 2\pi \int_0^x \int_0^1 \left( G \frac{1}{r'} \partial_{r'}(r' \partial_{r'} \psi) - \psi \frac{1}{r'} \partial_{r'}(r' \partial_{r'} G) \right) r' dr' dx' \\ - \int_0^x \int_0^1 \psi \delta(x' - x) \delta(r' - r) dr' dx' = 2\pi \int_0^1 [\psi G]_{x'=0}^x r' dr'. \end{aligned}$$

Applying Green's second identity on the first term on the left hand side and utilizing the fact that  $(\psi G)|_{x'=x} = 0$  gives

$$2\pi \int_0^x [r' G \partial_{r'} \psi - r' \psi \partial_{r'} G]_{r'=0}^1 dx' - \psi(r, x) = -2\pi \psi_{in} \int_0^1 G|_{x'=0} r' dr',$$

which can be written with the help of the boundary conditions as

$$\psi(r, x) = 2\pi \psi_{in} \int_0^1 G|_{x'=0} r' dr' + 2\pi \int_0^x G|_{r'=1} (a(x') \psi(1, x') + b(x')) dx'.$$

□

The advantage of the modified problem is that there exists an analytic expression for its solution  $G$  (cf. [23, 76]).

**Lemma B.2.** *The solution of the modified BVP (B.2) is given through*

$$G(r, x; r', x') = \frac{1}{\pi} \left( 1 + \sum_{m=1}^{\infty} \exp(-\beta_m^2(x - x')) \frac{J_0(\beta_m r) J_0(\beta_m r')}{J_0(\beta_m)^2} \right),$$

where  $J_i$ ,  $i \in \mathbb{N}_0$ , denote the  $i$ -th Bessel functions of first kind and  $\beta_m > 0$ ,  $m \in \mathbb{N}$ , are the ascending zeros of  $J_1$ , i.e.,  $J_1(\beta_m) = 0$ .

*Proof.* The idea of the proof follows [23, 76]. We consider the homogeneous problem corresponding to (B.2) with inhomogeneous initial values

Find  $H = H(r, x)$  with

$$\begin{aligned} \partial_x H - \frac{1}{r} \partial_r (r \partial_r H) &= 0, & \text{for } x > 0, \quad 0 < r < 1, \\ H|_{x=0} &= \psi_{in}, & \text{for } 0 \leq r \leq 1, \\ \partial_r H|_{r=0} &= 0, & \text{for } x > 0, \\ \partial_r H|_{r=1} &= 0, & \text{for } x > 0. \end{aligned} \tag{B.5}$$

To solve this problem we assume  $H$  is a solution of (B.5) and employ the separation ansatz  $H(r, x) = R(r)X(x)$ , which yields

$$R(r) \partial_x X(x) = \frac{X(x)}{r} \partial_r (r \partial_r R(r))$$

or equivalently (under the assumption  $H(r, x) \neq 0$  for  $x > 0$ ,  $0 < r < 1$ )

$$\frac{\partial_x X(x)}{X(x)} = \frac{1}{rR(r)} \partial_r (r \partial_r R(r)).$$

Since the left hand side only depends on  $x$  and the right hand side only on  $r$ , we follow

$$\frac{\partial_x X(x)}{X(x)} = -\beta_m^2, \quad \frac{1}{rR(r)} \partial_r (r \partial_r R(r)) = -\beta_m^2$$

for a constant  $\beta_m \in \mathbb{R}_0^+$ ,  $m \in \mathbb{N}_0$ , where the sign is chosen negative in order to achieve the correct physical solution behavior. In total the separation ansatz reduces the PDE in (B.5) to two ODEs. The first has the solution

$$X(x) = X_m \exp(-\beta_m^2 x)$$

with constant  $X_m \in \mathbb{R}$ . The second ODE reads

$$r^2 \frac{d^2}{dr^2} R(r) + r \frac{d}{dr} R(r) + (r\beta_m)^2 R(r) = 0,$$

which becomes the Bessel's differential equation under re-parameterization  $z(r) = \beta_m r$

$$z^2 \frac{d^2}{dz^2} R(z) + z \frac{d}{dz} R(z) + z^2 R(z) = 0.$$

A solution of this Bessel's differential equation is the Bessel function of first kind of order zero yielding

$$R(r) = R_m J_0(\beta_m r)$$

with constants  $R_m \in \mathbb{R}$ . This means a particular solution  $H$  has the form

$$H(r, x) = a_m \exp(-\beta_m^2 x) J_0(\beta_m r)$$

with  $a_m = X_m R_m$ . It remains to determine the constants  $a_m$  and  $\beta_m$ . For the latter we use the boundary condition  $\partial_r H(r, x)|_{r=1} = 0$  yielding

$$0 = -\beta_m a_m \exp(-\beta_m^2 x) J_1(\beta_m),$$

with the non-trivial solution

$$J_1(\beta_m) = 0.$$

The values  $\beta_m$  are tabulated in literature, see e.g. [23]. Due to  $J_1(0) = 0$  the further boundary condition  $\partial_r H(r, x)|_{r=0} = 0$  is fulfilled. Therefore, the general solution for  $H$  is

$$H(r, x) = \sum_{m=0}^{\infty} a_m \exp(-\beta_m^2 x) J_0(\beta_m r)$$

with  $J_1(\beta_m) = 0$ . The coefficients  $a_m$  can be determined from the initial condition

$$\psi_{in} = a_0 + \sum_{m=1}^{\infty} a_m J_0(\beta_m r).$$

This representation of  $\psi_{in}$  equals its representation as Fourier-Bessel series with corresponding coefficients (cf. [10])

$$a_0 = 2 \int_0^1 \psi_{in} r' dr', \quad a_m = \frac{\int_0^1 \psi_{in} J_0(\beta_m r') r' dr'}{\int_0^1 J_0^2(\beta_m r') r' dr'}.$$

Employing the relations  $\int_0^1 J_0^2(\beta_m r') r' dr' = (J_0^2(\beta_m) + J_1^2(\beta_m))/2 = J_0^2(\beta_m)/2$  and  $\beta_0 = 0, J_0(0) = 1$  yields

$$\begin{aligned} H(r, x) &= 2 \int_0^1 \psi_{in} r' dr' + \int_0^1 \psi_{in} \left( \sum_{m=1}^{\infty} J_0(\beta_m r') \frac{2}{J_0^2(\beta_m)} \exp(-\beta_m^2 x) J_0(\beta_m r) \right) r' dr' \\ &= 2\psi_{in} \int_0^1 \left( 1 + \sum_{m=1}^{\infty} \frac{J_0(\beta_m r) J_0(\beta_m r')}{J_0^2(\beta_m)} \exp(-\beta_m^2 x) \right) r' dr'. \end{aligned}$$

With Lemma B.1 we get the connection of  $H$  to the function  $G$

$$H(r, x) = 2\pi\psi_{in} \int_0^1 G(r, x; r', 0) r' dr',$$

from which we conclude the explicit expression for the function  $G$

$$G(r, x; r', x') = \frac{1}{\pi} \left( 1 + \sum_{m=1}^{\infty} \frac{J_0(\beta_m r) J_0(\beta_m r')}{J_0^2(\beta_m)} \exp(-\beta_m^2 (x - x')) \right)$$

with  $J_1(\beta_m) = 0, \beta_m > 0, m \in \mathbb{N}$ . □

Now we can give the final expression for the solution  $\psi$  of (B.1).

**Theorem B.3.** Let  $\psi : [0, 1]^2 \rightarrow \mathbb{R}$  be given through

$$\psi(r, x) = \psi_{in} + 2\pi \int_0^x g(r, x - x') k(x', \psi(1, x')) dx',$$

$$\text{with } g(r, z) = \frac{1}{\pi} \left( 1 + \sum_{m=1}^{\infty} \frac{J_0(\beta_m r)}{J_0(\beta_m)} \exp(-\beta_m^2 z) \right), \quad k(x, y) = a(x)y + b(x),$$

where  $\beta_m > 0, m \in \mathbb{N}$ , are the ascending zeros of the first Bessel function of first kind, i.e.,  $J_1(\beta_m) = 0$ . Then,  $\psi$  solves the BVP (B.1).

*Proof.* The statement follows directly from the previous Lemma B.1 and Lemma B.2 using the relation

$$\int_0^1 J_0(\beta_m r') r' dr' = \frac{J_1(\beta_m)}{\beta_m} = 0.$$

□

## B.3. Convergence and stability of the product integration method

In this section, we consider the convergence and stability properties of the product integration method (cf. Sec. 3.3) for the solution of radial advection-diffusion equations of the form

$$\partial_x \psi - \frac{1}{r} \partial_r (r \partial_r \psi) = 0,$$

$$\psi|_{x=0} = \psi_{in}, \quad \partial_r \psi|_{r=0} = 0, \quad \partial_r \psi|_{r=1} = a\psi|_{r=1} + b.$$

In particular, we compare Method (i) based on the implicit Euler scheme and Method (ii) based on Lobatto IIIa collocation. Note that this study has already been pre-published in [111].

We exemplarily consider constant functions  $a$ ,  $b$  and choose

$$a = -b = -5 \cdot 10^3, \quad \psi_{in} = 0.5.$$

We compute the solution  $\psi|_{r=1}$  on an equidistant grid with size  $\Delta x$ . For the convergence study we choose  $\Delta x = 1/(2^i \cdot 10)$ ,  $i \in \{0, \dots, 8\}$ , and calculate the reference solution with Method (ii) and  $\Delta x = 1/(2^9 \cdot 10)$ . Fig. B.2 shows that Method (i) converges with order one, whereas Method (ii) has order two. The underlying collocation scheme of Method (ii) is of order four. The order reduction results from the highly non-linear integral kernel  $g$  and its stiff behavior near  $x = 0$ . Due to the stability properties (cf. Rem. 3.6), Method (ii) produces oscillations near  $x = 0$  when  $\Delta x$  is not sufficiently small (see Fig. B.2). In contrast Method (i) is stable for all  $\Delta x \geq 0$ . Thus, the use of Method (i) seems preferable in situations where L-stable methods are required. If the corresponding problem is not excessively stiff or the number of grid points is sufficiently high, Method (ii) is certainly preferable due to its higher order of convergence. For applications we suggest the following procedure: Choose the higher order Method (ii) as standard product integration method. If oscillations occur, switch to Method (i) lowering the order of convergence but increasing the stability.

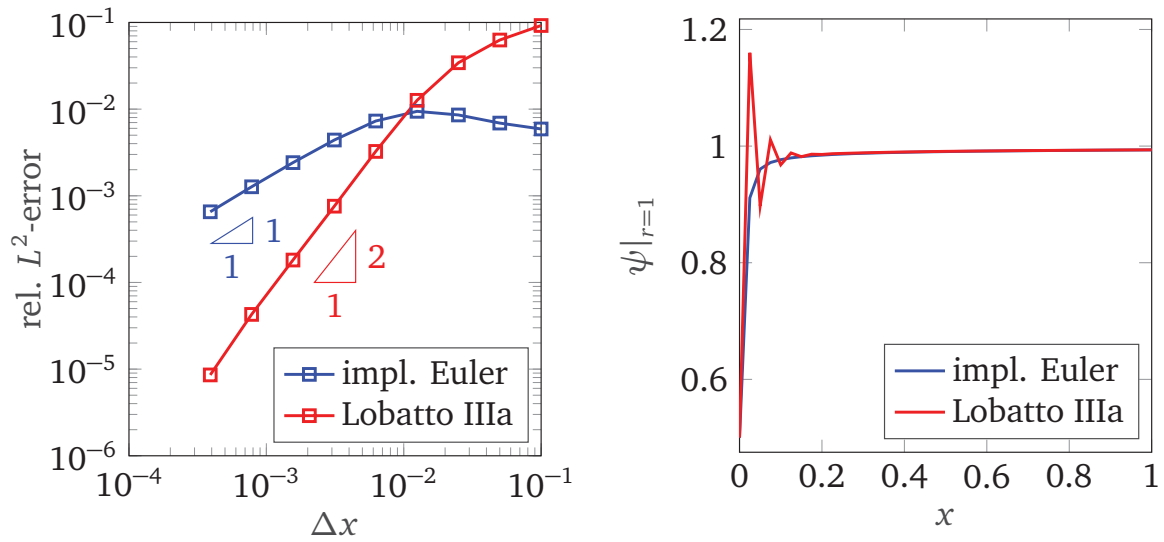


**Figure B.2.:** *Left:* Convergence behavior for product integration methods based on the implicit Euler scheme (Method (i)) and the Lobatto IIIa collocation scheme (Method (ii)). *Right:* Results for  $\Delta x = 1/40$  indicating the stability properties of the two methods for stiff problems.

## C. Studies on electrospinning

In electrospinning processes the curve of the electrified jets show a lateral jet movement known as whipping instability. The temporal stability analysis in [85] establishes a strong connection between this instability observed in experiments and the unstable solutions of the associated electrospinning model. In the following we adapt this study to our electrospinning model (System 5.5). Furthermore, in spinning setups with strongly evolved jet whipping boundary layers arise in the components of curvature  $\kappa$ , contact force  $\mathbf{n}$  and couple  $\mathbf{m}$ . By studying our electrospinning model in Lagrangian parameterization, we verify that this boundary layer is not a numerical artifact but an essential characteristic of our solution. Note that in great parts the following studies have been pre-published in [4].

### C.1. Global linear stability analysis

The whipping instability observed in experiments on electrospinning was investigated by means of classical perturbation theory in, e.g., [48, 59, 80, 120]. In the following we show that the unstable solutions of our transient electrospinning model (cf. Sec. 5.1) are directly related to the whipping instability as we can conclude from a global stability analysis.

In contrast to the rotating frame, which we used before in the study of electrospinning (cf. Sec. 5.1), we consider here a stationary outer basis  $\{\vec{\mathbf{a}}_1, \vec{\mathbf{a}}_2, \vec{\mathbf{a}}_3\}$  with predominant spinning direction  $\vec{\mathbf{a}}_3$  and the standard director basis  $\{\vec{\mathbf{d}}_1, \vec{\mathbf{d}}_2, \vec{\mathbf{d}}_3\}$ . This means, we proceed from the rod model given in System 2.8 with viscous material behavior. Additionally, we replace the kinematic equations for the time derivatives of curve and triad by the compatibility conditions (2.8). Moreover, we directly insert the capillary forces (5.3) assuming a space- and time-independent surface tension coefficient  $\gamma$ . As before we scale the equations, such that the considered space domain is the interval  $\mathcal{Q} = (0, 1)$ . For simplicity we suppress any labeling of dimensionless and scaled quantities. Supplementing the model equations with the electrospinning associated boundary conditions, the respective dimensionless system is given by

**System C.1** (Time-dependent viscous electrospinning model).

Kinematic and dynamic equations as well as material laws,  $s \in (0, 1)$ ,  $t > 0$ :

$$\begin{aligned}
 L^{-1}\partial_s \mathbf{r} &= \mathbf{R}(\mathbf{q})^T \cdot \mathbf{e}_3, \\
 L^{-1}\partial_s \mathbf{q} &= \mathbf{S}(\boldsymbol{\kappa}) \cdot \mathbf{q}, \\
 L^{-1}\partial_s (\mathbf{v} - u\mathbf{e}_3) &= \boldsymbol{\omega} \times \mathbf{e}_3 + \mathbf{v} \times \boldsymbol{\kappa}, \\
 \partial_t \boldsymbol{\kappa} + L^{-1}\partial_s (u\boldsymbol{\kappa} - \boldsymbol{\omega}) &= \boldsymbol{\kappa} \times \boldsymbol{\omega}, \\
 \partial_t \varrho_M + L^{-1}\partial_s (u\varrho_M) &= 0, \\
 \partial_t \varrho_V + L^{-1}\partial_s (u\varrho_V) &= 0, \\
 \partial_t (\rho_M \mathbf{v}) + L^{-1}\partial_s (u\rho_M \mathbf{v} - \mathbf{n} - \Gamma\pi\gamma R\mathbf{e}_3) &= \varrho_M \mathbf{v} \times \boldsymbol{\omega} + \boldsymbol{\kappa} \times \mathbf{n} \\
 &\quad + \Gamma\pi\gamma R\boldsymbol{\kappa} \times \mathbf{e}_3 + \mathbf{f}_{\text{el}} + \mathbf{f}_{\text{air}}, \\
 \partial_t (\varrho_M \varrho_V \mathbf{P}_2 \cdot \boldsymbol{\omega}) + L^{-1}\partial_s \left( u\varrho_M \varrho_V \mathbf{P}_2 \cdot \boldsymbol{\omega} - \frac{1}{\varepsilon^2} \mathbf{m} \right) &= \varrho_M \varrho_V (\mathbf{P}_2 \cdot \boldsymbol{\omega}) \times \boldsymbol{\omega} \\
 &\quad + \frac{1}{\varepsilon^2} \boldsymbol{\kappa} \times \mathbf{m} + \frac{1}{\varepsilon^2} \mathbf{e}_3 \times \mathbf{n}, \\
 L^{-1}\partial_s u &= \frac{\text{Re}}{3} \frac{n_3}{\mu \varrho_V}, \\
 L^{-1}\partial_s \boldsymbol{\omega} &= \boldsymbol{\omega} \times \boldsymbol{\kappa} + \frac{\text{Re}}{3\varepsilon^2} \frac{1}{\mu \varrho_V^2} \mathbf{P}_{2/3}^{-1} \cdot \mathbf{m},
 \end{aligned}$$

with outer forces:

$$\begin{aligned}
 \mathbf{f}_{\text{el}} &= \frac{\Xi}{4} I \Phi \left( \frac{4}{u} \mathbf{R}(\mathbf{q}) \cdot \mathbf{e}_3 - \Theta \frac{I}{u^2 \varepsilon_{p,*} \pi \Phi} \log \left( \frac{1}{\varepsilon} \frac{1}{R} \right) \boldsymbol{\kappa} \times \mathbf{e}_3 \right), \\
 \mathbf{f}_{\text{air}} &= \frac{A_*}{\text{Re}_*^2} \frac{\rho_* v_*^2}{2R} \mathbf{F} \left( \mathbf{e}_3, \text{Re}_* \frac{2R}{v_*} (\mathbf{v}_* - \mathbf{v}) \right),
 \end{aligned}$$

and initial-boundary conditions,  $t \in [0, 1]$ :

$$\begin{aligned}
 \mathbf{r}(0, t) &= \mathbf{0}, & \mathbf{q}(0, t) &= (1, 0, 0, 0), & \mathbf{v}(0, t) &= \mathbf{e}_3, & \boldsymbol{\kappa}(0, t) &= \mathbf{0}, \\
 \varrho_M(0, t) &= 1, & \varrho_V(0, t) &= 1, & \mathbf{n}(1, t) &= \mathbf{0}, & \mathbf{m}(1, t) &= \mathbf{0}, \\
 u(0, t) &= 1, & \boldsymbol{\omega}(0, t) &= \mathbf{0}, & r_3(1, t) &= 1.
 \end{aligned}$$

Assuming constant mass density  $\rho = \varrho_M / \varrho_V = \text{const}$  we treat  $\rho$  as parameter such that it is sufficient to consider either the mass or the volume balance equation exclusively. In the following we stick to the volume balance and omit the mass balance equation. The parameter  $\rho$  becomes unity in the dimensionless formulation.

Obviously, the BVP has the general conservation form

$$\partial_t \mathbf{h}(\mathbf{y}(s, t)) + \partial_s \mathbf{j}(\mathbf{y}(s, t)) = \mathbf{k}(\mathbf{y}(s, t)), \quad \mathbf{g}(\mathbf{y}(0, t), \mathbf{y}(1, t)) = \mathbf{0}, \quad (\text{C.1})$$

with  $\mathbf{y}$  the vector of unknowns. For the temporal stability analysis we assume a solution of the form

$$\mathbf{y}(s, t) = \mathbf{y}^\epsilon(s, t) = \mathbf{y}^0(s) + \epsilon \exp(\lambda t) \mathbf{y}^1(s)$$

with  $\lambda \in \mathbb{C}$  and  $0 < \epsilon \ll 1$ . By means of this ansatz and Taylor expansion around  $\mathbf{y}^0$ , (C.1) can be split into two systems, i.e.,

$$\frac{d}{ds} \mathbf{j}(\mathbf{y}^0(s)) = \mathbf{k}(\mathbf{y}^0(s)), \quad \mathbf{g}(\mathbf{y}^0(0), \mathbf{y}^0(1)) = \mathbf{0}, \quad (\text{C.2a})$$

for the stationary solution  $\mathbf{y}^0$  as well as

$$\left( \mathbf{K}(s) - \frac{d}{ds} \mathbf{J}(s) - \mathbf{J}(s) \frac{d}{ds} \right) \cdot \mathbf{y}^1(s) = \lambda \mathbf{H}(s) \cdot \mathbf{y}^1(s), \quad \mathbf{A} \cdot \mathbf{y}^1(0) + \mathbf{B} \cdot \mathbf{y}^1(1) = \mathbf{0}, \quad (\text{C.2b})$$

for the transient correction  $\mathbf{y}^1$  and  $\lambda$ , where  $\mathbf{H}(s) = \partial_{\mathbf{y}} \mathbf{h}(\mathbf{y}^0(s))$ ,  $\mathbf{J}(s) = \partial_{\mathbf{y}} \mathbf{j}(\mathbf{y}^0(s))$ ,  $\mathbf{K}(s) = \partial_{\mathbf{y}} \mathbf{k}(\mathbf{y}^0(s))$ ,  $\mathbf{A} = \partial_1 \mathbf{g}(\mathbf{y}^0(0), \mathbf{y}^0(1))$  and  $\mathbf{B} = \partial_2 \mathbf{g}(\mathbf{y}^0(0), \mathbf{y}^0(1))$ . Here, the sign of the real part of  $\lambda$  decides about stability or instability of  $\mathbf{y}^0$  for  $t \rightarrow \infty$ .

A solution of (C.2a) is obviously a stationary jet that forms a straight line from the nozzle towards the collector, i.e.,

$$\begin{aligned} \mathbf{r}^0(s) &= s \mathbf{e}_3, & \mathbf{q}^0(s) &= (1, 0, 0, 0), & \mathbf{v}^0(s) &= u^0(s) \mathbf{e}_3, & \boldsymbol{\kappa}^0(s) &= \mathbf{0}, \\ \varrho_V^0(s) &= 1/u^0(s), & \mathbf{n}^0(s) &= n_3^0(s) \mathbf{e}_3, & \mathbf{m}^0(s) &= \mathbf{0}, & \boldsymbol{\omega}^0(s) &= \mathbf{0}, \\ L &= 1 \end{aligned}$$

with  $u^0$ ,  $n_3^0$  being prescribed by the BVP

$$\begin{aligned} \partial_s u^0 &= \frac{\text{Re } u^0 n_3^0}{3 \mu}, & \partial_s n_3^0 &= \frac{\text{Re } u^0 n_3^0}{3} + \frac{\Gamma \text{Re}}{2 \cdot 3 \mu} \sqrt{\pi \gamma} \frac{n_3^0}{\sqrt{u^0}} - \Xi I \Phi \frac{1}{u^0} - \mathbf{f}_{\text{air}} \cdot \mathbf{e}_3, \\ u^0(0) &= 1, & n_3^0(1) &= 0. \end{aligned}$$

We determine  $u^0$  and  $n_3^0$  with the collocation method presented in Sec. 3.1. An adaption of the initial guess ( $u^0 = 1$ ,  $n_3^0 = 0$ ) in the sense of a continuation method is not necessary here due to the simplicity of the BVP. In order to solve (C.2b) we consider an equidistant grid of mesh size  $\Delta s$  with grid points  $s_i$ ,  $i \in \{0, \dots, N_s\}$ . Integrating the differential equation over the intervals  $[s_{i-1}, s_i]$  we apply the fundamental theorem of calculus and the trapezoidal quadrature rule respectively

$$\begin{aligned} \mathbf{0} &= \int_{s_{i-1}}^{s_i} \left( \lambda \mathbf{H}(s) \cdot \mathbf{y}^1(s) + \frac{d}{ds} (\mathbf{J}(s) \cdot \mathbf{y}^1(s)) - \mathbf{K}(s) \cdot \mathbf{y}^1(s) \right) ds \\ &\approx \lambda \frac{\Delta s}{2} (\mathbf{H}_i \cdot \mathbf{y}_i^1 + \mathbf{H}_{i-1} \cdot \mathbf{y}_{i-1}^1) + \mathbf{J}_i \cdot \mathbf{y}_i^1 - \mathbf{J}_{i-1} \cdot \mathbf{y}_{i-1}^1 - \frac{\Delta s}{2} (\mathbf{K}_i \cdot \mathbf{y}_i^1 + \mathbf{K}_{i-1} \cdot \mathbf{y}_{i-1}^1) \end{aligned}$$

with  $\mathbf{y}_i^1 = \mathbf{y}^1(s_i)$ ,  $\mathbf{H}_i = \mathbf{H}(s_i)$ ,  $\mathbf{J}_i = \mathbf{J}(s_i)$ , and  $\mathbf{K}_i = \mathbf{K}(s_i)$ . Incorporating the boundary conditions we obtain the generalized eigenvalue problem

$$\mathbf{W} \cdot \mathbf{Y} = \lambda \mathbf{Z} \cdot \mathbf{Y},$$

with  $\mathbf{W}, \mathbf{Z} \in \mathbb{R}^{N_v(N_s+1) \times N_v(N_s+1)}$

$$\mathbf{W} = \begin{pmatrix} \mathbf{A} & 0 & \cdots & 0 & \mathbf{B} \\ \mathbf{J}_0 + \frac{\Delta s}{2} \mathbf{K}_0 & -\mathbf{J}_1 + \frac{\Delta s}{2} \mathbf{K}_1 & 0 & \cdots & 0 \\ 0 & \mathbf{J}_1 + \frac{\Delta s}{2} \mathbf{K}_1 & -\mathbf{J}_2 + \frac{\Delta s}{2} \mathbf{K}_2 & 0 & \cdots & 0 \\ \vdots & & \ddots & \ddots & & \vdots \\ \vdots & & & \ddots & \ddots & 0 \\ 0 & \cdots & & 0 & \mathbf{J}_{N_s-1} + \frac{\Delta s}{2} \mathbf{K}_{N_s-1} & -\mathbf{J}_{N_s} + \frac{\Delta s}{2} \mathbf{K}_{N_s} \end{pmatrix},$$

$$\mathbf{Z} = \begin{pmatrix} 0 & 0 & \cdots & 0 & 0 \\ \frac{\Delta s}{2} \mathbf{H}_0 & \frac{\Delta s}{2} \mathbf{H}_1 & 0 & \cdots & 0 \\ 0 & \frac{\Delta s}{2} \mathbf{H}_1 & \frac{\Delta s}{2} \mathbf{H}_2 & 0 & \cdots & 0 \\ \vdots & & \ddots & \ddots & & \vdots \\ \vdots & & & \ddots & \ddots & 0 \\ 0 & \cdots & 0 & \frac{\Delta s}{2} \mathbf{H}_{N_s-1} & \frac{\Delta s}{2} \mathbf{H}_{N_s} \end{pmatrix},$$

$\mathbf{Y} = (\mathbf{y}_i^1)_{i=1, \dots, N_s} \in \mathbb{R}^{N_v(N_s+1)}$  the unknown (generalized) eigenvector and  $N_v$  the number of rod unknowns. We compute the solution using the MATLAB routine *eig.m*. Since  $\mathbf{Z}$  is singular it is convenient to consider the inverse problem  $\tilde{\lambda} \mathbf{W} \cdot \mathbf{Y} = \mathbf{Z} \cdot \mathbf{Y}$ ,  $\tilde{\lambda} = 1/\lambda$  transforming infinite eigenvalues to zero.

The observed whipping effect turns out to be a instability in the stated mathematical sense. Fig. C.1 (left) shows the eigenvalue spectrum to the model parameters of Example 2 in Sec. 5.4, i.e.,

$$(\varepsilon, \text{Re}, \Gamma, \Xi, \Theta, A_*, \text{Re}_*) = (5 \cdot 10^{-2}, 2.4, 60, 10^5, 360, 10^{-1}, 3). \quad (\text{C.3})$$

The computation is carried out on a mesh with  $N_s = 200$  equidistant points. Obviously, there exist (inverse) eigenvalues  $\tilde{\lambda}$  with positive real part. The corresponding solution  $\mathbf{y}^\epsilon$  moves away from the stationary solution  $\mathbf{y}^0$  for infinite times, which is hence unstable. The (discrete) eigenfunction  $r_1$  related to the eigenvalue  $\tilde{\lambda}$  with largest real part reveals the formation of the characteristic whipping, see Fig. C.1 (right). We study the transition from stable to unstable solutions in dependence on the electric force related parameters  $\Xi$  and  $\Theta$ . Remember that  $\Xi$  stands for the strength of the outer electric field, whereas  $\Theta$  represents the magnitude of Coulomb repulsion. For the computation of the phase diagram

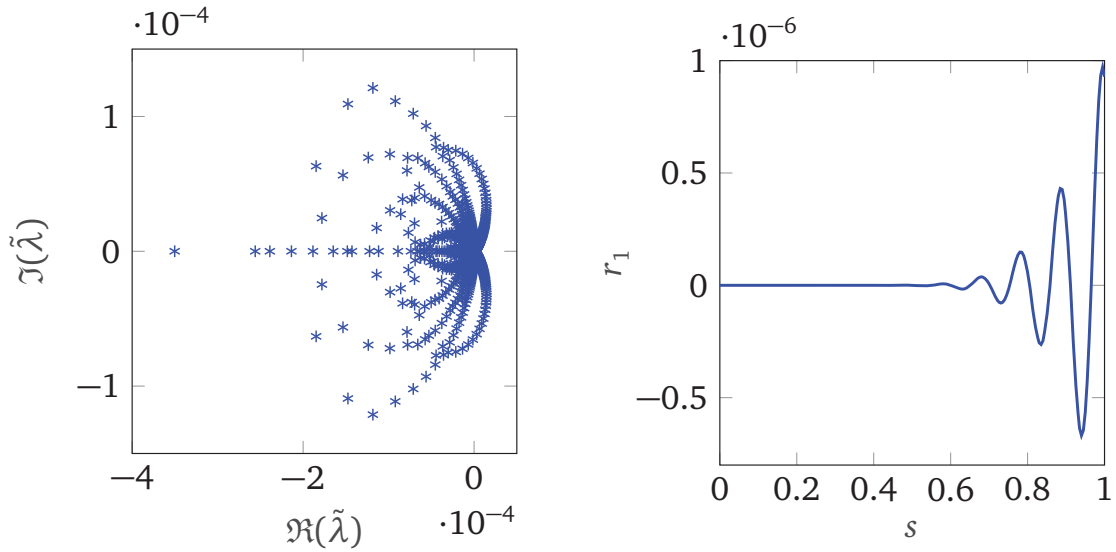


**Figure C.1.:** Results of stability analysis for the parameters given in (C.3) (cf. Example 2 in Sec. 5.4) and  $N_s = 200$ . *Left:* Spectrum of the inverse eigenvalues  $\tilde{\lambda}$  in the complex plane. *Right:* Eigenfunction  $r_1$  related to the eigenvalue  $\tilde{\lambda}$  with largest real part.

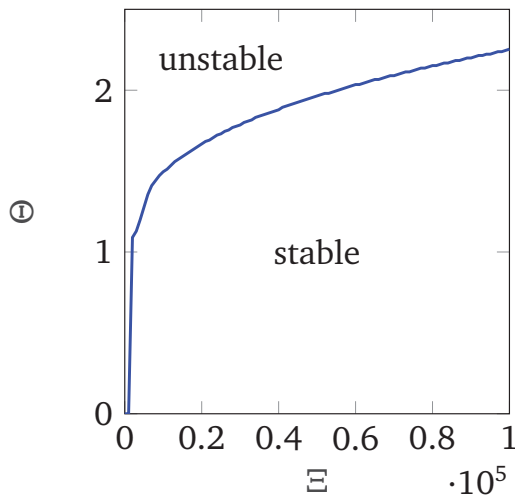


**Figure C.2.:** Stability diagram with respect to  $(\Xi, \Theta) \in [0, 10^5] \times \mathbb{R}_0^+$  for fixed parameters  $(\varepsilon, \text{Re}, \Gamma, A_*, \text{Re}_*) = (5 \cdot 10^{-2}, 2.4, 60, 0.1, 3)$  (cf. Example 2). The lower region indicates stable solutions, whereas the upper region characterizes unstable solutions.

we choose discrete test parameters  $\Xi_i = i \cdot 10^3$ ,  $i = 0, \dots, 10^2$  and determine the corresponding smallest  $\Theta_i$ , for which a solution of the eigenvalue problem with  $N_s = 200$  has an eigenvalue with positive real part. In Fig. C.2 the lower region bounded by the data points and the horizontal axis characterizes the stable

solutions, the upper region above the data points corresponds to the unstable solutions. As we have seen in Sec. 5.3 an increasing outer electric field stabilizes the jet, hence for larger values of  $\Xi$  the transition from stable to unstable solutions takes place for larger values of  $\Theta$ .

## C.2. Resolution of boundary layers

For strong jet whipping in electrospinning processes boundary layers arise in the variables  $\kappa$ ,  $\mathbf{n}$  and  $\mathbf{m}$  at the nozzle. This effect is observed in Fig. 5.7 for the choice of the dimensionless parameters (Example 2 in Sec. 5.4)

$$(\varepsilon, \text{Re}, \Gamma, \Xi, \Theta, A_*, \text{Re}_*) = (5 \cdot 10^{-2}, 2.4, 60, 10^5, 360, 10^{-1}, 3). \quad (\text{C.4})$$

To verify that these boundary layers are model-based and that our numerical scheme resolves them correctly, we re-compute the results in material (Lagrangian) description.

For the transformation of our electrospinning model (System 5.5) from Eulerian to Lagrangian description the concepts presented in Sec. 2.1.6 are utilized, i.e., we employ the general bijective mapping  $S(\cdot, t) : [\zeta_L(t), \zeta_R(t)] \rightarrow [s_L(t), s_R(t)]$ ,  $\zeta \mapsto S(\zeta, t)$  that satisfies the relations

$$\partial_t S(\zeta, t) = u(S(\zeta, t)), \quad S(\zeta, t_{in}(\zeta)) = 0$$

where  $t_{in}(\zeta)$  prescribes the time of the material point  $\zeta$  entering the steady flow domain  $S(\zeta, t) \in [0, 1]$ . Due to the (Euler-)stationary consideration the mapping  $S$  depends only on the run time  $\sigma(\zeta) = t - t_{in}(\zeta)$  and, following the procedure given in [3], the re-parameterization into the Lagrangian description simplifies: We set  $S(\zeta, t) = \hat{S}(t - t_{in}(\zeta)) = \hat{S}(\sigma(\zeta))$  and employ the concept of type- $n$ -fields,  $n \in \mathbb{Z}$ , as introduced in Sec. 2.1.6, i.e., to an arbitrary field  $f$  in Eulerian description the associated Lagrangian field  $\tilde{f}$  is related according to

$$\tilde{f}(\zeta, t) = j^n(\zeta, t)f(S(\zeta, t)), \quad j(\zeta, t) = \partial_\zeta S(\zeta, t).$$

The exclusive dependence on the run time  $\sigma$  is also valid for an arbitrary Lagrangian field,  $\tilde{f}(\zeta, t) = \hat{f}(t - t_{in}(\zeta)) = \hat{f}(\sigma(\zeta))$ . Using  $t_{in}(\zeta) = -\zeta/u(0) = -\sigma/u_{in}$  with  $u_{in} = 1$  in the dimensionless formulation we obtain

$$\partial_t \tilde{f}(\zeta, t) = \partial_t \hat{f}(t + \zeta) = \partial_\sigma \hat{f}(\sigma) = \partial_\zeta \hat{f}(t + \zeta) = \partial_\zeta \tilde{f}(\zeta, t)$$

and, therefore,

$$u(S(\zeta, t)) = \partial_t S(\zeta, t) = \partial_\zeta S(\zeta, t) = j(\zeta, t)$$

for all  $\zeta, t$ . Applying these concepts with the typification of the variables as given in Sec. 2.1.6, regarding the elongation  $\hat{e}(\sigma(\zeta)) = \tilde{e}(\zeta, t) = j(\zeta, t)$  and dropping the label  $\hat{\cdot}$ , the model for the jet's whipping in the Lagrangian description is given by

**System C.2** (Stationary viscous fiber electrospinning model in Lagrangian parameterization).

*Kinematic and dynamic equations as well as material laws,  $\sigma \in (0, 1)$ :*

$$\begin{aligned}
 T^{-1}\partial_\sigma \mathbf{r} &= e\mathbf{R}(\mathbf{q})^\top \cdot \mathbf{e}_3, \\
 T^{-1}\partial_\sigma \mathbf{q} &= \mathbf{S}(\boldsymbol{\kappa}) \cdot \mathbf{q}, \\
 T^{-1}\partial_\sigma \mathbf{n} &= \mathbf{n} \times \boldsymbol{\kappa} + T^{-1}(\partial_\sigma e)\mathbf{e}_3 + e\boldsymbol{\kappa} \times \mathbf{e}_3 + 2e\Omega(\mathbf{R}(\mathbf{q}) \cdot \mathbf{e}_3) \times \mathbf{e}_3 \\
 &\quad + \Omega^2\mathbf{R}(\mathbf{q}) \cdot (\mathbf{e}_3 \times (\mathbf{e}_3 \times \mathbf{r})) - \mathbf{f}_{\text{ca}} - \mathbf{f}_{\text{el}} - \mathbf{f}_{\text{air}}, \\
 T^{-1}\partial_\sigma \mathbf{m} &= \mathbf{m} \times \boldsymbol{\kappa} + e\mathbf{n} \times \mathbf{e}_3 + \varepsilon^2 \frac{1}{e} \mathbf{P}_2 \cdot \left( T^{-1}\partial_\sigma \boldsymbol{\kappa} - \frac{1}{e} T^{-1}(\partial_\sigma e)\boldsymbol{\kappa} - \Omega\boldsymbol{\kappa} \times \mathbf{e}_3 \right) \\
 &\quad - \varepsilon^2 \frac{\Omega}{e^2} \mathbf{P}_2 \cdot \left( T^{-1}\partial_\sigma e(\mathbf{R}(\mathbf{q}) \cdot \mathbf{e}_3 - \mathbf{e}_3) + e(\boldsymbol{\kappa} - \Omega\mathbf{e}_3) \times (\mathbf{R}(\mathbf{q}) \cdot \mathbf{e}_3) \right) \\
 &\quad - \varepsilon^2 \frac{1}{e} (\mathbf{P}_2 \cdot (\boldsymbol{\kappa} + \Omega(\mathbf{R}(\mathbf{q}) \cdot \mathbf{e}_3 - \mathbf{e}_3))) \times (\boldsymbol{\kappa} + \Omega(\mathbf{R}(\mathbf{q}) \cdot \mathbf{e}_3 - \mathbf{e}_3)), \\
 T^{-1}\partial_\sigma e &= \frac{\text{Re}}{3} \frac{1}{\mu} e^2 n_3, \\
 T^{-1}\partial_\sigma \boldsymbol{\kappa} &= \frac{\text{Re}}{3\varepsilon^2} \frac{e^3}{\mu} \mathbf{P}_{2/3}^{-1} \cdot \mathbf{m} + \Omega\boldsymbol{\kappa} \times \mathbf{e}_3,
 \end{aligned}$$

*with outer forces:*

$$\begin{aligned}
 \mathbf{f}_{\text{ca}} &= \Gamma\pi R\gamma \left( \boldsymbol{\kappa} \times \mathbf{e}_3 - \frac{1}{2e} T^{-1}(\partial_\sigma e)\mathbf{e}_3 \right), \\
 \mathbf{f}_{\text{el}} &= \frac{\Xi}{4} I\Phi \left( 4\mathbf{R}(\mathbf{q}) \cdot \mathbf{e}_3 - \Theta \frac{I}{e^2 \varepsilon_{p,*} \pi \Phi} \log \left( \frac{1}{\varepsilon} \frac{1}{R} \right) \boldsymbol{\kappa} \times \mathbf{e}_3 \right), \\
 \mathbf{f}_{\text{air}} &= e \frac{A_*}{\text{Re}_*^2} \frac{\rho_* v_*^2}{2R} F \left( \mathbf{t}, \text{Re}_* \frac{2R}{v_*} (\mathbf{v}_* - \mathbf{v}) \right),
 \end{aligned}$$

*and boundary conditions:*

$$\begin{aligned}
 \mathbf{r}(0) &= \mathbf{0}, & \mathbf{q}(0) &= (1, 0, 0, 0), & \boldsymbol{\kappa}(0) &= \mathbf{0}, & e(0) &= 1, \\
 r_1(1) &= 0, & r_3(1) &= 1, & \mathbf{n}(1) &= \mathbf{0}, & \mathbf{m}(1) &= \mathbf{0}.
 \end{aligned}$$

The fiber unit tangent is  $\mathbf{t} = \mathbf{e}_3$  and the radius function reads  $R = 1/\sqrt{\pi e}$ . The dimensionless end time is denoted by  $T$  addressing the unknown time of the material point reaching the device bottom. The corresponding reference value is  $T_0 = t_0 = r_0/v_0$ .

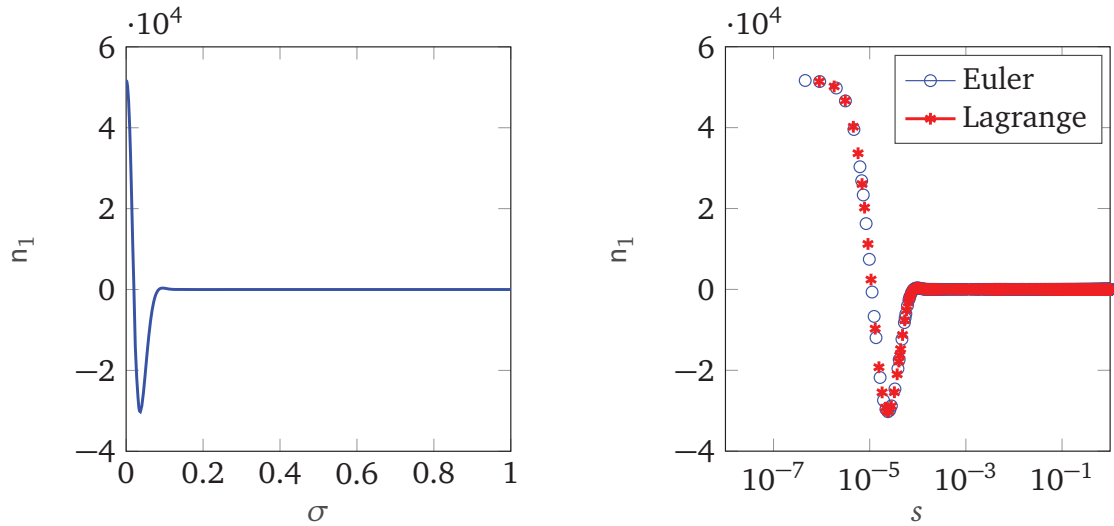


**Figure C.3.:** Boundary layer in the contact force component  $n_1$  for the parameters given in (C.4). *Left:* Zoom into the nozzle region in the Lagrangian setting. *Right:* Distribution of discretization points in the Eulerian and Lagrangian setting.

The Lagrangian description allows to zoom into the region at the nozzle, where the boundary layers are present for strong whipping setups (see Fig. C.3 (left) for the parameters given in (C.4)). Mapping the Lagrangian parameters  $\sigma_i$  used in the simulation as grid points onto the associated Eulerian arc length parameters  $s_i = \hat{S}(\sigma_i)$  by means of the nonlinear transformation  $\hat{S}$ , we see that both descriptions resolve the boundary layer in a similar good manner, Fig. C.3 (right). The reason why we generally prefer to use the Eulerian description is the desired consideration of high jet thinning which goes along with the development of boundary layers at the jet end in the Lagrangian description. The transformation from spatial to material description shifts layers from the nozzle region to the jet end.

# Notations

## Special vectors, matrices, sets, etc.

$\mathbb{N}$	Set of natural numbers
$\mathbb{Z}$	Set of integers
$\mathbb{R}$	Set of real numbers
$\mathbb{C}$	Set of complex numbers
$\mathbb{E}^3$	Three-dimensional Euclidean Space
$\mathbb{S}^2$	Two-dimensional sphere in $\mathbb{R}^3$
$SO(3)$	Special orthogonal group in $\mathbb{R}^3$
$\mathbb{1}$	Identity matrix
$\underline{\mathbf{1}}$	Tuple of ones in $\mathbb{R}^n$
$\mathbf{e}_i$	$i$ -th canonical basis vector $i = 1, 2, 3$ , e.g., $\mathbf{e}_1 = (1, 0, 0)$
$z$	Scalar in $\mathbb{R}$ or $\mathbb{C}$
$\vec{\mathbf{z}}$	Invariant vector in $\mathbb{E}^3$
$\mathbf{z} = (z_1, z_2, z_3)$	Representation of $\vec{\mathbf{z}}$ with respect to outer basis
$\mathbf{z} = (z_1, z_2, z_3)$	Representation of $\vec{\mathbf{z}}$ with respect to director basis
$\bar{\mathbf{z}}$	Invariant Tensor in $\mathbb{E}^3 \otimes \mathbb{E}^3$
$\text{diag}(\mathbf{z})$	Diagonal matrix with diagonal entries $\mathbf{z} \in \mathbb{R}^n$
$\Re(z)$	Real part of a scalar $z \in \mathbb{C}$
$\Im(z)$	Imaginary part of a scalar $z \in \mathbb{C}$
$ z $	Absolute value of $z \in \mathbb{R}$
$\ \mathbf{z}\ $	Euclidean norm of $\mathbf{z} \in \mathbb{R}^n$
$\ \mathbf{z}\ _\infty$	Maximum norm of $\mathbf{z} \in \mathbb{R}^n$
$\mathbf{x} \cdot \mathbf{y}$	Scalar product of $\mathbf{x}, \mathbf{y} \in \mathbb{R}^n$
$\mathbf{x} \times \mathbf{y}$	Cross product of $\mathbf{x}, \mathbf{y} \in \mathbb{R}^n$
$\mathbf{x} \otimes \mathbf{y}$	Dyadic product of $\mathbf{x}, \mathbf{y} \in \mathbb{R}^n$
$\partial_x f$	Partial derivative of $f$ w.r.t. $x$
$\frac{d}{dx} f$	Total derivative of $f$ w.r.t. $x$
$\nabla f$	Gradient of $f$
$\mathcal{O}(g)$	Landau notation, i.e., $f \in \mathcal{O}(g)$ means $\exists C > 0 \exists x_0 > 0$ $\forall x > x_0 :  f(x)  \leq C \cdot  g(x) $

## Model quantities

$\mathcal{D}$	Space-time domain
$\mathcal{Q}$	Space domain
$\zeta$	Lagrange parameter (coordinate of material point) [m]
$s$	Euler parameter (arc length) [m]
$t$	Time parameter [s]
$\{\vec{\mathbf{a}}_1, \vec{\mathbf{a}}_2, \vec{\mathbf{a}}_3\}$	Outer basis (time- and space-invariant)
$\{\vec{\mathbf{d}}_1, \vec{\mathbf{d}}_2, \vec{\mathbf{d}}_3\}$	Director basis
$\vec{\mathbf{r}}$	Curve (invariant) [m]
$\mathbf{r} = (r_1, r_2, r_3)$	Curve (outer basis) [m]
$\mathbf{r}$	Curve (director basis) [m]
$\vec{\mathbf{v}}$	Velocity (invariant) [m/s]
$\mathbf{v} = (v_1, v_2, v_3)$	Velocity (outer basis) [m/s]
$\mathbf{v}$	Velocity (director basis) [m/s]
$\vec{\boldsymbol{\tau}}$	Tangent (invariant)
$\boldsymbol{\tau} = (\tau_1, \tau_2, \tau_3)$	Tangent (outer basis)
$\boldsymbol{\tau} = (\tau_1, \tau_2, \tau_3)$	Tangent (director basis)
$\vec{\boldsymbol{\kappa}}$	Curvature (invariant) [1/m]
$\boldsymbol{\kappa} = (\kappa_1, \kappa_2, \kappa_3)$	Curvature (outer basis) [1/m]
$\boldsymbol{\kappa} = (\kappa_1, \kappa_2, \kappa_3)$	Curvature (director basis) [1/m]
$\vec{\boldsymbol{\omega}}$	Angular velocity (invariant) [1/s]
$\boldsymbol{\omega} = (\omega_1, \omega_2, \omega_3)$	Angular velocity (outer basis) [1/s]
$\boldsymbol{\omega} = (\omega_1, \omega_2, \omega_3)$	Angular velocity (director basis) [1/s]
$\bar{\mathbf{R}}$	Rotation between outer and director basis (invariant)
$\mathbf{R} = (R_{ij})_{i,j=1,2,3}$	Rotational matrix between outer and director basis
$\mathbf{q} = (q_0, q_1, q_2, q_3)$	Unit quaternion to parameterize the rotation $\mathbf{R}$
$\mathbf{S}$	Skew-symmetric matrix for the evolution of the quaternions
$\vec{\mathbf{n}}$	Contact force (invariant) [N]
$\mathbf{n} = (n_1, n_2, n_3)$	Contact force (outer basis) [N]
$\mathbf{n} = (n_1, n_2, n_3)$	Contact force (director basis) [N]
$\vec{\mathbf{m}}$	Contact couple (invariant) [N m]
$\mathbf{m} = (m_1, m_2, m_3)$	Contact couple (outer basis) [N m]
$\mathbf{m} = (m_1, m_2, m_3)$	Contact couple (director basis) [N m]
$\vec{\mathbf{f}}, \mathbf{f}, \mathbf{f}$	Body force density (invariant, outer basis, director basis) [N/m]
$\vec{\mathbf{l}}, \mathbf{l}, \mathbf{l}$	Body couple line density (invariant, outer basis, director basis) [N]

$\bar{\mathbf{J}}$	Inertia tensor (invariant) [m <sup>4</sup> ]
$\mathbf{J} = (J_{ij})_{i,j=1,2,3}$	Inertia matrix (director basis) [m <sup>4</sup> ]
$\mathbf{P}_x$	Scaling matrix $\mathbf{P}_x = \text{diag}(1, 1, x)/(4\pi)$
$\varrho_M$	Mass line density [kg/m]
$\varrho_V$	Volume line density [m <sup>2</sup> ]
$A$	Area of cross-sections [m <sup>2</sup> ], i.e., $A = \varrho_V/e$
$\rho$	Density [kg/m <sup>3</sup> ], i.e., $\rho = \varrho_M/\varrho_V$
$e$	Elongation, i.e., $e = \ \boldsymbol{\tau}\ $
$u$	Scalar speed (Euler) [m/s]
$\mu$	Dynamic viscosity [Pa s]
$\theta$	Relaxation time [s]
$E$	Elastic modulus [Pa]
$Q_M$	Mass flux [kg/s], i.e., $Q_M = \varrho_M u = \rho A u$ (Euler)
$Q_V$	Volume flux [m <sup>3</sup> /s], i.e., $Q_V = \varrho_V u = A u$ (Euler)
$N$	Tension [N], i.e., $N = n_3$
$M$	Twisting torque [N], i.e., $M = m_3$
$p$	Pressure [Pa]
$\sigma$	Stress [Pa]
$m$	Second stress variable [Pa], $m = \sigma + p$
$L$	Length [m]
$\varepsilon$	Slenderness parameter
Re	Reynolds number (ratio of inertial to viscous forces)
De	Deborah number (ratio of relaxation time to observation time)
Ma	Mach number (ratio of inertial to compressive forces), $\text{Ma}^2 = \text{ReDe}$

## Applications

$\{\vec{\mathbf{d}}_1^s, \vec{\mathbf{d}}_2^s, \vec{\mathbf{d}}_3^s\}$	Spin-associated director basis
$\{\vec{\mathbf{a}}_1^s, \vec{\mathbf{a}}_2^s, \vec{\mathbf{a}}_3^s\}$	Rotating outer basis
$\{\vec{\mathbf{a}}_r, \vec{\mathbf{a}}_\varphi, \vec{\mathbf{a}}_3\}$	Cylindrical basis
$\vec{\mathbf{f}}_g, \mathbf{f}_g, \mathbf{f}_g$	Gravitational force (invariant, outer basis, director basis) [N/m]
$\vec{\mathbf{e}}_g, \mathbf{e}_g$	Direction of gravity (invariant, outer basis)
$g$	Gravitational acceleration, i.e., $g = 9.81 \text{ m/s}^2$
Fr	Froude number (ratio of inertial to gravitational forces)

$\vec{f}_{air}, f_{air}, \mathbf{f}_{air}$	Aerodynamic force (invariant, outer basis, director basis) [N/m]
$t$	Normalized fiber tangent (outer basis), i.e., $t = \tau/e$
$\vec{v}_*, v_*, \mathbf{v}_*$	Airflow velocity (invariant, outer, director basis) [m/s]
$\rho_*$	Airflow density [kg/m <sup>3</sup> ]
$\nu_*$	Airflow kinematic viscosity [m <sup>2</sup> /s]
$Re_*$	Air-fiber Reynolds number
$A_*$	Air-drag associated number
$\vec{f}_{ca}, f_{ca}, \mathbf{f}_{ca}$	Capillary force (invariant, outer basis, director basis) [N/m]
$\gamma$	Surface tension coefficient [N/m]
$\Gamma$	Scaled inverse of capillary number (ratio of surface tension forces to viscous drag forces)
$\vec{f}_{el}, f_{el}, \mathbf{f}_{el}$	Electric force (invariant, outer basis, director basis) [N/m]
$\vec{E}$	External electric field [V/m]
$\varsigma$	Surface charge density [A s/m <sup>2</sup> ]
$\Phi$	Applied voltage [V]
$I$	Electric current [A]
$\lambda$	Electrical conductivity [A/(V m)]
$\epsilon_{p,*}$	Airflow electric permittivity [A s/(V m)]
$\Xi, \Theta, \Lambda$	Potential-current associated numbers
$T_*$	Airflow temperature [K]
$p_*$	Airflow pressure [Pa]
$e_*$	Airflow inner energy [J/kg]
$R_*$	Airflow specific gas constant [J/(kg K)]
$\xi_*$	Airflow second viscosity [Pa s]
$q_*$	Airflow specific heat capacity [J/(kg K)]
$\lambda_*$	Airflow heat conductivity [W/(m K)]
$\vec{f}_{fib}$	Fiber induced external loads [N/m <sup>3</sup> ]
$q_{fib}$	Fibers induced heat source [W/m <sup>3</sup> ]
$\rho_i$	Partial density of polymer ( $i = p$ ) and diluent phase ( $i = d$ ) [kg/m <sup>3</sup> ]
$\vec{v}_i$	Partial velocities, $i \in \{p, d\}$ , [m/s]
$h, h_i, h_i^0$	Enthalpy (Mixture, partial, pure phase $i \in \{p, d\}$ ) [J/kg]
$C, C_i$	Thermal conductivity (Mixture, partial $i \in \{p, d\}$ ) [W/(m K)]
$\bar{\bar{\Sigma}}, \bar{\bar{\Sigma}}_i$	Stress tensors (Mixture, partial $i \in \{p, d\}$ ) [Pa]
$\vec{f}, \vec{f}_i$	Body forces (Mixture, partial $i \in \{p, d\}$ ) [N/m <sup>3</sup> ]

$q, q_i^0$	Specific heat capacity (Mixture, pure phase $i \in \{p, d\}$ ) [J/(kg K)]
$c, \bar{c}$	Polymer mass fraction (radial profile and averaged over fiber-cross-sections), $c = \rho_p / \rho$
$T, \bar{T}$	Temperature (radial profile and averaged over fiber-cross-sections) [K]
$D$	Diffusion coefficient of diluent in polymer [m <sup>2</sup> /s]
$j_c$	Diluent mass flux in aerodynamic boundary layer [kg/(m <sup>2</sup> s)]
$j_T$	Heat flux in aerodynamic boundary layer [kg/(m <sup>2</sup> s)]
$\zeta_*$	Diluent density in air (at fiber surface) [kg/m <sup>3</sup> ]
$\rho_{d,*}$	Diluent density in air (away from fiber) [kg/m <sup>3</sup> ]
$\varrho_*$	Scaled diluent density in air (at fiber surface) [kg/m <sup>3</sup> ], $\varrho_* = \zeta_* \rho / \rho_d$
$c_{ref}$	Referential polymer mass fraction, $c_{ref} = 1 - \rho_{d,*} / \varrho_*$
$\beta$	Convective mass transfer coefficient [m/s]
$\gamma$	Mass fraction associated transfer coefficient [kg/(m <sup>2</sup> s)]
$\alpha$	Heat transfer coefficient [W/(m <sup>2</sup> K)]
$\delta$	Diluent evaporation enthalpy [J/kg]
$Pe_c, Pe_T$	Mass/temperature Peclet number (ratio of advective to diffusive transport)
$St_c, St_T$	Mass/temperature Stanton number (ratio of mass/heat transferred into a fluid to the ability to accumulate mass/heat)
$Sh_*$	Sherwood number (ratio of convective to diffusive mass transfer in aerodynamic boundary layer)
$Sc_*$	Schmidt number (ratio of viscous diffusion rate to mass diffusion rate in aerodynamic boundary layer)
$Nu_*$	Nusselt number (ratio of convective to conductive heat transfer in aerodynamic boundary layer)
$Pr_*$	Prandtl number (ratio of momentum diffusion rate to thermal diffusion rate in aerodynamic boundary layer)
$D_{d,*}$	Diffusion coefficient of diluent in air [m <sup>2</sup> /s]
$M_d, M_*$	Molecular weight of diluent/air [kg/mol]
$V_d, V_*$	Molar volumes of diluent/air [m <sup>3</sup> /mol]
$\phi_d$	Volume fraction of diluent, i.e., $\phi_d = (1 - c)\rho / \rho_d^0$
$\chi$	Flory-Huggins interaction parameter, default value $\chi = 0.5$
$p_{vap}$	Vapor pressure of diluent [Pa]
$r$	Spatial parameter in radial direction [m]
$R$	Radius of fiber cross-sections [m]
$H$	device height [m]

$Q$	Polymer mass flux [kg/s], i.e., $Q = \bar{c}\rho_M u$ (Euler)
$\mathcal{A}$	Fiber cross-sections
$\langle f \rangle_{\mathcal{A}}$	Integration of $f$ over $\mathcal{A}$
$Dr$	Drawing number (ratio of take up to referential velocity)
$v$	Strain rate [1/s], i.e., $v = \partial_t e/e$
$\varphi, \vartheta$	Azimuth and polar angles of tangent vector $\mathbf{t}$
$\{\mathbf{t}, \mathbf{n}, \mathbf{b}\}$	Local orthogonal basis of $\mathbb{R}^3$ utilized in the description of the fiber tangent evolution w.r.t. spherical coordinates
$\bar{\mathbf{v}}_*, \mathbf{v}'_*$	Mean/fluctuating part of airflow velocity [m/s], $\mathbf{v}_* = \bar{\mathbf{v}}_* + \mathbf{v}'_*$
$\mathbf{v}'_{*,loc}$	Local turbulent airflow velocity fluctuations [m/s]
$k_*$	Turbulent kinetic energy [ $\text{m}^2/\text{s}^2$ ]
$\epsilon_*$	Viscous dissipation rate [ $\text{m}^2/\text{s}^3$ ]
$Tu_*$	Degree of turbulence (airflow)
$Tt_*$	Turbulent time scale ratio (airflow)
$\mathcal{D}_d, \mathcal{D}_s$	Deterministic and stochastic fiber domains
$\mathcal{C}$	Coupling point between deterministic and stochastic fiber domain, i.e., $\mathcal{C} = \mathcal{D}_d \cap \mathcal{D}_s$
$\Omega$	Rotational frequency [1/s]

## Numerical schemes

$\Delta\zeta$	Spatial grid size (Lagrange)
$\Delta s$	Spatial grid size (Euler)
$\Delta t$	Temporal grid size
$\mathbf{y}$	Vector of unknowns
$\mathbf{g}$	Boundary condition function
$\mathbf{h}$	Initial condition function
$\mathbf{p}$	Continuation parameter tuple, $\mathbf{p} \in [0, 1]^n$
$\Delta p$	Step size in continuation method
$\psi$	Unknown in radial advection-diffusion equation
$g$	Green's function in implicit solution expression for $\psi$
$J_i$	$i$ -th Bessel function of first kind, $i \in \mathbb{N}_0$
$\beta_m$	Non-trivial zeros of $J_1$ in ascending order, $m \in \mathbb{N}$

# Bibliography

- [1] S. S. Antman. *Nonlinear Problems of Elasticity*. Springer, New York, 2nd edition, 2005.
- [2] W. Arne, N. Marheineke, A. Meister, S. Schiessl, and R. Wegener. Finite volume approach for the instationary Cosserat rod model describing the spinning of viscous jets. *J. Comput. Phys.*, 294:20–37, 2015.
- [3] W. Arne, N. Marheineke, A. Meister, and R. Wegener. Numerical analysis of Cosserat rod and string models for viscous jets in rotational spinning processes. *Math. Mod. Meth. Appl. Sci.*, 20(10):1941–1965, 2010.
- [4] W. Arne, N. Marheineke, M. Pérez-Saborid, J. Rivero-Rodríguez, R. Wegener, and M. Wieland. Whipping of electrified visco-capillary jets in airflows. *SIAM J. Appl. Math.*, 78(1):343–371, 2018.
- [5] W. Arne, N. Marheineke, J. Schnebele, and R. Wegener. Fluid-fiber-interactions in rotational spinning process of glass wool production. *J. Math. Ind.*, 1(2):1–26, 2011.
- [6] W. Arne, N. Marheineke, and R. Wegener. Asymptotic transition from Cosserat rod to string models for curved viscous inertial jets. *Math. Mod. Meth. Appl. Sci.*, 21(10):1987–2018, 2011.
- [7] W. Arne, N. Marheineke, and R. Wegener. Viscoelastic Cosserat rod model for spinning processes. In P. Quintela, P. Barral, D. Gómez, F. J. Pena, J. Rodríguez, P. Salgado, and M. E. Vázquez-Méndez, editors, *Progress in Industrial Mathematics at ECMI 2016*, pages 235–241. Springer, 2017.
- [8] W. Arne, N. Marheineke, R. Wegener, and M. Wieland. Setup and numerical solution of a viscous Cosserat rod model describing electrospinning. In S. Petrik, editor, *NART 2017 – Nanofibers, Applications and Related Technologies*, pages 9–16. Technical University of Liberec, 2017.
- [9] W. Arne, J. Rivero-Rodríguez, M. Pérez-Saborid, N. Marheineke, and R. Wegener. Homotopy method for viscous Cosserat rod model describing electrospinning. In G. Russo, V. Capasso, G. Nicosia, and V. Romano, editors,

- Progress in Industrial Mathematics at ECMI 2014*, pages 979–984. Springer, 2016.
- [10] V. S. Arpaci. *Conduction heat transfer*. Pearson Custom Pub, 1991.
- [11] V. Bansal and R. L. Shambaugh. On-line determination of diameter and temperature during melt blowing of polypropylene. *Ind. Eng. Chem. Res.*, 37(5):1799–1806, 1998.
- [12] H. A. Barnes. *A Handbook of Elementary Rheology*. The University of Wales Institute of Non-Newtonian Fluid Mechanics, 2000.
- [13] F. Baus, A. Klar, N. Marheineke, and R. Wegener. Low-Mach-number–slenderness limit for elastic Cosserat rods. arXiv:1507.03432, 2015.
- [14] M. Bercea, J. Eckelt, and B. A. Wolf. Vapor pressure of polymer solutions and the modeling of their composition dependence. *Ind. Eng. Chem. Res.*, 48(9):4603–4606, 2009.
- [15] P. K. Bhattacharjee, T. M. Schneider, M. P. Brenner, G. H. McKinley, and G. C. Rutledge. On the measured current in electrospinning. *J. Appl. Phys.*, 107(4):044306, 2010.
- [16] I. Brazinsky, A. G. Williams, and H. L. LaNieve. The dry spinning process: Comparison of theory with experiment. *Polym. Eng. Sci.*, 15(12):834–841, 1975.
- [17] R. R. Bresee and W. C. Ko. Fiber formation during melt blowing. *Int. Nonwovens J.*, 12(2):21–28, 2003.
- [18] T. Chen and X. Huang. Modeling polymer air drawing in the melt blowing nonwoven process. *Textile Res. J.*, 73(7):651–654, 2003.
- [19] T. Chen, X. Wang, and X. Huang. Effects of processing parameters on the fiber diameter of melt blown nonwoven fabrics. *Textile Res. J.*, 75(1):76–80, 2005.
- [20] C. Chung and S. Kumar. Onset of whipping in the melt blowing process. *J. Non-Newtonian Fluid Mech.*, 192:37–47, 2012.
- [21] T. M. Cibis, C. Leithäuser, N. Marheineke, and R. Wegener. Homogenization strategies for fiber curtains and bundles in air flows. In G. Russo, V. Capasso, G. Nicosia, and V. Romano, editors, *Progress in Industrial Mathematics at ECMI 2014*, pages 971–978. Springer, 2017.

- 
- [22] T. M. Gibis, N. Marheineke, and R. Wegener. Asymptotic modeling framework for fiber-flow interactions in a two-way coupling. In M. Fontes, M. Günther, and N. Marheineke, editors, *Progress in Industrial Mathematics at ECMI 2012*, pages 109–117. Springer, 2014.
- [23] K. D. Cole, J. V. Beck, A. Haji-Sheikh, and B. Litkouhi. *Heat Conduction Using Green’s Functions (Series in Computational Methods and Physical Processes in Mechanics and Thermal Sciences)*. CRC Press, 2nd edition, 2010.
- [24] F. J. de la Mora and I. Loscertales. The current emitted by highly conducting Taylor cones. *J. Fluid Mech.*, 260:155–184, 1994.
- [25] F. De Vuyst. Stable and accurate hybrid finite volume methods based on pure convexity arguments for hyperbolic systems of conservation law. *J. Comput. Phys.*, 193:426–468, 2004.
- [26] J. N. Dewynne, J. R. Ockendon, and P. Wilmott. A systematic derivation of the leading-order equations for extensional flows in slender geometries. *J. Fluid Mech.*, 244:323–338, 1992.
- [27] J. Doshi and D. H. Reneker. Electrospinning process and application of electrospun fibers. *J. Electrostat.*, 35:151–160, 1995.
- [28] K. C. Dutton. Overview and analysis of the meltblown process and parameters. *J. Textile Apparel Technology Management*, 6(1):1–24, 2009.
- [29] C. J. Ellison, A. Phatak, D. W. Giles, C. W. Macosko, and F. S. Bates. Melt blown nanofibers: Fiber diameter distributions and onset of fiber breakup. *Polymer*, 48:3306–3316, 2007.
- [30] V. M. Entov and A. L. Yarin. The dynamics of thin liquid jets in air. *J. Fluid Mech.*, 140:91–111, 1984.
- [31] J. J. Feng. The stretching of an electrified non-Newtonian jet: A model for electrospinning. *Phys. Fluids*, 14(11):3912–3926, 2002.
- [32] J. B. Fenn, M. Mann, C. K. Meng, S. F. Wong, and C. M. Whitehouse. Electrospray ionization for mass spectrometry of large biomolecules. *Science*, 246(4926):64–71, 1989.
- [33] J. H. Ferziger and M. Peric. *Numerische Strömungsmechanik*. Springer, Berlin Heidelberg, 1st edition, 2008.
- [34] U. S. Fjordholm and M. Siddhartha. Accurate numerical discretizations of non-conservative hyperbolic systems. *ESIAM M2AN*, 46:187–206, 2012.

- [35] S. Y. Fok and R. G. Griskey. Mass transfer during dry spinning of fibers. *J. Appl. Polym. Sci.*, 11:2417–2426, 1967.
- [36] E. N. Fuller, P. D. Schettler, and J. C. Giddings. A new method for prediction of binary gas-phase diffusion coefficients. *Ind. Eng. Chem.*, 58(5):18–27, 1966.
- [37] A. Ghosal, S. Sinha-Ray, S. Sinha-Ray, A. L. Yarin, and B. Pourdeyhimi. Numerical modeling and experimental study of solution-blown nonwovens formed on a rotating drum. *Polymer*, 105:255–263, 2016.
- [38] A. Ghosal, S. Sinha-Ray, A. L. Yarin, and B. Pourdeyhimi. Numerical prediction of the effect of uptake velocity on three-dimensional structure, porosity and permeability of meltblown nonwoven laydown. *Polymer*, 85:19–27, 2016.
- [39] W. Gilbert. *De Magnete*. J. Wiley & Sons, New York, 1893. Translated by P. F. Mottelay, original work from 1600.
- [40] T. Götz, A. Klar, A. Unterreiter, and R. Wegener. Numerical evidence for the non-existence of stationary solutions of the equations describing rotational fiber spinning. *Math. Mod. Meth. Appl. Sci.*, 18(10):1829–1844, 2008.
- [41] Z. Gou and A. J. McHugh. A comparison of Newtonian and viscoelastic constitutive models for dry spinning of polymer fibers. *J. Appl. Polym. Sci.*, 87:2136–2145, 2003.
- [42] Z. Gou and A. J. McHugh. Two-dimensional modeling of dry spinning of polymer fibers. *J. Non-Newton. Fluid*, 118(2-3):121–136, 2004.
- [43] S. Gramsch, A. Klar, G. Leugering, N. Marheineke, C. Nessler, C. Strohmeyer, and R. Wegener. Aerodynamic web forming: Process simulation and material properties. *J. Math. Ind.*, 6:13, 2016.
- [44] J. Guerrero, J. Rivero, V. R. Gundabala, M. Pérez-Saborid, and A. Fernandez-Nieves. Whipping of electrified jets. *Proc. Nat. Acad. Sci. USA*, 111(38):13763–13767, 2014.
- [45] E. Hairer, S. P. Nørsett, and G. Wanner. *Solving Ordinary Differential Equations I, Nonstiff Problems*. Springer, Berlin, 2nd edition, 1993.
- [46] X. Hao, H. Huang, and Y. C. Zeng. Simulation of jet velocity in the meltblowing process using the coupled air–polymer model. *Textile Res. J.*, page 0040517518809048, 2018.

- [47] M. M. Hohman, M. Shin, G. Rutledge, and M. P. Brenner. Electrospinning and electrically forced jets. I. Stability theory. *Phys. Fluids*, 13:2201–2220, 2001.
- [48] M. M. Hohman, M. Shin, G. Rutledge, and M. P. Brenner. Electrospinning and electrically forced jets. II. Applications. *Phys. Fluids*, 13:2221–2236, 2001.
- [49] P. D. Howell. *Extensional thin layer flows*. PhD thesis, St. Catherin’s College Oxford, 1994.
- [50] F. Hübsch, N. Marheineke, K. Ritter, and R. Wegener. Random field sampling for a simplified model of melt-blowing considering turbulent velocity fluctuations. *J. Stat. Phys.*, 150(6):1115–1137, 2013.
- [51] S. Kase and T. Matsuo. Studies on melt spinning. I. Fundamental equations on the dynamics of melt spinning. *J. Polym. Sci.*, 3:2541–2554, 1965.
- [52] J. Kierzenka and L.F. Shampine. A bvp solver that controls residual and error. *JNAIAM*, 3(1-2):27–41, 2008.
- [53] H. Y. Kim, M. Lee, K. J. Park, S. Kim, and L. Mahadevan. Nanopottery: Coiling of electrospun polymer nanofibers. *Nano Lett.*, 10(6):2138–2140, 2010.
- [54] A. Klar, N. Marheineke, and R. Wegener. Hierarchy of mathematical models for production processes of technical textiles. *Z. Angew. Math. Mech.*, 89:941–961, 2009.
- [55] R. J. LeVeque. *Finite Volume Methods for Hyperbolic Problems*. Cambridge University Press, 2002.
- [56] D. Li and Y. Xia. Direct fabrication of composite and ceramic hollow nano fibers by electrospinning. *Nano. Lett.*, 4(5):933–938, 2004.
- [57] D. Li and Y. Xia. Electrospinning of nanofibers: Reinventing the wheel. *Adv. Mat.*, 16(14):1151–1170, 2004.
- [58] F. Li, X. Y. Yin, and X. Z. Yin. Instability of a viscous coflowing jet in a radial electric field. *J. Fluid Mech.*, 596:285–311, 2008.
- [59] F. Li, X. Y. Yin, and X. Z. Yin. Axisymmetric and non-axisymmetric instability of an electrified viscous coaxial jet. *J. Fluid Mech.*, 632:199–225, 2009.
- [60] M. Lorenz, N. Marheineke, and R. Wegener. On simulations of spinning processes with a stationary one-dimensional upper convected Maxwell model. *J. Math. Ind.*, 4(1):2, 2014.

- [61] I. G. Loscertales, A. Barrero, Guerrero I., R. Cortijo, M. Marquez, and A. M. Ganan-Calvo. Micro/nano encapsulation via electrified coaxial liquid jets. *Science*, 295(5560):1695–1698, 2002.
- [62] V. Majer and V. Svoboda. *Enthalpies of Vaporization of Organic Compounds: A Critical Review and Data Compilation*. Blackwell Scientific Publications, Oxford, 1st edition, 1985.
- [63] S. R. Malkan. An overview of spunbonding and meltblowing. *Tappi J.*, 78(6):185–190, 1995.
- [64] M. Manninen and V. Taivassalo. On the mixture model for multiphase flow. *VTT Publications*, 288:1–67, 1996.
- [65] N. Marheineke, B. Liljegren-Sailer, M. Lorenz, and R. Wegener. Asymptotic and numerics for the upper-convected Maxwell model describing transient curved viscoelastic jets. *Math. Mod. Meth. Appl. Sci.*, 26(3):569–600, 2016.
- [66] N. Marheineke and R. Wegener. Fiber dynamics in turbulent flows: General modeling framework. *SIAM J. Appl. Math.*, 66(5):1703–1726, 2006.
- [67] N. Marheineke and R. Wegener. Asymptotic model for the dynamics of curved viscous fibres with surface tension. *J. Fluid Mech.*, 662:345–369, 2009.
- [68] N. Marheineke and R. Wegener. Modeling and application of a stochastic drag for fibers in turbulent flows. *Int. J. Multiphase Flow*, 37:136–148, 2011.
- [69] M. A. Matovich and J. R. A. Pearson. Spinning a molten threadline. Steady-state isothermal viscous flows. *Ind. Eng. Chem. Fundam.*, 8:512–520, 1969.
- [70] W. J. Moore. *Physical Chemistry*. Prentice-Hall, Inc., 3rd edition, 1962.
- [71] S. T. Munkejord, S. Evje, and T. Flatten. A MUSTA scheme for a non-conservative two-fluid model. *SIAM J. Sci. Comput.*, 31(4):2587–2622, 2009.
- [72] C. Norberg. Fluctuating lift on a circular cylinder: Review and new measurements. *J. Fluids Struct.*, 17:57–96, 2003.
- [73] S. Noroozi, H. Alamdari, W. Arne, R. G. Larson, and S. M. Taghavi. Regularized string model for nanofibre formation in centrifugal spinning methods. *J. Fluid Mech.*, 822:202–234, 2017.

- [74] Y. Ohzawa and Y. Nagano. Studies on dry spinning. I. Fundamental equations. *J. Appl. Polym. Sci.*, 13:257–283, 1969.
- [75] Y. Ohzawa and Y. Nagano. Studies on dry spinning. II. Numerical solutions for some polymer–solvent systems based on the assumption that drying is controlled by boundary-layer mass transfer. *J. Appl. Polym. Sci.*, 14(7):1879–1899, 1970.
- [76] M. N. Özisik. *Boundary Value Problems of Heat Conduction*. Dover Books on Engineering, 2013.
- [77] S. Panda, N. Marheineke, and R. Wegener. Systematic derivation of an asymptotic model for the dynamics of curved viscous fibers. *Math. Meth. Appl. Sci.*, 31(10):1153–1173, 2008.
- [78] L. S. Pinchuk, V. A. Goldade, A. V. Makarevich, and V. N. Kestelman. *Melt Blowing: Equipment, Technology and Polymer Fibrous Materials*. Springer, 2002.
- [79] D. H. Reneker and A. L. Yarin. Electrospinning jets and polymer nano fibers. *Polymer*, 49:2387–2425, 2008.
- [80] D. H. Reneker, A. L. Yarin, H. Fong, and S. Koombhongse. Bending instability of electrically charged liquid jets of polymer solutions in electrospinning. *J. App. Phys.*, 87(9):4531–4547, 2000.
- [81] N. M. Ribe. Coiling of viscous jets. *Proc. Roy. Soc. Lond., A*, 460(2051):3223–3239, 2004.
- [82] N. M. Ribe. Liquid rope coiling: a synoptic view. *J. Fluid Mech.*, 812:R2, 2017.
- [83] N. M. Ribe, M. Habibi, and D. Bonn. Stability of liquid rope coiling. *Physics of Fluids*, 18:268–279, 2006.
- [84] G. Riboux, A. G. Marin, I. G. Loscertales, and A. Barrero. Whipping instability characterization of an electrified visco-capillary jet. *J. Fluid Mech.*, 671:226–253, 2011.
- [85] J. Rivero-Rodríguez. *Estudio numérico de modelos unidimensionales en la interacción fluido-estructura y en la dinámica de chorros y gotas electrificados*. PhD thesis, Universidad de Sevilla, 2016.
- [86] J. Rivero-Rodríguez, W. Arne, N. Marheineke, R. Wegener, and M. Pérez-Saborid. Setup of viscous Cosserat rod model describing electrospinning. In R. Russo, V. Capasso, G. Nicosia, and V. Romano, editors, *Progress in Industrial Mathematics at ECMI 2014*, pages 985–992. Springer, 2016.

- [87] J. Rivero-Rodríguez and M. Pérez-Saborid. Numerical investigation of the influence of gravity on flutter of cantilevered pipes conveying fluid. *J. Fluids Structures*, 55:106–121, 2015.
- [88] Y. Sano. Drying behavior of acetate filament in dry spinning. *Drying Tech.*, 19(7):1335–1359, 2001.
- [89] S. Schießl. *Jet and Fiber Dynamics with High Elongations: Models, Numerical Strategies and Applications*. PhD thesis, FAU Erlangen-Nürnberg, 2017.
- [90] H. Schlichting and K. Gersten. *Grenzschicht-Theorie*. Springer, Berlin Heidelberg, 10th edition, 2006.
- [91] B. R. Shambaugh, D. V. Papavassiliou, and R. L. Shambaugh. Next-generation modeling of melt blowing. *Ind. Eng. Chem. Res.*, 50:12233–12245, 2011.
- [92] Y. M. Shin, H. H. Hohman, M. P. Brenner, and G. C. Rutledge. Experimental characterization of electrospinning: The electrically forced jet and instabilities. *Polymer*, 42:9955–9967, 2001.
- [93] S. Sinha-Ray, A. L. Yarin, and B. Pourdeyhimi. Meltblowing: I-basic physical mechanisms and threadline model. *J. Appl. Phys.*, 108(3):034912, 2010.
- [94] S. Sinha-Ray, A. L. Yarin, and B. Pourdeyhimi. Prediction of angular and mass distribution in meltblown polymer lay-down. *Polymer*, 54:860–872, 2013.
- [95] D. Sucker and H. Brauner. Stationärer Stoff- und Wärmeübergang an stationär quer angeströmten Zylindern. *Wärme- und Stoffübertragung*, 9(1):1–12, 1976.
- [96] Y. C. Sun, Y. F. Zeng, and X. H. Wang. Three-dimensional model of whipping motion in the processing of microfibers. *Ind. Eng. Chem. Res.*, 50(2):1099–1109, 2011.
- [97] Y. F. Sun, B. W. Liu, X. H. Wang, and Y. C. Zeng. Air-flow field of the melt-blowing slot die via numerical simulation and multiobjective genetic algorithms. *J. Appl. Polym. Sci.*, 122:3520–3527, 2011.
- [98] D. H. Tan, P. K. Herman, A. Janakiraman, F. S. Bates, S. Kumar, and C. W. Macosko. Influence of laval nozzles on the air flow field in melt blowing apparatus. *Chem. Eng. Sci.*, 80:342–348, 2012.

- 
- [99] D. H. Tan, C. Zhou, C. J. Ellison, and S. Kumar. Meltblown fibers: Influence of viscosity and elasticity on diameter distribution. *J. Non-Newtonian Fluid Mech.*, 165:892–900, 2010.
- [100] G. Taylor. Disintegration of water drops in an electric field. *Proc. Royal Soc. Lond., A*, 280(1382):383–397, 1964.
- [101] S. A. Theron, A. L. Yarin, E. Zussman, and E. Kroll. Multiple jets in electrospinning: Experiment and modeling. *Polymer*, 46(9):2889–2899, 2005.
- [102] S. A. Theron, E. Zussman, and A. L. Yarin. Experimental investigation of the governing parameters in the electrospinning of polymer solutions. *Polymer*, 45(6):2017–2030, 2004.
- [103] C. J. Thompson, G. G. Chase, A. L. Yarin, and D. H. Reneker. Effects of parameters on nanofiber diameter determined from electrospinning model. *Polymer*, 48(23):6913–6922, 2007.
- [104] M. A. J. Uyttendaele and R. L. Chambaugh. Melt blowing: general equation development and experimental verification. *AIChE J.*, 36(2):175–186, 1990.
- [105] D. W. van Krevelen. *Properties of Polymers*. Elsevier, Amsterdam, 3rd edition, 1990.
- [106] G. D. Verros and N. A. Malamataris. Estimation of diffusion coefficients in acetone-cellulose acetate solutions. *Ind. Eng. Chem. Res.*, 38:3572–3580, 1999.
- [107] J. S. Vrentas and J. L. Duda. Diffusion in polymer-solvent systems. I. Reexamination of the free-volume theory. *Polym. Phys.*, 15:403–416, 1977.
- [108] J. S. Vrentas and J. L. Duda. Diffusion in polymer-solvent systems. II. A predictive theory for the dependence of diffusion coefficients on temperature, concentration and molecular weight. *Polym. Phys.*, 15:417–439, 1977.
- [109] R. Wegener, N. Marheineke, and H. Hietel. Virtual production of filaments and fleeces. In H. Neunzert and D. Prätzel-Wolters, editors, *Currents in Industrial Mathematics: From Concepts to Research to Education*, pages 103–162. Springer, Berlin, Heidelberg, 1st edition, 2015.
- [110] M. Wieland, W. Arne, R. Feßler, N. Marheineke, and R. Wegener. Modeling and efficient simulation of dry spinning in airflows. *J. Comput. Phys.*, 384:326–348, 2018.

- [111] M. Wieland, W. Arne, R. Feßler, N. Marheineke, and R. Wegener. Product integration method for simulation of radial effects in dry spinning processes. In *PAMM – Proc. Appl. Math. Mech.*, volume 18, page e201800055. Wiley, 2018.
- [112] M. Wieland, W. Arne, R. Feßler, N. Marheineke, and R. Wegener. On a dry spinning model using two-phase flow. In I. Faragó, F. Izsák, and P. Simon, editors, *Progress in Industrial Mathematics at ECMI 2018*, pages 19–25. Springer, 2019.
- [113] M. Wieland, W. Arne, N. Marheineke, and R. Wegener. Melt-blowing of viscoelastic jets in turbulent airflows: Stochastic modeling and simulation. *Appl. Math. Model.*, 76:558–577, 2019.
- [114] M. Wieland, W. Arne, N. Marheineke, and R. Wegener. Model hierarchy of upper-convected Maxwell models with regard to simulations of melt-blowing processes. In *PAMM – Proc. Appl. Math. Mech.*, volume 19, page e201900018. Wiley, 2019.
- [115] M. Wieland, W. Arne, N. Marheineke, and R. Wegener. Modeling and simulation of curved fibers in dry spinning scenarios. *Results Appl. Math.*, 3:100013, 2019.
- [116] T. T. Wu and R. L. Shambaugh. Characterization of the melt blowing process with laser doppler velocimetry. *Ing. Eng. Chem. Res.*, 31(1):379–389, 1992.
- [117] X. F. Wu, Y. Salkovskiy, and Y. A. Dzenis. Modeling of solvent evaporation from polymer jets in electrospinning. *Appl. Phys. Lett.*, 98(22):223108, 2011.
- [118] S. Xie and Y. Zeng. Turbulent air flow field and fiber whipping motion in the melt blowing process: Experimental study. *Ind. Eng. Chem. Res.*, 51:5346–5352, 2012.
- [119] A. L. Yarin. *Free liquid jets and films: Hydrodynamics and rheology*. Longman, New York, 1993.
- [120] A. L. Yarin, S. Koombhongse, and D. H. Reneker. Bending instability in electrospinning of nanofibers. *J. Appl. Phys.*, 89(5):3018–3026, 2001.
- [121] A. L. Yarin, B. Pourdeyhimi, and S. Ramakrishna. *Fundamentals and Applications of Micro- and Nanofibers*. Cambridge University Press, 2014.
- [122] A. L. Yarin, S. Sinha-Ray, and B. Pourdeyhimi. Meltblowing: II-linear and nonlinear waves on viscoelastic polymer jets. *J. Appl. Phys.*, 108(3):034913, 2010.

- [123] A. L. Yarin, S. Sinha-Ray, and B. Pourdeyhimi. Meltblowing: Multiple polymer jets and fiber-size distribution and lay-down patterns. *Polymer*, 52:2929–2938, 2011.
- [124] Y. C. Zeng, Z. G. Pei, and X. H. Wang. Numerical simulation of whipping process in electrospinning. In S. Y. Chen and Q. Li, editors, *Proceedings of the 8th WSEAS International Conference on Applied Computer and Applied Computational Science (ACACOS '09)*, pages 309–317. WSEAS Press, 2009.
- [125] Y. C. Zeng, Y. F. Sun, and X. H. Wang. Numerical approach to modeling fiber motion during melt blowing. *J. Appl. Polym. Sci.*, 119:2112–2123, 2011.
- [126] Y. C. Zeng, Y. Wu, Z. G. Pei, and C. W. Yu. Numerical approach to electrospinning. *Int. J. Nonl. Sci. Num. Sim.*, 7(4):385–388, 2006.
- [127] H. Zerze and A. McHugh. Two-dimensional modeling of polymer wet spinning: The effects of mass transfer dynamics on structural properties. *J. Appl. Polym. Sci.*, 132(14):41772, 2015.
- [128] C. Zhou, D. H. Tan, A. P. Janakiraman, and S. Kumar. Modeling the melt blowing of viscoelastic materials. *Chem. Eng. Sci.*, 66:4172–4183, 2011.
- [129] A. Ziabicki. *Fundamentals of Fibre Formation*. John Wiley & Sons, 1976.

In the technical textile industry models and simulations of underlying manufacturing processes increasingly gain attention in order to optimize existing spinning devices. Since the underlying three-dimensional multiscale-multiphase problems require unfeasible computation times, direct numerical simulations of the fiber dynamics are not practical. Thus, the special Cosserat theory with one-dimensional descriptions of the fibers builds our model basis. In this work we suitably extended this model basis to describe all physically relevant effects present in industrial setups and develop problem tailored numerical solution strategies. To show the capability and efficiency of our model-simulation framework we investigate three industrial spinning processes: dry spinning, electrospinning, and melt-blowing. For the first time in literature we present simulation results of multiple dry spun fibers in a two-way interaction with an outer airflow, a detailed investigation of the fiber's whipping movement present in electrospinning utilizing a rotating reference frame as well as simulation results of melt-blown fibers including turbulent airflow effects leading to realistically thin fibers.

ISBN 978-3-8396-1573-7



**FRAUNHOFER VERLAG**